

Understanding Low-Energy Nuclear Recoils in Liquid Xenon for Dark Matter  
Searches and the First Results of XENON1T.

Matthew Duschl Anthony

Submitted in partial fulfillment of the  
requirements for the degree of  
Doctor of Philosophy  
in the Graduate School of Arts and Sciences

COLUMBIA UNIVERSITY

2017

© 2017  
Matthew D Anthony  
All rights reserved

ABSTRACT

Understanding Low-Energy Nuclear Recoils in Liquid Xenon for Dark Matter  
Searches and the First Results of XENON1T.

Matthew Duschl Anthony

[Abstract Text]



# Contents

<b>Contents</b>	<b>i</b>
<b>List of Figures</b>	<b>vii</b>
<b>Acknowledgements</b>	<b>xxiii</b>
<b>1 Dark Matter</b>	<b>1</b>
1.1 $\Lambda$ CDM Model . . . . .	1
1.2 Evidence of Dark Matter . . . . .	3
1.2.1 Dynamical Constraints from Clusters of Galaxies . . . . .	3
1.2.2 Dynamical Constraints from Galactic Rotation Curves . . . . .	3
1.2.3 Evidence from Gravitational Lensing . . . . .	5
1.2.4 Evidence from the Cosmic Microwave Background . . . . .	7
1.3 Dark Matter Candidates . . . . .	9
1.3.1 Axions . . . . .	10
1.3.2 WIMPs . . . . .	11
1.4 Detecting WIMPs . . . . .	12
1.4.1 Indirect Detection . . . . .	13
1.4.2 Collider Detection . . . . .	14
1.4.3 Direct Detection . . . . .	15
1.4.4 Direct Detection Experiments . . . . .	19
1.4.4.1 Heat . . . . .	19
1.4.4.2 Scintillation . . . . .	20

1.4.4.3	Ionization . . . . .	21
1.4.4.4	Heat-Scintillation . . . . .	22
1.4.4.5	Heat-Ionization . . . . .	22
1.4.4.6	Scintillation-Ionization . . . . .	22
<b>2</b>	<b>Liquid Xenon and Dual-Phase TPCs</b>	<b>25</b>
2.1	General Properties . . . . .	25
2.2	Energy Deposition of Charged Particles in Liquid Xenon . . . . .	28
2.3	Electronic Recoils in Liquid Xenon . . . . .	31
2.3.1	Sources of Electronic Recoils . . . . .	31
2.3.1.1	Beta Decays . . . . .	32
2.3.1.2	Photons . . . . .	33
2.3.1.3	Neutrons . . . . .	35
2.3.1.4	Neutrinos . . . . .	37
2.3.2	Observables Production for Electronic Recoils . . . . .	37
2.4	Nuclear Recoils in Liquid Xenon . . . . .	39
2.4.1	Sources of Nuclear Recoils . . . . .	39
2.4.1.1	Neutrons . . . . .	40
2.4.1.2	Neutrinos . . . . .	40
2.4.2	Observables Production for Nuclear Recoils . . . . .	41
2.5	Dual-Phase Time Projection Chambers . . . . .	44
2.5.1	Operating Principle . . . . .	44
2.5.1.1	Reconstructing Interaction Type . . . . .	45
2.5.1.2	Reconstructing Energy . . . . .	46
2.5.1.3	Reconstructing Position . . . . .	48
2.5.2	Detecting Observables . . . . .	50
2.5.2.1	Detection of Scintillation Photons: S1 . . . . .	50
2.5.2.2	Detection of Ionization Electrons: S2 . . . . .	52
<b>3</b>	<b>The First Dark Matter Search with XENON1T</b>	<b>57</b>
3.1	The XENON1T Detector . . . . .	57

3.1.1	Laboratori Nazionali del Gran Sasso . . . . .	58
3.1.2	Muon Veto . . . . .	58
3.1.3	Cryostat . . . . .	60
3.1.4	Cryogenics System . . . . .	63
3.1.5	Purification Systems . . . . .	64
3.1.5.1	Electronegative Impurities . . . . .	64
3.1.5.2	$^{85}\text{Kr}$ . . . . .	65
3.1.6	Recovery and Storage . . . . .	66
3.1.7	Calibration Systems . . . . .	66
3.1.8	Photomultiplier Tubes . . . . .	68
3.1.9	XENON1T TPC . . . . .	69
3.1.10	Data Acquisition and Processing . . . . .	70
3.2	The Background for the XENON1T Detector . . . . .	73
3.2.1	Background in XENON1T from Detector Materials . . . . .	73
3.2.2	Electronic Recoil Background in XENON1T . . . . .	73
3.2.2.1	$^{222}\text{Rn}$ . . . . .	74
3.2.2.2	$^{85}\text{Kr}$ . . . . .	76
3.2.2.3	Solar Neutrinos . . . . .	78
3.2.2.4	$^{136}\text{Xe}$ . . . . .	78
3.2.3	Nuclear Recoil Background in XENON1T . . . . .	78
3.2.3.1	Coherent Neutrino-Nucleon Scattering . . . . .	79
3.2.3.2	Nuclear Recoils from muon-induced neutrons . . . . .	80
3.3	The Calibration and Characterization of XENON1T for the First Science Run . . . . .	80
3.3.1	PMT Characterization . . . . .	80
3.3.2	Position Reconstruction . . . . .	81
3.3.3	Position Dependent Corrections . . . . .	84
3.3.3.1	S1 Position Correction . . . . .	84
3.3.3.2	S2 Transverse Position Correction . . . . .	86
3.3.3.3	S2 Depth Correction Correction: Electron Lifetime .	87

3.3.4	Single Electron Gain . . . . .	89
3.3.5	Average Light Collection Efficiency and Extraction Efficiency	90
3.3.6	Cut Acceptance . . . . .	92
3.4	Electronic and Nuclear Recoil Characterization of XENON1T . . . . .	93
3.4.1	Significance of the Calibrations . . . . .	94
3.4.2	Parameter Estimation via Monte Carlo . . . . .	94
3.4.2.1	Light and Charge Production for Electronic Recoils .	97
3.4.2.2	Light and Charge Production for Nuclear Recoils .	98
3.4.2.3	Detector Model for Signal Production . . . . .	103
3.4.2.4	Comparing Data and Monte Carlo . . . . .	110
3.4.2.5	Estimating the Posterior Probability Distribution Using a Markov Chain Monte Carlo . . . . .	111
3.4.3	ER and NR Calibration Results . . . . .	113
3.4.3.1	Results of the Electronic Recoil Calibration . . . . .	113
3.4.3.2	Results of the Nuclear Recoil Calibration . . . . .	115
3.4.4	Propagating Results to the WIMP Search . . . . .	119
3.5	Results of the First WIMP Search with XENON1T . . . . .	123
3.5.1	First Science Run Data . . . . .	123
3.5.2	Background Expectations . . . . .	124
3.5.3	Searching for WIMPs . . . . .	126

<b>4</b>	<b>Measuring the Low Energy Light and Charge Yield of Nuclear Recoils in Liquid Xenon</b>	<b>131</b>
4.1	Experimental Setup . . . . .	133
4.1.1	neriX Detector . . . . .	135
4.1.1.1	TPC . . . . .	136
4.1.1.2	Cryostat . . . . .	137
4.1.1.3	Purification and Cryogenics System . . . . .	139
4.1.1.4	Pressure Relief System . . . . .	140
4.1.1.5	Xenon Storage . . . . .	141

4.1.1.6	Electric Field Strength and Uniformity . . . . .	141
4.1.1.7	Data Acquisition System and Processing . . . . .	142
4.1.2	Neutron Generator . . . . .	142
4.1.2.1	Neutron Energy Spectrum . . . . .	144
4.1.2.2	Neutron Yield . . . . .	146
4.1.3	Liquid Scintillators . . . . .	148
4.1.4	Data Acquisition System . . . . .	150
4.2	Characterization and Calibration of neriX . . . . .	152
4.2.1	PMT Characterization . . . . .	154
4.2.2	Position Reconstruction and Position Dependence . . . . .	157
4.2.3	Single Electron Response . . . . .	160
4.2.4	Anticorrelation . . . . .	162
4.2.5	Trigger Efficiency . . . . .	163
4.2.6	Peak Finding Efficiency . . . . .	165
4.3	Nuclear Recoil Data Collection . . . . .	165
4.4	Analysis of Nuclear Recoils in Liquid Xenon . . . . .	172
4.4.1	Monte Carlo Simulation of Energy Spectra . . . . .	173
4.4.2	Light and Charge Production for Nuclear Recoils . . . . .	174
4.4.3	Detector Model for Signal Production . . . . .	177
4.4.3.1	Detection of Scintillation Photons . . . . .	178
4.4.3.2	Detection of Electrons . . . . .	179
4.4.4	Energy Inputs for Fast Monte Carlo . . . . .	180
4.4.5	Posterior Estimation . . . . .	181
4.4.6	Results . . . . .	182
4.4.6.1	Remarks on the Light and Charge Production Model	183
4.4.6.2	Remarks on the Detector Physics Model . . . . .	193
4.4.7	Systematic Uncertainties . . . . .	194
4.5	Conclusions . . . . .	194

<b>Appendix A GPUs and Fast Monte Carlo Matching for Parameter Estimation</b>	<b>213</b>
A.1 Motivation . . . . .	213
A.2 Parameter Estimation through Monte Carlo . . . . .	214
A.2.1 Overview . . . . .	214
A.2.2 Estimating the Likelihood Using Monte Carlo . . . . .	215
A.2.3 Drawbacks of Monte Carlo Likelihood Estimation . . . . .	216
A.3 Graphical Processing Units for Monte Carlo Matching for Parameter Estimation . . . . .	218
A.3.1 Graphical Processing Units . . . . .	218
A.3.2 GPU-Based MC Matching Framework . . . . .	218
A.3.3 Speed Gains for GPUs versus CPU . . . . .	220
A.3.4 Parallelizing GPUs . . . . .	220
A.4 Discussion . . . . .	222
<b>Appendix B Characterization of Photomultiplier Tubes with the Cascade Model</b>	<b>223</b>
B.1 Motivation . . . . .	223
B.2 The Cascade Single Photoelectron Charge Response Model . . . . .	224
B.3 Data Collection . . . . .	229
B.4 Results . . . . .	229
B.4.1 Response Characterizations . . . . .	229
B.4.2 Hamamatsu R11410 Analysis . . . . .	231
B.4.3 Hamamatsu R6041-406 Analysis . . . . .	235
B.5 Conclusions . . . . .	238

# List of Figures

1.1	A composite image of the Coma Cluster combining X-ray data and optical data. The gas in the cluster is shown in purple. Image Credit: X-ray - NASA/CXC/MPE/J.Sanders et al, Optical - SDSS . . . . .	3
1.2	The rotation curve of the galaxy NGC 6503 broken down into individual components: visible matter (dashed), gas (dotted), and dark matter (dash dotted) [3]. . . . .	4
1.3	A cartoon showing the deflection of light due to the warping of spacetime caused by the presence of a massive galaxy cluster. Note that for very strong lensing, one expects multiple images of the source object and sometimes even an Einstein Ring around the lense. Image Credit: NASA/ESA.	5
1.4	In this optical image you see the massive MACS J1149.6+2223 cluster. In the zoomed portion, you can actually see the same supernova, SN Refsdal, in four smaller images around a large galaxy within the cluster. Image Credit: HST. . . . .	6
1.5	Infrared (left) and X-ray (right) maps of the Bullet Cluster (1E0657-558). While the plasma in the clusters interacts during the collision of the two individual clusters, as is seen by the shockwave in the center, the majority of the mass passes right through [5]. . . . .	7
1.6	The Planck 2015 measurement of the temperature anisotropy of the CMB. Note that the largest deviations from the mean are on the order of $200\mu K$ from the $2.725$ K mean (roughly 1 in $10^4$ ). Image Credit: IRSA, Ref. [8].	8

1.7	The power spectrum of the temperature anisotropies measured by Planck along with the best fit prediction from the $\Lambda$ CDM model. $\mathcal{D}_l^{TT}$ is a proxy for $C_i$ and is defined $\mathcal{D}_l^{TT} \equiv l(l+1)C_l/2\pi$ . Image Credit: Ref. [8]. . . . .	9
1.8	The projected sensitivity of the ADMX Generation 2 axion search (shaded regions). Note that strong cosmological constraints are placed on the mass range and the axion coupling is also constrained by the mass. The ADMX collaboration predicts that the searches shown will be completed by 2022 [21]. . . . .	11
1.9	The three general approaches to WIMP detection: indirect detection, collider detection, and direct detection. Image Credit: [25]. . . . .	12
1.10	An image of a potential WIMP event in the CMS detector at CERN. If a WIMP is present in a collision, momentum would not be conserved after all jets and particles have been accounted for in the collision. Here we can see that after the three jets are reconstructed that there is still a large MET that could potentially be attributed to a WIMP. Image Credit: Matevz Tadel, UC San Diego/CMS. . . . .	14
1.11	On the left are the differential scattering rates for a $100 \text{ GeV}/c^2$ WIMP with a spin independent cross section of $10^{-47} \text{ cm}^2$ . On the right are the differential recoil spectra for WIMPs scattering with a xenon nuclei with a spin independent cross section of $10^{-47} \text{ cm}^2$ assuming different WIMP masses. . . . .	18
1.12	A diagram showing the possible observables and observable combinations along with the most common detector types for each. Image courtesy: [34]. . . . .	19
1.13	The annual modulation seen by the DAMA collaboration. The modulation is statistically significant yet is in contrast to other experiments who fail to see the same signal. Image Credit: [34]. . . . .	21

1.14 Spin-independent WIMP limits from selected experiments and the discovery contour from DAMA’s annual modulation. The dashed line shown in brown marks the point where neutrinos will become a background source in WIMP searches. Notice that the three liquid xenon dual-phase TPC based experiments (PandaX-II, LUX, and XENON1T) set the strongest limit over a wide range of WIMP masses [39, 47, 48, 50–55]. . . . .	23
2.1 The phase diagram for xenon. Dual-phase xenon TPCs typically operate in the range of 2–3 atm. . . . .	26
2.2 A diagram showing the modes in which charged particles may lose energy in liquid xenon. Note that when an electric field is applied, the electron freed during ionization can be extracted such that it can be measured. . . . .	29
2.3 The kinetic energy spectrum of electrons resulting from the $\beta^-$ decay of $^{85}\text{Kr}$ [68]. Note that roughly 3.1% of decays are below 15 keV (shaded red region) which puts them inside the energy region of interest of WIMP searches. . . . .	32
2.4 The mass attenuation coefficient and the attenuation lengths for photons of different energies in liquid xenon [73]. . . . .	34
2.5 The cross-sections of the three main interaction modes of neutrons in liquid xenon. Note that elastic scattering is the dominant process for almost all energies in the range shown. The data for each isotope of xenon is from Ref. [74] and the figure shows the cross-sections weighted by abundance of each isotope in natural xenon. . . . .	35
2.6 Solar neutrino fluxes from different processes assuming the BS05(OP) standard solar model. Image Credit: [78]. . . . .	37

2.7 An example of an interaction in a dual-phase liquid xenon time projection chamber. The interaction produces both scintillation light and free electrons. The light is promptly detected by the PMT arrays at the top and bottom of the detector while the free electrons are drifted to the liquid-gas interface where they are extracted and accelerated through the gaseous xenon. This acceleration through the gaseous xenon causes secondary excitations that result in more scintillation light that is detected by the PMT arrays. The time difference between these interactions can be used to extract the depth of the interaction while the PMT hit patterns for the secondary signal can be used to find the interactions position in the transverse plane. . . . .	45
2.8 Low energy electronic and nuclear recoils in liquid xenon. Note that for a given S1 that the S2 for electronic recoils are usually significantly higher than the corresponding S2 for nuclear recoils. The nuclear recoils are from an americium-beryllium (AmBe) source while the electronic recoils are from the $^{222}\text{Rn}$ decay chain that results in a $\beta^-$ emission with a maximum energy of 1.02 MeV. . . . .	47
2.9 The field dependence of scintillation and ionization yield in liquid xenon for 122 keV electronic recoils and 56.5 keV nuclear recoils. In blue are the light yields of interactions at a given field relative to the light yield with no applied electric field. In red are the charge yields of interactions relative to the charge yield assuming no recombination. Image Credit: Ref. [62] .	48
2.10 The positions of all events during the first science run of XENON1T. Notice that the overwhelming majority of events occur at the very edge of the detector and can be removed using a fiducial volume. . . . .	49
2.11 The waveform of the first event seen by XENON1T. . . . .	51
2.12 The Hamamatsu R11410 PMT and a schematic illustration of its various components. Image Credit: Ref. [95]. . . . .	52

2.13 An example of an electron lifetime analysis from XENON1T. In this analysis, the 41 keV $^{83m}\text{Kr}$ electronic recoil is used and the decay's S2 signal size is plotted versus drift time (a proxy for depth). Image Credit: Ref. [97].	54
2.14 An example of a gas gain analysis from XENON100. This fit was performed using electrons from photoionization of metal inside of the detector. Image Credit: Ref. [98].	55
3.1 The neutron flux due to cosmogenic muons versus kilometers water equivalent depth for various underground laboratories. Image Credit: Ref. [99].	58
3.2 A cartoon of the muon veto with the TPC centered inside the water tank.	59
3.3 A photo of the inside of the muon veto water tank. The 8" PMTs can be seen along the edges of the tank and the TPC can be seen in the center of the tank (left side of the photo).	60
3.4 A photo from inside the watertank with the inner cryostat installed. Note the mylar foil around the vessel for insulation against radiative heat transfer.	61
3.5 A diagram of the cryostat, the TPC, and the subsystems of each. Image Credit: Ref. [102].	62
3.6 A diagram of the cryostat, the cryogenics system, and the purification systems. Image Credit: Ref. [102].	63
3.7 A photograph of RESToX prior to instillation at LNGS.	67
3.8 A diagram showing the external calibration systems. The “U-Belt”, which allows for placement of external sources below the TPC, is shown in red while the “I-Belt”, which allows for the placement of external sources at different heights along the side of the TPC, is shown in blue. Shown in green is the neutron generator which can be raised and lowered along the side of the detector.	68

- 3.9 The quantum efficiencies of the PMTs installed in the XENON1T PMT arrays. Note that, with a few exceptions due to higher radioactivity levels, the highest quantum efficiency PMTs are placed towards the center to maximize light collection. Also note that in general the PMTs used in the bottom array have a higher quantum efficiency than those in the top array since the much smaller S1 signal is mainly seen by the bottom array. Image Credit: Ref. [97]. . . . .

3.10 The field simulations for the TPC during the first science run of XENON1T. During this run, a cathode voltage of  $-12$  kV was used and an anode voltage of  $+4$  kV was used. Image Credit: Ref. [97]. . . . .

3.11 The PAX output for the first waveform in XENON1T. Shown in blue is the S1 and shown in green is the S2. The grey highlighted areas represent unidentified peaks that are likely due to the high noise rate at this point in the detector operation. Also shown are the timestamps of each signal, used to extract the depth of the interaction, and the PMT hit patterns of the top and bottom PMT arrays, which are used for position reconstruction.

3.12 The electronic recoil energy spectrum expected from major background sources. While radiation from materials and the double beta decay of  $^{136}\text{Xe}$  dominate at high energies,  $^{222}\text{Rn}$  dominates at the lowest energies as can be seen here and in Fig. 3.13. This low energy region is of the most concern for dark matter searches. Image Credit: Ref. [77]. . . . .

3.13 The electronic recoil energy spectrum from background at low energies. Note that under 15 keV, the upper threshold for electronic recoils relevant to the dark matter search,  $^{222}\text{Rn}$  is the dominant source of electronic recoils. Image Credit: Ref. [77]. . . . .

3.14 The  $^{238}\text{U}$  (left) and  $^{232}\text{Th}$  (right) decay chains. The  $^{238}\text{U}$  chain ultimately produces an intrinsic and the largest background source of electronic recoils in XENON1T while the  $^{232}\text{Th}$  chain results in a very useful electronic recoil calibration source. Image Credit: Berkely Nuclear Forensics Group.

3.15 The energy spectra of the different sources of nuclear recoil background. Image Credit: Ref. [77]. . . . .	79
3.16 A fit of the low light response of one of the XENON1T PMTs in order to characterize the single photoelectron response. Image Credit: Ref. [107]. . .	82
3.17 A plot of the width of an S2 versus the drift time for 32 keV events from $^{83m}\text{Kr}$ . Note that at a certain drift time, no more events are seen. This cut-off in events represents the location of the cathode since interactions below it will not produce an S2. . . . .	83
3.18 The distribution of positions of 32 keV events from $^{83m}\text{Kr}$ during the first science run of XENON1T. . . . .	84
3.19 The S1 correction map of XENON1T. This correction map shows the relative light yield of events at specific positions relative to the average light yield of the detector for monoenergetic events. One can see the clear trend that events closer to the bottom PMT array have higher light yields than those closer to the liquid-gas interface. . . . .	85
3.20 The S2 transverse position correction map of XENON1T. This correction map shows the relative charge yield of events at specific positions relative to the average charge yield of the detector. One can see the trend for the bottom PMT array that events closer to the center of the detector have higher charge yields than events closer to the edges. . . . .	86
3.21 An example of an electron lifetime analysis from XENON1T. In this anal- ysis, the 41 keV $^{83m}\text{Kr}$ electronic recoil is used and the decay's S2 signal size is plotted versus drift time (a proxy for depth). Image Credit: Ref. [97].	88
3.22 The electron lifetime over the course of the first science run of XENON1T. Notice the two drops in the electron lifetime corresponding to periods when the purification system was not operating. Shown in red is a prediction of the electron lifetime given the detector operating parameters and out- gassing estimates from materials. . . . .	88

3.23 A fit of the single electron gain from the first science run of XENON1T. Hits are defined as excursions above threshold for individual PMTs in a time window defined by the waveform summed across all PMTs. . . . .	90
3.24 The Doke plot for XENON1T along with the best fit. Note that only the bottom PMT array is used for the S2 signal and that we use the position corrected values of S1 and S2. While the de-excitation from neutron captures in water is shown ( $^2\text{H}$ with an de-excitation energy of 2.225 MeV), it is not used for the fit. . . . .	92
3.25 The estimated cut acceptances in S1 and S2 for the first science run of XENON1T. . . . .	93
3.26 The probability distribution function for the first science run of XENON1T plotted with the cumulative density contours of a $50 \text{ GeV}/c^2$ WIMP. The combined signal and background PDF is used to either set a limit on the WIMP mass and cross section or claim a discovery. . . . .	95
3.27 A flowchart summarizing how a fast Monte Carlo is used to estimate the parameters in the signal production model. Orange steps are done in each iteration of the parameter estimation where as black arrows represent steps that are only done a single time. . . . .	96
3.28 The energy spectrum of single scatter and unresolvable multiple scatter nuclear recoils from the americium-beryllium (AmBe) source located in the water tank as predicted by Geant4. . . . .	100
3.29 The location of single scatter and unresolvable multiple scatter nuclear recoils from the americium-beryllium (AmBe) source located in the water tank as predicted by Geant4. . . . .	101
3.30 The estimated processor efficiency for identifying S1 signals in XENON1T. These efficiencies were found via simulation and the shaded region represents the equally probable values for the efficiency at a given photon level. . . . .	105
3.31 The estimated bias and smearing of S1 signals due to the processing of the waveform for scintillation signals. . . . .	106

3.32 The estimated bias and smearing of S2 signals due to the processing of the waveform for scintillation signals. . . . .	109
3.33 The PDF of accidental coincidence background events in $\log\left(\frac{cS2_b}{cS1}\right)$ versus cS1 space for the first dark matter run. . . . .	116
3.34 The best-fit PDF for electronic recoils during the $^{220}\text{Rn}$ electronic recoil calibration. Outside of the two outliers, the agreement between the model and data is extremely good. . . . .	117
3.35 Comparison of the band median and width during the electronic recoil calibration. One can see that the fit provides excellent agreement in the region of interest. . . . .	117
3.36 Comparison of the electronic recoil band in S1 signal space and S2 signal space in different S1 regions. Again, the band parameterization used describes the shape of the data very well. . . . .	118
3.37 The best-fit PDF for nuclear recoils during the AmBe nuclear recoil calibration. Both the electronic and nuclear recoil band can clearly be seen.	120
3.38 Shown on top is the nuclear recoil data in S1 space overlaid with the 68% credible region. In the middle panel is the nuclear recoil data in S1 and S2 signal space and in the bottom panel is the best-fit nuclear recoil Monte Carlo output in S1 and S2 signal space. Overlaid in both of these are the medians of each distribution. . . . .	121
3.39 The nuclear recoil data in S2 signal space for various cuts in S1 signal space overlaid with the 68% credible region. . . . .	122
3.40 Observed data in $cS2_b$ vs. $cS1$ for (a) $^{220}\text{Rn}$ electronic recoil calibration, (b) AmBe nuclear recoil calibration, and (c) the 34.2 day dark matter search. The lines shown represent the median (solid) and the $\pm 2\sigma$ (dashed) quantiles of the electronic and nuclear recoils band as measured in the relevant calibration. In panel (c), the purple distribution shows the estimated probability distribution function of a 50 $\text{GeV}/c^2$ WIMP. Only data above 3 PE is used in all analyses (unused data shown in gray box).	
Image Credit: Ref. [48]. . . . .	125

3.41 The expected backgrounds and their rates during the first science run of XENON1T. The electronic recoil and nuclear recoil backgrounds were found by inputting their respective energy spectra into the signal models found via the calibrations discussed earlier. The remaining background spectra were determined empirically. . . . .	127
3.42 The spin-independent WIMP-nucleon cross section limits as a function of WIMP mass at 90% confidence level (black) for this run of XENON1T. In green and yellow are the $1\sigma$ and $2\sigma$ sensitivity bands. Shown for reference are the final XENON100 results [125] and the most recent results from LUX [53] and Panda-X II [49]. Image Credit: Ref. [48]. . . . .	129
4.1 A schematic for the experimental setup used in this measurement of the light and charge yields for nuclear recoils. 2.45 MeV neutrons are produced at an angle of $\frac{\pi}{2}$ in the neutron generator. Some of these neutrons scatter a single time in the liquid xenon and then deposit some of their energy in the M510 detectors, filled with EJ301 liquid scintillator, for discrimination versus background. Image Credit: Ref. [128]. . . . .	134
4.2 A photo of the fixed-angle scattering setup with the neriX detector. On the left is our neutron generator inside of its stainless steel case. In the center is the outer portion of the cryostat and on the right are four of the M510 liquid scintillator detectors. . . . .	135
4.3 Two photos of the neriX TPC following routine detector maintenance. In both photos, one can see the plates holding the single 2" PMTs (bottom) and the array of four 1" PMTs (top). In the left image, one can see the high voltage feedthrough for the anode. In the right image, one can see the high voltage feedthrough for the cathode and the voltage divider for the field shaping ring. One can also see the stainless steel pipe used to extract xenon from the inner cryostat's buffer and the plastic tube used to feed re-condensed xenon into the system. . . . .	137
4.4 The neriX TPC with meshes and PMTs labelled. . . . .	138

4.5	A photo of one of the meshes used in neriX. . . . .	138
4.6	The neriX TPC inside of the cryostat. Note that excluding the buffer volume (left side of the image) and the space left for the high voltage feedthroughs (right side of the image), very little space is left between the cryostat and the TPC, effectively reducing the amount of inactive xenon for undetectable energy losses. . . . .	139
4.7	A schematic of the cryogenics and purification system for neriX. Also shown are the pressure relief system and the xenon storage system. . . .	140
4.8	The deuterium-deuterium neutron generator used to produce 2.45 MeV neutrons. . . . .	143
4.9	The electronics of the minitron neutron generator. Image Credit: Ref. [131].	144
4.10	On the left, the minitron in its partially constructed case. Notice that the teflon leaves very little room between the steel and minitron to maximize the potential voltage that can be used without causing an electrical breakdown. On the right, the minitron in its final set position. While not visible, the minitron case has been filled with mineral oil at this point to reduce risk of electrical breakdowns. . . . .	145
4.11	The expected angular distribution of neutrons as a function of emission angle for a maximum deuteron energy of 80 keV. . . . .	147
4.12	The NP-2 neutron detector signal rate as a function of beam current, holding the high voltage fixed, and high voltage, holding the beam current fixed. Shaded regions represents 68% credible region while dotted lines show the best fits. . . . .	149
4.13	The expected neutron flux from the minitron neutron generator at a distance of 180 cm at an angle of $\frac{\pi}{2}$ . . . . .	149
4.14	Discrimination space for one of the four M510 detectors from coincidence data. Notice that a hardware cut is made via a threshold discriminator at approximately 500 mV in order to remove events with poor pulse shape discrimination. . . . .	150

4.15	The trigger schematic for the neriX nuclear recoil measurement. For details on the triggers please refer to the text in Sec. 4.1.4. . . . .	153
4.16	The fit of the cascade (blue) and Gaussian (red) single photoelectron response model for the bottom PMT at 800 V. The statistics shown are for the cascade model which results in a marginally better fit as can be seen from the log likelihood difference. The dotted lines shown are the best fits and the shaded region is the 68% credible region. . . . .	156
4.17	The 68% credible region for the single photoelectron response for fully-amplified electrons for the bottom PMT at 800 V. Notice that the Gaussian model (red) results in a non-physical response a non-negligible fraction of the time while the cascade model (blue) does not exhibit this behavior. . . . .	156
4.18	On the left is the neriX MPE spectrum for the bottom PMT including the collection efficiency function shown on the right. . . . .	157
4.19	The spatial distributions of high-energy nuclear recoil events taken at 490 V/cm after fiducial volume and other quality cuts. . . . .	158
4.20	The distribution of small S2s in time after a large S2 at a field of 1020 kV/cm. Notice the two sharply spike peaks around 1.5 and 13 $\mu$ s — these peaks are due to electrons from the photoionization of the gate and cathode mesh, respectively. Since we know the distance between these two meshes we can measure the drift velocity at this field. . . . .	159
4.21	The depth correction of the S1 (left) and S2 (right) signals as a function of depth in the detector. . . . .	160
4.22	The single electron response as measured by the top and bottom PMTs in neriX. Note that the response, even for a single electron, appears to follow a Gaussian distribution. The contours show the outline of the fit and the pink line represents the edge of the fit range. . . . .	161
4.23	Anticorrelation analysis performed on the full absorption peaks $^{137}\text{Cs}$ and $^{22}\text{Na}$ at five different electric fields. One can also see the best fit of the model shown overlayed. . . . .	163

4.24 The neriX trigger efficiency as measured using a random trigger. Shown overlaid are the best fit alongside the 68% credible region. . . . .	164
4.25 The neriX peak finding efficiency from empirically based waveform simulations. . . . .	166
4.26 Coincidence data taken with a drift field of 190 V/cm. . . . .	168
4.27 Coincidence data taken with a drift field of 490 V/cm. . . . .	169
4.28 Coincidence data taken with a drift field of 1020 V/cm. . . . .	170
4.29 High energy nuclear recoil band data without a coincidence trigger at the three fields measured. . . . .	171
4.30 The expected energy spectra for coincidence data (top) and nuclear recoil band data (bottom). Both of these are used as inputs for the fast Monte Carlo used to estimate the PDF given assumptions on parameters in the signal response model. . . . .	175
4.31 Coincidence data taken with a drift field of 190 V/cm compared to Monte Carlo generated spectra. From top to bottom: data in two-dimensions, the best-fit results in two dimensions, data projected into S1 space overlaid with the best-fit model and 68% credible region, and data projected into S2 space in different S1 regions overlaid with the best-fit model and 68% credible region. . . . .	184
4.32 Coincidence data taken with a drift field of 490 V/cm compared to Monte Carlo generated spectra. From top to bottom: data in two-dimensions, the best-fit results in two dimensions, data projected into S1 space overlaid with the best-fit model and 68% credible region, and data projected into S2 space in different S1 regions overlaid with the best-fit model and 68% credible region. . . . .	185

4.33 Coincidence data taken with a drift field of 1020 V/cm compared to Monte Carlo generated spectra. From top to bottom: data in two-dimensions, the best-fit results in two dimensions, data projected into S1 space overlaid with the best-fit model and 68% credible region, and data projected into S2 space in different S1 regions overlaid with the best-fit model and 68% credible region. . . . .	186
4.34 The high-energy nuclear recoil band data at all three fields compared to Monte Carlo generated spectra. From top to bottom: data in two-dimensions, the best-fit results in two dimensions, data projected into S1 space overlaid with the best-fit model and 68% credible region, and data projected into S2 space in different S1 regions overlaid with the best-fit model and 68% credible region. . . . .	187
4.35 Our estimate of the posterior for the light and charge production model from the MCMC. . . . .	190
4.36 Measured light and charge yields in this work (red, green, and blue band) compared with previous measurements [62, 115, 124, 126, 128, 139, 141–143]. The red, green, and blue bands are the results from using the physical observables model while the points come from the matching technique used in previous fixed-angle scattering measurements. The reference line is the best-fit global result from Ref. [86] at 490 V/cm. An energy cutoff of 3 keV is chosen as this represents an approximately 10% detection efficiency assuming a light yield of 5.5 photons/keV and charge yield of 7.5 electrons/keV (shown in gray). Note that all measurements of light yield with the exception of this work and of Ref. [124] are extrapolations from $\mathcal{L}_{eff}$ using a light yield of 63 photons/keV for 122 keV electronic recoils.. . . . .	191

A.1 The memory flow in the Monte Carlo Matching Framework. The black arrows represent memory transfers that are performed a single time while orange arrows represent memory transfers that are performed in each log-likelihood calculation. . . . .	220
A.2 The GPU-based server used for the analyses in this work. The actual GPU cards can be seen towards the back of the server (three on the left and right sides). . . . .	221
B.1 The three possible scenarios for photoelectrons in the cascade model. Scenario 1 shows the standard full-amplification: a photon is absorbed in the photocathode and an electron is amplified through the dynode chain. Scenario 2 shows a non-ideal trajectory: a photon is absorbed in the photocathode but the electron follows a slightly different trajectory, due to field imperfections, and suffers a slightly lower amplification. Scenario 3 shows a photon passing through the photocathode and releasing an electron on the first dynode. Note that in this scenario the amplification at each dynode may depend on where the incident photon strikes the first dynode. . . . .	226
B.2 The laser calibration charge spectra for the R11410 PMT at different voltages and attenuation levels with the best-fit models and 95% credible regions overlaid. The cascade model is shown in blue while the Gaussian model is shown in red. The statistics shown are for the cascade model. .	234



# Acknowledgements

[Acknowledgments]



To my parents, Elizabeth and Robert, and my wife, Laura.

*If I have seen further it is by standing on the shoulders of giants.*



# Chapter 1

## Dark Matter

For nearly a century, experimental evidence has suggested that a large portion of the universe is made up of a non-luminous type of matter. While this dark matter has only been detected indirectly via its interaction with normal matter through the gravitational force, recent experiments conclude that approximately 26% of the entire energy density of the universe is comprised by dark matter.

In this chapter, I will focus on the leading dark matter model, the experimental evidence for its existence, the different candidates for particle dark matter, and the current detection methods employed in the search for particle dark matter.

### 1.1 $\Lambda$ CDM Model

One of the guiding principles of cosmology are the assumptions that the universe is both homogeneous and isotropic at large enough scales (typically on the order 100 Mpc or  $10^5$  light years). Continuing with these principles and maintaining generality, we can arrive at the Robertson-Walker space-time metric

$$ds = -c^2 dt^2 + a(t)^2 \left( \frac{dr^2}{1 - kr^2} + r^2 d\Omega^2 \right) \quad (1.1)$$

Here,  $a(t)$  is called the *scale factor*, an arbitrary function of time allowing for time dependent changes of the universe, and  $k$  is a constant modeling the curvature of the

## 1. DARK MATTER

---

universe. For  $k = -1$ , the universe is considered open, for  $k = 1$ , the universe is considered closed, and at  $k = 0$  we are left with our Euclidean (flat) universe. Note that for  $a(t) = 1$  and  $k = 0$  the Robertson-Walker metric reduces to the Minkowski metric.

Using this metric in combination with Einstein's equation we can derive the equations for the Friedmann-Robertson-Walker universe described by the Friedmann equations.

$$\frac{\ddot{a}}{a} = -\frac{4\pi G}{3} (\rho + 3p) \quad (1.2)$$

$$\left(\frac{\dot{a}}{a}\right)^2 = \frac{8\pi G}{3}\rho - \frac{k}{a^2} \quad (1.3)$$

We can define several useful (and commonplace) parameters to simplify the second Friedmann equation further.

**Hubble Parameter:**  $H = \frac{\dot{a}}{a}$

**Critical Density:**  $\rho_{crit} = \frac{3H^2}{8\pi G}$

**Density Parameters:**  $\Omega_i = \frac{8\pi G \rho_i}{3H^2} = \frac{\rho_i}{\rho_{crit}}$

$$\Omega - 1 = \frac{k}{H^2 a^2}, \quad \Omega = \sum_i \Omega_i = \Omega_\Lambda + \Omega_{CDM} + \Omega_{Baryon} + \Omega_{Rad} \dots \quad (1.4)$$

Here the critical density is defined such that the universe is flat ( $k = 0$ ). One can think of  $\frac{\Omega_i}{\Omega}$  as what part of the total matter and energy budget a particular component makes up. The main contributors to the density of the universe are dark energy and cold dark matter hence the  $\Lambda$ CDM Model. The density parameters give insight into the large scale structure of the universe and measurements of the various density parameters and other  $\Lambda$ CDM parameters has been a major focus of research over the last two decades and will be discussed later in this chapter [1].

## 1.2 Evidence of Dark Matter

### 1.2.1 Dynamical Constraints from Clusters of Galaxies

The first evidence of dark matter came from Fritz Zwicky in 1933. Zwicky used a basic application of the virial theorem on galaxies in the Coma Cluster to estimate the mass of the cluster. He then estimated the total mass based on the brightness of the cluster and found significant disagreement between the results leading him to the conclusion that “if this would be confirmed we would get the surprising result that dark matter is present in much greater amount than luminous matter” [2].



Figure 1.1: A composite image of the Coma Cluster combining X-ray data and optical data. The gas in the cluster is shown in purple. Image Credit: X-ray - NASA/CXC/MPE/J.Sanders et al, Optical - SDSS

### 1.2.2 Dynamical Constraints from Galactic Rotation Curves

Nearly forty years later, stronger evidence was provided for the existence of dark matter by Vera Rubin and Kent Ford in their 1970 paper looking at the rotation curve of the Andromeda Galaxy [4]. In this paper, Rubin used the H $\alpha$  lines to determine the

## 1. DARK MATTER

---

orbital velocities of different stars in the galaxy. Later measurements used the 21 cm hyperfine transition line to measure orbital velocities within other galaxies and the results of one of these measurements, Ref. [3], is shown in Fig. 1.2.

From simple Newtonian arguments, one gets the following description of the orbital velocity inside a galaxy:

$$v(r) = \sqrt{\frac{GM(r)}{r}} \quad (1.5)$$

In this equation,  $M(r)$  is the sum of all the mass within a radius  $r$ . Under the assumption that most of the mass is concentrated at the center of the galaxy (in the form of a supermassive blackhole), one would expect that at large distances from the center of the galaxy, the orbital velocity would fall off as  $v \propto r^{-1/2}$ .

However, what is seen differs from this simple approximation drastically. Fig. 1.2 is taken from Ref. [3] but the results are similar to what Rubin and Ford saw decades earlier: the asymptotic behavior of the orbital velocity is constant and does not show any polynomial roll-off. By isolating the contributions from measurable mass densities (such as visible matter and gas), one can get an idea of the density distribution of dark matter in a galaxy. From the figure below, one could asymptotically estimate

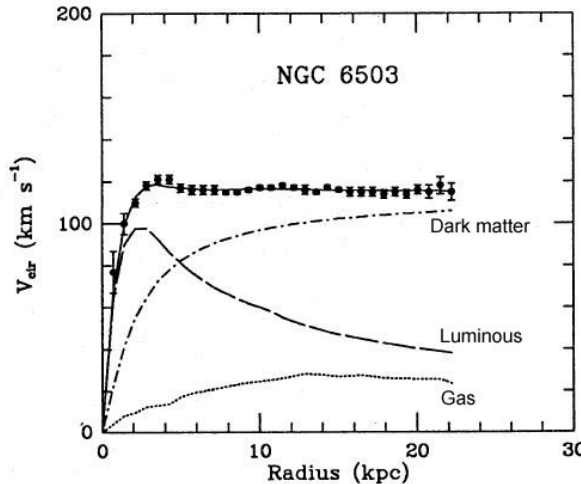


Figure 1.2: The rotation curve of the galaxy NGC 6503 broken down into individual components: visible matter (dashed), gas (dotted), and dark matter (dash dotted) [3].

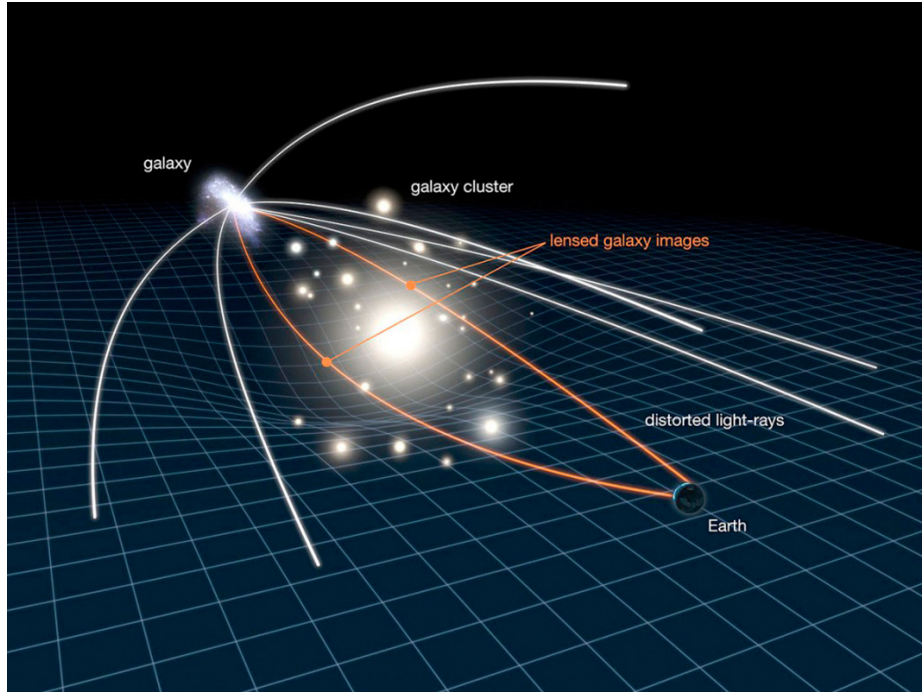


Figure 1.3: A cartoon showing the deflection of light due to the warping of spacetime caused by the presence of a massive galaxy cluster. Note that for very strong lensing, one expects multiple images of the source object and sometimes even an Einstein Ring around the lense. Image Credit: NASA/ESA.

that  $M(r) \propto r$  which would imply that  $\rho(r) \propto r^{-2}$ . One quickly realizes that this cannot be the true density since the mass of the galaxy diverges but approximates the density within an effective radius.

### 1.2.3 Evidence from Gravitaional Lensing

Gravitational lensing is the distortion of light coming from a source due to the warping of spacetime from the presence of large amounts of matter or energy. This effect is illustrated in Fig. 1.3 and actually captured in the form of an Einstein Cross in Fig. 1.4. In a gravitational lensing system, if we know the redshift (distance) of the source and the lens, we can estimate the gravitational field of the lensing system and hence its mass.

Mass estimation via gravitational lensing in itself is very useful for finding large discrepancies in mass from known sources and true mass (the discrepancy being

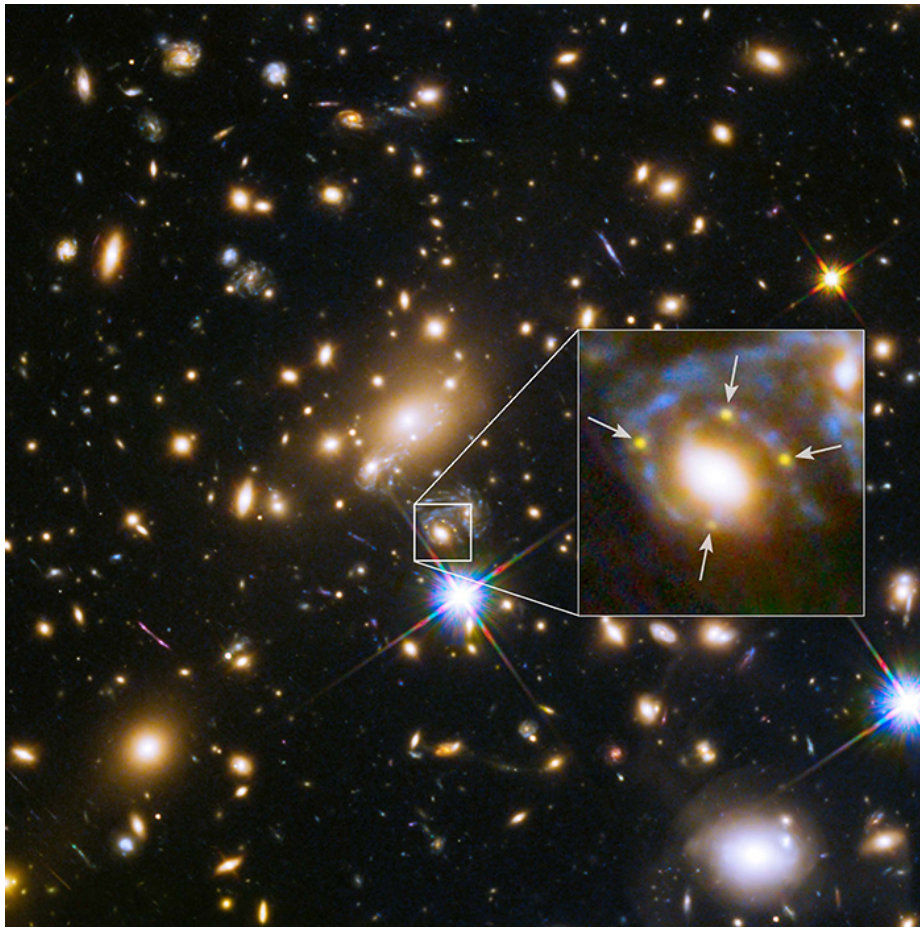


Figure 1.4: In this optical image you see the massive MACS J1149.6+2223 cluster. In the zoomed portion, you can actually see the same supernova, SN Refsdal, in four smaller images around a large galaxy within the cluster. Image Credit: HST.

attributed to dark matter). However, when combined with x-ray measurements, as seen in Fig. 1.5, one gets even more interesting results. Shown in Fig. 1.5 is the Bullet Cluster (1E0657-558) which actually consists of two colliding sub-clusters. In the image on the left, one can see the infrared image from Magellan that is used, along with optical images from Hubble, to estimate the mass distribution of each galaxy cluster through gravitational lensing. In the right image, one can see the X-ray map of the Bullet Cluster from the Chandra X-ray observatory with the same mass contours: one can see that the plasma from the clusters interacts giving the cone shapes in the center. However, the mass contours largely remain centered on the individual clusters (as seen in the optical image) implying that the majority of the matter interacted

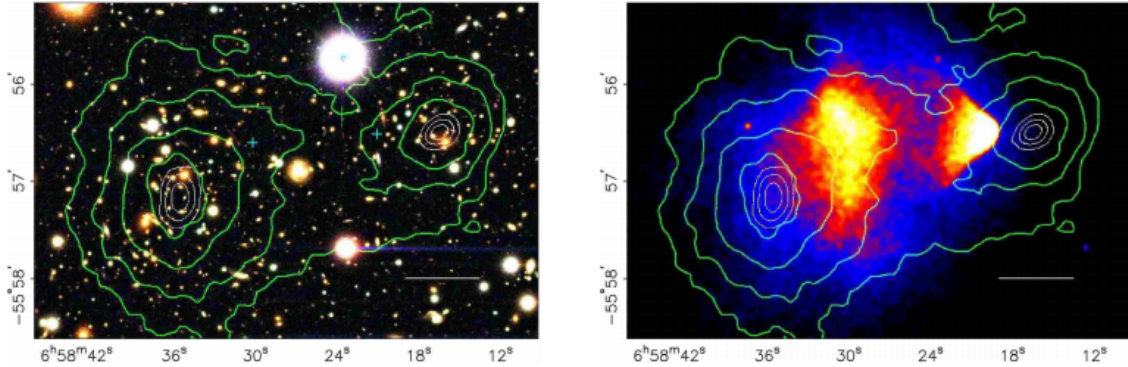


Figure 1.5: Infrared (left) and X-ray (right) maps of the Bullet Cluster (1E0657-558). While the plasma in the clusters interact during the collision of the two individual clusters, as is seen by the shockwave in the center, the majority of the mass passes right through [5].

minimally during the collision [5]. Since we know that the galaxies make up only a small fraction of the mass in a cluster from the virial theorem, this implies that the dark matter hardly interacts with itself or ordinary matter.

#### 1.2.4 Evidence from the Cosmic Microwave Background

The Cosmic Microwave Background (CMB) has proven to be one of the richest discoveries in all of cosmology. Accidentally discovered in 1964 by Penzias and Wilson [6], the radiation from the CMB is almost perfectly isotropic and described by a blackbody spectrum at 2.725 K [7]. The isotropy in the CMB provides the strongest evidence to date of the Big Bang Hypothesis. It helped to formulate our current picture of the early universe down to the recombination epoch, where the universe was sufficiently cool such that hydrogen could form from the free electrons and protons in turn allowing photons to travel freely through the universe.

As the CMB has been studied in more detail, cosmologists began to see that there are in fact very small temperature fluctuations on the order of  $\lesssim 100 \mu K$  [8–10]. These temperature fluctuations, as seen in the 2015 measurement of the CMB by the Planck satellite, are shown in Fig. 1.6. To characterize the temperature fluctuations of the entire sky, we use the spherical harmonics,  $Y_{lm}(\theta, \phi)$ .

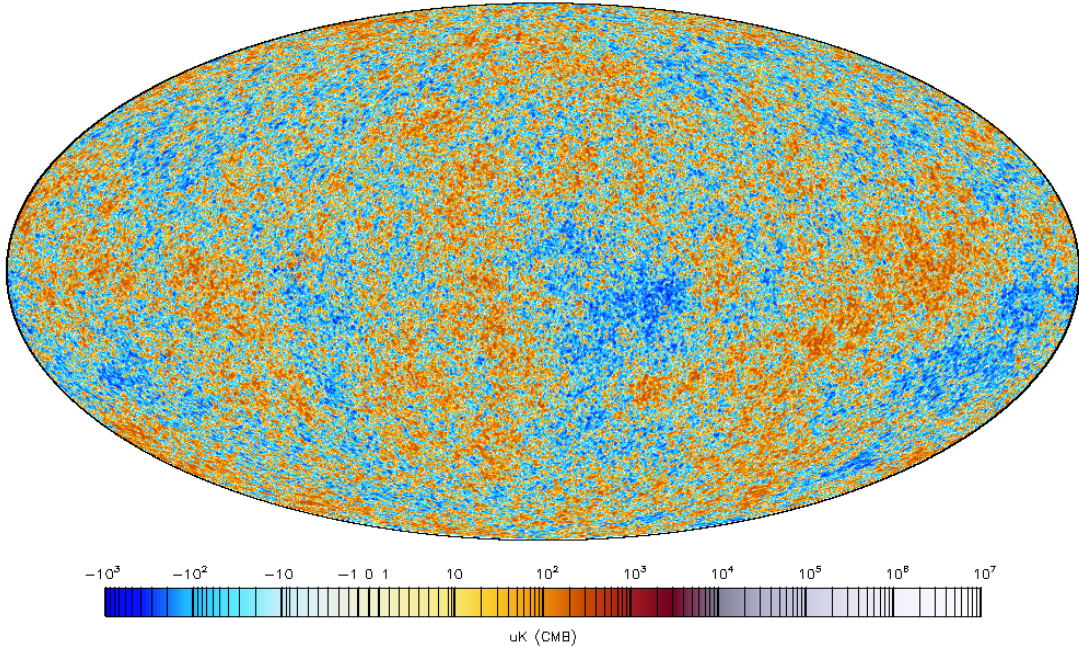


Figure 1.6: The Planck 2015 measurement of the temperature anisotropy of the CMB. Note that the largest deviations from the mean are on the order of  $200\mu K$  from the  $2.725\text{ K}$  mean (roughly  $1$  in  $10^4$ ). Image Credit: IRSA, Ref. [8].

$$T(\theta, \phi) = \sum_{l=0}^{\infty} \sum_{m=-l}^l a_{lm} Y_{lm}(\theta, \phi) \quad (1.6)$$

We assume that the distribution of  $a_{lm}$  should be described by a Gaussian distribution, as predicted by inflation, with a mean of  $2.725\text{ K}$  for any given multipole moment  $l$ . Therefore, the only piece missing to completely describe these  $a_{lm}$  for each multiple moment is the variance of this distribution so we define  $C_l \equiv \langle |a_{lm}|^2 \rangle$ . These  $C_l$  form the power spectrum of the CMB and can be used to test various formation models of the universe. Planck tested the  $\Lambda$ CDM model described in Sec. 1.1 against their power spectrum (Fig. 1.7) and found remarkable agreement between prediction and data while constraining some of the universal constants including  $H_0$ ,  $\Omega_\Lambda$ ,  $\Omega_{CDM}$ ,  $\Omega_{Baryon}$ , and  $\Omega_{Rad}$ . It is from this fit that we find that our universe has a curvature very close to zero and therefore is flat and that our universe is comprised of roughly 68.3% dark energy, 26.8% dark matter, and 4.9% ordinary matter [8].

The  $\Lambda$ CDM model has been tested since its inception using N-body simulations

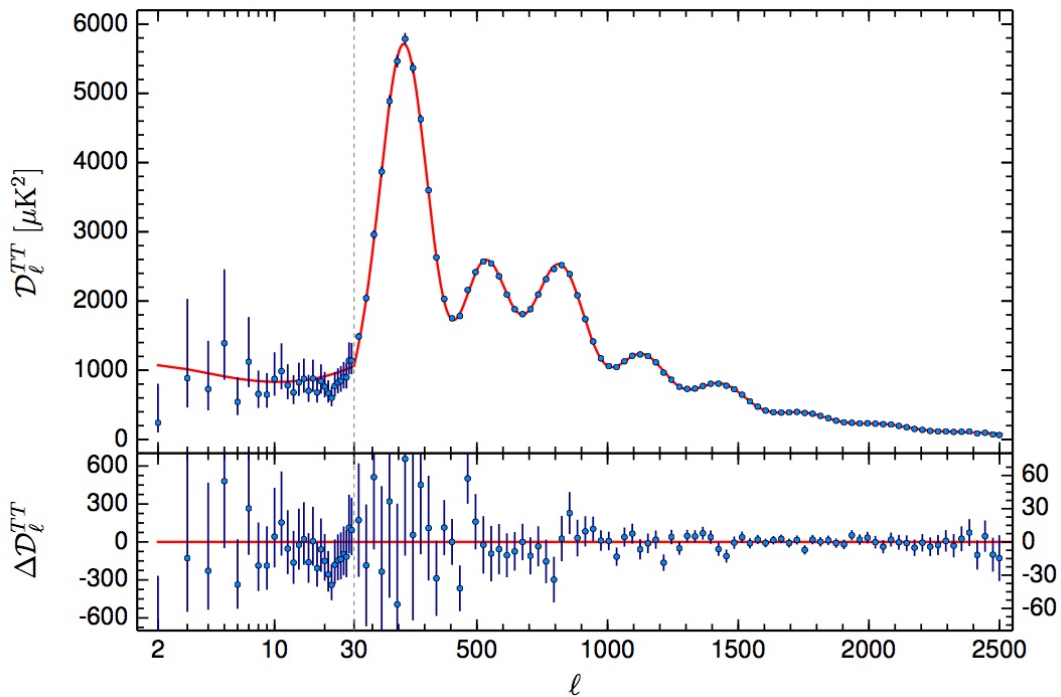


Figure 1.7: The power spectrum of the temperature anisotropies measured by Planck along with the best fit prediction from the  $\Lambda\text{CDM}$  model.  $\mathcal{D}_\ell^{TT}$  is a proxy for  $C_i$  and is defined  $\mathcal{D}_\ell^{TT} \equiv l(l+1)C_\ell/2\pi$ . Image Credit: Ref. [8].

to propagate the formation of large-scale structure in the universe. While small discrepancies between simulation and observation have been found, it is clear from these simulations that without cold dark matter it is extremely difficult to explain the large scale structure we see in the universe given the anisotropies of the CMB [11–13].

## 1.3 Dark Matter Candidates

While there is an abundance of evidence to suggest that dark matter exists, we have little evidence to suggest what this cold dark matter actually is. In this section, we will discuss two of the most popular candidates for dark matter and their physical motivations. It should be noted that the candidates discussed do not form an exhaustive list but do satisfy the most basic requirements of a dark matter candidate:

- The lifetime of the particle is much greater than the age of the universe (or is stable)
- The particle must be electrically neutral and interact very weakly with ordinary matter
- The particle must be able to provide the correct relic density of cold dark matter predicted by the CMB

### 1.3.1 Axions

Axions are hypothetical Standard Model particles that are introduced via the Peccei-Quinn mechanism as a solution to the strong-CP problem, one of the largest remaining deficiencies in the Standard Model [14]. CP (charge and parity) symmetry violation is required to explain the imbalance of matter and antimatter in the universe (why more matter exists) and has been observed in electroweak theory in a wide variety of measurements [15–19]. CP violation has never been observed in quantum chromodynamics (QCD) even though there is a natural term in the QCD Lagrangian that would allow it. Therefore, this term in the Lagrangian, must be fine-tuned to exactly zero, hence the strong-CP problem. The axion introduced by Peccei-Quinn theory replaces this term with a field and gives the Lagrangian natural CP symmetry.

While the discovery of the axion would solve one of the largest problems of Standard Model, it also has the potential to solve one of the largest open mysteries of cosmology by making up at least a part of the cold dark matter density of the universe. Even though the axion is expected to have a very small mass ( $10^{-6} - 10^{-2}$  eV) it could still be produced cosmologically such that the large scale structure that we observe in the universe today is explained and we arrive at the CDM density estimated by Planck [20].

There are a number of experiments that can provide information about axions, both directly and indirectly. The mass range of axions is essentially restricted from cosmological evidence from the CMB and stellar evolution. Simultaneously, cavity microwave experiments such as ADMX [21] and NMR based searches such as CASPeR [22] try to directly detect these low mass CDM candidates.

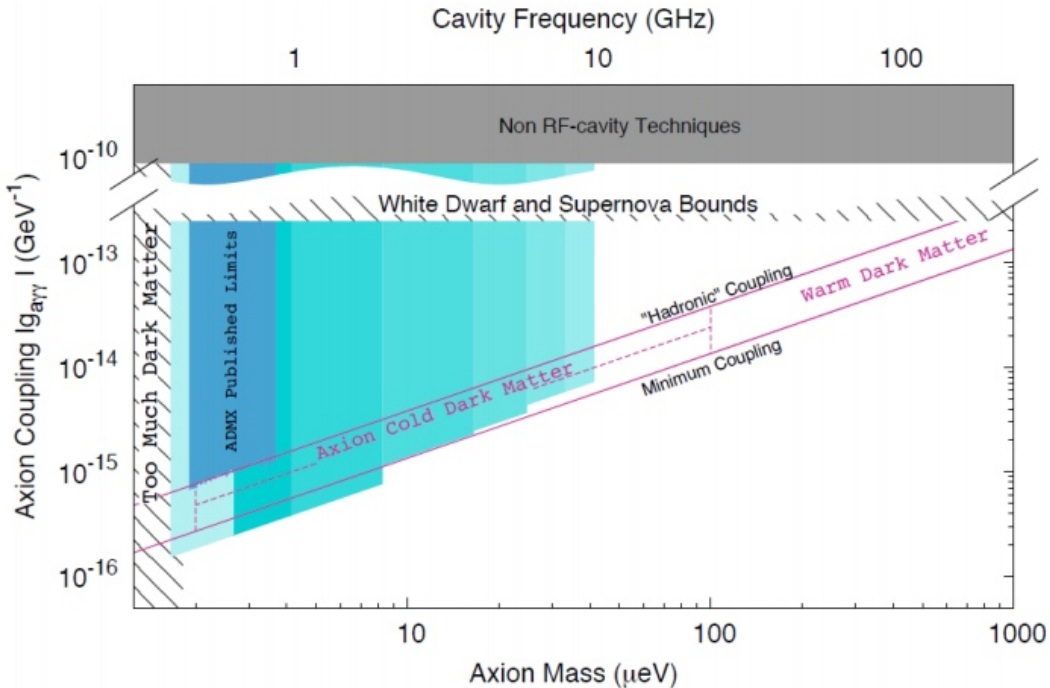


Figure 1.8: The projected sensitivity of the ADMX Generation 2 axion search (shaded regions). Note that strong cosmological constraints are placed on the mass range and the axion coupling is also constrained by the mass. The ADMX collaboration predicts that the searches shown will be completed by 2022 [21].

### 1.3.2 WIMPs

Weakly interacting massive particles (WIMPs), which will be the focus of the remainder of this work, have proven to be the most popular dark matter candidate historically. WIMPs not only satisfy the basic criteria listed at the beginning of this section but additionally they appear to agree with the observed relic density of cold dark matter in what is referred to as the “WIMP Miracle”. In the early stages of the universe, the temperature and density were so large that all particles were in a state of chemical equilibrium. A dark matter particle could annihilate by colliding with its anti-particle partner to form any type of particle and vice versa. As time passed, however, the universe expanded and cooled making it more unlikely for these dark matter particles to be created or destroyed. Using this thermal equilibrium model alongside the  $\Lambda$ CDM model, one can infer that the CDM density in the universe today is approximately given by [23, 24]

$$\Omega_{CDM} h^2 \approx \frac{3 \times 10^{-27} \text{cm}^3 \text{s}^{-1}}{\langle \sigma_{ann} v \rangle} \quad (1.7)$$

where  $\langle \sigma_{ann} v \rangle$  is thermally averaged annihilation cross-section of cold dark matter. Incredibly enough, if we assume that cold dark matter has properties such as cross-section and mass on the weak scale, we find that  $\Omega_{CDM} h^2 \approx 0.1$ , which is in agreement with cosmological constraints.

In addition to WIMPs agreeing with cosmological evidence, several WIMP-like particles that have masses on the order of 100 GeV and very long lifetimes naturally fall out of extensions of the Standard Model, such as supersymmetry.

## 1.4 Detecting WIMPs

Over the last few decades there has been an enormous concerted effort to detect WIMPs. This effort has been focused in three general approaches: indirect detection, collider detection, and direct detection. Fig. 1.9 shows the idea behind these approaches:

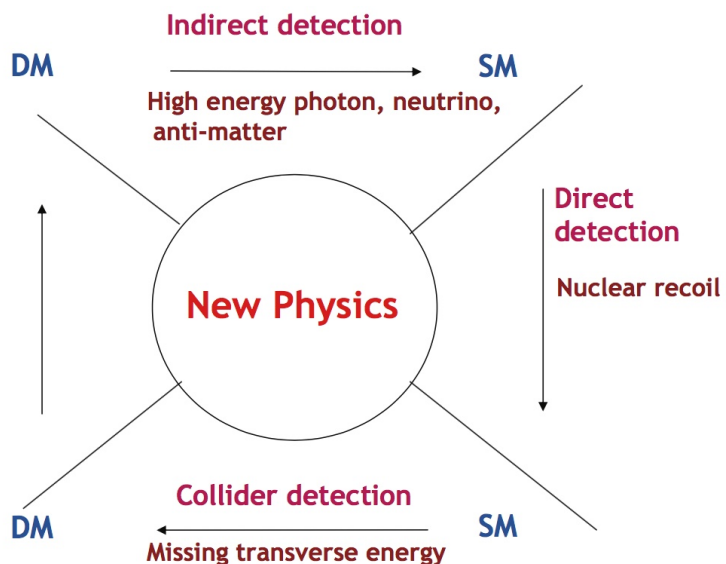


Figure 1.9: The three general approaches to WIMP detection: indirect detection, collider detection, and direct detection. Image Credit: [25].

- Indirect detection looks for the annihilation of WIMPs in our galaxy into ordinary matter
- Collider detection is an attempt at creating WIMPs by colliding ordinary matter
- Direct detection looks for the scattering of WIMPs with ordinary matter

In this section we will discuss these three detection approaches with an emphasis on direct detection. We will conclude with a brief discussion of the current direct detection experiments and notable results from this sector.

### 1.4.1 Indirect Detection

As we know from previous sections, WIMPs, if they make up all (or some) of the dark matter in the universe, must reside in galaxies to explain the odd behavior of rotation curves and the mass discrepancies. Given the observational evidence, simulations have been created that can predict both the distribution of dark matter within our own and other galaxies [26, 27] and the density of dark matter in our own solar system (roughly  $0.2 - 0.4 \frac{\text{GeV}}{\text{cm}^3}$  [28]). Indirect detection experiments look at high density regions of dark matter halos, such as in or around the Milky Way center and dwarf galaxies, to search for annihilations of WIMPs into detectable particles.

The goal of indirect detection is to capture a dark matter annihilation by observing its byproducts. In the ideal case, two dark matter particles would annihilate and create two photons with energies equal to the mass of the dark matter particle. Even though this would be the “smoking gun” evidence of dark matter, this process should be highly suppressed because WIMPs should have no charge and therefore would not couple directly to photons. Instead, these indirect experiments are more likely to observe the annihilation of WIMPs into other particles which in turn will produce photons [25].

A major difficulty in indirect detection experiments is distinguishing potential signals from normal astrophysical processes. Since areas of high dark matter density are also typically areas of high astrophysical activity it becomes difficult to separate potential dark matter signals from potentially new astrophysics [29]. However, in recent

years, astrophysicists have started turning their telescopes towards dwarf galaxies, which are dark matter dominated but have negligible astrophysical backgrounds [30].

### 1.4.2 Collider Detection

The main idea behind collider detection is that since the WIMP is expected to have a mass on the order of  $1 - 10^3$  GeV we can create it in particle accelerators. Of course, detectors at particle accelerators are not designed to detect dark matter directly so when searching for WIMPs physicists must actually search for missing transverse energy (MET) in a collision. The MET can be reconstructed by observing the outgoing particles and jets in a collision and using momentum conservation to indirectly observe the missing energy. This reconstruction is shown in Fig. 1.10. Ultimately, this MET can be used to determine the mass and the new physics processes of the WIMP [25].

One important note is that while we can potentially “see” WIMPs in detectors at

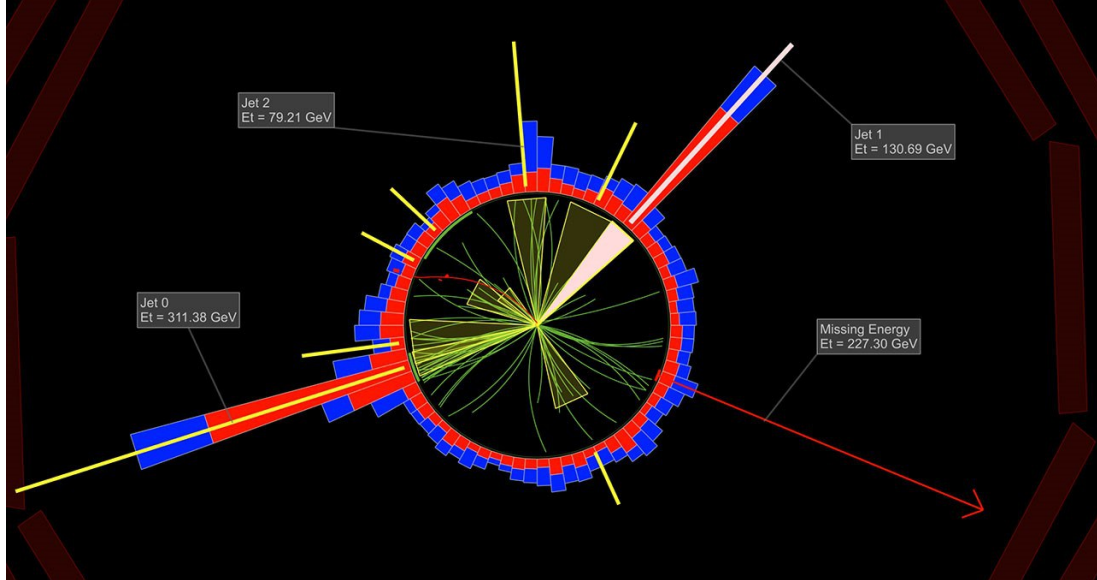


Figure 1.10: An image of a potential WIMP event in the CMS detector at CERN. If a WIMP is present in a collision, momentum would not be conserved after all jets and particles have been accounted for in the collision. Here we can see that after the three jets are reconstructed that there is still a large MET that could potentially be attributed to a WIMP. Image Credit: Matevz Tadel, UC San Diego/CMS.

colliders, it is impossible to be certain that this WIMP is what makes up the majority of the matter in the universe. The same signal would need to be seen in indirect and direct searches as well to make such a confirmation [31].

### 1.4.3 Direct Detection

In purely theoretical terms, any detector that is sensitive to a potential WIMP interaction could be considered a direct detection dark matter search. At the same time, to try and detect a dark matter signal from a NaI detector in your lab would be preposterous (unless your detector is 250 kg and located deep underground!). The reason being that any of the rare dark matter signals would be drowned out by the countless background events you would also detect. This is why direct detection experiments are located deep underground, surrounded with shielding, built with low radiation materials, and take great care to understand their background: if WIMPs are scattering in the detector they want to be able to know.

The goal of direct detection experiments is to detect the scattering of WIMPs off of Standard Model particles. As mentioned, since these scatters should be extremely rare, it is essential to have the background of the detector used be as low as possible. As a simple example, consider two otherwise identical experiments who both have measured their backgrounds perfectly: experiment A expects a single background event per year while experiment B expects 1,000 background events per year. In the case that both detectors see an excess of ten events in a given year over their background, it should be clear that experiment A can make a very strong claim that they have seen WIMP scatterings whereas experiment B cannot since this excess could very well be a fluctuation from their expected background.

It cannot be emphasized strongly enough how crucial the understanding of background is for direct detection experiments. Returning to the above example, imagine experiment A missed a source of background in their estimate and that their true expected background rate is ten events per year, not one. If they saw the same eleven events as before, they might claim a discovery even though the eleven events are very likely to be a statistical fluctuation of the background.

## 1. DARK MATTER

---

The most basic models describing WIMPs predict that they are most likely to interact with atomic nuclei (although some predict leptonic interactions [32]). This assumption, along with cosmological evidence that WIMPs are non-relativistic, surprisingly gives way to a fairly straight-forward derivation of the rate of scattering that one could expect for different nuclei assuming a given scattering cross-section and mass for the WIMP. For a complete derivation one should refer to Ref. [23] and Ref. [33].

It can be shown that the differential scattering rate is given by [34]

$$\frac{dR}{dE}(E) = \frac{\rho_0}{m_\chi m_A} \int_{v_{\min}(E)}^{v_{\text{esc}}} v f(v) \frac{d\sigma}{dE}(E, v) dv \quad (1.8)$$

where  $\rho_0$  is the local dark matter density,  $m_\chi$  is the mass of the WIMP,  $m_A$  is the mass of the target nucleus,  $f(v)$  is the velocity distribution of dark matter locally,  $v_{\min}$  is the minimum velocity that can produce a recoil of energy  $E$ ,  $v_{\text{esc}}$  is the maximum velocity in which WIMPs are still gravitationally bound to the galactic halo, and  $\frac{d\sigma}{dE}$  is the differential cross-section of WIMP-nucleon scattering.

As discussed in Sec. 1.4.1, N-body simulations give us a prediction of roughly  $0.2 - 0.4 \frac{\text{GeV}}{\text{cm}^3}$  for the local dark matter density [28]. We will use the standard halo model (SHM), which is standard for dark matter experiments, such that the velocity of WIMPs in the halo follows a Maxwell-Boltzmann distribution. The minimum velocity of a WIMP to transfer an energy  $E$  to a nucleus,  $v_{\min}$ , is found kinematically to be

$$v_{\min} = \sqrt{\frac{m_A E}{2\mu^2}}, \quad \mu = \frac{m_A m_\chi}{m_A + m_\chi} \quad (1.9)$$

while astrophysical measurements of the Milky Way estimate the local escape velocity to be  $v_{\text{esc}} = 533^{+54}_{-41} \text{ km s}^{-1}$  [35]. It is worth noting that while the Maxwell-Boltzmann distribution is the standard, other models of the velocity distribution exist [36].

The particle physics of the WIMPs comes in at the differential cross-section. The most basic WIMP models predict two potential interactions: a spin-independent or

spin-dependent. Focusing on the former, the differential cross-section is given by

$$\frac{d\sigma}{dE}(E, v) = \frac{m_A}{2\mu^2 v^2} \sigma_0 F(E)^2 \quad (1.10)$$

where  $F(E)$  is nuclear form factor. The nuclear form factor is the Fourier transform of the ground state mass density and is used to correct the zero-momentum transfer cross-section in the case of a momentum transfer. The nuclear form factor can be approximated by

$$F(q) = \frac{3j_1(qR_0)}{qR_0} e^{-\frac{(qs)^2}{2}}, \quad q = \sqrt{2m_A E}, \quad R_0^2 = \left(1.2A^{\frac{1}{3}} \text{ fm}\right)^2 - 5s^2 \quad (1.11)$$

where  $q$  is the momentum transfer in the scatter,  $R_0$  is the approximate nuclear radius,  $s$  is the approximate thickness of the nucleus (roughly 1 fm), and  $j_1$  is the spherical Bessel function of the first kind [37].

We can reduce  $\sigma_0$ , the cross-section of an interaction with zero momentum transfer, by accounting for the coupling to the individual nucleons in the following way

$$\sigma_0 = \frac{(Zf_p + (A-Z)f_n)^2}{f_p^2} \frac{\mu^2}{\mu_{\chi p}^2} \sigma_p \quad (1.12)$$

In this equation,  $f_p$  and  $f_n$  are the WIMP couplings to the proton and neutron, respectively,  $\mu_{\chi p}$  is the reduced mass of the WIMP-proton system, and  $\sigma_p$  is the spin-independent cross-section of the WIMP with the proton. We approximate that  $f_p \approx f_n$  which allows us to simplify to

$$\sigma_0 \approx A^2 \frac{\mu^2}{\mu_{\chi p}^2} \sigma_p \quad (1.13)$$

All of this can be combined such that we are only dependent on two variables: the mass of the WIMP and its cross-section with a proton.

$$\frac{dR}{dE} = \frac{\rho_0 A^2 \sigma_p}{2m_\chi \mu_{\chi p}^2} F(E)^2 \int_{v_{\min}(E)}^{v_{\text{esc}}} \frac{f(v)}{v} dv \quad (1.14)$$

With the differential scattering rate, we can predict the number of WIMPs of a

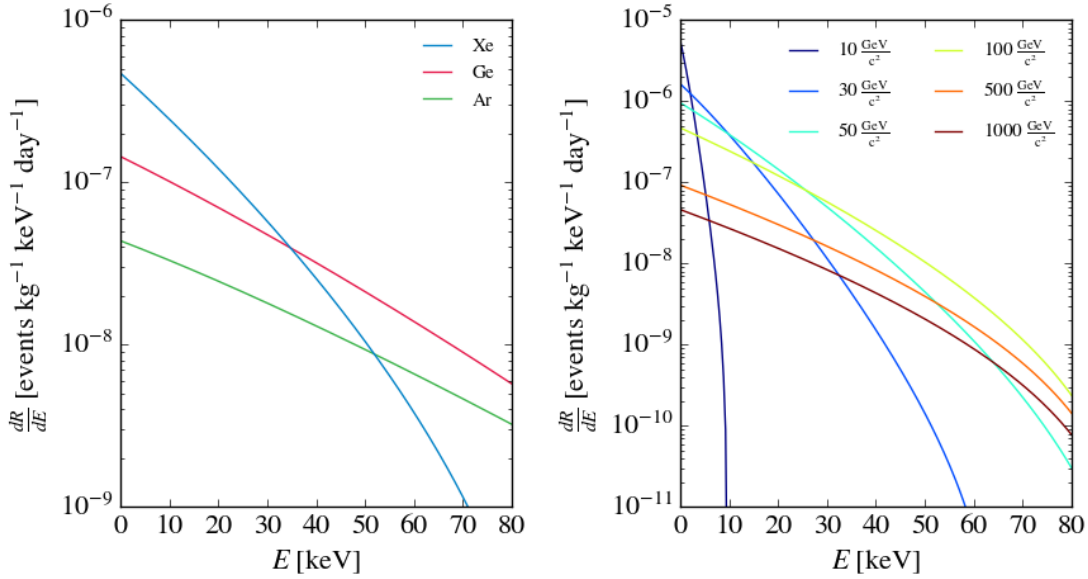


Figure 1.11: On the left are the differential scattering rates for a  $100 \text{ GeV}/c^2$  WIMP with a spin independent cross section of  $10^{-47} \text{ cm}^2$ . On the right are the differential recoil spectra for WIMPs scattering with a xenon nuclei with a spin independent cross section of  $10^{-47} \text{ cm}^2$  assuming different WIMP masses.

given cross-section and mass we would expect to scatter in a detector with a certain target mass,  $M$ , in a given time period,  $T$ , as shown in Eqn. 1.15. Notice in Eqn. 1.15, as expected, the larger your detector is, given by the mass  $M$ , and the longer you collect data, signified by the time  $T$ , the more likely you are to observe a WIMP scattering with a nucleus.

$$N(\sigma_p, m_\chi) = M T \int \frac{dR}{dE} dE \quad (1.15)$$

The differential scattering rates for a few targets and for different WIMP masses can be seen in Fig. 1.11. Notice that xenon, with its very large nucleus, gives a significantly higher scattering rate versus most other targets for a wide range of energies. Also notice that as the mass of the WIMP decreases, the differential scattering rate curve becomes steeper and steeper meaning that low mass WIMPs become increasingly difficult to observe.

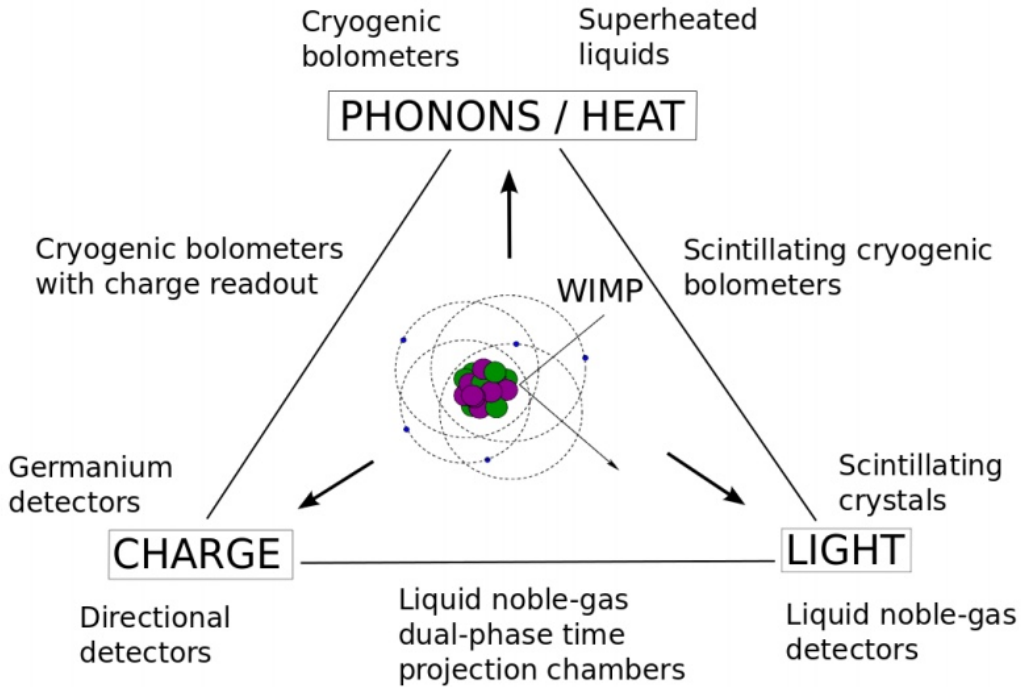


Figure 1.12: A diagram showing the possible observables and observable combinations along with the most common detector types for each. Image courtesy: [34].

#### 1.4.4 Direct Detection Experiments

The field of direct detection experiments is likely best described as diverse. A WIMP interacting in a detector can deposit energy resulting in heat, ionization, or scintillation. Current direct detection experiments leverage all three of these possibilities and many use two of these channels simultaneously to better discriminate between electronic and nuclear recoils, which is important as the former typically constitutes background while the latter is expected from a WIMP interaction.

##### 1.4.4.1 Heat

There are two basic strategies of measuring the heat deposit of potential WIMP interactions that are on opposite sides of the temperature spectrum: cryogenic thermometers and super-heated liquids (bubble chambers). Cryogenic thermometers are detectors cooled down to mK levels that measure the energy deposited by an interaction via the increase in temperature. In recent years, these cryogenic thermometers

have been coupled with light and charge detectors in order to discriminate between electronic and nuclear recoils to some extent [38].

Bubble chambers operate by filling a detector with a super-heated liquid that is just below its boiling point. When ionizing radiation enters, it will form bubbles that can be detected by acoustic sensors. One major advantage of bubble chambers is that they are almost completely insensitive to radiation that interacts electronically which is the main source of background for almost all other experiments. The PICO collaboration uses bubble chamber technology to search for dark matter and they currently have the most stringent spin-dependent dark matter limits [39].

### 1.4.4.2 Scintillation

Scintillators have proven to be some of the most useful detectors in all of physics. The operating principle is that as radiation pass through a detector, it excites the atoms and molecules in the medium which in turn produce light. In single-channel scintillation experiments, scintillating inorganic crystals, such as NaI, are typically used. Inorganic crystals are typically doped with an additional element, most commonly thallium, to increase their light yield and alter the wavelength to one that is more sensitive to photomultiplier tubes (the devices that are used to convert the light into an electrical signal). The major downside of using an inorganic crystal, however, is that one cannot discriminate between different types of recoils in the detector [34]. The most famous direct detection experiment to use an inorganic crystal is the DAMA collaboration, which utilized a 250 kg NaI(Tl) crystal. Since their operation began they have seen a statistically significant annual modulation in their event rate that agrees with predictions of how a dark matter signal would vary over the course of the year according to the standard halo model [40]. Fig. 1.13 shows this annual modulation. However, the claim that the signal is dark matter has been extremely controversial since other experiments have been unable to replicate the results [41–43].

While many experiments use condensed noble gasses that scintillate, they typically measure both scintillation and ionization in the medium. However, there are

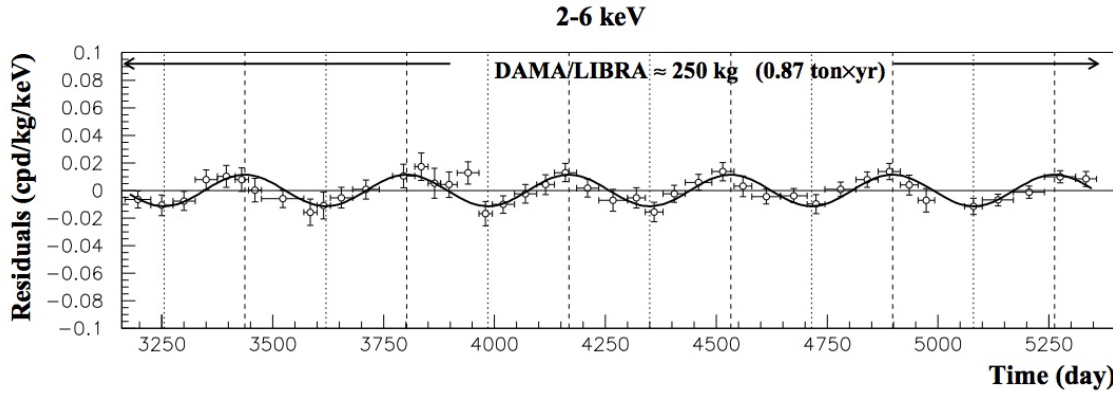


Figure 1.13: The annual modulation seen by the DAMA collaboration. The modulation is statistically significant yet is in contrast to other experiments who fail to see the same signal. Image Credit: [34].

some experiments that are hoping to witness a WIMP interaction while only measuring scintillation. XMASS-I, for example, is a detector with an 832 kg liquid xenon target that, like DAMA, employed an annual modulation approach in their search for WIMPs. Unlike DAMA, however, they see no annual modulation in their data [42].

A useful property of condensed noble gasses is that there are usually two states in which the atoms or molecules can be excited into, a singlet and triplet state each with different decay times. Different types of interactions (electronic versus nuclear) will produce each in different fractions. For argon, this difference in lifetime between the states is from less than 6 ns to 1,300 ns [44] meaning that pulse shape discrimination (PSD) is possible, while for xenon the difference is only 4.3 ns to 22 ns meaning that PSD is very difficult. DEAP-3600, a 3600 kg liquid argon detector, uses this pulse shape discrimination technique to identify nuclear recoils in their detector [45].

#### 1.4.4.3 Ionization

The majority of experiments that used charge as their only channel utilized high-purity germanium detectors. These type of detectors operate by having incoming particles free electrons in a consistent and linear fashion as function of energy. These types of detectors are able to observe interactions at much lower energies than most other detectors, allowing them to probe lower WIMP masses. The most recent of these

single-channel HPGe experiments was CoGeNT. In early 2014, CoGeNT announced that they also had seen an annual modulation that matched the standard halo model [46] however this was found to be an error in the estimation of the background [41].

### 1.4.4.4 Heat-Scintillation

As mentioned earlier, many of the experiments that use heat as a channel also couple it with another channel. CRESST-II is an example of such an experiment — CREST-II uses a roughly 5 kg target of CaWO<sub>4</sub> that is cooled to mK temperatures. The detector also utilizes a small silicon-on-sapphire absorber to measure the scintillation light produced. The addition of this scintillation detector enables the detector to discriminate between electronic recoil background and potential nuclear recoil signals [38].

### 1.4.4.5 Heat-Ionization

The HPGe crystals used to detect ionization signals can also be cooled such that measuring heat signals is possible. One example of this procedure is in the EDELWEISS-III experiment. In EDELWEISS-III, 24 800 g HPGe detectors cooled to 18 mK were employed in their search for WIMPs. Again, this combination of channels allows EDELWEISS-III to discriminate electronic from nuclear recoils in their detector [47].

### 1.4.4.6 Scintillation-Ionization

While many of the experiments mentioned excel at low mass, none have been as successful as dual-channel scintillation-ionization experiments above masses of approximately 5 GeV. Specifically, dual-phase xenon time projection chambers (TPCs) have led the field in the WIMP search from roughly 5 GeV to 1 TeV for almost a decade. As of this writing, XENON1T, the first ton-scale dual-phase TPC, holds the strongest limit of spin-independent WIMP scattering, as can be seen in Fig. 1.14 [48, 49]. Not only are these detectors capable of a high level discrimination between electronic and nuclear recoils but they are also capable of measuring the position of an

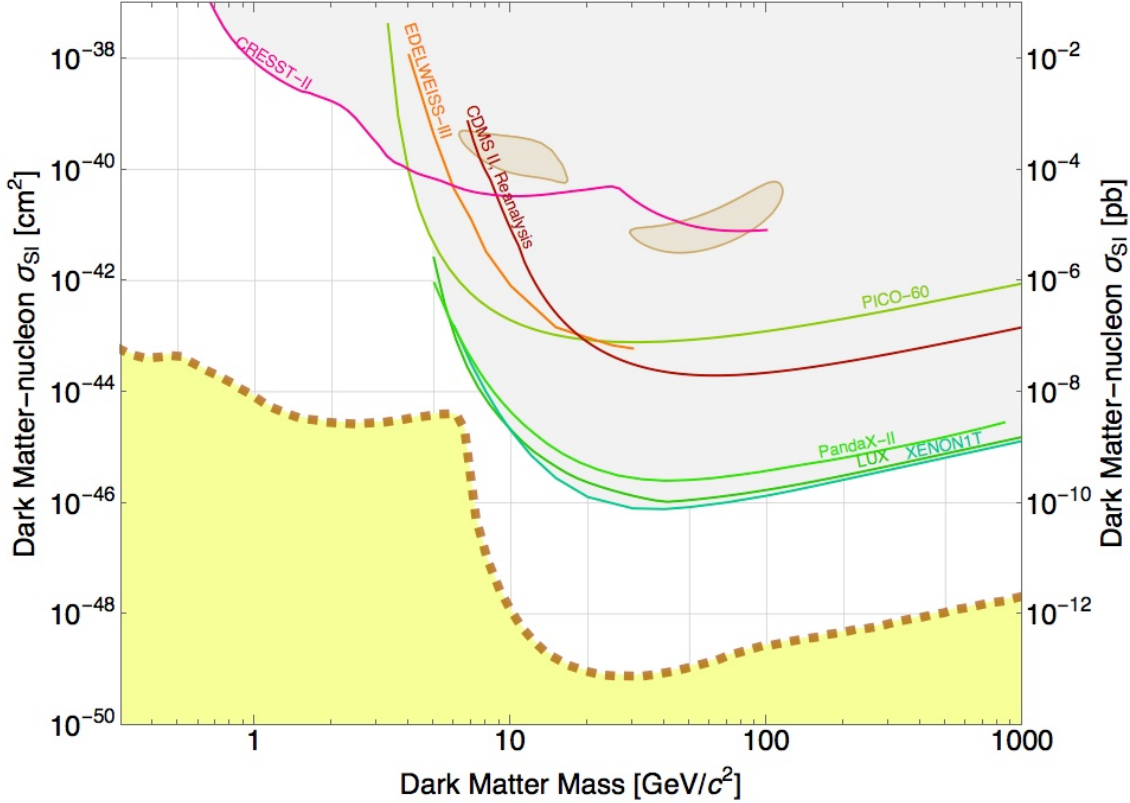


Figure 1.14: Spin-independent WIMP limits from selected experiments and the discovery contour from DAMA’s annual modulation. The dashed line shown in brown marks the point where neutrinos will become a background source in WIMP searches. Notice that the three liquid xenon dual-phase TPC based experiments (PandaX-II, LUX, and XENON1T) set the strongest limit over a wide range of WIMP masses [39, 47, 48, 50–55].

interaction in the detector allowing further elimination of background sources. However, one of the major difficulties of these types of experiments is that the response of liquid xenon to low energy electronic and nuclear recoils is not well understood. A great deal of effort has gone into measuring the response of xenon to these low energy interactions as this is the main region of interest for WIMPs as can be seen from the differential scattering rates shown in Fig. 1.11 and later we will focus on an experiment designed for exactly this purpose.



# Chapter 2

## Liquid Xenon and Dual-Phase TPCs

This chapter will focus on liquid xenon as a detector medium. In Sec. 2.1 we will discuss the general properties of liquid xenon along with some of the benefits and considerations of these properties. In Sec. 2.2 we will discuss how charged particles in xenon deposit their energy. In Sec. 2.3 we will discuss the production of observable light and charge from electron recoils while in Sec. 2.4 we will discuss observable production from elastic nuclear recoils. Finally, in Sec. 2.5, we will discuss how these observables are detected in dual-phase xenon time projection chambers.

### 2.1 General Properties

Xenon, with an atomic number of 54, is a noble gas meaning that it has a full valence electron shell. Because of the full valence shell, xenon is very unlikely to interact chemically with other elements and molecules. Xenon is also the heaviest noble gas that is, for practical purposes, naturally non-radioactive — an essential quality for a detector medium as long-lived radioactive isotopes would be a source of background that would be very difficult to remove.  $^{136}\text{Xe}$ , with a natural abundance of 8.857%, has been shown to undergo double beta decay with a half-life of  $2.165 \cdot 10^{21}$  years so strictly speaking natural xenon is radioactive although this process is extremely

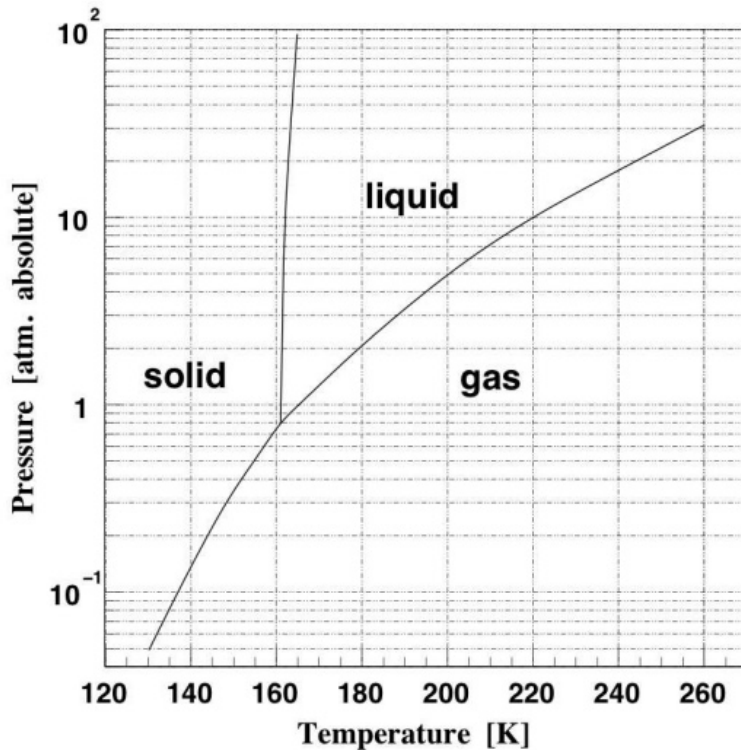


Figure 2.1: The phase diagram for xenon. Dual-phase xenon TPCs typically operate in the range of 2–3 atm.

rare and has little relevance for even low background dark matter experiments [56]. However, we will still discuss the implications of  $^{136}\text{Xe}$  with respect to our electronic recoil background in Sec. 3.2.2.4.

While natural xenon is not radioactive, it is actually possible to excite xenon nuclei such that they decay and emit gamma rays. None of these excited states have very long lifetimes that would cause issues for low background experiments but two of these neutron activated states ( $^{131\text{m}}\text{Xe}$  and  $^{129\text{m}}\text{Xe}$  which decay emitting 164 keV and 236 keV photons, respectively) have half-lives on the order of ten days. These excited states be very useful in the calibration of large detectors since over this period of time the excited states would be approximately uniformly distributed inside of a detector [57] — these neutron activated states are used as one of the many sources used for calibrations in XENON1T which will be discussed in Sec. 3.3.

Xenon is extracted from the atmosphere as a byproduct of the separation of

Isotope	Abundance	Spin	Half-life	Decay Mode
$^{124}\text{Xe}$	0.095%	0	$> 1.6 \cdot 10^{14} \text{ y}$	$2\nu\beta^+\beta^+$ <a href="#">1</a>
$^{126}\text{Xe}$	0.089%	0	$4.7 - 12 \cdot 10^{25} \text{ y}$	$2\nu\beta^-\beta^-$ <a href="#">1</a>
$^{128}\text{Xe}$	1.910%	0	Stable	-
$^{129}\text{Xe}$	16.400%	$\frac{1}{2}$	Stable	-
$^{130}\text{Xe}$	4.071%	0	Stable	-
$^{131}\text{Xe}$	21.232%	$\frac{3}{2}$	Stable	-
$^{132}\text{Xe}$	26.909%	0	Stable	-
$^{134}\text{Xe}$	10.436%	0	$> 5.8 \cdot 10^{22} \text{ y}$	$2\nu\beta^-\beta^-$ <a href="#">1</a>
$^{136}\text{Xe}$	8.857%	0	$2.2 \cdot 10^{21} \text{ y}$	$2\nu\beta^-\beta^-$

Table 2.1: Abundances, half-lives, and decay modes of various xenon isotopes. Note that  $^{136}\text{Xe}$  is the only isotope whose decay has been measured. Half-life data: [\[60\]](#).

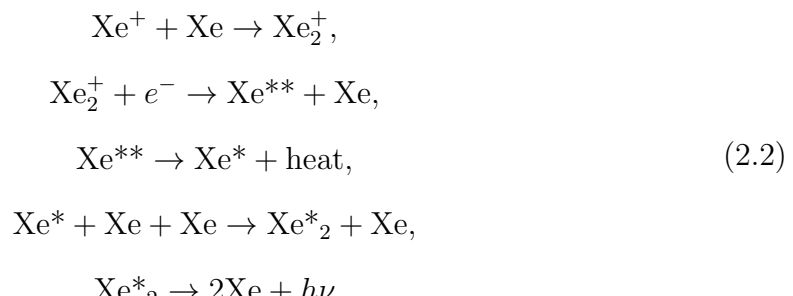
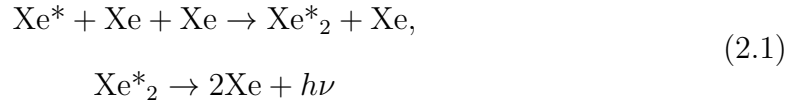
oxygen and nitrogen. Once the oxygen is separated, it will contain trace amounts of krypton and xenon that can be separated out further by distillation or adsorption. The xenon that is purchased commercially typically will have a final Kr/Xe ratio of  $\sim 10^{-6} - 10^{-9} \frac{\text{mol}}{\text{mol}}$ . Natural krypton is not radioactive on a relevant time scale but  $^{85}\text{Kr}$ , which is released into the atmosphere via nuclear fuel reprocessing and nuclear weapons tests, beta decays with a mean energy of 251 keV and with a half-life of roughly 10.8 years [\[58\]](#). So while natural xenon is not radioactive, the process of extracting xenon from the atmosphere does leave a radioactive isotope that could be a potential source of background for dark matter experiments. Significant effort has gone into reducing the Kr/Xe levels to reduce this background as much as possible. In XENON1T, the lowest level to date was achieved with a natural krypton to xenon ratio of less than 200 ppq (1 ppq =  $10^{-15} \frac{\text{mol}}{\text{mol}}$ ) [\[59\]](#).

Dual-phase xenon experiments typically operate at roughly 2–3 atm, which translates to a boiling point of roughly 180 K ( $-93.2^\circ \text{ C}$ ). The density of liquid xenon (LXe) at this temperature is roughly 2.84 g/cm<sup>3</sup> which is significantly higher than all of the other noble elements, with the exception of radon [\[61\]](#). The high density of LXe is partly responsible for its high electronic stopping power, which will be discussed further in the next section.

## 2.2 Energy Deposition of Charged Particles in Liquid Xenon

Both nuclear and electronic recoils, which will be discussed in the following sections, ultimately result in a charged particles traversing the LXe - in the case of an electronic recoil the resulting charged particle is an electron and in the case of nuclear recoils it is the xenon nucleus. Given the high density and atomic number of xenon, the electronic stopping power is large for both electrons and xenon ions ( $\sim 1 - 30 \text{ keV}/\mu\text{m}$ ). This means that the tracks of low energy electronic and nuclear recoils will be very small and approximately point-like [62]. In this section, we will discuss the process by which these electronic and nuclear recoils produce light and charge that can ultimately be detected in liquid xenon TPCs. A visual diagram of these mechanisms is shown in Fig. 2.2.

In liquid xenon (and other noble liquids), scintillation light is produced via the excitation of atomic electrons and the ionization and subsequent recombination of free electrons and ions. The excitation scintillation process is shown in Eqn. 2.1 and the ionization scintillation process is shown in Eqn. 2.2.



The excitation process proceeds when an atomic electron in xenon is excited (the excited xenon is referred to as an *exciton*) and the excited atom forms a dimer

---

<sup>1</sup>This decay is predicted but has not yet been observed.

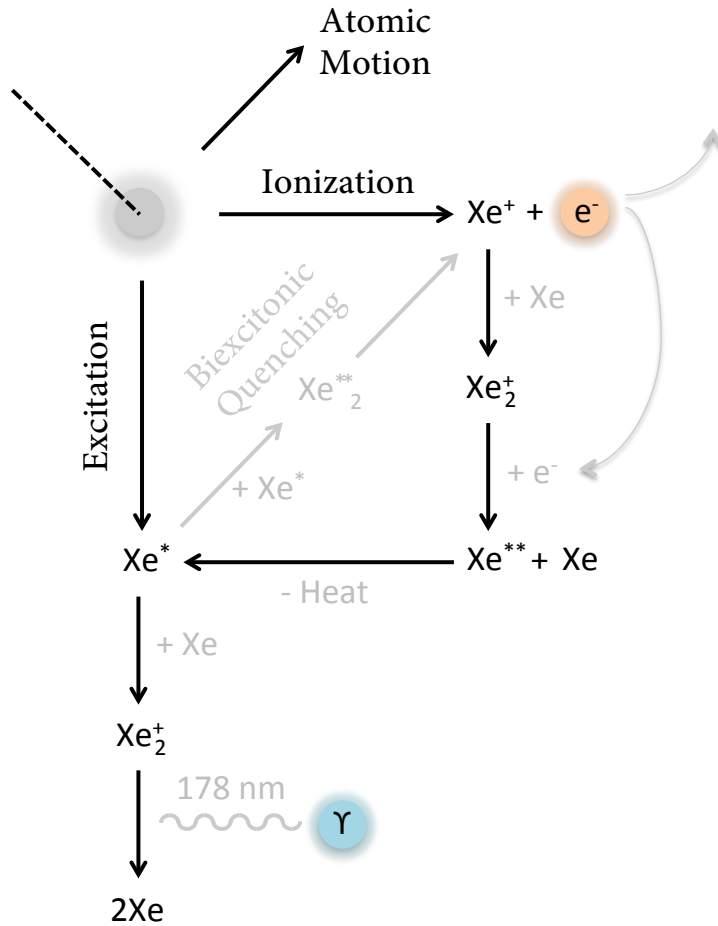


Figure 2.2: A diagram showing the modes in which charged particles may lose energy in liquid xenon. Note that when an electric field is applied, the electron freed during ionization can be extracted such that it can be measured.

with another xenon atom, which is called an *excimer*. This excited excimer can be formed in either the singlet state (spin of excited electron anti-parallel to electron originally sharing state) or triplet state (spin of excited electron parallel to electron originally sharing state). The excimers in the singlet and triplet states each have their own characteristic lifetimes (roughly 4 ns and 22 ns)<sup>2</sup> and decay into xenon atoms and a 178 nm photon (the photon falls in UV portion of the spectrum) [63, 64].

The ionization process begins when a charged particle ionizes a xenon atom, leaving singly-ionized xenon and a free electron. The singly-ionized xenon atom can then

<sup>2</sup>In xenon the difference in lifetimes of the singlet and triplet states is fairly small but for argon the singlet lifetime is 7 ns while the triplet lifetime is 1.3  $\mu\text{s}$  [44]!

## 2. LIQUID XENON AND DUAL-PHASE TPCs

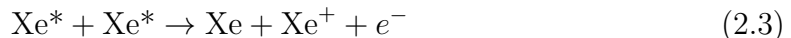
---

form an ionized dimer and subsequent excited xenon state. This excited xenon state leads to an excimer through non-radiative heat loss. The excimer produces scintillation light in the manner described above.

Implicit in the ionization process outlined above is the assumption that the electron freed during ionization recombines with the singly-ionized dimer. However, in the presence of an electric field, this recombination can be reduced such that a charge signal can also be read out in addition to the scintillation signal. Incomplete recombination can also occur at zero electric field and these electrons are called *escape electrons* (although you cannot extract the charge signal without an applied electric field) [64].

It is important to note that while these electronic excitation and ionization mechanisms are dominant for electronic recoils, the energy deposition for nuclear recoils is split between these and atomic motion. This distinction is extremely important - the energy given to electrons in a recoil cannot cause atomic motion however atomic motion, if sufficiently slow, will not be able to cause excitation or ionization in other atoms and hence some energy is lost. This effect was first discussed by Lindhard in 1963 [65] and the effort to quantify this effect continues today and in this work. This effect will henceforth be referred to as nuclear quenching.

A second form of quenching has been observed in high linear energy transfer (LET) interactions, specifically with  $\alpha$  scatters in xenon (which will not be discussed in detail) and high energy nuclear recoils. This quenching is called biexcitonic quenching and is the result of two excitons colliding to produce an electron-ion pair as shown in Eqn. 2.3.



Since this form of electronic quenching requires the collision of two excitons, it is expected that the track density ultimately determines the level of quenching [66].

A diagram showing all of the mentioned energy deposition methods for charged particles is shown in Fig. 2.2.

## 2.3 Electronic Recoils in Liquid Xenon

In this section, we will discuss the sources of electronic recoils in liquid xenon, their properties, and how they result in detectable observables. For dual-phase LXe TPCs (which we will focus on in more detail later) searching for “standard” WIMPs, electronic recoils constitute the background. With a precise understanding of what causes electronic recoils and how they interact in LXe, we can better discriminate between electronic recoils and potential signals that are expected to interact via nuclear recoils. Additionally, if WIMPs do interact with atomic electrons rather than the nucleus, a precise understanding of the electronic recoil background would be crucial for a discovery.

### 2.3.1 Sources of Electronic Recoils

There are two main sources of energetic electrons in liquid xenon: (1) beta decays from contaminants inside of a detector and (2) photons interacting through matter via photoelectric absorption, Compton scattering, or pair production. In either case, the resulting energetic electron creates a track through the xenon, mainly losing its energy from inelastic collisions with atomic electrons. In standard WIMP hypotheses, WIMPs are expected to interact with the atomic nucleus, however there are certain theories of WIMPs that allow interactions between a WIMP and atomic electrons that would result in an electronic recoil.

In general, we consider the different source of electronic recoils as potential background sources and calibration sources. Calibration sources are sources that we knowingly introduce into the detector system such that we can measure the response of the xenon and our detector to these types of interactions. They are controllable in such a way that we can both introduce them and remove them without consequence. Calibration sources will not be present during dark matter searches. Background sources, on the other hand, are sources that would be present when we are actively searching for WIMPs that we actively try to reduce but cannot be completely removed.

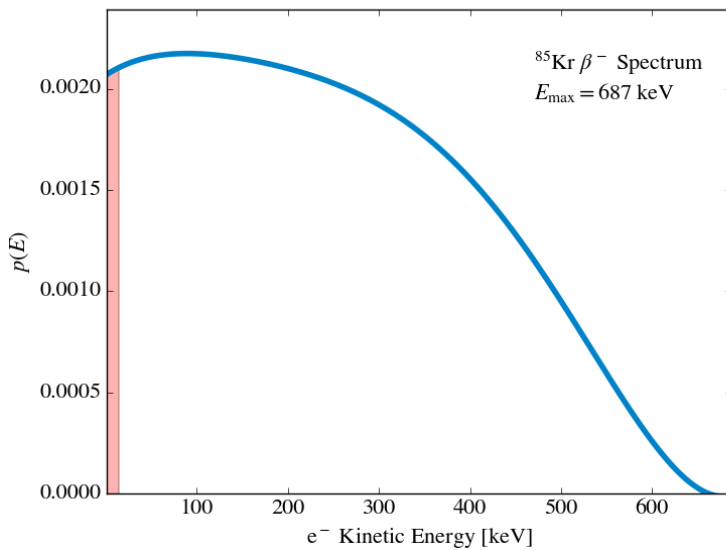


Figure 2.3: The kinetic energy spectrum of electrons resulting from the  $\beta^-$  decay of  $^{85}\text{Kr}$  [68]. Note that roughly 3.1% of decays are below 15 keV (shaded red region) which puts them inside the energy region of interest of WIMP searches.

### 2.3.1.1 Beta Decays

While there are both  $\beta^-$  and  $\beta^+$  decays, we will focus on  $\beta^-$  decays since they are relevant to WIMP searches.  $\beta^-$  decay is a radioactive decay in which a neutron is converted to a proton inside of the nucleus and a subsequent electron and anti-electron neutrino are emitted. This type of decay is made possible by the weak force which allows a quark to change its type via a W boson and an electron and anti-neutrino (positron and neutrino) pair [67].

While the maximum energy of the energetic electron in the decay is fixed, because an anti-neutrino is also emitted in  $\beta^-$  decay, the energy spectra of the electron is continuous. This continuous energy spectrum is what makes long-lived  $\beta^-$  emitters very dangerous potential sources of background - they can, with non-negligible probabilities, produce electrons with energies of interest for WIMP detection ( $\lesssim 15$  keV). The energy spectrum for  $^{85}\text{Kr}$  is shown in Fig. 2.3.

In liquid xenon based detectors, the two biggest sources of background beta decays are from  $^{85}\text{Kr}$  and  $^{214}\text{Pb}$ , which comes from the  $^{222}\text{Rn}$  decay chain [48]. Both of these

background sources, which are discussed in more detail in Sec. 3.2.2.2 and Sec. 3.2.2.1, must be carefully reduced, however other isotopes that  $\beta^-$  decay have proven to be extremely useful for detector calibrations.  $^{212}\text{Pb}$ , from the decay chain of  $^{220}\text{Rn}$  which can easily be introduced into TPCs, has proven useful for calibrations since approximately 10% of electrons have an energy less than 15 keV (the maximum energy is 570 keV) [69].  $^{220}\text{Rn}$  as a calibration source will be discussed in more detail in Sec. 3.2.2.1. Perhaps even more exciting for the low energy calibrations of electronic recoils is the use of tritium, which has a maximum energy of only 18.6 keV [70, 71]!<sup>3</sup>

### 2.3.1.2 Photons

Another source of electronic recoils in LXe comes from photons. Photons, via photoelectric absorption, Compton scattering, or pair production, can create energetic electrons inside of a detector. While pair production is not relevant in the energy range of interest, photoelectric absorption is one of the most tried and tested calibration tools for LXe (and other detectors) and electrons from Compton scatters can make up part of the background in WIMP searches since the energy of the electron can be arbitrarily low.

Photoelectric absorption is the process by which a photon is absorbed by an atom from which an electron is subsequently ejected (typically from the K shell). This implies that the energy of the ejected electron is equal to the energy of the photon minus the binding energy. However, the newly ionized atom will have a free electron bind with it, usually on a very short time scale, and an X-ray or auger electron will be emitted [72]. Therefore the energy detected from photoelectric absorption will be very close to the initial energy of the photon. Photoelectric absorption is the dominant mode of interaction up to a few hundred keV in most media, including xenon as can be seen in Fig. 2.4.

Compton scattering is the process by which a photon interacts with an atomic

---

<sup>3</sup>Molecular tritium ( $\text{T}_2$ ) cannot be used because it adsorbs to surfaces very easily and the half-life of  $\text{T}_2$  is 12.3 years. Instead, tritiated methane ( $\text{CH}_3\text{T}$ ) is used since this will not adsorb and can be easily removed.

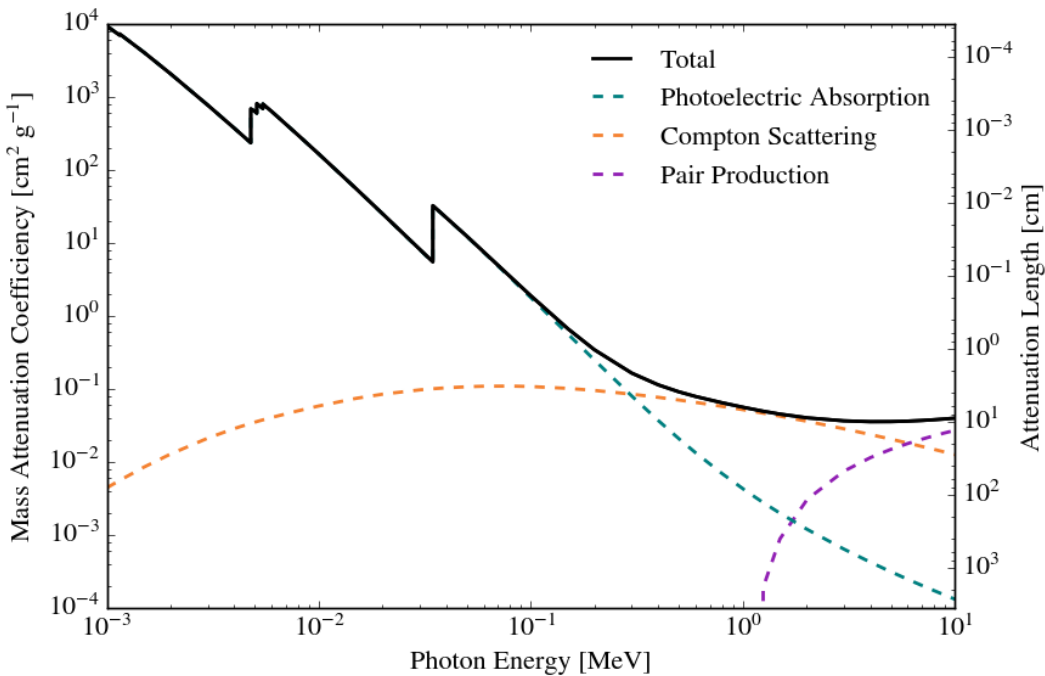


Figure 2.4: The mass attenuation coefficient and the attenuation lengths for photons of different energies in liquid xenon [73].

electron resulting in the deflection of the photon at a specific angle and a transfer of energy to the electron. The angle of the scattering completely describes the energy transferred to the electron. Compton scattering is the dominant mode of interaction from a few hundred keV to a few MeV in most media, including xenon as can be seen in Fig. 2.4.

Fig. 2.4 shows the mass attenuation coefficient of photons in LXe and the individual contributions of each process. Because of xenon's high atomic number, all processes have very high attenuation coefficients. This is valuable for background reduction since low energy photons are absorbed at the very edge of the detector (since their attenuation length is  $< 1$  cm) although it does make calibration with external gamma ray sources very difficult for large detectors.<sup>4</sup> Photons with an energy of a few hundred keV to a few MeV are most likely to Compton scatter and not be absorbed and have an attenuation length on the order of several centimeters which means that

---

<sup>4</sup>This is the reason why many large scale LXe detectors are calibrated using internal sources now such as the beta emitters mentioned earlier and metastable activated xenon.

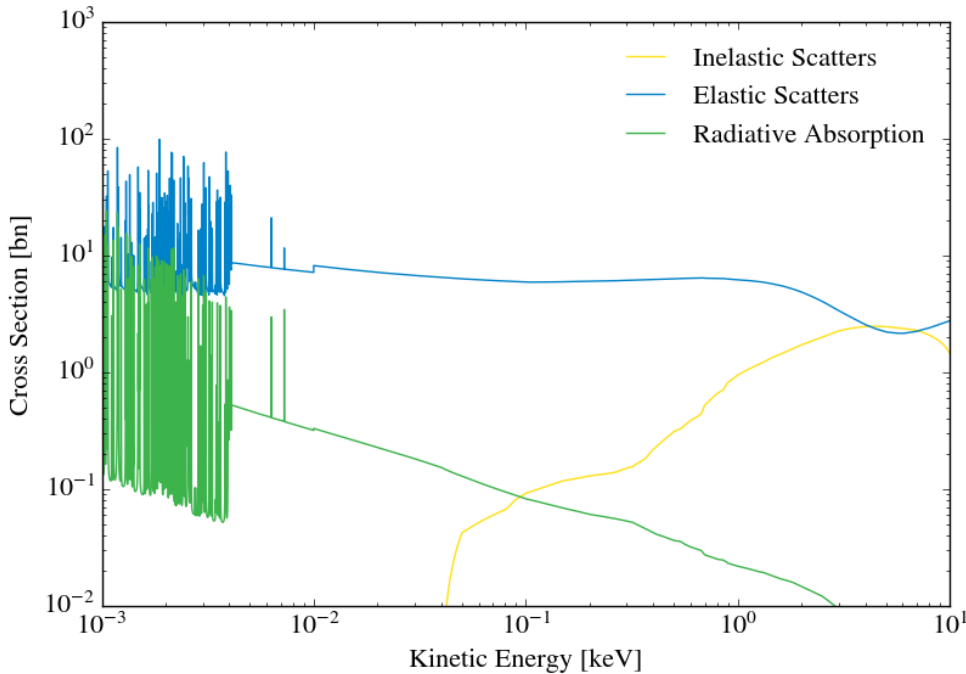


Figure 2.5: The cross-sections of the three main interaction modes of neutrons in liquid xenon. Note that elastic scattering is the dominant process for almost all energies in the range shown. The data for each isotope of xenon is from Ref. [74] and the figure shows the cross-sections weighted by abundance of each isotope in natural xenon.

they will contribute to the background of LXe detectors at some level.

### 2.3.1.3 Neutrons

Neutrons can interact in liquid xenon mainly through three mechanisms: radiative absorption and inelastic scattering, which result in electronic interaction in the medium, and elastic scattering, which ultimately results in a nuclear recoil and will be discussed in Sec. 2.4. The cross-sections of each of these mechanisms for xenon can be seen in Fig. 2.5. Note that for almost all energies between 1 keV – 10 MeV that elastic scattering is the dominant process.

Radiative absorption is the absorption of neutrons by a nucleus. The nucleus thus increases by one in mass number with atomic number staying the same. Fortunately, since the isotopes of xenon that could be produced are not radioactive, with the

## 2. LIQUID XENON AND DUAL-PHASE TPCs

---

exception of  $^{133}\text{Xe}$  and  $^{135}\text{Xe}$ , this process produces very little background.  $^{133}\text{Xe}$  and  $^{135}\text{Xe}$  both result in short  $\beta^-$  chains and will therefore result in electronic recoils inside of a detector. With this said, for the neutron energies of background and calibrations in liquid xenon WIMP detectors, radiative absorption is largely irrelevant.

Inelastic scattering is the process by which a particle interacts with the atomic nucleus and kinetic energy is lost due to the excitation of the nucleus. The excitation of the nucleus, also called *activation*, is then followed by the nucleus decaying from this excited state back down to a stable state through the emission of a particle. For xenon, there are two inelastic collisions of note: an inelastic scattering with  $^{129}\text{Xe}$  or  $^{131}\text{Xe}$ . A neutron scattering inelastically with  $^{129}\text{Xe}$  can result in the nucleus being in an excited state with a 0.96 ns half-life that decays into gamma ray at an energy of approximately 40 keV or in an excited metastable state with a half-life of 8.8 days that results in a 197 keV photon followed by a 40 keV photon (the 40 keV photon is from the same very short lived state that the metastable state decays into) [75]. A neutron scattering inelastically with  $^{131}\text{Xe}$  can result in the nucleus being in a metastable state with a half-life of 11.84 days that decays emitting a 164 keV photon [76]. While these processes are not relevant for background considerations during a WIMP search, they are very useful when calibrating a detector since they each result in electronic recoils at a low and fixed energy.

There are three major sources of neutrons in dark matter experiments. The first major source is from heavy elements in various detector components decaying via spontaneous fission resulting in neutrons with energies typically from 1 – 10 MeV. Neutrons also come from high-energy muons interacting with the rock and materials around the detector. Finally, neutrons can be produced artificially using a neutron generator (typically either through a deuterium-deuterium reaction or deuterium-tritium reaction). The first two sources of neutrons make up background in dark matter searches while the third source of neutrons is used to calibrate detectors (for both electronic and nuclear recoils).

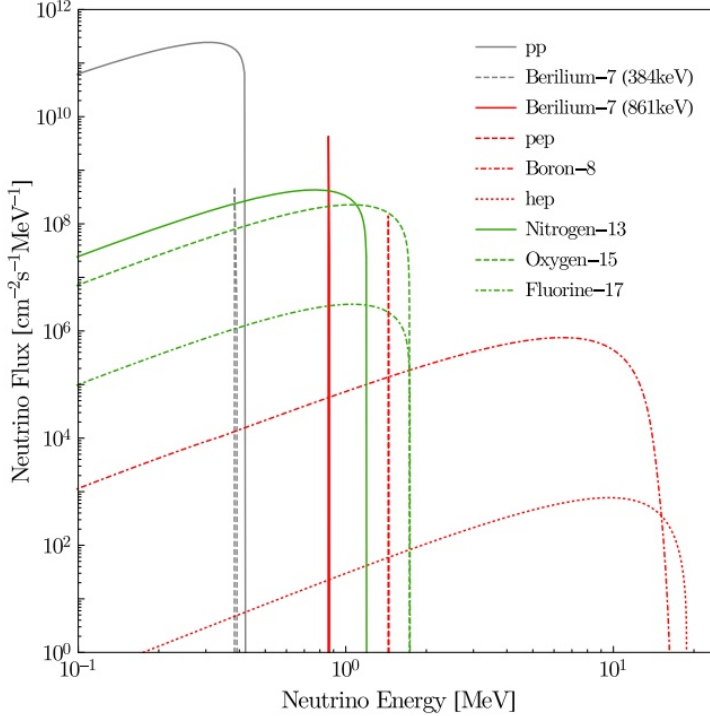


Figure 2.6: Solar neutrino fluxes from different processes assuming the BS05(OP) standard solar model. Image Credit: [78].

#### 2.3.1.4 Neutrinos

Neutrinos can elastically scatter with electrons either via charged-current (exchange of W boson) or neutral-current (exchange of Z boson) interactions. For electronic recoils, the main sources of neutrinos are from initial deuterium production and  $^{7}\text{Be}$  reactions inside the sun (roughly 92% and 7% of the neutrino background, respectively) [77]. Like electronic recoils from beta decays, the kinetic energy of the recoiling electron will follow a spectrum where only very low energies ( $\lesssim 15$  keV) are relevant. Unlike other sources of electronic recoils, the solar neutrino background cannot be reduced and will scale with the size of the detector.

#### 2.3.2 Observables Production for Electronic Recoils

In Sec. 2.2, we discussed the modes by which charged particles deposit energy in LXe. We will now quantify these observables production methods for electronic recoils under the assumption of an applied electric field.

## 2. LIQUID XENON AND DUAL-PHASE TPCs

---

As mentioned in Sec. 2.2, electronic recoils result in either excitation or the creation of electron-ion pairs. Assuming the recoils occur in the presence of an electric field, we do not need to be concerned about quenching with respect to escape electrons (since these can be extracted by the electric field and ultimately measured). Additionally, electronic recoils have relatively sparse tracks (as can be seen by their low stopping power in liquid xenon) [62] so it is expected that biexcitonic quenching will not play a large role in observables production.

Since there are no major forms of quenching, we can completely separate the energy deposited in the electronic recoil into excitons and electron-ion pairs. Typically the total number of quanta (excitons and electron-ion pairs) is used to describe this relationship — specifically, the average energy required to produce a single quanta. For xenon, this value is  $W = 13.7 \pm 0.2 \text{ eV}$  [79] and the relationship is given by Eqn. 2.4.

$$N_q = \frac{E_{\text{ER}}}{W} = N_{\text{ex}} + N_{\text{ion}} \quad (2.4)$$

This relationship, while looking very simple, turns out to be extremely useful for calibrations in dual-phase xenon TPCs, as we will discuss in later chapters. The breakdown of excitons to electron-ion pairs is simply described by the ratio of the two quantities such that we can define probabilities of a given quanta being an exciton or electron-ion pair.

$$p_{\text{ion}} = \frac{1}{1 + \frac{N_{\text{ex}}}{N_{\text{ion}}}}, \quad p_{\text{ex}} = 1 - p_{\text{ion}} \quad (2.5)$$

The exciton-to-ion ratio,  $\frac{N_{\text{ex}}}{N_{\text{ion}}}$ , has been theoretically calculated to be 0.06 for sub-MeV electronic recoils [80] however measurements and theoretical predictions have also suggested a value of  $0.20 \pm 0.13$  [64, 81].

As mentioned previously, electron-ion pairs have a finite probability of recombining to form excitons and eventually producing a scintillation signal (as opposed to a charge signal). While in the past this recombination probability was modelled using Birks' saturation law [82] for large tracks and the Thomas-Imel model [83] (which

will be discussed in more detail for nuclear recoils) for short tracks, recently a great deal of work has gone into directly measuring recombination in liquid xenon and its potential fluctuations without the assumption of a model [70, 71]. Recombination is simply inserted to the model of observables production as shown in Eqn. 2.6.

$$N_{\text{ex}} \leftarrow N_{\text{ex}} + rN_{\text{ion}}, \quad N_{\text{ion}} \leftarrow (1 - r)N_{\text{ion}} \quad (2.6)$$

Following recombination in electronic recoils, these excitons and electron-ion pairs directly translate into the number of photons and electrons that are observable.

$$N_{\gamma} = N_{\text{ex}}, \quad N_e = N_{\text{ion}} \quad (2.7)$$

## 2.4 Nuclear Recoils in Liquid Xenon

It is expected that WIMPs could potentially dissipate energy in xenon via elastic nuclear recoils so understanding these type of interactions is of crucial importance for WIMP direct detection experiments. In this section, we will discuss the sources of nuclear recoils in liquid xenon based WIMP searches (besides potential WIMPs) and the observables production process for elastic nuclear recoils, which is substantially more complicated due to the nuclear and electronic quenching first mentioned in Sec. 2.2.

### 2.4.1 Sources of Nuclear Recoils

The two sources of nuclear recoils in liquid xenon based WIMP searches, besides potential WIMPs, are neutrons and neutrinos. While neutrons are, as one would expect, the main background and calibration source in liquid xenon based WIMP searches, neutrinos are no longer negligible and, as detectors become more and more sensitive to lower cross-sections, will soon comprise an irreducible background of elastic nuclear recoils in detectors. Understanding the sources of nuclear recoils in liquid xenon based WIMP direct detection experiments is very important since an

underestimation of the background could lead to potential claims of a false WIMP signal since interactions would be indistinguishable on an event-by-event basis.

The sources discussed in this section are either considered to be background sources or calibration sources. Calibration sources are sources that we knowingly introduce into the detector system such that we can measure the response of the xenon and our detector to these types of interactions. They are controllable in such a way that we can both introduce them and remove them without consequence. Calibration sources will not be present during dark matter searches. Background sources, on the other hand, are sources that would be present when we are actively searching for WIMPs that we actively try to reduce but cannot be completely removed.

#### 2.4.1.1 Neutrons

Electronic recoils from neutron scattering were discussed in Sec. 2.3 — in this section we will focus on nuclear recoils from elastic scattering. Elastic scattering is the process by which a particle interacts with the atomic nucleus and kinetic energy is conserved. The recoiling nucleus then deposits its energy in the medium which can ultimately be detected. Particles scattering elastically with nuclei is also called a nuclear recoil. Of course, this process is not unique to neutrons but is the main mode of interaction for many massive particles (and hopefully WIMPs).

Each of the sources of neutrons mentioned in Sec. 2.3, spontaneous fission of heavy materials, high-energy muons, and artificially generated muons, can also result in nuclear recoils.

#### 2.4.1.2 Neutrinos

Neutrinos can interact with both electrons, as discussed in Sec. 2.3, and atomic nuclei, via coherent neutrino-nucleon scattering (CNNS). The maximum energy of a recoiling nucleus is given by  $E_r^{\max} = \frac{2E_\nu^2}{m_N + 2E_\nu}$ , where  $m_N$  is the mass of the nucleus and  $E_\nu$  is the energy of the neutrino. This implies that neutrinos must have energies on the order of 10 MeV to cause nuclear recoils on the order of 1 keV. Therefore, high energy neutrino sources like  ${}^8\text{B}$  in the sun as well as neutrinos from supernovae and

the atmosphere will contribute the most to the CNNS background in dark matter experiments.

### 2.4.2 Observables Production for Nuclear Recoils

We will now discuss the details of the observables production process for nuclear recoils that was generally outlined in Sec. 2.2. Like electronic recoils, nuclear recoils can lead to the excitation or ionization of other xenon atoms. However, unlike energetic electrons in liquid xenon, recoiling xenon atoms will also interact with other xenon nuclei. This distinction is extremely important since energy can effectively be “lost” if the energy transferred during a collision is too low to cause excitation or ionization.

Lindhard proposed a theory to describe this nuclear quenching in Ref. [65]. To describe the quenching of signals due to atomic motion, it is standard to work with the dimensionless energy given in Eqn. 2.8.

$$\epsilon = 11.5 \left( \frac{E}{\text{keV}} \right) Z^{-7/3} \quad (2.8)$$

Lindhard showed that at low velocities ( $v < v_F$ ) the stopping power of a heavy ion in a medium is approximately given  $S_e = k\epsilon^{1/2}$ , where  $k$  is a proportionality constant, assuming the Thomas-Fermi screening model. Under the same assumptions, it can be shown that  $k = 0.133Z^{2/3}A^{-1/2}$ , which would give  $k \approx 0.165$  for xenon, although in his original paper Lindhard names the calculation of the proportionality factor as the largest source of uncertainty in the stopping power. Shown in Eqn. 2.9 is Lindhard’s semi-empirical numerical solution for the fraction of the total energy that goes to electronic interactions for recoiling atoms.

$$L(\epsilon) = \frac{kg(\epsilon)}{1 + kg(\epsilon)}, \quad g(\epsilon) = 3\epsilon^{0.15} + 0.7\epsilon^{0.6} + \epsilon \quad (2.9)$$

Note that  $g(\epsilon)$  is not derived from first principles but is a fit to Lindhard’s numerical solution from  $\epsilon = 0.001 - 100$  (roughly 1 keV – 100 MeV nuclear recoils for xenon).

## 2. LIQUID XENON AND DUAL-PHASE TPCs

---

Similar to observables production in electronic recoils, we assume that all energy that goes towards electronic interactions is converted into excitons and ions by way of the W value as is shown in Eqn. 2.10.

$$N_q = \frac{L(E)E_{\text{NR}}}{W} = N_{\text{ex}} + N_{\text{ion}} \quad (2.10)$$

As with electronic recoils, the split into excitons and ions can be defined by a single parameter,  $\frac{N_{\text{ex}}}{N_{\text{ion}}}$ .

$$p_{\text{ion}} = \frac{1}{1 + \frac{N_{\text{ex}}}{N_{\text{ion}}}}, \quad p_{\text{ex}} = 1 - p_{\text{ion}} \quad (2.11)$$

Unlike electronic recoils, however, it is expected that  $\frac{N_{\text{ex}}}{N_{\text{ion}}} \approx 1$  for nuclear recoils [84–86].

RIVAL (Recoiling Ions in Various Atomic Liquids) simulations show that nuclear recoils, unlike electronic recoils, lose the majority of their energy in a large number of secondary tracks and have a short track size relative to electronic recoils. With short tracks and with applied electric fields we can use the Thomas-Imel recombination model to describe the recombination of electrons and ions into excitons shown in Eqn. 2.2 [79]. The Thomas-Imel box model [83] begins by using the modified diffusion equation presented by Jaffe [87] with the assumptions that Coulomb forces are negligible, due to the high coefficient of polarization for xenon. Jaffe’s model is described by Eqn. 2.12.

$$\frac{\partial N_{\pm}}{\partial t} = \mp u_{\pm} \mathbf{E} \cdot \nabla N_{\pm} + D_{\pm} \nabla^2 N_{\pm} - \alpha N_{+} N_{-} \quad (2.12)$$

In Eqn. 2.12  $N_{\pm}$  are the ion and electron charge distributions,  $u_{\pm}$  are the ion and electron mobilities, and  $\alpha$  is the recombination constant. Thomas and Imel improved upon this model by making appropriate approximations for liquid xenon and argon: the diffusion rate is very small and ion drift is much slower than electron drift (3 – 5 orders of magnitude). These simplifications lead to the set of equations 2.13.

$$\begin{aligned}\frac{\partial N_+}{\partial t} &= -\alpha N_+ N_- \\ \frac{\partial N_-}{\partial t} &= u_- E \frac{\partial N_-}{\partial z} - \alpha N_+ N_-\end{aligned}\tag{2.13}$$

Assuming that the electron-ion pairs are isolated, that the initial distribution of ions and electrons uniformly populates a box of dimension  $a$ , and that  $N_{ion}$  electron-ion pairs initially fill the box, we can solve equations 2.13 to find the probability of recombination.

$$r = 1 - \frac{\ln(1 + N_{ion}\sigma)}{N_{ion}\sigma}, \quad \sigma = \frac{\alpha}{4a^2\mu_- E}\tag{2.14}$$

We redefine the number of excitons and electron-ion pairs following recombination in the same way as with electronic recoils.

$$N_{ex} \leftarrow N_{ex} + rN_{ion}, \quad N_{ion} \leftarrow (1 - r)N_{ion}\tag{2.15}$$

Since nuclear recoils result in smaller and more dense tracks, we must also account for biexcitonic quenching. Biexcitonic quenching occurs by the process outlined in Eqn. 2.3: two excitons collide ultimately leading to the formation of a single electron-ion pair. This process effectively reduces the two potential photons to a single observable photon. This electronic quenching is typically parameterized using the quenching term from Birks' saturation law, as shown in Eqn. 3.14, since one would expect that the density of excitons in a track to be proportional to the electronic stopping power [88–90].

$$f_B = \frac{1}{1 + \eta \frac{dE}{dx}} = \frac{1}{1 + \eta k \epsilon^{-1/2}}\tag{2.16}$$

This quenching ultimately reduces the number of photons that will be observable in a given interaction, as shown in Eqn. 2.17.

$$N_\gamma = N_{ex} f_B, \quad N_e = N_{ion}\tag{2.17}$$

## 2.5 Dual-Phase Time Projection Chambers

Having discussed how different types of particles deposit their energy in liquid xenon, we can now discuss dual-phase xenon time projection chambers (TPCs), the leading detector type in the search for WIMPs, and how they identify interaction types and reconstruct the position and energy of interactions in a TPC.

### 2.5.1 Operating Principle

On an interaction-by-interaction basis, the goal of dual-phase xenon TPC is three-fold: determine the type of the interaction (nuclear or electronic recoil), determine the energy of the interaction, and determine the position of the interaction. While we will discuss in more detail how each of these goals is achieved in a TPC, it is important to understand how the observables are extracted from the liquid xenon.

For both nuclear and electronic recoils, an interaction in the liquid xenon with an applied electric field results in both photons and free electrons. The number of photons are measured by using photomultipler tube (PMT) arrays at the top and bottom of the detector. These PMTs convert the light signal into a proportional charge signal that can be read by a standard digitizer. This prompt scintillation signal is referred to as the S1 of the interaction. The electric field that is applied vertically in the detector is used to extract the free electrons from the interaction site and to the liquid-gas boundary in the detector. An additional electric field is applied to extract the electrons from the liquid and to accelerate the electrons through the gas, exciting xenon atoms that lead to secondary scintillation photons in the process. This process occurs at a time directly related to the depth of the interaction in the liquid (discussed in more detail in Sec. 2.5.1.3). This secondary scintillation process, which is proportional to the number of electrons extracted from the interaction site, is referred to as the S2 of the interaction. This entire process is depicted in Fig. 2.7 and will be discussed in significantly more detail throughout the remainder of this chapter.

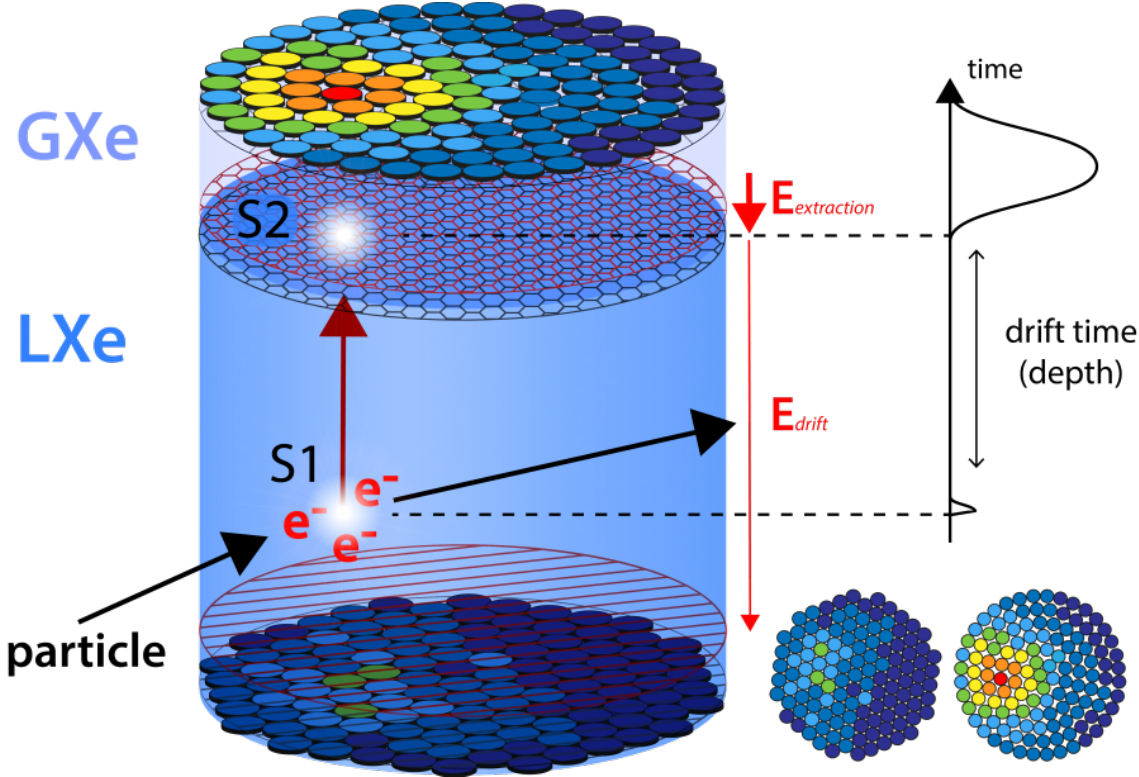


Figure 2.7: An example of an interaction in a dual-phase liquid xenon time projection chamber. The interaction produces both scintillation light and free electrons. The light is promptly detected by the PMT arrays at the top and bottom of the detector while the free electrons are drifted to the liquid-gas interface (maroon arrow) where they are extracted and accelerated through the gaseous xenon. This acceleration through the gaseous xenon causes secondary excitations that result in more scintillation light that is detected by the PMT arrays. The time difference between these interactions can be used to extract the depth of the interaction while the PMT hit patterns for the secondary signal can be used to find the interactions position in the transverse plane.

### 2.5.1.1 Reconstructing Interaction Type

Since the most basic function of these TPCs is to search for WIMPs via elastic nuclear recoils, it becomes crucially important to be able say what is likely background (electronic recoils) and what is a potential signal (nuclear recoils). Without this type of discrimination, searches are limited to counting techniques like those discussed in the first chapter. Since the electronic recoil background rate is typically several orders of magnitudes larger than the nuclear recoil background, an experiment that can discriminate between the two interactions will be significantly more sensitive than

a similar detector that is not.

As mentioned throughout this chapter, even though the energy deposition processes of electronic and nuclear recoils are similar they are far from identical. These differences in track structure and interaction cross-sections lead to very large discrepancies in the amount of charge produced in an interaction relative to the amount of light produced at a given field. For energies relevant to the WIMP search, the relationship shown in Eqn. 2.18 holds for electronic and nuclear recoils and can be used to discriminate between them. Fig. 2.8 shows this difference between electronic and nuclear recoils for XENON1T with a drift field of  $116.7 \pm 7.5 \text{ V/cm}$  [48].

$$\left(\frac{S_2}{S_1}\right)_{\text{ER}} > \left(\frac{S_2}{S_1}\right)_{\text{NR}} \quad (2.18)$$

This difference in the ratio of charge to light can actually be enhanced further: while  $\frac{S_2}{S_1}$  for nuclear recoils has little to no dependence on the electric field applied in the TPC,  $\frac{S_2}{S_1}$  for electronic recoils is heavily dependent on the electric field [62, 91], as can be seen in Fig. 2.9. Therefore, the discrimination power between the two types of interactions can be increased by increasing the electric field used in the TPC.

### 2.5.1.2 Reconstructing Energy

A significant portion of this chapter was dedicated to understanding the production process of the observable photons and electrons in liquid xenon with an applied electric field. With a perfect understanding of the observables production process and the detector effects, one could reconstruct the probability distribution for the energy of an event. The reason you could not say the energy precisely, even with a perfect understanding of the physical processes described and the detector physics, is because there is an associated smearing at each stage in the observables process – in other words, two nuclear recoils depositing 10 keV at the same position in the detector will not produce exactly the same measured event each time.

However, even being able to approximate the energy of an event is extremely important. More precisely, an understanding of the process between energy deposition

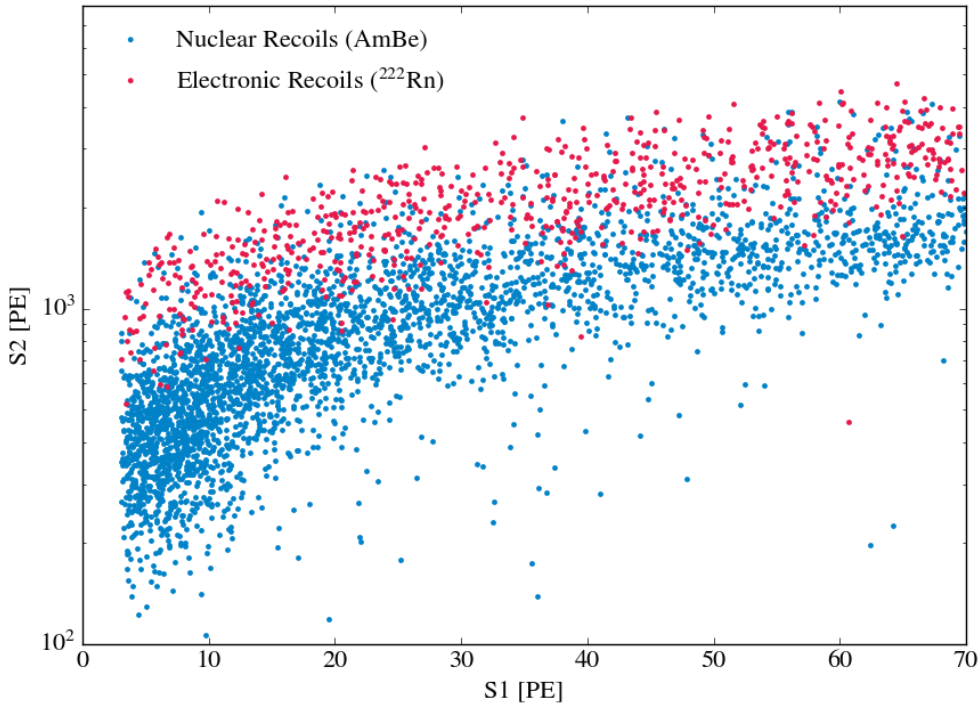


Figure 2.8: Low energy electronic and nuclear recoils in liquid xenon. Note that for a given S1 that the S2 for electronic recoils are usually significantly higher than the corresponding S2 for nuclear recoils. The nuclear recoils are from an americium-beryllium (AmBe) source while the electronic recoils are from the  $^{222}\text{Rn}$  decay chain that results in a  $\beta^-$  emission with a maximum energy of 1.02 MeV.

to the readout of observables is essential for the most sensitive dark matter searches. The reason for this is because all predicted signals in the detector, including both background and potential WIMP signals, have a predictable energy spectrum. Therefore, we can not only predict how many electronic and nuclear recoils there should be but we can also say *where* they should be in an S1 and S2 spectrum. As a concrete example, we expect the nuclear recoil background to fall off exponentially with increasing energy. Therefore, an excess of events at high energies is more significant (or indicates a misunderstanding regarding the background) than an excess of events at low energies.

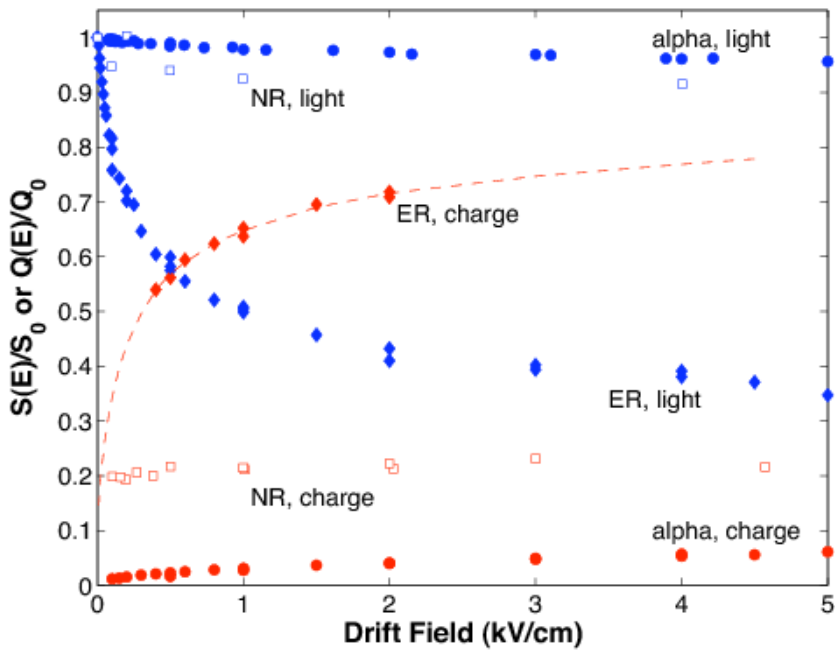


Figure 2.9: The field dependence of scintillation and ionization yield in liquid xenon for 122 keV electronic recoils and 56.5 keV nuclear recoils. In blue are the light yields of interactions at a given field relative to the light yield with no applied electric field. In red are the charge yields of interactions relative to the charge yield assuming no recombination. Image Credit: Ref. [62]

### 2.5.1.3 Reconstructing Position

An additional piece of information that proves to be very useful that can be extracted from TPCs is the position of an event. As mentioned earlier, an approximately uniform electric field is applied in the TPC to extract the electrons created in an interaction from the vertex to the liquid-gas interface where they will produce the secondary signal, the S<sub>2</sub>. Of course, the scintillation light from the interaction is measured extremely quickly (on the order of nanoseconds such that we approximate the delay as zero) so the S<sub>1</sub> can be used as the start of a timer that ends with the S<sub>2</sub>. This drift time can then be used to reconstruct the depth of the interaction since the electron will travel with a constant velocity through the liquid xenon as given by  $v_d = \mu E$ , where  $v_d$  is the drift velocity,  $\mu$  is the mobility of electrons in liquid xenon, and  $E$  is the electric field applied. This analysis to determine the depth is shown on

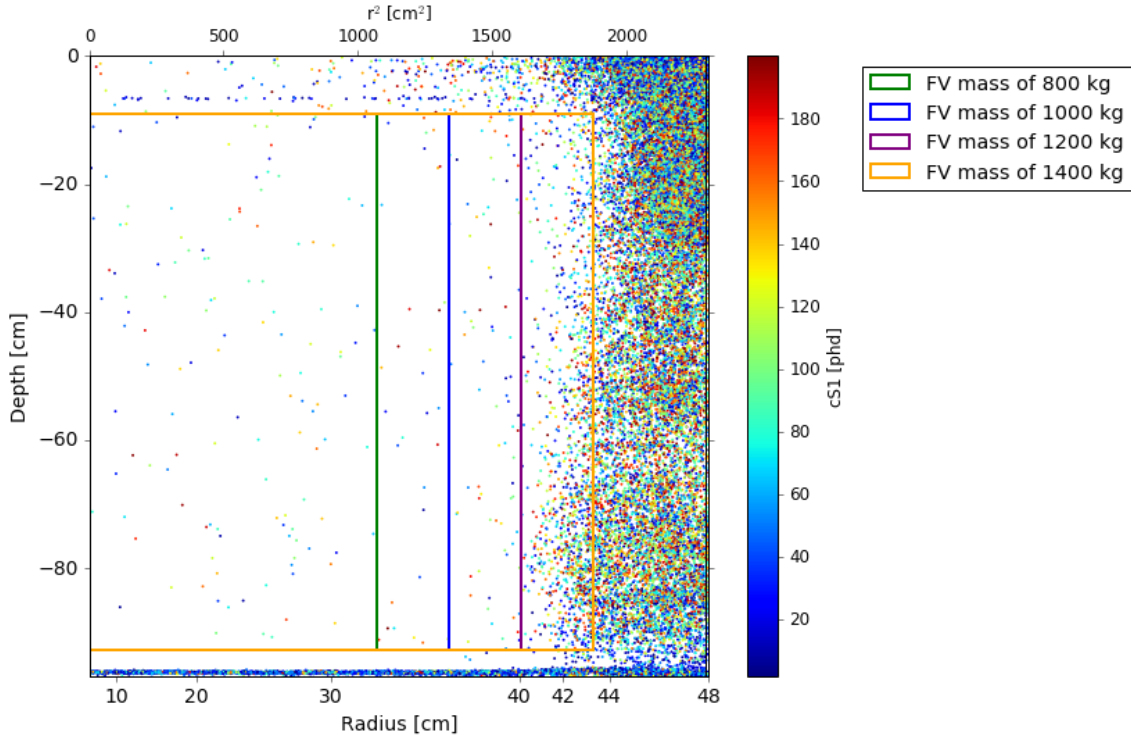


Figure 2.10: The positions of all events during the first science run of XENON1T. Notice that the overwhelming majority of events occur at the very edge of the detector and can be removed using a fiducial volume.

the right side of Fig. 2.7.

As mentioned earlier in this chapter, the stopping power for different charged particles in liquid xenon is high enough such that interactions will be stopped in  $\lesssim 10 \mu\text{m}$ . Diffusion for electrons in liquid xenon is also small: even assuming a very large drift time of 1 ms, the expected transverse diffusion is on the order of  $\sqrt{D_t t_d} \sim 20 \text{ mm}$  so the electrons should still be very localized when arriving at the liquid-gas interface. Once these electrons are accelerated through the gas layer they create the secondary photons (S2), which are then detected using the PMT arrays at the top and the bottom of the detector. The hit pattern of the PMT arrays, specifically the top array because of its proximity, can be used to approximate the location of extraction at the liquid-gas interface, which should be a very good approximation of the position at the depth found using the drift time. The PMT hit patterns are shown on the bottom-right of Fig. 2.7.

The three-dimensional location of an event inside a detector proves to be very important for WIMP searches. To understand why, it is useful to consider a WIMP event in a detector. Since the cross-section of the WIMP is so small, one would expect two features in a WIMP event: it would only scatter a single time and it could scatter anywhere in the liquid xenon with equal probability. However, this is very different from almost all of our external background sources (the exception, of course, being neutrinos) - both external gamma, beta, and neutron sources that emit particles into the liquid xenon are expected to lose energy through multiple scatters, which can easily be identified and removed by observing multiple S2 peaks (called a *multiple scatter cut*), and/or are expected to travel only a short distance before depositing all of their energy. The latter effect can be seen in Fig. 2.10, taken from XENON1T’s first science run, which shows that the overwhelming majority of events occur at the very edges of the TPC. One can then remove these events by making a *fiducial volume cut* that removes all events not within a certain distance from the center of the detector — four of these potential fiducial volume cuts are shown in Fig. 2.10. By using a multiple scatter cut and a fiducial volume cut, it is straightforward to remove almost all of the external background events, although it is important to note that this will not remove events from internal sources such as  $^{85}\text{Kr}$  or  $^{222}\text{Rn}$  or events from neutrino interactions. Additionally, by removing the edges of the TPC the expected rate of WIMPs will decrease linearly with the target mass excluded. Therefore, the volume must be chosen carefully such that the gain from background exclusion outweighs the loss in the expected WIMP scattering rate.

### 2.5.2 Detecting Observables

In this section we will discuss the details of how the observables produced by an interaction, the light and charge, are actually measured in TPCs to produce *waveforms* like the one shown in Fig. 2.11.

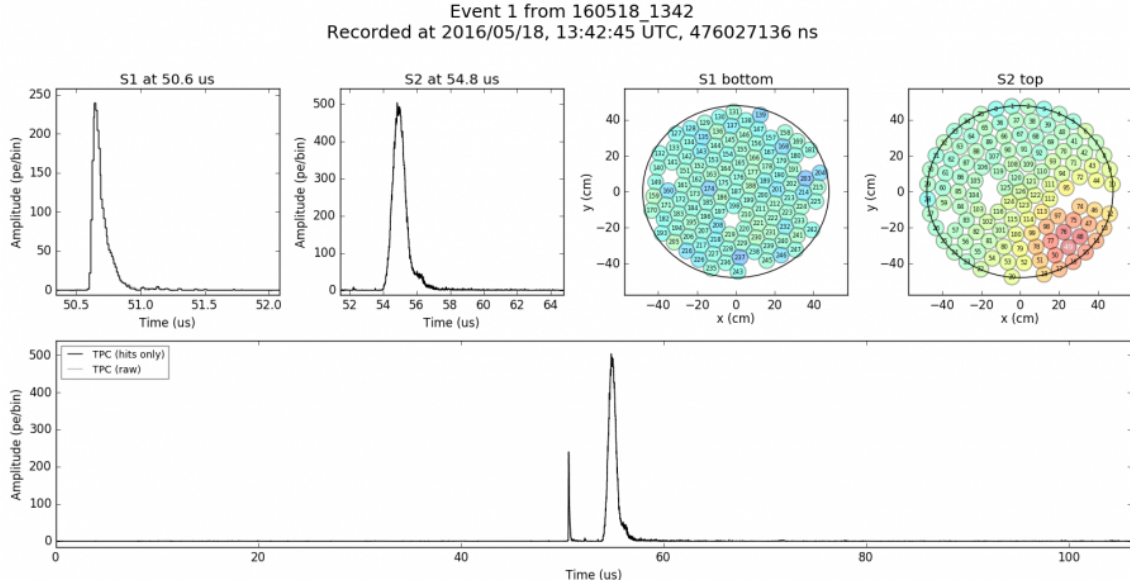


Figure 2.11: The waveform of the first event seen by XENON1T.

### 2.5.2.1 Detection of Scintillation Photons: S1

The excited xenon dimers, excimers, decay very quickly (on the order of 10 ns) and produce 178 nm photons regardless of the interaction type. These photons can be detected by the use of photomultiplier tubes (PMTs) that are designed to have peak efficiency for UV light. In TPCs, the PMT arrays are placed at the top and bottom of the detector, as shown in Fig. 2.7, but cannot be placed around the sides of the TPC as the high voltage of the PMTs will prevent the electric field used to drift the electrons from being uniform in the vertical direction. Because of this, light will typically reflect off of multiple surfaces before reaching the face of the PMT. Since detectable light is lost during reflections, the position of the event will be important in understanding how much of the initial light is likely to be detected (with events closer to the PMTs and towards the center having a high detection efficiency than events near the edge of the TPC). There is also an efficiency loss in the PMTs themselves since only roughly a third of photons that reach the photocathode of the PMT produce a signal — this efficiency is referred to as the *quantum efficiency* (QE). These losses lead to roughly

## 2. LIQUID XENON AND DUAL-PHASE TPCs

---

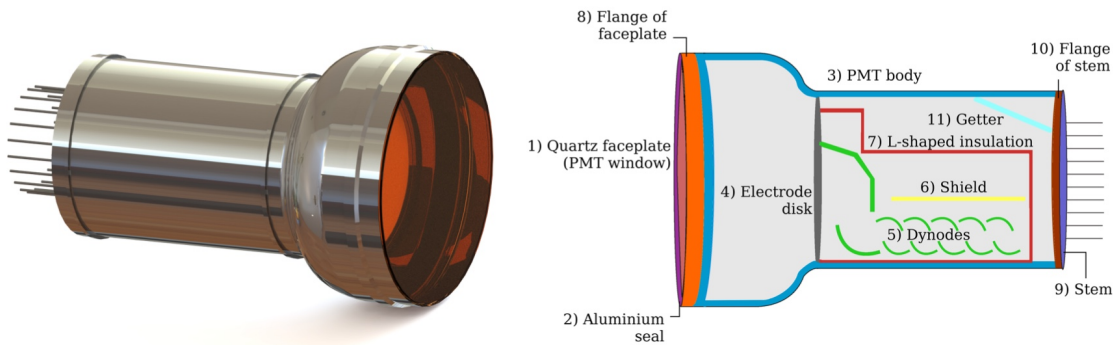


Figure 2.12: The Hamamatsu R11410 PMT and a schematic illustration of its various components. Image Credit: Ref. [95].

90% of light from an interaction not being detected!<sup>5</sup>

The main function of a PMT is to convert light signals into electrical signals, which can subsequently be digitized. A schematic of a photomultiplier tube is shown in Fig. 2.12. When light shines upon the PMT window, there is a probability defined by the quantum efficiency that an electron is emitted by the photoelectric effect — this electron is called a photoelectron. This photoelectron is then guided and accelerated by an electric field to a stage of dynodes by which the initial electron produces secondary electrons at each stage in the chain. The electrons reaching the end of the stage will be proportional to the initial number of photoelectrons and result in a current that can be digitized.

Since both the deexcitation of the excimers and the photomultiplication are both very fast processes (on the order of 10 ns), the S1 signal is considered to be a prompt signal. This is very different from the S2 signal which will have a long delay (on the order of tens to hundreds of microseconds) depending on the depth of the interaction in the liquid xenon and the strength of the applied drift field.

---

<sup>5</sup>Because of this large loss of scintillation light, a great deal of effort has gone into choosing and preparing material for the TPC to maximize the reflectivity [92–94].

### 2.5.2.2 Detection of Ionization Electrons: S2

The S2 signal is a result of the electrons that do not recombine with an ion that was also created in the interaction. These electrons are drifted using an approximately uniform vertical electric field to the liquid-gas interface. Then, using a second electric field typically much stronger than the drift field (thousands of V/cm compared to hundreds), they are extracted from the liquid and accelerated through the gas, as shown in Fig. 2.7. The accelerated electrons will create xenon excimers while being accelerated through the gas which will result in our secondary light signal that can be detected by PMTs.

The constant electron drift through the medium is actually an average over a series of many accelerations and decelerations. The electrons are accelerated by the electric field and quickly lose energy in the liquid xenon through elastic scatters [96]. While this complicated series of interactions on a macro scale is quite simple, there is a complicating factor: electrons drifting through the liquid can be absorbed by electronegative impurities in the xenon, the most common of which is oxygen. This process can also be examined from a larger scale and we can actually describe it with a single parameter: the so-called *electron lifetime*. The probability that an electron is not absorbed while drifting in the xenon is described in Eqn. 2.19.

$$P(z) = \frac{1}{\tau_{e^-}} e^{-\frac{z}{v_d \tau_{e^-}}} \quad (2.19)$$

In Eqn. 2.19,  $z$  is the vertical distance between the electron and liquid-gas interface,  $v_d$  is the drift velocity, and  $\tau_{e^-}$  is the electron lifetime. The xenon in a TPC must be constantly cleaned of these electronegative impurities to maintain a reasonable electron lifetime which proves to be technically challenging. However, measuring the electron lifetime is relatively straight-forward. The basic idea is that you look at an electronic recoil of known energy (the electronic recoil resulting from the decay of  $^{83m}\text{Kr}$ , for example) and look at the S2 signal as a function of depth. Since the light produced in the gaseous xenon is proportional to the number of electrons, one should see an exponential decrease in the size of the S2 as a function of depth according to

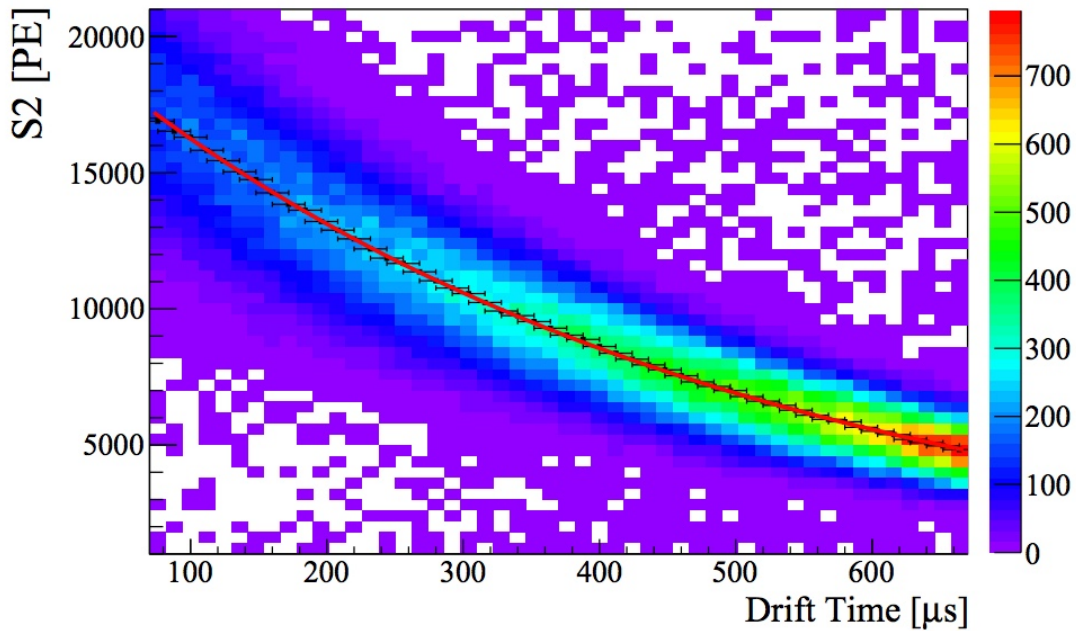


Figure 2.13: An example of an electron lifetime analysis from XENON1T. In this analysis, the 41 keV  $^{83\text{m}}\text{Kr}$  electronic recoil is used and the decay's S2 signal size is plotted versus drift time (a proxy for depth). Image Credit: Ref. [97].

Eqn. 2.19. An example of this type of electron lifetime measurement and the resulting exponential fit to the S2 size is shown in Fig. 2.13. As detectors grow in size it is critical that they are still able to clean the xenon of the increased level of impurities still since a low electron lifetime results in a large reduction in signal and smearing in S2 (which reduces discrimination power).

Finally, the number of excitations produced in the gaseous xenon will be proportional to the number of electrons accelerated through. The resulting number of photons for a single electron approximately follows a Gaussian distribution. The mean of this Gaussian is referred to as the *gas gain*. Therefore, the number of electrons from the interaction can be inferred by looking at the number of photons detected by the photomultiplier tubes. The response of the TPC to a single electron accelerated through gaseous xenon can also be measured in a relatively simple manner by looking at single electrons that drift to the liquid-gas interface (these single electrons often come from the photoionization of the stainless steel grids used to produce the drift field in the TPC). This method is described in more detail in Ref. [98], as well as in

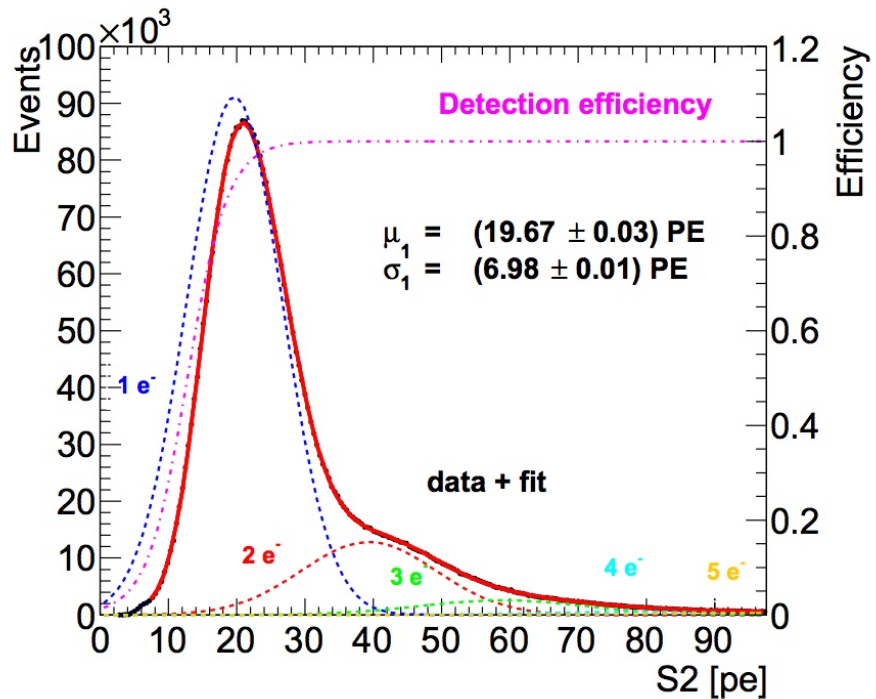


Figure 2.14: An example of a gas gain analysis from XENON100. This fit was performed using electrons from photoionization of metal inside of the detector. Image Credit: Ref. [98].

Sec. 3.3.4 and Sec. 4.2.3. An example of this analysis is shown in Fig. 2.14.



# Chapter 3

## The First Dark Matter Search with XENON1T

XENON1T is the third generation detector of the XENON Dark Matter Collaboration. With a fiducial mass of over 1,000 kg, it is expected to be the most sensitive detector in the world to WIMPs. This chapter will focus on the XENON1T Dark Matter Experiment and the results from its first WIMP search. The first section will focus on the design of the detector and its subsystems while the second section will focus on background considerations and estimation for the detector. The following section will focus on the general calibration of the detector followed by a section on the calibration of the detector to electronic and nuclear recoils. Finally, we will discuss the results of the first dark matter search and its implications.

### 3.1 The XENON1T Detector

In this section we will focus on the XENON1T detector and its individual subsystems that are needed for it to operate according to the working principle discussed in Sec. 2.5. For more details on the design and construction of the detector, please refer to Ref. [97].

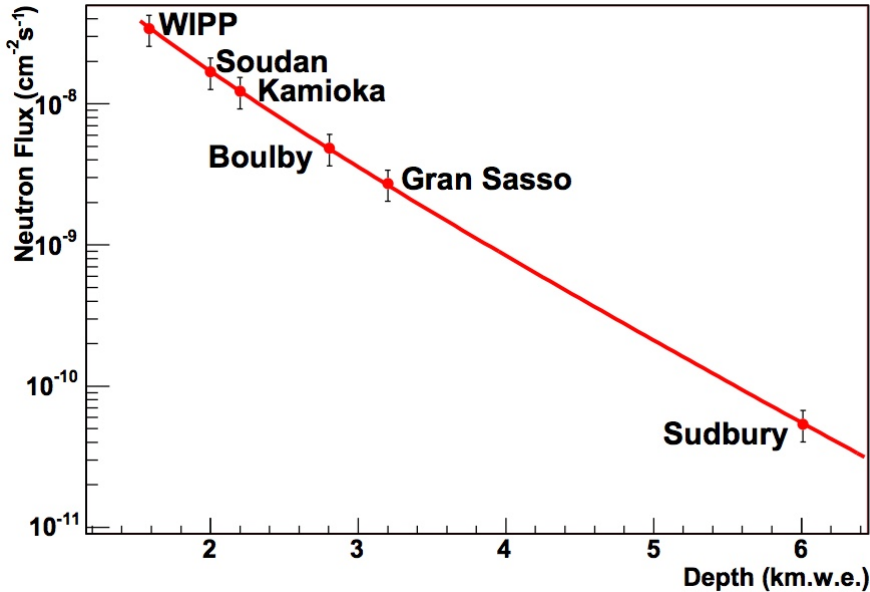


Figure 3.1: The neutron flux due to cosmogenic muons versus kilometers water equivalent depth for various underground laboratories. Image Credit: Ref. [99].

### 3.1.1 Laboratori Nazionali del Gran Sasso

Laboratori Nazionali del Gran Sasso (LNGS) is an Italian national laboratory located underneath the Gran Sasso mountain range in central Italy. In order to shield from cosmogenic backgrounds, dark matter detectors, and detectors for low background experiments in general, are placed deep underground. Even deep underground, very high energy muons are still not completely shielded and are a dangerous background source for dark matter searches because they can produce fast neutrons in the rock that could recoil in the detector. The flux of these neutrons at different laboratories has been measured in Ref. [99] and a plot of the fluxes is shown in Fig. 3.1.

To shield against these neutrons, the TPC is inside the center of a cylinder filled with water that is roughly ten meters in diameter and ten meters tall. This will be the focus of Sec. 3.1.2.

### 3.1.2 Muon Veto

As mentioned in the previous section, to shield against the potential cosmogenic neutron background, the TPC is placed inside of a very large water tank ( $\sim 10$  meter

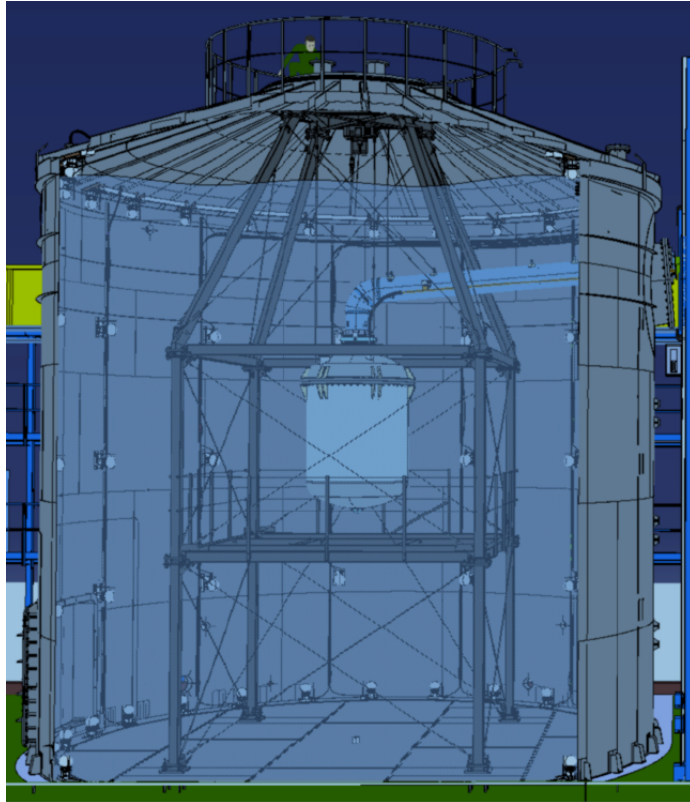


Figure 3.2: A cartoon of the muon veto with the TPC centered inside the water tank.

diameter and  $\sim 10$  meter height). This muon veto is outfitted with 84 8" diameter Hamamatsu R5912ASSY high quantum efficiency PMTs to detect the light from interactions inside of the water tank and the DF2000MA reflective foil to maximize the potential measured signal [100]. A diagram showing the water tank and its PMT is shown in Fig. 3.2 and a photo of the interior of the water tank during filling is shown in Fig. 3.3. A detailed Geant4 simulation [101] of the muon events originating in the rock surrounding the laboratory shows that the efficiency of the veto is  $99.78 \pm 0.05\%$  for neutrons accompanied by the muon and  $71.4 \pm 0.5\%$  for neutrons without the initial muon. Neutrons are accompanied by muons roughly  $1/3$  of the time [100].

In addition to screening cosmogenic neutrons, the muon veto also acts as a shield to external gamma ray and neutron sources. The neutrons mainly come from the spontaneous fission of  $^{238}\text{Ur}$  and the  $^{232}\text{Th}$  ( $\alpha, n$ ) reactions, both of which are found in small quantities in the surrounding rock and concrete. Detailed Geant4 simulations [101] show that the external gamma ray background is reduced by approximately 7

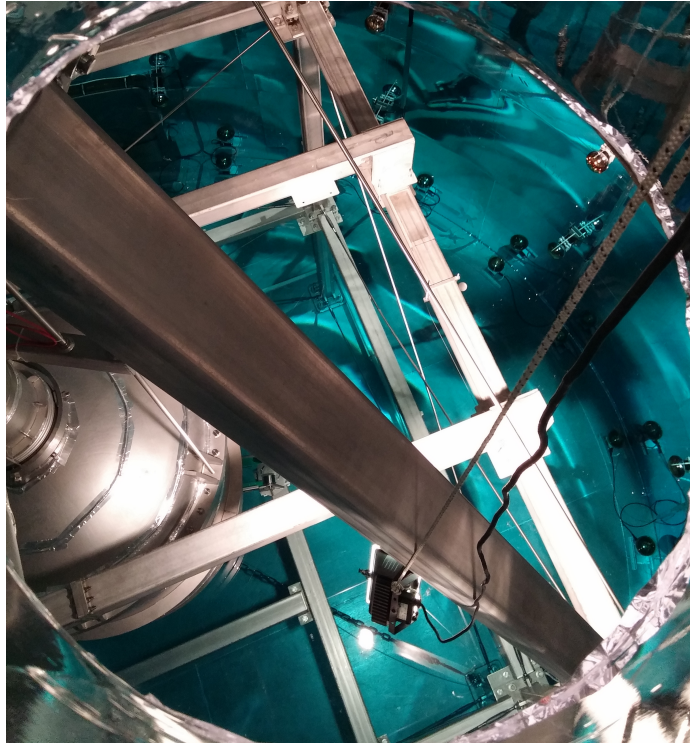


Figure 3.3: A photo of the inside of the muon veto water tank. The 8" PMTs can be seen along the edges of the tank and the TPC can be seen in the center of the tank (left side of the photo).

orders of magnitude across 4 meters of water and the external neutron background is reduced by approximately 6 orders of magnitude per meter of water.

Given the expected fluxes for cosmogenic neutrons and radiogenic neutrons from the rock and concrete,  $8.1 \cdot 10^{-10}$  above 1 MeV [99] and  $8.7 \cdot 10^{-7} \frac{n}{\text{cm}^2\text{s}}$  above 1 keV, respectively, combined with the expected attenuation and cut efficiency result in a negligible external neutron background  $< 0.01 \frac{\text{events}}{\text{y}}$  [77].

### 3.1.3 Cryostat

In between the TPC itself and the water of the water tank is the cryostat. The cryostat is a double-walled vacuum insulated vessel designed to contain the detector assembly and 3.5 tons of liquid xenon. The cryostat itself is made of 5 mm thick, low radioactivity stainless steel. The inner part of the cryostat, since it needs to house such a large amount of liquid xenon at roughly  $-96^\circ\text{C}$ , is covered in a blanket



Figure 3.4: A photo from inside the watertank with the inner cryostat installed. Note the mylar foil around the vessel for insulation against radiative heat transfer.

of aluminized mylar foil to minimize radiative heat transfer (shown in Fig. 3.4). The outer cryostat is large enough to hold and support XENON1T’s inner vessel and TPC but also the inner vessel and TPC of XENONnT, a planned upgrade of XENON1T. A diagram of the cryostat and the TPC is shown in Fig. 3.5.

The cryostat is connected to external systems such as the purification and cryogenic systems via a double-walled vacuum insulated pipe. This pipe not only carries liquid xenon and gaseous xenon to and from the different systems but also houses the various cables that need to go into the detector (mainly signal and high voltage cables). These cables are stored inside of a smaller pipe so that radon emanations lead away from the TPC. One of the gaseous xenon lines is used to pressurize the xenon diving bell, which is used to set the liquid level in the detector.

The weight of the cryostat and TPC are supported by three stainless steel rods. These rods are connected to several motion feedthroughs such that the level of the xenon in the TPC is approximately  $100 \mu\text{m}$ . These systems are also designed for XENON1T and XENONnT.

A schematic of the cryostat, TPC, and many of the subsystems that will be

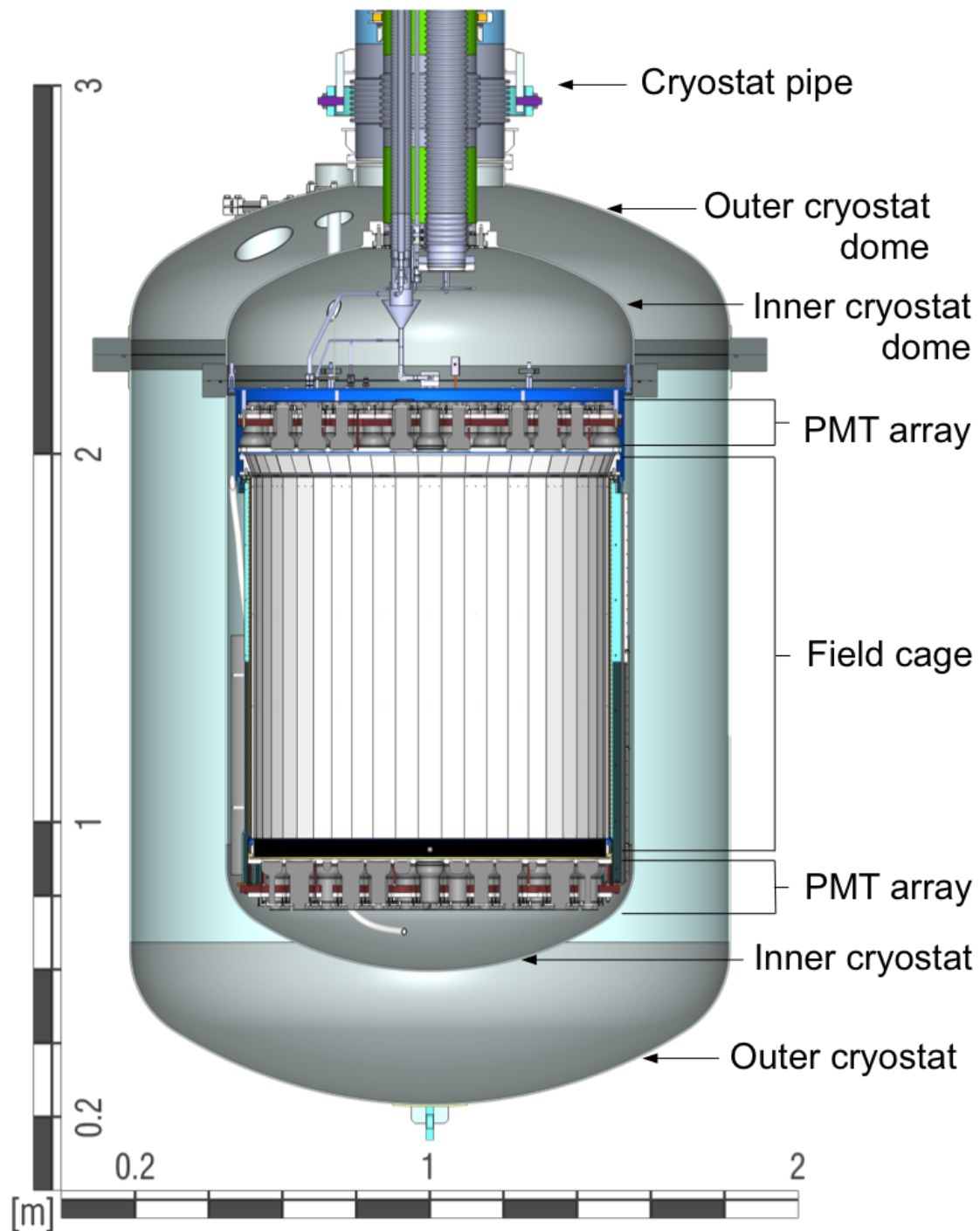


Figure 3.5: A diagram of the cryostat, the TPC, and the subsystems of each. Image Credit: Ref. [102].

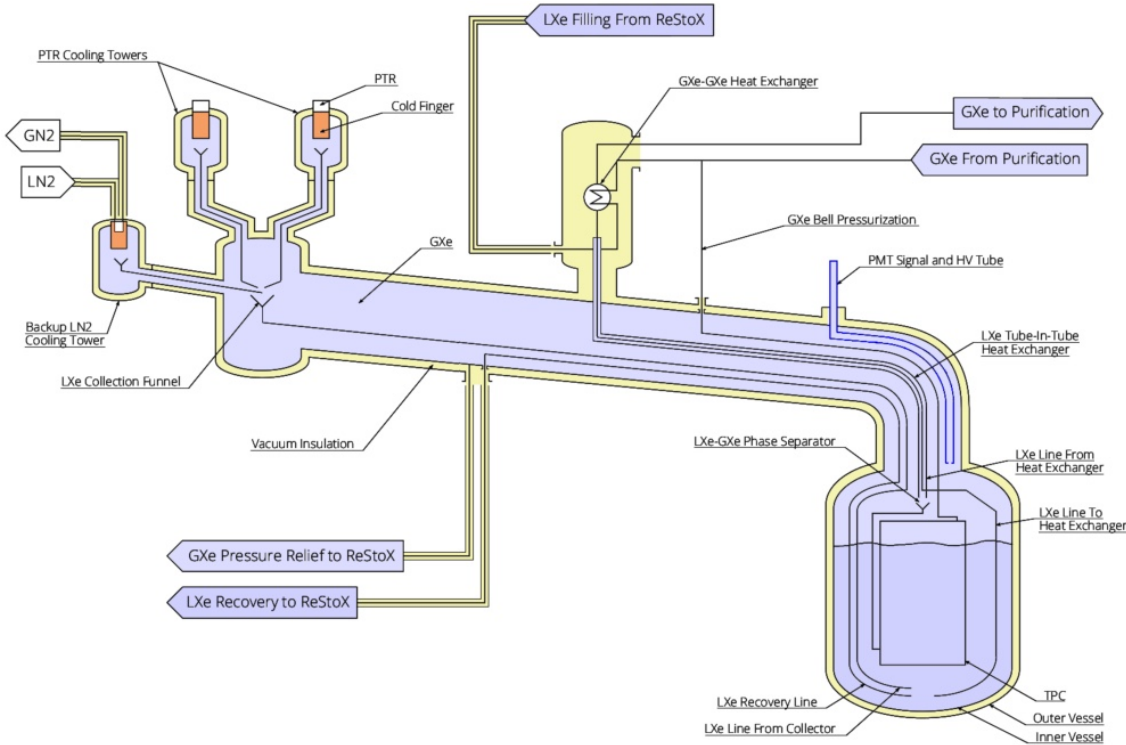


Figure 3.6: A diagram of the cryostat, the cryogenics system, and the purification systems. Image Credit: Ref. [102].

discussed is shown in Fig. 3.6.

### 3.1.4 Cryogenics System

To keep the 3.5 tons of liquid xenon cool, two pulse tube refrigerators (Iwatani PC-150 PTRs) are used. Each of the PTRs provides a cooling power of approximately 250 W while the estimated total heat load of the system (including the removal of electronegative impurities which will be discussed in Sec. 3.1.5.1) is less than 150 W. Therefore, this system is doubly-redundant and designed such that a PTR can be removed and replaced during operation of the detector. These PTRs are connected to copper cold fingers on which the gaseous xenon condensates and flows back into the detector. The xenon pressure inside of the cryostat is controlled via resistive heaters thermally connected to the copper cold fingers. These resistive heaters are controlled by a proportional-integral-derivative (PID) controller that adjusts the power of the heaters to maintain a desired cold-finger temperature [97].

### 3. THE FIRST DARK MATTER SEARCH WITH XENON1T

---

The photomultiplier tubes (which will be discussed in Sec. 3.1.8) are susceptible to damage if the pressure in the detector becomes too high. For this reason, it is crucial to be able to keep the pressure stable even in the event of an emergency. XENON1T was designed such that if there is a sudden increase in pressure, a cold finger that is cooled using liquid nitrogen is used in place of the PTRs. To maintain normal operating conditions in the detector only  $\sim$ 100 liters per day are required (the tank containing liquid nitrogen can store up to 10,000 L) [97].

The three redundant cooling systems can be seen on the left side of Fig. 3.6. The gas in the pipe condenses on the cold fingers and then is fed back into the cryostat.

#### 3.1.5 Purification Systems

There are two main purification systems in XENON1T: one for electronegative impurities and a second for the removal of  $^{85}\text{Kr}$ .

##### 3.1.5.1 Electronegative Impurities

As mentioned in Sec. 2.5.2.2, electronegative impurities, mainly oxygen, enter the liquid xenon through the various materials used when constructing the detector. These electronegative impurities can capture free electrons that are drifted to produce the secondary signal, the S2. This causes a complete loss of signal in the case of high concentrations but will still cause large smearing effects at low levels of concentration (ppb levels of  $\text{O}_2$  relative to xenon), reducing the discrimination power of liquid xenon for electronic and nuclear recoils.

Materials are cleaned before being installed in the detector. However these electronegative impurities are constantly outgassing into the detector and therefore the xenon must be constantly cleaned. To achieve high purity, a doubly redundant purification system that is connected to the cryostat is used (center of Fig. 3.6). This system includes two loops with a gas driving pump (CHART QDrive) and a high-temperature rare-gas purifier (SAES PS4-MT50-R getter) [97]. The SAES getter is able to reduce the  $\text{O}_2$ ,  $\text{H}_2\text{O}$ ,  $\text{CO}$ ,  $\text{CO}_2$ ,  $\text{H}_2$ ,  $\text{N}_2$ , and  $\text{CH}_4$  concentrations to low

ppb or below by having the impurities form irreversible chemical bonds with the material inside of the getter. One drawback of the getter is that it must be operated at high temperatures ( $\sim 50^\circ \text{C}$ ). However, this effect can be reduced by using heat exchangers between both the hot and cold liquid and gaseous xenon. The gaseous heat exchanger can be seen in the center of Fig. 3.6 and the liquid heat exchanger (tube-in-tube) can be seen on the right side of Fig. 3.6. These heat exchangers are approximately 96% efficient and significantly reduce the heat input of the getters to 0.39 W/SLPM for a total of approximately 20 W [97].

### 3.1.5.2 $^{85}\text{Kr}$

A cryogenic distillation column is used to reduce the natural krypton to xenon level to below 200 ppq (part per quadrillion). The cryogenic distillation column leverages the different vapor pressures of the two elements around the xenon boiling point: the vapor pressure of krypton is roughly 10.8 times higher than the vapor pressure of xenon at 175 K and 2 bars. For a dual-phase system in equilibrium, this implies that the gaseous phase will be enriched with krypton relative to the liquid by this factor of 10.8 — this simple dual-phase system is referred to as a single distillation stage. To improve this separation efficiency, one can put several of these distillation stages in series with each other. This multi-stage distillation column can practically be achieved via a package material that replicates these additional stages when placed inside of a single stage. The height of the material ultimately translates into the number of stages added [103].

The concentration can be measured with an RGMS (residual gas mass spectrometer) or an RGA (residual gas analyzer). A distillation column with 2.8 meters of the Sulzer EX package material was deployed for XENON1T and achieved natural krypton to xenon levels of  $< 48 \text{ ppq}$  [59]. An atom trap trace analysis (ATTA) that was built at Columbia University [104] can also be used to measure low levels of krypton concentration in xenon. However, this was not used during the first science run.

A similar distillation column was also built to test the possibility of radon removal. Using 1 meter of package material, a radon reduction factor of  $> 27$  was achieved

[105].

### 3.1.6 Recovery and Storage

For small detectors, it sufficed to fill detectors via cooling the xenon stored in bottles and to empty the detector by evaporating the liquid xenon. While simple, this method is inefficient and would require approximately 250 W of cooling power over 2 months to fill the XENON1T detector [97]. While an emergency situation is unlikely in XENON1T due to its many redundancies, this simple method would also make recovery of all of the xenon very difficult.

Instead of storing unused xenon in bottles kept at room temperature, a new approach to recovery and storage of xenon was applied: a single 5 cubic meter vacuum-insulated stainless steel sphere rated for pressures up to 73 bar was built for this purpose, appropriately name RESToX (recovery and storage of xenon). Similar to the detector’s cryostat, several layers of aluminized mylar blanket the inner wall of this system such that the heat load on this system is only roughly 50 W. RESToX is cooled using 16 liquid nitrogen lines that are welded to the outside of the inner wall. To assure that the xenon inside of RESToX is kept at a precise temperature and pressure (to avoid freezing), a heating system has also been installed in the center of the vessel.

RESToX is directly connected to the cryostat for filling and recuperation of the xenon gas as well as both purification systems such that the xenon stored can be kept clean and ready for use. Xenon can be transferred into the cryostat via the pumps of the purification system (up to a maximum speed of 50 SLPM). Xenon is transferred from the cryostat to RESToX solely due to the pressure difference between the two systems.

### 3.1.7 Calibration Systems

While, like LUX [106], internal sources, such as  $^{83\text{m}}\text{Kr}$ , can be injected through the purification system, a new method for introducing external sources needed to be



Figure 3.7: A photograph of RESToX prior to instillation at LNGS.

developed due to the massive water tank surrounding the TPC. The solution was the installation of two belts that could be used to move external sources around the bottom of the detector (the “U-Belt”) and along the sides of the detector (the “I-Belt”) and an additional mechanism to move the neutron generator vertically along the side of the TPC. The main external sources used are  $^{228}\text{Th}$  (which has several  $\gamma$  lines between 511 and 2,614 keV),  $^{137}\text{Cs}$  (which has a single  $\gamma$  line at 662 keV), and AmBe (which produces MeV energy neutrons). The neutron generator (NSD Gradel Fusion NSD-35-DD-C-W-S) uses the deuterium-deuterium fusion process to create neutrons with energies between 2.2 and 2.7 MeV. This generator has been specially designed to provide very low neutron rates ( $\mathcal{O}(10^{\text{n/s}})$ ) as well as high neutron rates ( $\mathcal{O}(10^6 \text{n/s})$ ). These external source systems are shown in Fig. 3.8.

Like previous generations of detectors, the PMTs are calibrated using pulsed blue light fed into the detector by fiber optic cables. In XENON1T, four such fiber optic cables are fed into the detector at different heights and positions.

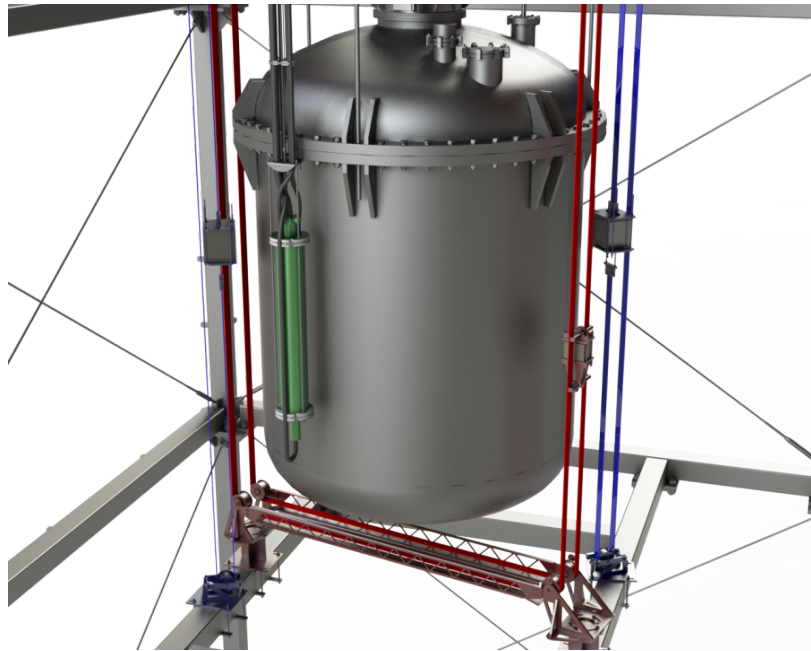


Figure 3.8: A diagram showing the external calibration systems. The “U-Belt”, which allows for placement of external sources below the TPC, is shown in red while the “I-Belt”, which allows for the placement of external sources at different heights along the side of the TPC, is shown in blue. Shown in green is the neutron generator which can be raised and lowered along the side of the detector.

### 3.1.8 Photomultiplier Tubes

XENON1T utilizes a total of 248 high quantum efficiency R11410-21 3 inch PMTs — 127 of these PMTs are located in the top array and the remaining 121 are located in the bottom array. The R11410-21 was specifically designed for XENON1T to have a high quantum efficiency, high collection efficiency, low radioactivity, and operate stably at liquid xenon temperatures.

321 of the R11410-21 PMTs were tested for quantum efficiency, dark rate, stability, and single photoelectron response. Of the 321 PMTs, 78 were rejected: 12 due to high or unstable dark count rates and 53 due to after-pulsing (44 of which were confirmed to have a leak). The PMTs were found to have an average quantum efficiency of  $34.5 \pm 2.8\%$  at 178 nm and a collection efficiency of 90 – 95% [107]. PMTs that were found to have a higher quantum efficiency and collection efficiency were placed in the center to maximize potential light collection as shown in Fig. 3.9. The bottom PMT

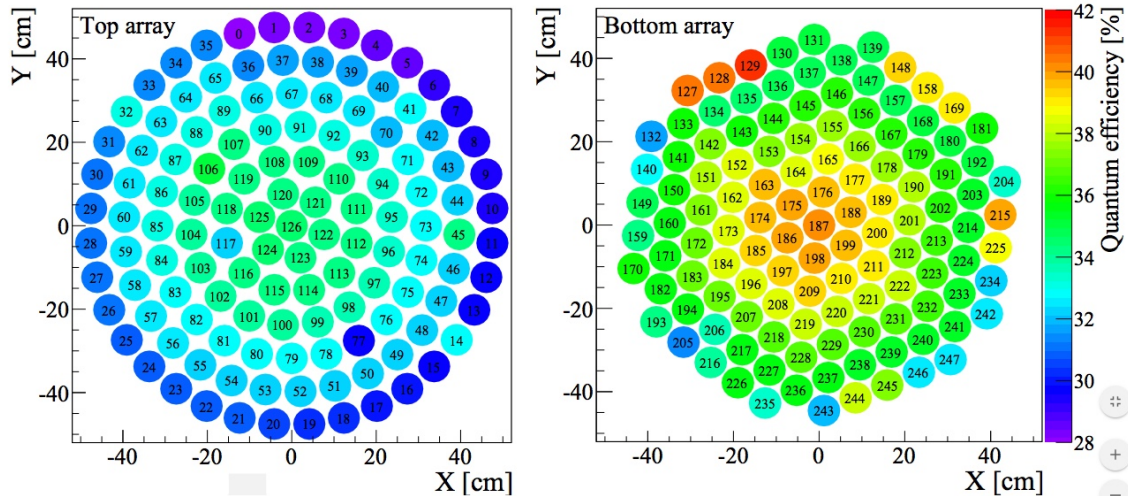


Figure 3.9: The quantum efficiencies of the PMTs installed in the XENON1T PMT arrays. Note that, with a few exceptions due to higher radioactivity levels, the highest quantum efficiency PMTs are placed towards the center to maximize light collection. Also note that in general the PMTs used in the bottom array have a higher quantum efficiency than those in the top array since the much smaller S1 signal is mainly seen by the bottom array. Image Credit: Ref. [97].

array sees the majority ( $\sim 90\%$ ) of the light for S1s due to the reflection of light at the liquid-gas interface — therefore, the higher quantum efficiency PMTs were placed in the bottom array.

Of the 248 PMTs installed, only 213 could be used for the first science run of XENON1T. The reasons for omission in the final analysis varied from high levels of noise, frequent trips and flashing, and low single photoelectron acceptance at the trigger threshold. The remaining PMTs were set such that they had a gain from  $2 - 5 \cdot 10^6 e^-$  and a resolution of approximately 30%. The gains of individual PMTs were stable over the course of data taking.

### 3.1.9 XENON1T TPC

The XENON1T TPC has a cylindrical shape with a diameter of 96 cm and height of 97 cm at room temperature. The TPC outer wall is made of PTFE (polytetrafluoroethylene), otherwise known as teflon. Teflon is chosen for several reasons: it has a high reflectivity, it can be made such that it is highly radio-pure, it has low out-

gassing rates, it is chemically inert (so no special considerations need to be made for handling or storage), and it is an excellent insulator [94]. Teflon does have a high thermal coefficient of expansion resulting in a length contraction of approximately 1.4% from room temperature to liquid xenon temperatures [108].

Throughout this and second half of the previous chapter, it has been assumed that one can provide a uniform drift field in the TPC in order to extract the electrons from the interaction site to the liquid-gas interface and a uniform extraction field to extract the electrons from the liquid into the gas for amplification. Ideally, one would use sets of parallel plates to create these uniform fields however this has the obvious drawback of not allowing for the detection of light. Instead, the plates are replaced with ultrafine grids that can approximate a uniform field while keeping a high transparency ( $\gtrsim 90\%$  from optical simulations). The width of the wires used in the grids is  $\mathcal{O}(0.2 \text{ mm})$  and the size of the cells in the grid is  $\mathcal{O}(5 \text{ mm})$ . To create the two fields mentioned, the drift and extraction fields, we need three meshes: the cathode mesh ( $\mathcal{O}(10 - 100 \text{ kV})$ ), the gate mesh (ground), and the anode mesh ( $\mathcal{O}(5 \text{ kV})$ ). To protect the PMTs from the high electric field, screening meshes kept at similar voltages to the PMTs ( $\sim -1.5 \text{ kV}$ ) are also installed. To reduce edge effects and keep the field as uniform as possible out to the edge of the TPC, 74 field shaping rings made of oxygen-free high thermal conductivity copper are installed between the cathode and the anode via a chain of  $5 \text{ G}\Omega$  resistors [97]. Shown in Fig. 3.10 are the field simulations made using the final detector design and the voltages used during the first science run of XENON1T ( $V_c = -12 \text{ kV}$  and  $V_a = 4 \text{ kV}$ ).

### 3.1.10 Data Acquisition and Processing

The final subsystem of XENON1T is the data acquisition and processing system. The signals from the 248 TPC PMTs and 84 muon veto PMTs, after being amplified by a factor of ten using a Phillips Scientific 776 Amplifier, are fed into V1724 flash ADCs. These V1724 ADCs operate at 100 MHz (resulting in a time resolution of 10 ns), with 14 bit resolution, 40 MHz bandwidth, and a 2.25 or 0.5 V dynamic range. Each ADC can handle eight channels simultaneously [109].

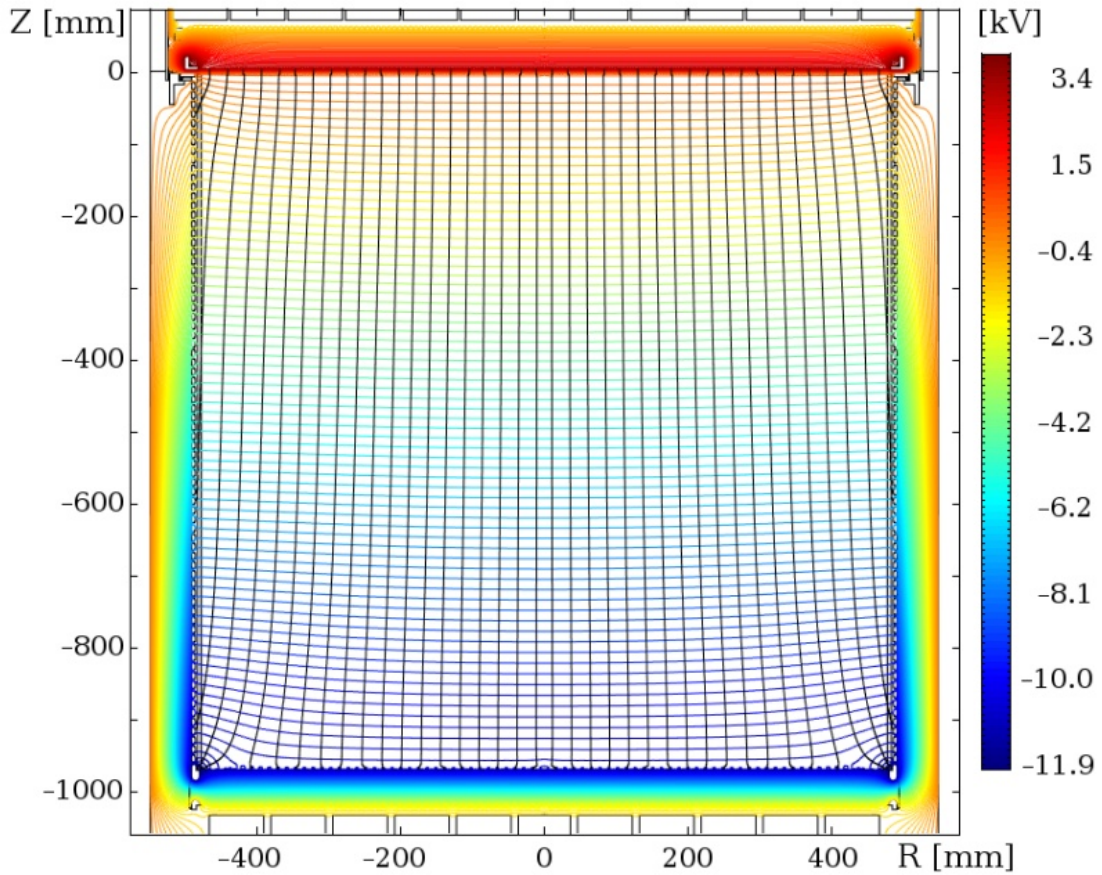


Figure 3.10: The field simulations for the TPC during the first science run of XENON1T. During this run, a cathode voltage of  $-12\text{ kV}$  was used and an anode voltage of  $+4\text{ kV}$  was used. Image Credit: Ref. [97].

The data acquisition does not have an external trigger — instead, all pulses are digitized for each channel. The pulses for each channel are then analyzed together to determine whether or not an event occurred and should be saved. These events (saved as *waveforms* that are simply ADC counts versus time) can then be processed to extract relevant information, including, but not limited, to the size of S1 and S2 signal. The processor, *PAX* (Processor for Analyzing Xenon), was designed for XENON1T but is portable enough to be used for other dual-phase TPCs.

Since the expected WIMP energy spectra (and most of the nuclear recoil background sources) exponentially decay with energy, it is crucially important to understand the efficiency with which events are saved and S1s and S2s are found in the waveforms by the processor. For the coincidence conditions, thresholds, and algo-

### 3. THE FIRST DARK MATTER SEARCH WITH XENON1T

---

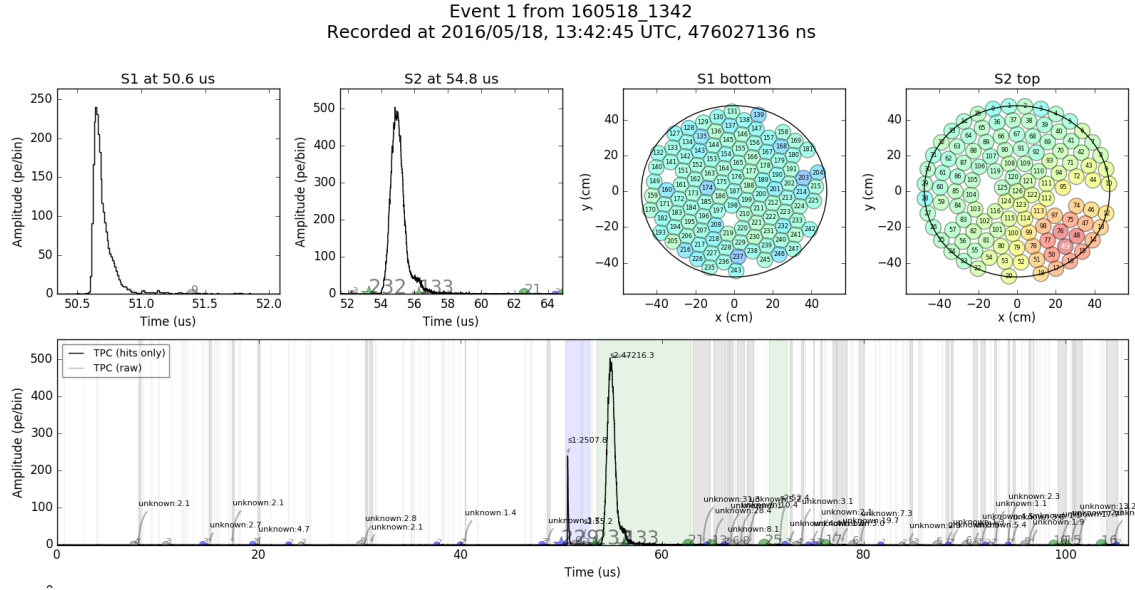


Figure 3.11: The PAX output for the first waveform in XENON1T. Shown in blue is the S1 and shown in green is the S2. The grey highlighted areas represent unidentified peaks that are likely due to the high noise rate at this point in the detector operation. Also shown are the timestamps of each signal, used to extract the depth of the interaction, and the PMT hit patterns of the top and bottom PMT arrays, which are used for position reconstruction.

rithms used in the first science run of XENON1T, it was found, via simulation, that S2s are identified with 100% efficiency when produced with two or more electrons accelerated through the gaseous xenon. This implies that even the smallest events are successfully saved. However, given the threshold and algorithm choices of the first science run, it was found, again via simulation, that five or more photons are needed to correctly identify an S1 for an event with above an 80% probability. Therefore, even with the event saved, we may not be able to extract the necessary information since the processor cannot identify the S1 in the waveform. These efficiencies will be discussed in more detail with respect to the electronic and nuclear recoil calibration of XENON1T.

## 3.2 The Background for the XENON1T Detector

Many of the potential sources of background were first discussed in the second chapter. In this section we quantify the expected rate of each of these sources as a function of energy. As mentioned previously, the higher the expected rate of background is in your region of interest, the harder it is to make a claim that excess events are due to WIMPs.

### 3.2.1 Background in XENON1T from Detector Materials

The first source of background that we will discuss is from the detector materials themselves. The detector material background contributes to both the electronic and nuclear recoil background. Even though incredible care is taken to select the most radio-pure detector components for the detector, this background will prove to be non-negligible for XENON1T, as with all other dual-phase TPCs.

To quantify the background from the different detector components, materials were screened using a high-purity germanium detector and using mass spectrometry. A detailed breakdown of the radioassay results of the various detector materials can be found in Ref. [102]. To estimate the background, the twelve largest background contributors and the eight most relevant backgrounds are considered [77]. We can simulate the background by assuming the contaminants are spread uniformly in the various detector materials and by requiring the interaction occur inside of a fiducial volume and with only a single scatter in the liquid xenon volume. The resulting energy spectrum from the simulation for electronic recoils can be seen in Fig. 3.12 and Fig. 3.13 and the resulting energy spectrum from the simulation for nuclear recoils can be seen in Fig. 3.15. Each of these spectra can be integrated to determine the rate per kilogram of xenon in the fiducial volume per day.

### 3.2.2 Electronic Recoil Background in XENON1T

Even though electronic recoils can be rejected with high confidence due to their larger charge signal relative to nuclear recoils, they still pose a dangerous background for

dark matter searches since the electronic recoil and nuclear recoil band overlap (as seen in Fig. 2.8). Putting aside the possibility that dark matter may interact with atomic electrons, in which case this is our most relevant background, a higher overall rate of electronic recoils in our detector translates to a higher probability of an electronic recoil mimicking a nuclear recoil (simply from statistical fluctuations).

The full electronic recoil background energy spectrum can be seen in Fig. 3.12 and Fig. 3.13. It is important to recall that since electronic recoils efficiently convert energy into observables, only electronic recoils under 15 keV are relevant to the WIMP search. We will briefly discuss each component of the background in the remainder of this section with the exception of the materials background, which is discussed in Sec. 3.2.1.

### 3.2.2.1 $^{222}\text{Rn}$

Radon, unlike all of the other noble gasses, has no stable isotope. Therefore, “natural” radon is the result of the  $\alpha$  decays of  $^{226}\text{Ra}$  into  $^{222}\text{Rn}$  and  $^{224}\text{Ra}$  into  $^{220}\text{Rn}$ . These maternal isotopes are part of primordial  $^{238}\text{U}$  and  $^{232}\text{Th}$  chains, respectively, that are shown in Fig. 3.14.

However similar these two chains might seem, they prove to have drastically different effects for dark matter detectors. Both  $^{238}\text{U}$  and  $^{232}\text{Th}$ , and therefore their daughter isotopes, are found in trace quantities in almost all materials, including the ones used for the construction of XENON1T. When either chain reaches the decay of radium into radon, the recoiling radon isotope has a chance of emanating from the surface that it is found on, for example from the inside of a stainless steel pipe into the gaseous xenon. This is where the difference in the two chains materializes itself. First, notice that the  $^{238}\text{U}$  chain essentially ends at  $^{210}\text{Pb}$  because of its long half-life. Second, notice that with the exception of  $^{214}\text{Pb}$  and  $^{212}\text{Pb}$  all decays are either  $\alpha$  decays or  $\beta$  decays in close coincidence with an  $\alpha$  decay such that events can be tagged and cut. These two isotopes of lead both beta decay with continuous energy spectra down to zero energy, making them both potentially dangerous background. However, the decays leading to and the decay of  $^{212}\text{Pb}$  are relatively quick (55 seconds, 0.14

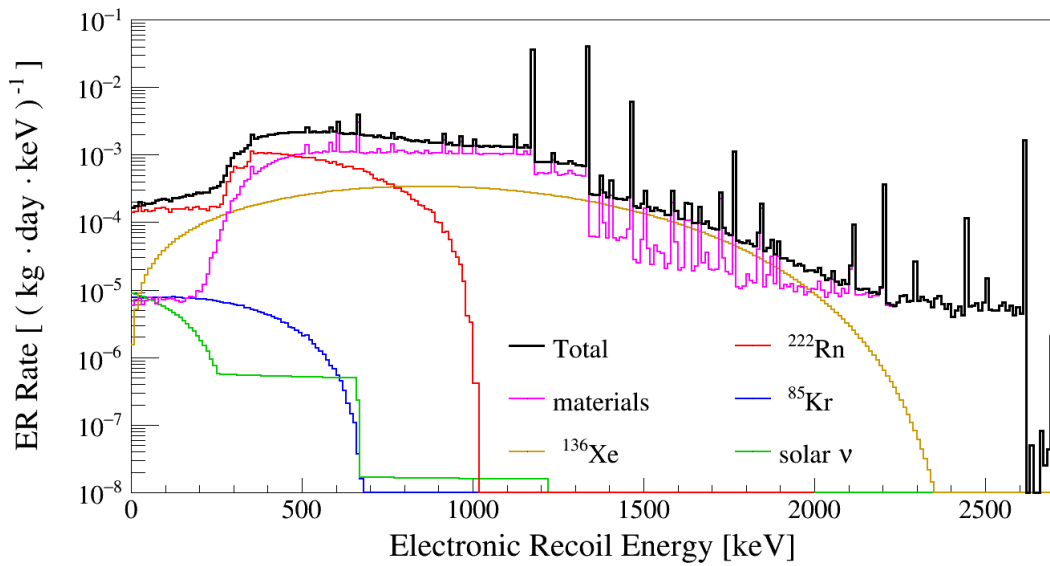


Figure 3.12: The electronic recoil energy spectrum expected from major background sources. While radiation from materials and the double beta decay of  $^{136}\text{Xe}$  dominate at high energies,  $^{222}\text{Rn}$  dominates at the lowest energies as can be seen here and in Fig. 3.13. This low energy region is of the most concern for dark matter searches.  
Image Credit: Ref. [77].

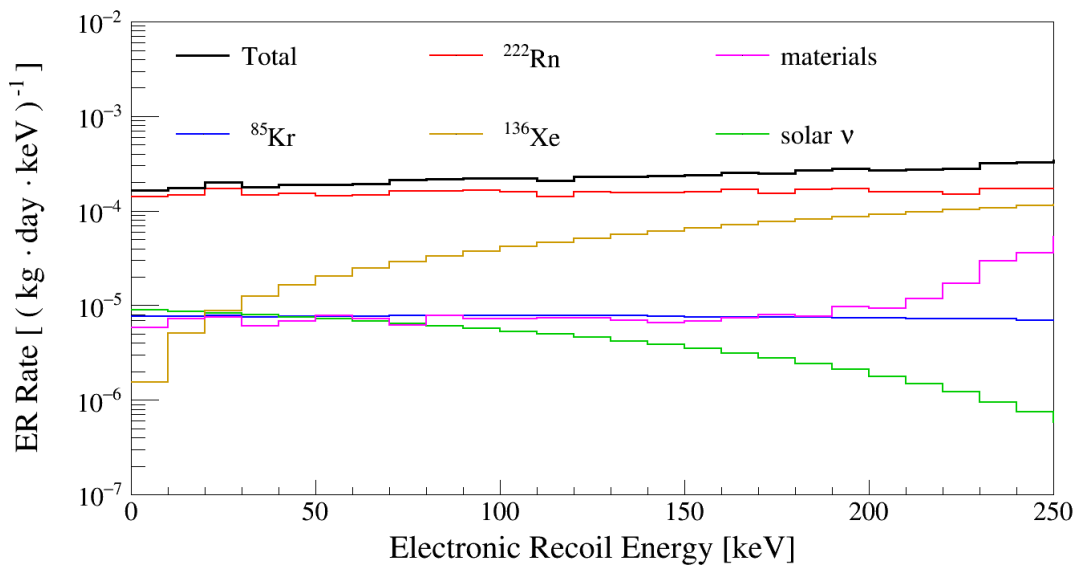


Figure 3.13: The electronic recoil energy spectrum from background at low energies. Note that under 15 keV, the upper threshold for electronic recoils relevant to the dark matter search,  $^{222}\text{Rn}$  is the dominant source of electronic recoils. Image Credit: Ref. [77].

seconds, and 10.6 minutes) — this implies that the  $^{212}\text{Pb}$  will still be almost entirely concentrated at the edge of the detector and easily removed via a fiducial volume cut (much like the materials background). This is clearly seen in Fig. 5 of Ref. [110]. On the other hand, the decays leading up to and the decay of  $^{214}\text{Pb}$  are relatively slow (3.8 days, 3.1 minutes, and 26.8 minutes) implying that the impurity has plenty of time to spread throughout the entirety of the detector. There is a small possibility of tagging these  $^{214}\text{Pb}$  using the coincidence of  $^{214}\text{Bi}-^{214}\text{Po}$  but the 20 minute half-life of  $^{214}\text{Bi}$  makes this very difficult. This is why  $^{222}\text{Rn}$  is considered to be an intrinsic and unremovable background.

At the same time,  $^{220}\text{Rn}$  turns out to be a very useful calibration source [110]. The short half lives of  $^{220}\text{Rn}$  and  $^{216}\text{Po}$  can first be used to measure the flow of liquid xenon in the TPC. Second,  $^{212}\text{Pb}$  has a half-life of 10.6 hours, giving it ample time to spread uniformly throughout the detector before decaying. While the Q-value of the beta decay is 570 keV, the beta decay spectrum is continuous down to zero energy meaning that a small fraction of the events will be useful for calibration the low-energy electronic recoil calibration. After the  $^{212}\text{Pb}$  decay, we can use the close time coincidence of  $^{212}\text{Bi}$  and  $^{212}\text{Po}$  (colloquially referred to as a *BiPo* event) to measure the decrease in the contamination and to confirm the uniformity of the  $^{212}\text{Pb}$  events in the detector. These features make  $^{220}\text{Rn}$  one of the most desirable electronic recoil calibration sources available with the exception of perhaps tritiated methane [70, 71].

### 3.2.2.2 $^{85}\text{Kr}$

$^{85}\text{Kr}$  is the other major internal source of background in liquid xenon based experiments. While  $^{85}\text{Kr}$  has a short half-life on a terrestrial scale (10.8 years), it is produced as the byproduct of nuclear fuel reprocessing and weapons tests.  $^{85}\text{Kr}$   $\beta$  decays with a maximum energy of 687 keV with the spectrum decreasing steadily down to zero energy (as seen in Fig. 2.3). Commercial xenon will retain ppm to ppb levels of natural krypton (which contains  $^{85}\text{Kr}$  at  $2 \cdot 10^{-11}$  levels [111]) as a result of the distillation process used to extract the xenon. Due to its decay energy spectra, which allows for low energy electronic recoils, and relatively long half-life, which allows the  $^{85}\text{Kr}$

### 3.2. The Background for the XENON1T Detector

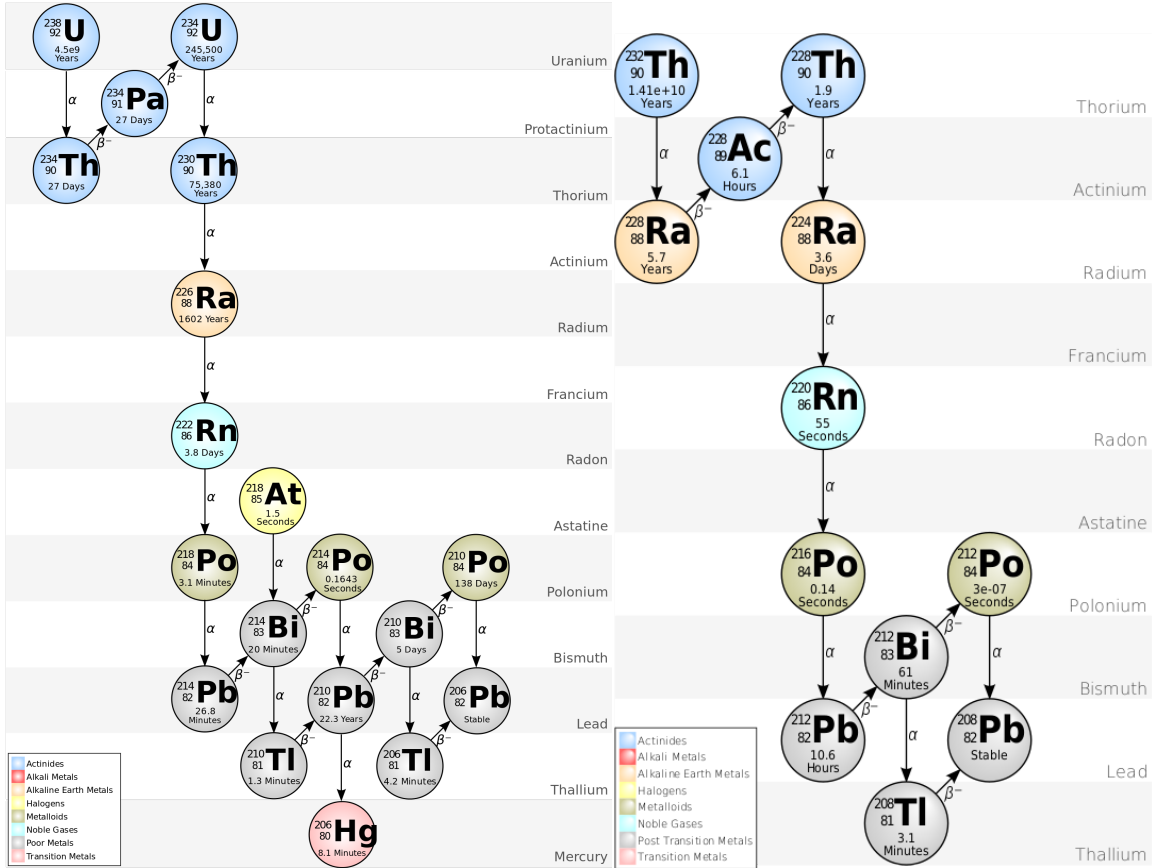


Figure 3.14: The  $^{238}\text{U}$  (left) and  $^{232}\text{Th}$  (right) decay chains. The  $^{238}\text{U}$  chain ultimately produces an intrinsic and the largest background source of electronic recoils in XENON1T while the  $^{232}\text{Th}$  chain results in a very useful electronic recoil calibration source. Image Credit: Berkely Nuclear Forensics Group.

to disperse uniformly in the detector,  $^{85}\text{Kr}$  is also considered to be one of the most dangerous backgrounds in XENON1T.

Of course, ideally one would like to lower the krypton to xenon levels to as low levels as possible but the design goal of XENON1T was 0.2 ppt which translates to approximately 30 low energy electronic recoils per year in a 1 ton fiducial volume. Using the krypton distillation column discussed in Sec. 3.1.5.2, krypton to xenon levels of  $0.36 \pm 0.06$  ppt were reached for the first science run putting XENON1T within a factor of two of the ultimate goal [97].

### 3.2.2.3 Solar Neutrinos

Due to the mass difference between electrons and nucleons, significantly lower energy neutrinos are required for electronic recoils versus nuclear recoils. This implies neutrinos from the sun, *solar neutrinos*, will be the dominant source of neutrinos for the electronic recoil background. The energy spectra of solar neutrinos is shown in Fig. 2.6.

Like electronic recoils from beta decays, the kinetic energy of the recoiling electron will follow a spectrum where only very low energies are relevant. Unlike most of the other sources of electronic recoils, the solar neutrino background cannot be reduced and will scale with the size of the detector used.

### 3.2.2.4 $^{136}\text{Xe}$

One source of background that has been mentioned in passing is the only radioisotope of natural xenon,  $^{136}\text{Xe}$ .  $^{136}\text{Xe}$  was shown to decay via a  $2\nu\beta\beta$  decay with a half-life of  $2.2 \cdot 10^{21} \text{ y}$  [60]. The  $2\nu\beta\beta$  decay energy spectrum from  $^{136}\text{Xe}$  is shown in Fig. 3.12 and Fig. 3.13 – fortunately, unlike the beta decays resulting from the  $^{222}\text{Rn}$  chain and  $^{85}\text{Kr}$  decay, the spectrum of  $^{136}\text{Xe}$  decreases rapidly as electron momentum approaches zero [112].

While at the current sizes of xenon detectors this background is subdominant, it will eventually become a large source of irreducible background.

## 3.2.3 Nuclear Recoil Background in XENON1T

Since WIMPs are expected to interact with xenon via nuclear recoils, any source of background that could cause a nuclear recoil in xenon is particularly troubling. Care must be taken to make sure that all potential sources of nuclear recoils are understood and accounted for — otherwise an experiment would be susceptible to artificially strong limits or potential false discoveries.

The three major sources of nuclear recoil background are the detector materials themselves, which was discussed in Sec. 3.2.1, neutrinos, and neutrons produced by

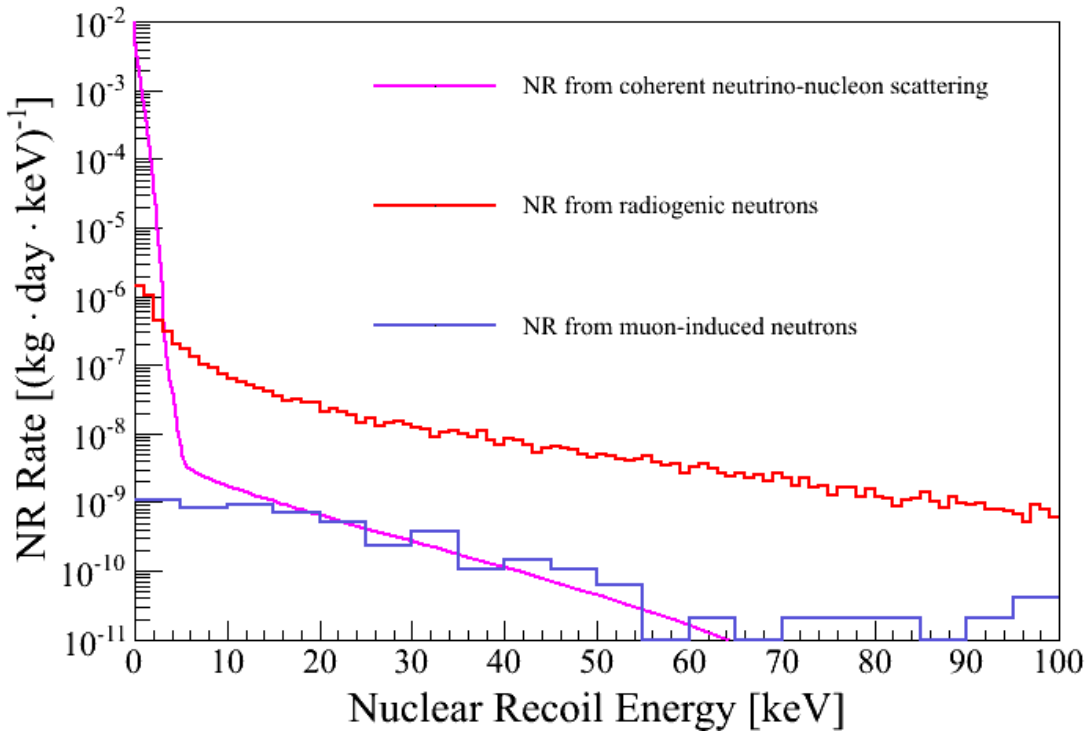


Figure 3.15: The energy spectra of the different sources of nuclear recoil background.  
Image Credit: Ref. [77].

high energy muons. Each of these sources of background is shown in the full nuclear recoil background energy spectrum found in Fig. 3.15.

### 3.2.3.1 Coherent Neutrino-Nucleon Scattering

Neutrinos can interact with both electrons, as discussed in Sec. 2.3 and Sec. 3.2.2.3, and atomic nuclei, via coherent neutrino-nucleon scattering (CNNS). The maximum energy of a recoiling nucleus is given by  $E_r^{\max} = \frac{2E_\nu^2}{m_N + 2E_\nu}$ , where  $m_N$  is the mass of the nucleus and  $E_\nu$  is the energy of the neutrino. This implies that neutrinos must have energies on the order of 10 MeV to cause nuclear recoils on the order of 1 keV. Therefore, high energy neutrino sources like  ${}^8\text{B}$  in the sun as well as neutrinos from supernovae and the atmosphere will contribute the most to the CNNS background in dark matter experiments.

Unlike nuclear recoils from radiogenic neutrons and muon-induced neutrons, this background cannot be shielded and cannot be reduced, in any reasonable sense, by

a fiducial volume cut. Therefore, as dark matter detectors become more and more sensitive this will constitute an irreducible background.

#### 3.2.3.2 Nuclear Recoils from muon-induced neutrons

We discussed the possibility of a neutron background as the result of high-energy cosmogenic muons interacting in the rock and concrete surrounding the laboratory and the detector in Sec. 3.1.2. Given the efficiency of the muon veto and the low flux of muons expected because of the rock above the laboratory, the expected rate of nuclear recoils from muon-induced neutrons is extremely low, as can be seen in Fig. 3.15.

## 3.3 The Calibration and Characterization of XENON1T for the First Science Run

In this section we will discuss the most important calibrations needed for the first science run of XENON1T. We will also briefly discuss the basic cuts made during the first science run and their acceptance. All of these cuts and calibrations are necessary for the discussions of the following two sections regarding the calibration of XENON1T to electronic and nuclear recoils (the latter performed by the author) and the first dark matter search.

### 3.3.1 PMT Characterization

One of the most basic tasks in TPCs of any size is to characterize the response of PMTs (Sec. 3.1.8) to photons that create a single photoelectron (SPE). While the ideal case is that we completely understand the shape of the response function of the PMT (essentially the probability distribution function of how large the output signal will be given a single photoelectron), most experiments settle for understanding only the mean and variance of the distribution. The reason for this practical compromise is that the single photoelectron response of a PMT is roughly normal and that when

dealing with a large number of photoelectrons ( $\gtrsim 20$  PE), by the central limit theorem, the response will appear to be a normal distribution defined by only the mean and the variance of the single photoelectron response. Therefore, an understanding of the full photoelectron response will never be necessary for S2s. However, a full understanding of the response of a PMT to a single photoelectron could be beneficial in understanding very small S1 signals.

Two methods were used to characterize the response of the PMTs for XENON1T during the first science run. Both involved using low levels of blue light to illuminate the PMTs such that the probability distribution of photons detected is approximately Poissonian. The first method involves assuming a distribution for the background distribution (no light detected) and the SPE response and using these assumptions to fit the low light spectrum. In XENON1T, it was assumed that the background distribution is Gaussian with an exponential component and that the single photoelectron response, before convolution with the background, is Gaussian. A sample fit with the labeled components is shown in Fig. 3.16.

The second method used to calibrate the charge response of single photoelectrons in a completely statistical and model-independent way. While this method requires a background measurement that is completely compatible with the measurement at low light levels (for example, the electronics of the light source causing additional background would be an example of incompatibility), one can extract the mean and variance of the single photoelectron response very easily and without assumptions [113].

PMT characterization will be discussed in further detail in App. B where we will describe a method that the author developed for the non-analytical characterization of PMTs using the cascade model.

### 3.3.2 Position Reconstruction

It has been mentioned several times that TPCs have the unique capability of reconstructing the three-dimensional position of an interaction within a detector. We

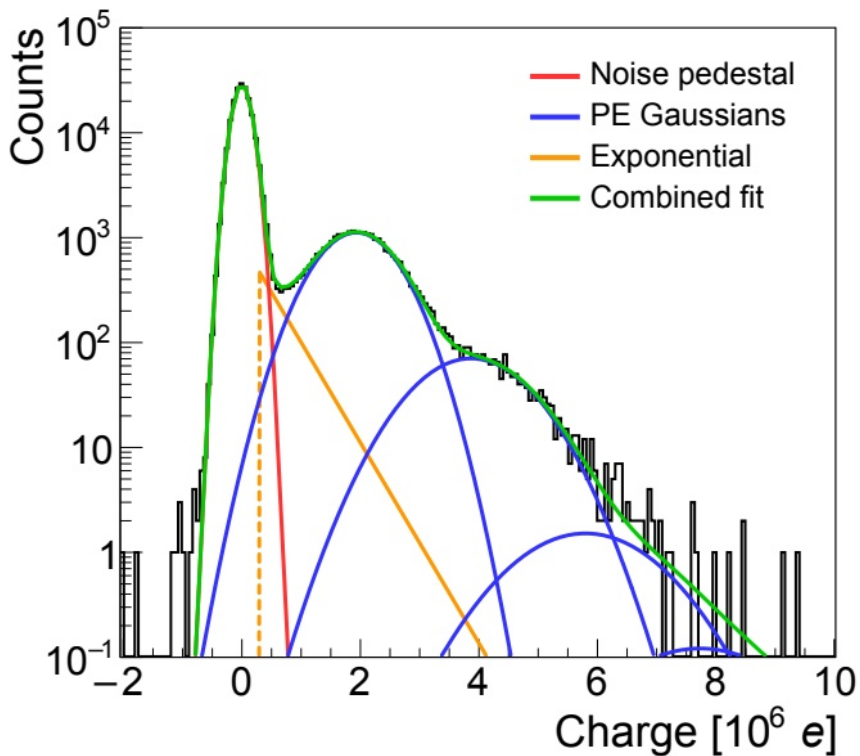


Figure 3.16: A fit of the low light response of one of the XENON1T PMTs in order to characterize the single photoelectron response. Image Credit: Ref. [107].

will now discuss how the interaction vertex was found during the first science run of XENON1T.

As was discussed in Sec. 2.5.1.3, in a dense medium such as xenon with a large uniform electric field across it, one would expect that free electrons are quickly accelerated to their drift velocity and stay at this velocity until reaching the liquid-gas interface. Therefore, if one knows the drift velocity at the given electric field then one can measure the depth of the event from the drift time (very closely estimated by the time difference between the S1 and S2 of a given event). Measuring the drift velocity is very simple — the distance between the cathode and the gate (which is just below the liquid-gas interface) is known so by looking at the maximum drift time (the time it takes to travel from the cathode to the gate) one can approximate the drift velocity at the given field. The maximum drift time can be found using a spectrum like the one shown in Fig. 3.17. For the first science run of XENON1T, the maximum drift

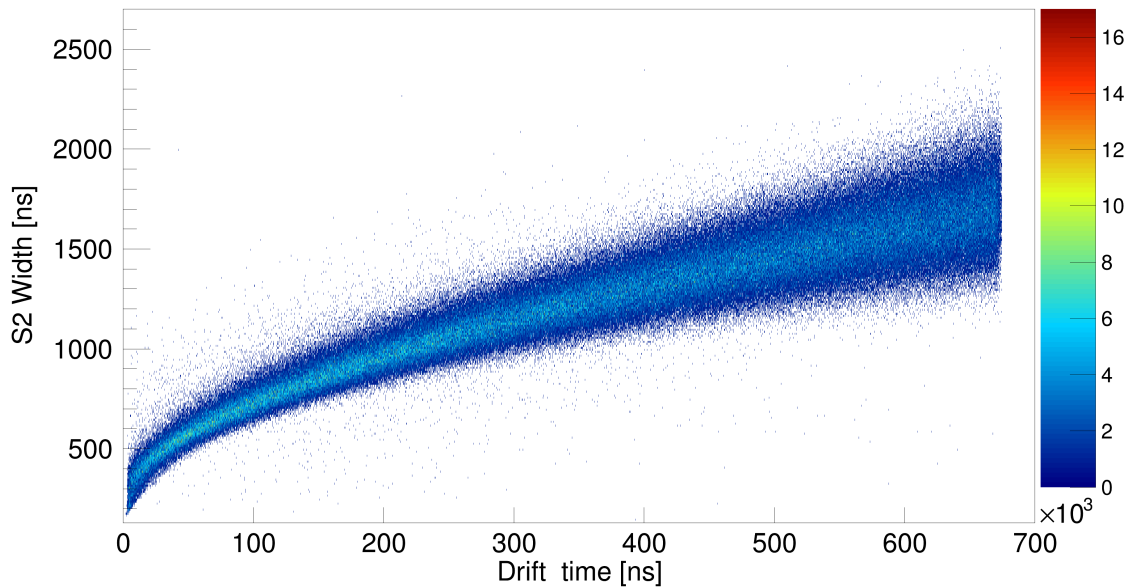


Figure 3.17: A plot of the width of an S2 versus the drift time for 32 keV events from  $^{83}\text{mKr}$ . Note that at a certain drift time, no more events are seen. This cut-off in events represents the location of the cathode since interactions below it will not produce an S2.

time to cover the 96.9 cm at approximately  $12 \text{ kV/cm}$  was  $673 \mu\text{s}$  which gives a drift velocity of  $1.43 \text{ mm}/\mu\text{s}$ .

Finding the location of electron extraction (a good proxy for the position given the field uniformity in the detector) for an event can be done by looking at the light pattern resulting from a given S2. While this might seem relatively simple, consistently reconstructing the position within 2 cm of its actual location is a very complicated task due to detector effects. Current methods of position reconstruction are reliant on simulation to produce either training data for a neural network or light collection efficiency maps for each of the top PMTs.

While using multiple algorithms for position reconstruction is useful for consistency checks, ultimately only one algorithm can be used. In the first science run of XENON1T, this algorithm used the simulated light collection efficiency maps for each PMT as part of likelihood function to find the position in the highest agreement with the measured pattern. This method resulted in a less than 2 cm mean reconstruction

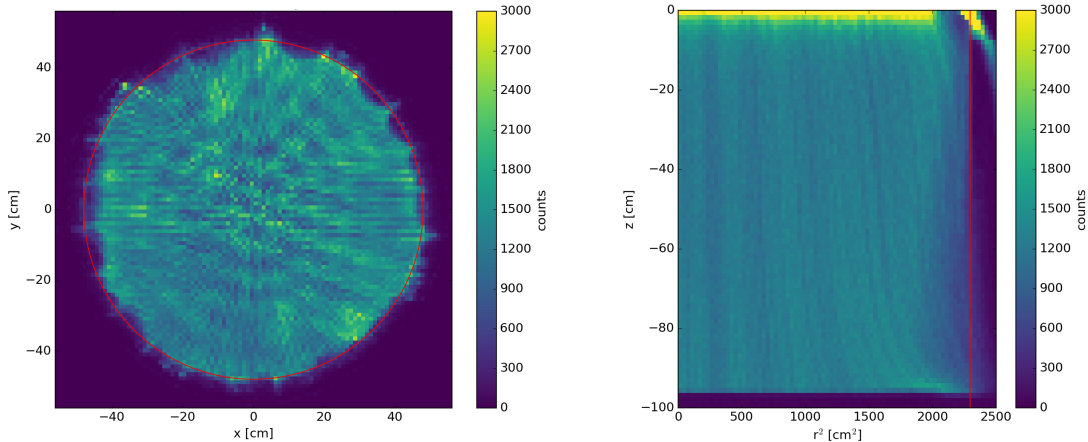


Figure 3.18: The distribution of positions of 32 keV events from  $^{83\text{m}}\text{Kr}$  during the first science run of XENON1T.

error for simulated data with a signal size above the trigger threshold. This error continuously decreases as the size of the S2 signal increases. The more important test, though, is how the algorithm reconstructed the position of real events in the detector. While we cannot compare positions event-by-event, we can look at the overall distribution of positions for a given source and compare that to our expectations. Fig. 3.18 shows the distribution of positions in all dimensions for 32 keV events from  $^{83\text{m}}\text{Kr}$ , which should be uniformly distributed inside of the detector.

### 3.3.3 Position Dependent Corrections

#### 3.3.3.1 S1 Position Correction

One subtle, but critical, detector effect is the fact that the position of an event will affect the size of the S1 seen. Understanding these losses as a function of position are critical to improve the energy resolution of the detector. Fortunately, this S1 position dependence can be measured in a very simple way. By introducing a source that will cause events throughout the entire detector and give a monoenergetic recoil, we can measure the difference in light yield for given positions. Uniform sources are very useful this type of measurement but they are not necessary, especially for small

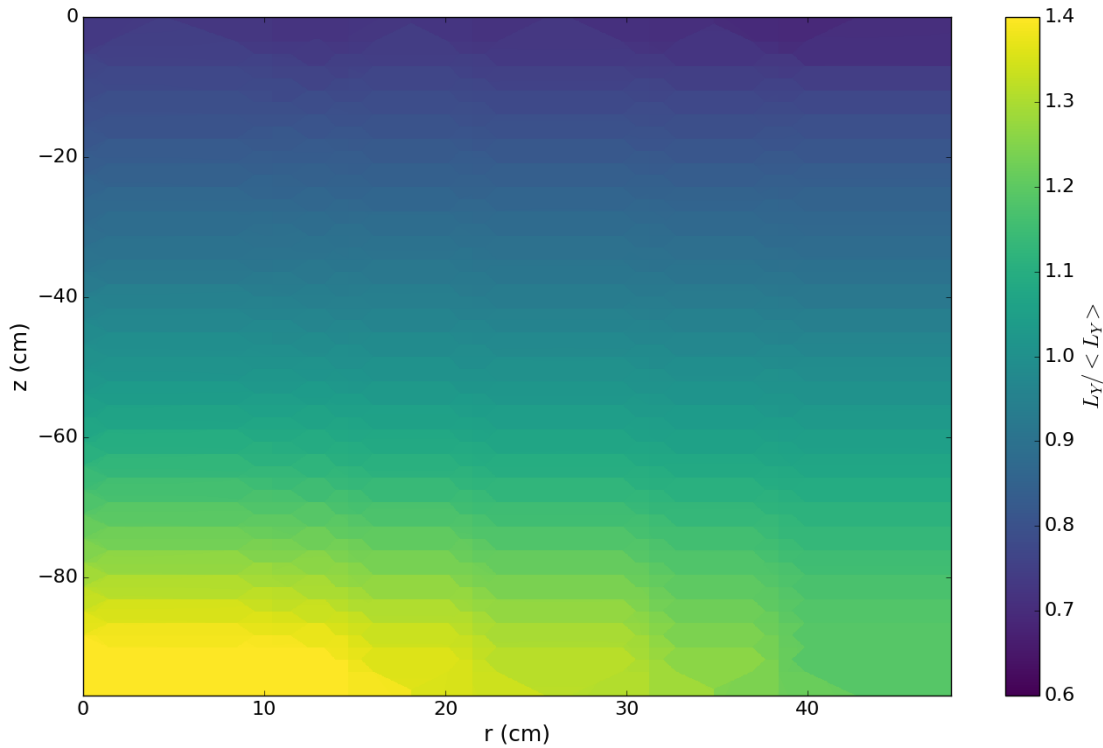


Figure 3.19: The S1 correction map of XENON1T. This correction map shows the relative light yield of events at specific positions relative to the average light yield of the detector for monoenergetic events. One can see the clear trend that events closer to the bottom PMT array have higher light yields than those closer to the liquid-gas interface.

detectors.

In XENON1T, the 32 keV emission of  $^{83\text{m}}\text{Kr}$  was used to find the S1 correction map, which is shown in Fig. 3.19. The decay of  $^{83\text{m}}\text{Kr}$  not only creates a 32 keV electronic recoil but actually is followed by a second decay with a lifetime of 154 ns and energy of 9.4 keV. This close time coincidence can be used to further confirm that only 32 keV events are being kept for the analysis. This correction map, which shows the light yield at a given position relative to the average light yield in the detector, can then be used to correct recoils of all energies and types to improve the detector resolution. While the correction map could be in three dimensions, since the TPC is cylindrically symmetric, we only correct in radial and depth coordinates.

A clear trend can be seen in Fig. 3.19: the closer to the bottom PMT array an event is, the higher the light yield will be. To a lesser extent, the closer the event is

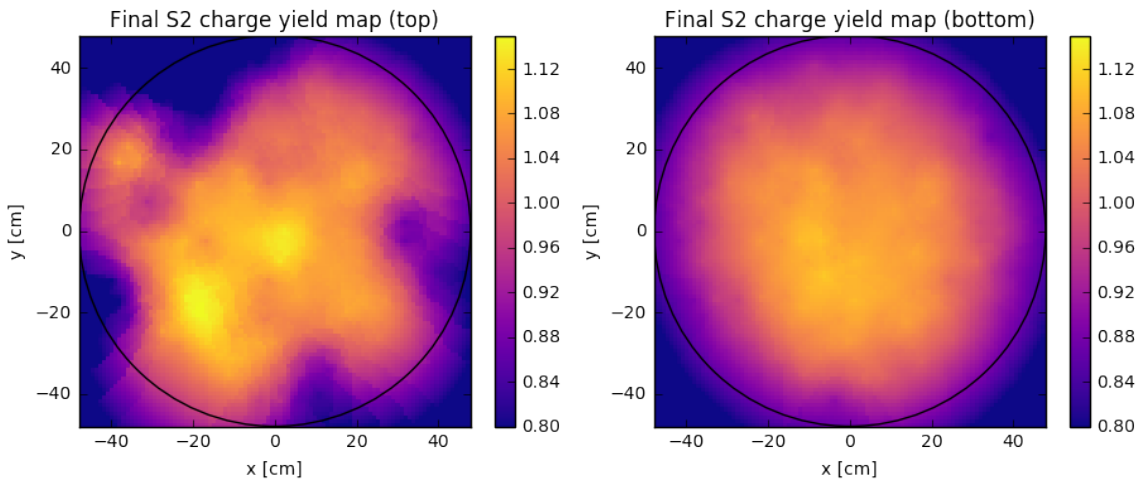


Figure 3.20: The S2 transverse position correction map of XENON1T. This correction map shows the relative charge yield of events at specific positions relative to the average charge yield of the detector. One can see the trend for the bottom PMT array that events closer to the center of the detector have higher charge yields than events closer to the edges.

to the center of the detector, the higher the light yield will be. This trend is related to the longer path length and larger number of reflections events towards the top and edge of the detector will have versus events very close to the bottom PMT array.

In theory, the position dependence of S1 could also be simulated but given the many factors that need to be understood and fed into the simulation, such as the absorption length and the Rayleigh scattering length in liquid xenon for 178 nm, the reflectivity of the different materials, and the optical transparency of the meshes, this is impractical (especially given the simplicity of a direct measurement).

### 3.3.3.2 S2 Transverse Position Correction

In almost the same way that we can find the S1 correction map, we find S2 transverse position correction map. However, instead of only using the 32 keV signal, we used the S2 of both the 32 keV and 9 keV decays (since they can only be resolved in S1 and not S2). The correction maps for the top and bottom PMT arrays are shown in Fig. 3.20.

As one can see, the correction maps look quite different. This is mainly due to the

close proximity of the S2 light to the top PMT array such that non-functional PMTs cause features in the map. The S2 transverse position correction map for the bottom PMT array, on the other hand, is very smooth because the light must travel further and is less dependent on individual PMTs. Ultimately, in the first science run, it was decided that only the bottom PMT array would be used for calculating signal sizes so only the smoother bottom PMT map was needed.

In the bottom PMT map, one can again see the trend that events towards the center of the detector have higher charge yields than events closer to the edge of the TPC. This effect is believed to be from charge collecting on the teflon, edge effects for the electric field produced by the anode and the gate, and again from the longer path lengths and larger number of reflections for photons originating closer to the edge of the detector.

### 3.3.3.3 S2 Depth Correction Correction: Electron Lifetime

As mentioned in Sec. 2.5.2.2, the free electrons extracted from the interaction site by the drift field can be absorbed by electronegative impurities contaminating the liquid xenon. These impurities, mostly oxygen, will therefore decrease the size of the S2 signal measured. It turns out that the probability that an electron successfully reaches the liquid-gas interface is well described by the fairly simply relationship shown in Eqn. 3.1.

$$p_{\text{EL}}(z) = \frac{1}{\tau_{e^-}} e^{-\frac{z}{v_d \tau_e}} \quad (3.1)$$

Since the S2 signal size is directly proportional to the number of electrons accelerated through the gaseous xenon, Eqn. 3.1 should manifest itself as an exponential decrease in the S2 size as a function of depth. A plot of this effect can be seen in Fig. 3.21.

Electronegative impurities emanate from the materials used to construct the detector and therefore are constantly introduced into the system. Therefore, these impurities must constantly be cleaned out. This cleaning also does not remove all

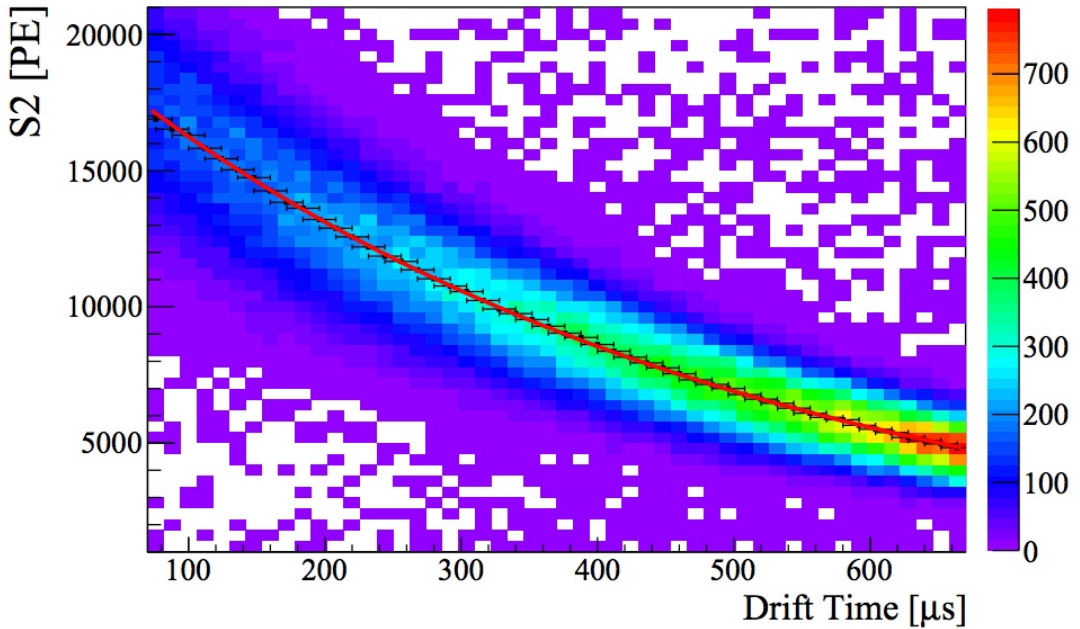


Figure 3.21: An example of an electron lifetime analysis from XENON1T. In this analysis, the 41 keV  $^{83\text{m}}\text{Kr}$  electronic recoil is used and the decay's S2 signal size is plotted versus drift time (a proxy for depth). Image Credit: Ref. [97].

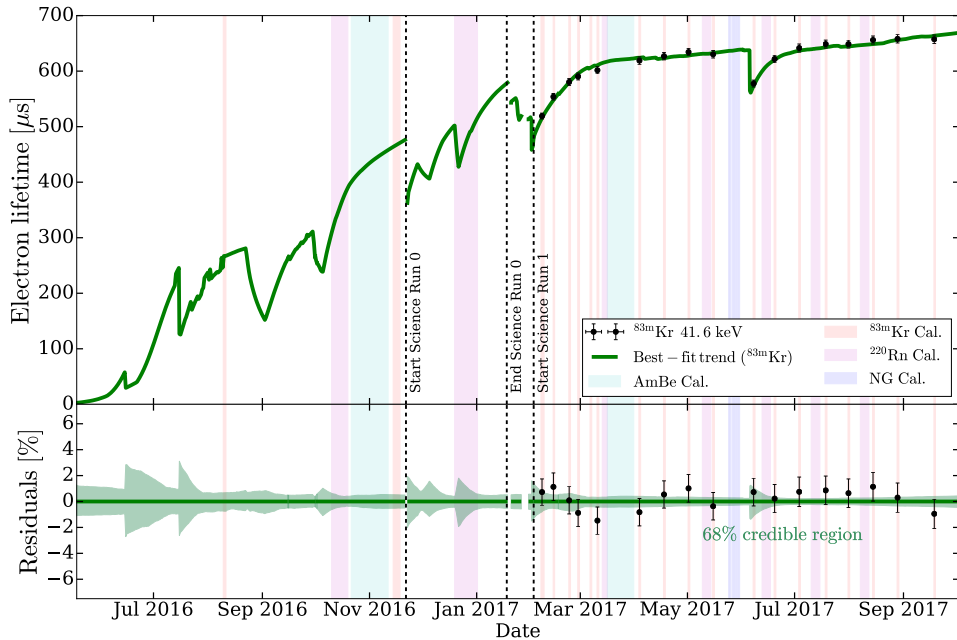


Figure 3.22: The electron lifetime over the course of the first science run of XENON1T. Notice the two drops in the electron lifetime corresponding to periods when the purification system was not operating. Shown in red is a prediction of the electron lifetime given the detector operating parameters and outgassing estimates from materials.

impurities instantaneously — the electron lifetime must be measured routinely in order to monitor its day-to-day changes. These effects can be seen in Fig. 3.22 which shows both drops from when the purification went offline and the steady increase in purity from continuous cleaning.

In XENON1T, this cleaning is done by the purification system described in Sec. 3.1.5.1. Because a low electron lifetime has an adverse impact on the S2 resolution (and hence energy resolution and discrimination power), significant effort has gone into and will continue to go into improving electronegative purification for large scale detectors.

### 3.3.4 Single Electron Gain

The single electron gain, also referred to as the *gas gain*, is used to quantify the number of photons detected per electron extracted from the liquid into the gas phase. Both the production of scintillation light from electrons exciting gaseous xenon atoms and the detection of scintillation photons are both well approximated by Poisson processes. However, detector effects such as the per PMT detection efficiency and variations in the field in the gaseous xenon will cause further smearing of the number of photons detected from a single electron. If we assume that this smearing is Gaussian, then we can actually fit the number of photons detected with a Poisson convolved with a Gaussian to determine the final probability mass function.

An example of a fit of the gas gain is shown in Fig. 3.23 where hits are found by looking at voltage excursions over threshold on a per-PMT basis in a time window defined by the waveform summed across all PMTs.

Since it is expected that the gas gain is sensitive to the electric field in the gas phase, the gas gain is susceptible to change with small changes in the liquid level. Therefore, the gas gain is constantly monitored throughout data taking to ensure that it is stable.

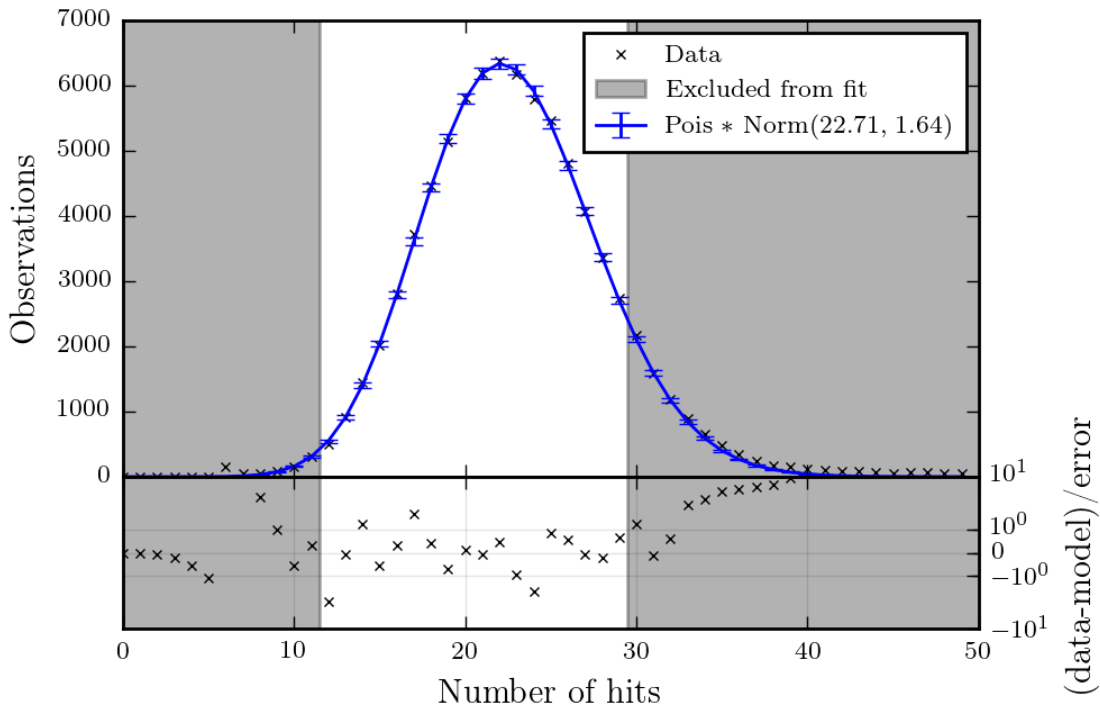


Figure 3.23: A fit of the single electron gain from the first science run of XENON1T. Hits are defined as excursions above threshold for individual PMTs in a time window defined by the waveform summed across all PMTs.

### 3.3.5 Average Light Collection Efficiency and Extraction Efficiency

In Sec. 2.3.2, we discussed the observables production process for electronic recoils and found a relationship between the energy of electronic recoils and the number of photons and free electrons produced because of the lack of quenching factors in the observables production mechanism. This relationship is shown in Eqn. 3.2 where  $N_q$  is the number of quanta,  $E_{\text{ER}}$  is the energy of the electronic recoil,  $W$  is the average energy required to produce an exciton or electron-ion pair ( $13.7 \pm 0.2$  eV [79]),  $N_\gamma$  is the number of photons produced in the electronic recoil, and  $N_e$  is the number of free electrons extracted from the interaction site.

$$N_q = \frac{E_{\text{ER}}}{W} = N_\gamma + N_e \quad (3.2)$$

While Eqn. 3.2 looks very simple, it actually proves to be very valuable when measuring two otherwise very difficult to measure/simulate detector parameters: the average light collection efficiency of photons and the extraction efficiency of electrons from the liquid into the gas.

We can easily convert the number of photons and free electrons from the interaction into the observables measured by our detector, S1 and S2. Since S1 is the number of photons detected, we say that  $S1 = N_\gamma \cdot g_1$ , where  $g_1$  is the average light collection efficiency. The S2 signal is directly proportional to the number of electrons extracted from the liquid into the gaseous xenon. Therefore, we can say that  $S2 = N_e g_2 = N_e \cdot G_e \eta$  where  $G_e$  is the single electron gain (see Sec. 3.3.4) and  $\eta$  is the efficiency of extracting electrons from the liquid into the gaseous xenon (often referred to as the *extraction efficiency*).

This allows us to put Eqn. 3.2 into terms of measured parameters.

$$\frac{E_{ER}}{W} = \frac{S1}{g_1} + \frac{S2}{G_e \eta} \quad (3.3)$$

We can now look at multiple monoenergetic peaks or the same monoenergetic peak at different electric fields (or multiple monoenergetic peaks at multiple electric fields). A simple rearrangement of Eqn. 3.3 shows us that the S1 and S2 values of these peaks should fall along a line defined by  $g_1$ ,  $\eta$ , and  $G_e$ .

$$\frac{S2}{E_{ER}} = \frac{G_e \eta}{g_1} \frac{S1}{E_{ER}} - \frac{G_e \eta}{W} \quad (3.4)$$

We can fit what is colloquially referred to as a *Doke plot* (after Tadayoshi Doke) with the mean S1 and S2s of various monoenergetic electronic recoils (potentially at different fields) using Eqn. 3.4 in order to extract  $g_1$  and  $\eta$ . Note that  $\eta$  can only be extracted if one independently measures the single electron gain since otherwise the two parameters will be completely correlated. The fit of multiple monoenergetic electronic recoils to find the extraction efficiency and the average light collection efficiency of XENON1T is shown in Fig. 3.24.

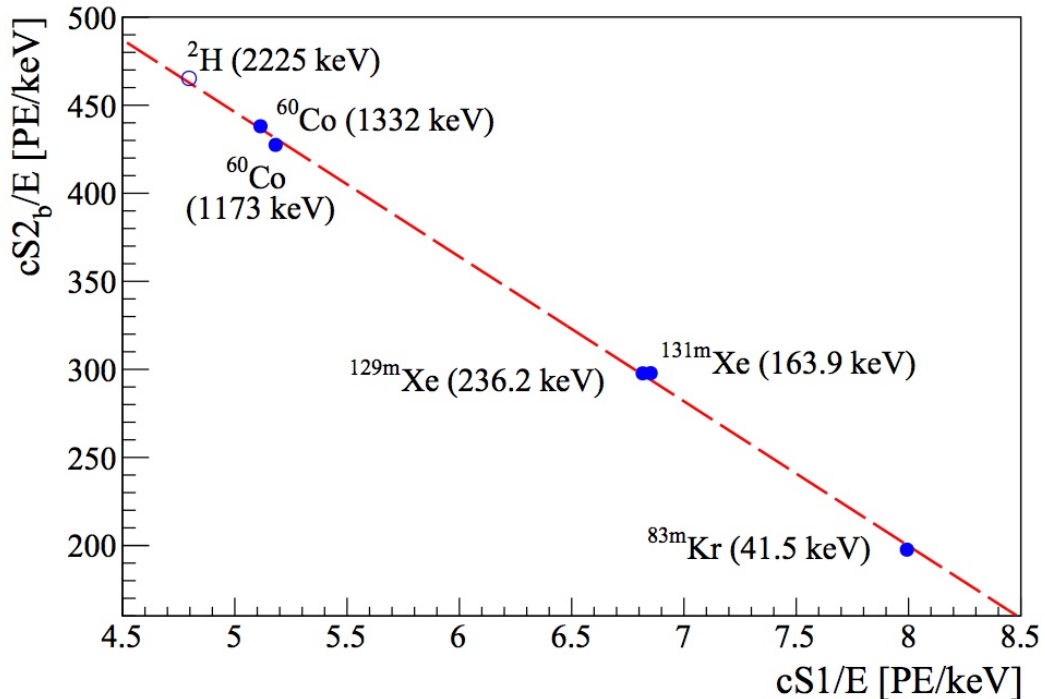


Figure 3.24: The Doke plot for XENON1T along with the best fit. Note that only the bottom PMT array is used for the S2 signal and that we use the position corrected values of S1 and S2. While the de-excitation from neutron captures in water is shown ( $^2\text{H}$  with an de-excitation energy of 2.225 MeV), it is not used for the fit.

### 3.3.6 Cut Acceptance

Cuts in XENON1T are used to eliminate background sources, like the fiducial volume cut and the single scatter cut, or to remove events that show non-standard behavior, such as the S2 width cut that uses the diffusion model to define appropriate widths given a drift time (this relationship between drift time and width can actually be seen in Fig. 3.17). Once the cuts are in place, it is important to understand the population of good events that are removed as a function of signal size — this is referred to as the *cut acceptance*.

To define the cut acceptance, we use the “N-1” approximation. The N-1 approximation calls for applying all but a single one of the cuts to define the control sample which is then compared to the sample after applying the final cut. It is important to note that this does not account for potential correlations between cuts. Using the N-1 approximation for each of the cuts and combining the individual acceptances, we

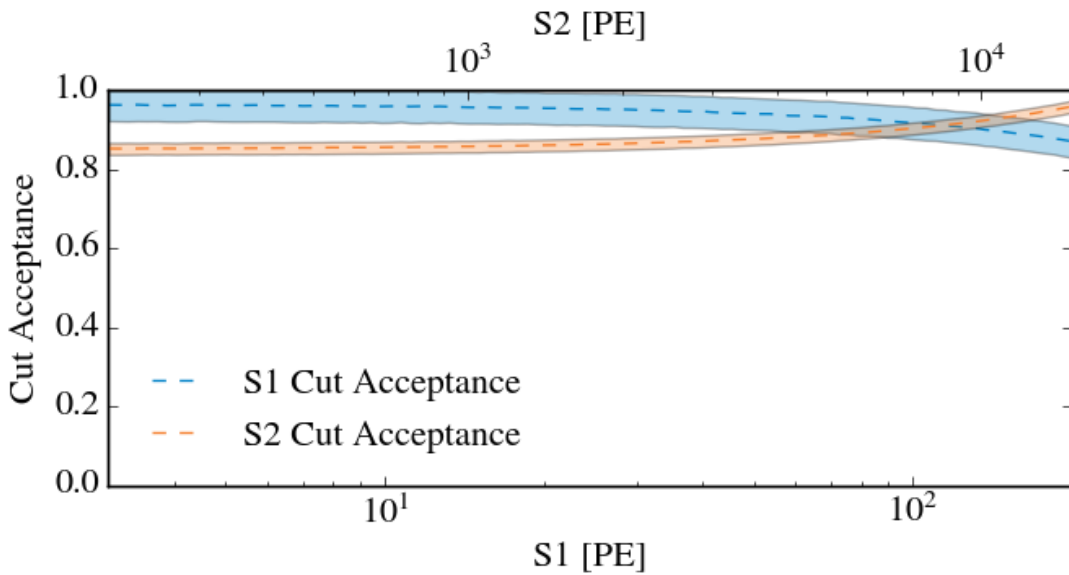


Figure 3.25: The estimated cut acceptances in S1 and S2 for the first science run of XENON1T.

can find the overall cut acceptance of the first science run of XENON1T as a function of S1 and S2 (shown in Fig. 3.25).

It is important to note that, with a sufficiently trust-worthy physics and detector simulator, one could estimate the cut acceptances using simulation.

## 3.4 Electronic and Nuclear Recoil Characterization of XENON1T

The electronic and nuclear recoil calibrations are two of the most important studies required for a liquid xenon TPC. For the first time in xenon detectors, these calibrations were performed such that a realistic approximation of the microphysics process was accounted for alongside the detector effects discussed. This was only made possible with the use of a fast Monte Carlo (MC) framework that was developed by the author and will be discussed in App. A that leveraged graphical processing units (GPUs) for dramatic increases in speed (two to three orders of magnitudes).

While these calibrations can (and in future science runs will be) performed together due to the large number of shared parameters, in the first science run of XENON1T they were performed separately.

### 3.4.1 Significance of the Calibrations

Before discussing the details of the calibrations, it is helpful to understand why these calibrations are of such high importance. Ultimately, the goal of each science run is to search for a WIMP signal in the detector. While this can be done in a purely statistical fashion (as discussed in Sec. 1.4.3), more sophisticated methods have been developed that drastically improve the sensitivity of TPCs to WIMPs.

Since the background in XENON1T is thoroughly understood, as outlined in Sec. 3.2.2 and Sec. 3.2.3, we can actually create a probability distribution function (PDF) in our signal space (S1 and S2 space or some variation of this) *if* our calibration captures the various processes between energy deposition all the way to signal extraction by the processor. This probability distribution function can be made with WIMPs (or other dark matter candidates) to determine whether or not the data agrees with a WIMP of a given mass and cross section. Determining how well WIMPs of given masses and cross sections agree with the data ultimately determines the limit set (if all WIMPs below a given cross section agree with the data) or whether a discovery was made (if the data favors a WIMP with a particular mass and cross section more than all others).

Fig. 3.26 shows the PDF of the background distribution for the first science run with the cumulative density contours of a  $50 \text{ GeV}/c^2$  WIMP. These PDF and contours were made using the signal production models that were measured via the electronic and nuclear recoil calibrations.

### 3.4.2 Parameter Estimation via Monte Carlo

Fig. 3.27 shows a flowchart that summarizes how the calibration of electronic and nuclear recoils is performed. The main idea is that a detailed Monte Carlo is used to es-

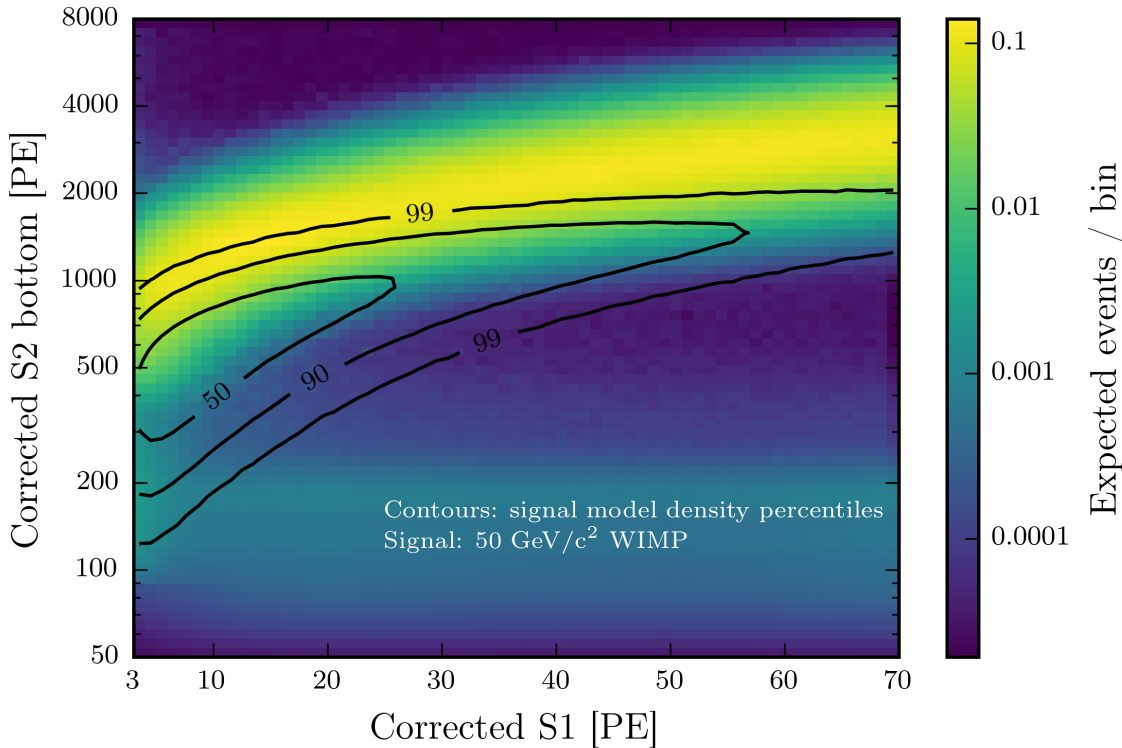


Figure 3.26: The probability distribution function for the first science run of XENON1T plotted with the cumulative density contours of a  $50 \text{ GeV}/c^2$  WIMP. The combined signal and background PDF is used to either set a limit on the WIMP mass and cross section or claim a discovery.

timate the expected distribution of events in signal space (S1 and S2 for XENON1T), which can then be compared to the actual measured distribution of events to determine what values for the parameter model cause the highest level of agreement.

In more technical terms, the Monte Carlo is used to create a PDF which is then compared with data which results in a likelihood. This likelihood can be combined with prior distributions of the model parameters (from previous measurements or calibrations). As you vary the parameters in the signal production model, you would expect this likelihood to increase and decrease. One can then use different algorithms to find either the set of parameters best in agreement with the data (via a minimizer) or the posterior distribution of the parameters (via a Markov Chain Monte Carlo or MCMC).

The benefit to using a Monte Carlo to define a likelihood for parameter estimation

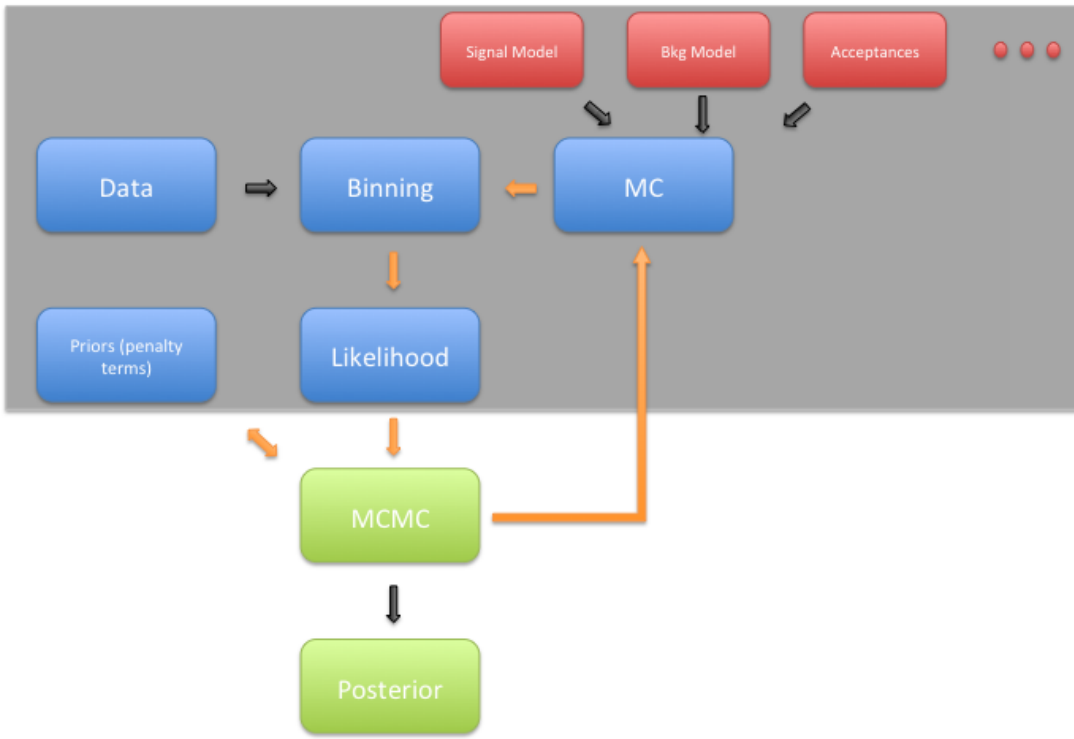


Figure 3.27: A flowchart summarizing how a fast Monte Carlo is used to estimate the parameters in the signal production model. Orange steps are done in each iteration where as black arrows represent steps that are only done a single time.

is that your signal production model can be arbitrarily complex. The downside of using a MC to estimate your likelihood is that it is extremely inefficient, typically rendering this approach impractical. However, using graphical processing units, the author was able to develop an analysis framework that made this type of analysis feasible. The details of the framework will be discussed in detail in App. A.

The details of Monte Carlo event production will be discussed in Sec. 3.4.2.1, Sec. 3.4.2.2, and Sec. 3.4.2.3. These Monte Carlo events are used to fill a histogram that is compared with a histogram filled with data via a binned likelihood, which will be discussed in Sec. 3.4.2.4. In this way we can quantify how well a given set of parameters agrees with what we have measured. The set of parameters to be tested is chosen in this analysis by a Markov Chain Monte Carlo (MCMC) but realistically

could be done with most parameter estimation algorithms — we will briefly discuss how the posterior probability space of the parameters was calculated in Sec. 3.4.2.5.

### 3.4.2.1 Light and Charge Production for Electronic Recoils

The details of the light and charge production model for electronic recoils are very similar to the details from the calibration discussed in Ref. [71].

Given an electronic recoil of a known energy, the first quantity of interest is the number of quanta produced in the interaction. For electronic recoils, this is approximated as a Fano process as shown in Eqn. 3.5.

$$N_q \sim N \left( \mu = \frac{E}{W}, \sigma^2 = \frac{FE}{W} \right) \quad (3.5)$$

The Fano factor in liquid xenon is estimated to be 0.059 [114] and was fixed during parameter estimation. Since little quenching is expected for electronic recoils in liquid xenon, these quanta can take the form of only excitons and electron-ion pairs. To simulate the individual number of excitons and ions, we use a binomial process with a probability defined by the *exciton-to-ion* ratio.

$$N_{\text{ion}} \sim B \left( N = N_q, p = \frac{1}{1 + \frac{N_{\text{ex}}}{N_{\text{ion}}}} \right), \quad N_{\text{ex}} = N_q - N_{\text{ion}} \quad (3.6)$$

We now must consider the possibility of electron-ion pairs recombining to form excitons, resulting in a single photon rather than an electron extracted from the site. The recombination fraction  $r$  depends on the energy and field present in the liquid and it has a non-negligible intrinsic recombination fluctuation  $\Delta r$  [70, 71]. It is assumed that the recombination is normally distributed as shown in Eqn. 3.7

$$r \sim N(\mu = \langle r \rangle, \sigma^2 = (\Delta r)^2) \quad (3.7)$$

We then approximate the recombination of electron-ion pairs as a binomial process as shown in Eqn. 3.8.

$$N_{\text{rec}} \sim B(N = N_{\text{ion}}, p = r), \quad (3.8)$$

$$N_{\text{ion}} \leftarrow N_{\text{ion}} - N_{\text{rec}}, \quad N_{\text{ex}} \leftarrow N_{\text{ex}} + N_{\text{rec}}$$

Recombination was only considered above a certain energy threshold  $E_t$ .

In total, eight free parameters were included in the observables production model: five from the fourth-order polynomial used to describe the light yield relative to a reference curve, one from the energy threshold for recombination (below which recombination is no longer considered), and two for the parameterization of the recombination fluctuation ( $\Delta r = A \cdot (1 - e^{E/\tau_r})$ ). A normal prior was assumed for  $W$  with a mean of 13.7 eV and width of 0.2 eV while a uniform prior between 0.06 to 0.20 [80, 81] was assumed for the exciton-to-ion ratio due to the discrepancy between measured values.

Since the electronic recoil calibration was performed with  $^{220}\text{Rn}$ , a flat energy spectrum between 0–30 keV was used to draw the input energy for each Monte Carlo event. Additionally, it was assumed that events occurred uniformly throughout the detector.

### 3.4.2.2 Light and Charge Production for Nuclear Recoils

If you recall from Sec. 2.4.2, unlike electronic recoils, nuclear recoils will also lose energy due to atomic motion that can ultimately not be detected in a liquid xenon TPC. We model this loss using Lindhard theory, which gives the energy lost to atomic motion as a function of energy. This is shown in Eqn. 3.9 in terms of the dimensionless energy  $\epsilon$ .

$$\epsilon = 11.5 \left( \frac{E}{\text{keV}} \right) Z^{-7/3}, \quad (3.9)$$

$$L(\epsilon) = \frac{kg(\epsilon)}{1 + kg(\epsilon)}, \quad g(\epsilon) = 3\epsilon^{0.15} + 0.7\epsilon^{0.6} + \epsilon$$

The Lindhard factor,  $L$ , is then used to approximate the number of quanta as shown in Eqn. 3.10.

$$N_q \sim P \left( \mu = \frac{E \cdot L}{W} \right) \quad (3.10)$$

Note that the choice of the Poisson distribution is an approximation and not derived from first principles. The actual distribution is likely more complicated due to complex track structure of nuclear recoils in liquid xenon.

Once we have the number of quanta, we can find the number of excitons and electron-ion pairs in the same way that we did for electronic recoils.

$$N_{\text{ion}} \sim B \left( N = N_q, p = \frac{1}{1 + \frac{N_{\text{ex}}}{N_{\text{ion}}}} \right), \quad N_{\text{ex}} = N_q - N_{\text{ion}} \quad (3.11)$$

We also must consider the recombination of electron-ion pairs for nuclear recoils. Unlike electronic recoils, though, recombination fluctuations have not been observed for nuclear recoils.

$$\begin{aligned} N_{\text{rec}} &\sim B(N = N_{\text{ion}}, p = r), \\ N_{\text{ion}} &\leftarrow N_{\text{ion}} - N_{\text{rec}}, \quad N_{\text{ex}} \leftarrow N_{\text{ex}} + N_{\text{rec}} \end{aligned} \quad (3.12)$$

Given the small track size of nuclear recoils, we approximate that the recombination is described by the Thomas-Imel model [83] as defined in Eqn. 3.13.

$$r = 1 - \frac{\ln(1 + N_{\text{ion}}\sigma)}{N_{\text{ion}}\sigma} \quad (3.13)$$

Finally, we must consider biexcitonic quenching, which results from the collision of two excitons. This quenching is typically parameterized using the quenching term from Birks' saturation law, as shown in Eqn. 3.14, since one would expect that the density of excitons in a track is proportional to the electronic stopping power [88–90].

$$f_B = \frac{1}{1 + a \frac{dE}{dx}} = \frac{1}{1 + \eta e^{-\lambda}} \quad (3.14)$$

We then approximate that the number of excitons quenched is given by Eqn. 3.15.

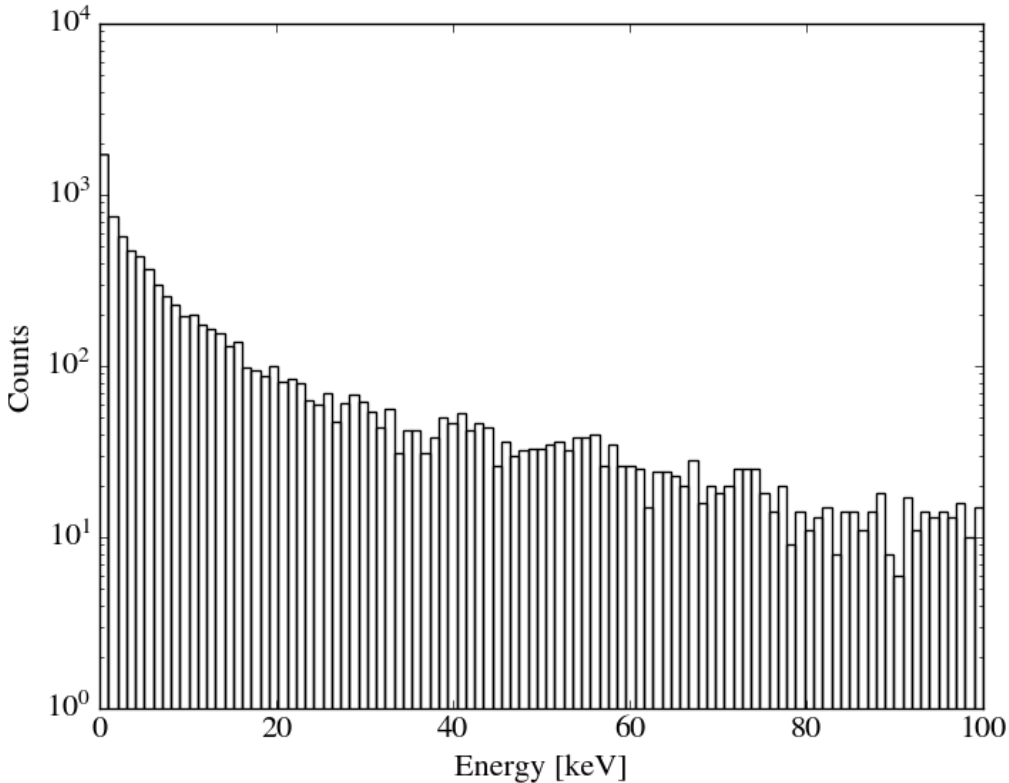


Figure 3.28: The energy spectrum of single scatter and unresolvable multiple scatter nuclear recoils from the americium-beryllium (AmBe) source located in the water tank as predicted by Geant4.

$$N_{\text{bq}} = B(N = N_{\text{ex}}, p = f_B), \quad (3.15)$$

$$N_{\text{ex}} \leftarrow N_{\text{ex}} - N_{\text{bq}}$$

Note that we are assuming that the biexcitonic quenching process is binomial and that this is not from first principles. There is also no requirement that excitons are quenched in pairs. However, this quenching only is relevant at high energies so the effect from this approximation will be small<sup>1</sup>.

The nuclear recoil data that was used for the calibration was from an americium-beryllium (AmBe) source, which produces neutrons of energies below 11 MeV. The expected energy spectrum of single scatters in the medium (or multiple scatters that

---

<sup>1</sup>At high energies ( $> 50$  keV) we will expect hundreds to thousands of excitons after recombination meaning the effect will be sub-1%

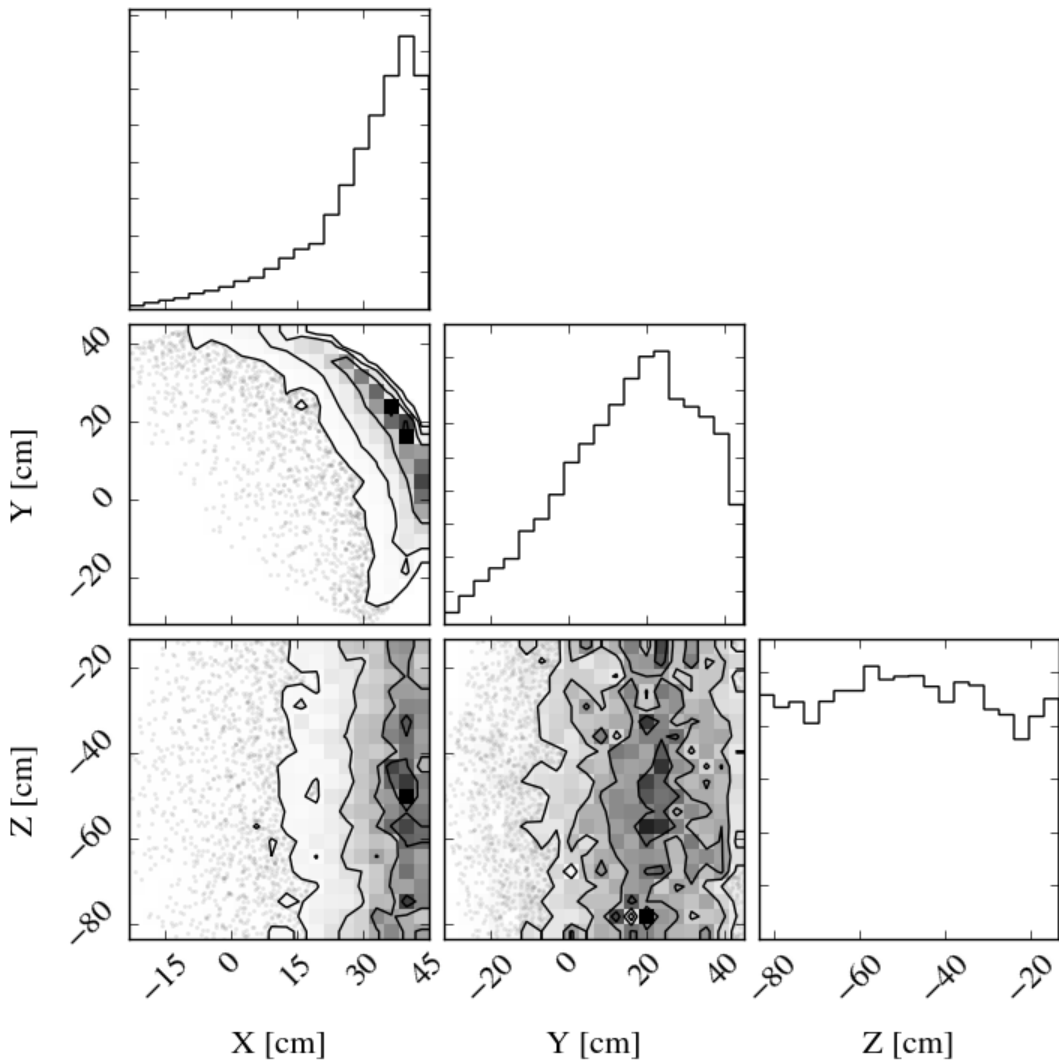


Figure 3.29: The location of single scatter and unresolvable multiple scatter nuclear recoils from the americium-beryllium (AmBe) source located in the water tank as predicted by Geant4.

cannot be resolved in XENON1T due to their close proximity) from AmBe is shown in Fig. 3.28. Unlike the electronic recoil calibration, the expected distribution of positions of nuclear recoils in the detector is not expected to be uniform since the AmBe source is outside the TPC. The expected maps of location of nuclear recoils are shown in Fig. 3.29. The energy spectra and interaction positions were extracted from a detailed Monte Carlo simulation produced in Geant4 [101].

It was decided to constrain the response model of liquid xenon to nuclear re-

coils described in this section using previous measurements of the light and charge yield in place of performing an independent measurement like the one performed in XENON100 [115]. While the featureless energy spectrum played a large role in this decision, ultimately this decision was made so that we could conclusively demonstrate an understanding of the XENON1T detector. If the response model had been left free, discrepancies and issues in the detector model could be made up through changes to the liquid xenon response model.

To constrain the the liquid xenon response model for nuclear recoils, we used the global analysis performed in Ref. [86]. Ref. [86] examined past independent measurements of the light and charge yield of nuclear recoils and fit the model described in this section to the final yields of each of the measurements presented. While no previous measurements used in Ref. [86] were performed that simultaneously measured the light and charge yield, all of the independent measurements of light and charge yield were used simultaneously in Ref. [86] to fit the model in an attempt to account for correlations.

Ultimately, eight free parameters are used to describe the mean light and charge yield in liquid xenon in Ref. [86].  $k$ ,  $\eta$ , and  $\lambda$  from Eqn. 3.9 and Eqn. 3.14 are left free in the model. Additionally,  $\alpha$ ,  $\zeta$ ,  $\beta$ ,  $\gamma$ , and  $\delta$  are introduced to parameterize the exciton-to-ion ratio and Thomas-Imel model as shown in Eqn. 3.16 and Eqn. 3.17, respectively.

$$\frac{N_{\text{ex}}}{N_{\text{ion}}} = \alpha F^{-\zeta} (1 - e^{-\beta \epsilon}) \quad (3.16)$$

$$\sigma = \gamma F^{-\delta} \quad (3.17)$$

The results of the fit are shown in Tab. 3.1. These results were used to set prior likelihoods for the nuclear recoil calibration<sup>2</sup> — in this way, the data from XENON1T could be used to further constrain the model and results presented in Ref. [86]. It is

---

<sup>2</sup>An asymmetric gaussian is used with widths defined by the asymmetric uncertainties of each parameter.

Parameter	Result
$\alpha$	$1.240^{+0.079}_{-0.073}$
$\zeta$	$0.0472^{+0.0088}_{-0.0073}$
$\beta$	$239^{+28}_{-8.8}$
$\gamma$	$0.01385^{+0.00058}_{-0.00073}$
$\delta$	$0.0620^{+0.0056}_{-0.0064}$
$k$	$0.1394^{+0.0032}_{-0.0026}$
$\eta$	$3.3^{+5.3}_{-0.7}$
$\lambda$	$1.14^{+0.45}_{-0.09}$

Table 3.1: The results of the fit from Ref. [86] of the nuclear recoil response model to independent measurements of the light and charge yield.

important to note that the results of this calibration do not constitute an independent measurement like the ones used to fit the model in Ref. [86].

### 3.4.2.3 Detector Model for Signal Production

Having discussed the light and charge production models for electronic and nuclear recoils, we can move onto how the S1 and S2 signals are produced from the light and charge. While the detector processes will be the same for both the electronic and nuclear recoil calibrations, the parameters used to describe these properties will sometimes be different since the calibrations were performed at different times (e.g., the electron lifetime).

**Detection of Scintillation Photons** We begin by examining the photons produced by the interaction and the probability that they are detected. In Sec. 3.3.5 we discussed how we can find the average light collection efficiency of the detector and in Sec. 3.3.3.1 we discussed how this light collection efficiency varies with position by examining the light yield of a fixed energy source.

One effect that was not previously discussed, however, was the possibility of double photoelectron emission from a single incoming photon. The double photoelectron emission (DPE) process was studied in Ref. [116] for the Hamamatsu R11410 PMT

used in XENON1T and it was found that for incoming photons with a wavelength  $\lesssim 200$  nm, two photoelectrons are released from the photocathode, rather than a single photoelectron, approximately 23% of the time. Since the wavelength of xenon scintillation light is 178 nm, this effect should be present in XENON1T and will be included in our calculation of the average light collection efficiency of the detector,  $g_1$ .

We make the approximation that the number of photons that are absorbed in a photocathode of one of the PMTs is described by a binomial process with the probability given by the light collection efficiency at the position of the interaction. This approximation is shown in Eqn. 3.18, where  $g_1$  is the average light collection efficiency,  $c_{\text{LCE}}(r, z)$  is the correction to the light collection efficiency as a function of radius and depth (shown in Fig. 3.19),  $p_{\text{DPE}}$  is the probability that two photoelectrons are emitted for a single incoming photon instead of one,  $N_\gamma$  is the number of photons produced in the interaction, and  $N_i$  is the number of photons producing at least a single photoelectron at the photocathode.

$$N_i \sim B \left( N = N_\gamma, p = \frac{g_1 \cdot c_{\text{LCE}}(r, z)}{1 + p_{\text{DPE}}} \right), \quad (3.18)$$

For very small S1 signals, we also need to account for effects due to our data processor's efficiency, potential bias, and smearing. The efficiency is essentially the probability that a signal of a certain number of photons detected will be identified by the processor. Due to the coincidence condition required in the classification algorithm, at least three photons must produce photoelectrons for the event to have a chance of being detected. This efficiency is very difficult to measure directly and in XENON1T was done via a waveform simulation under a variety conditions. The processor efficiency is shown in Fig. 3.30 — note that since the electronic and nuclear recoil data and the science run were taken at different times and with different noise conditions the processor effects were different for each (although conditions during the electronic recoil calibration and science run were very close such that only difference in processor efficiency are considered). The shaded region for the efficiency can be

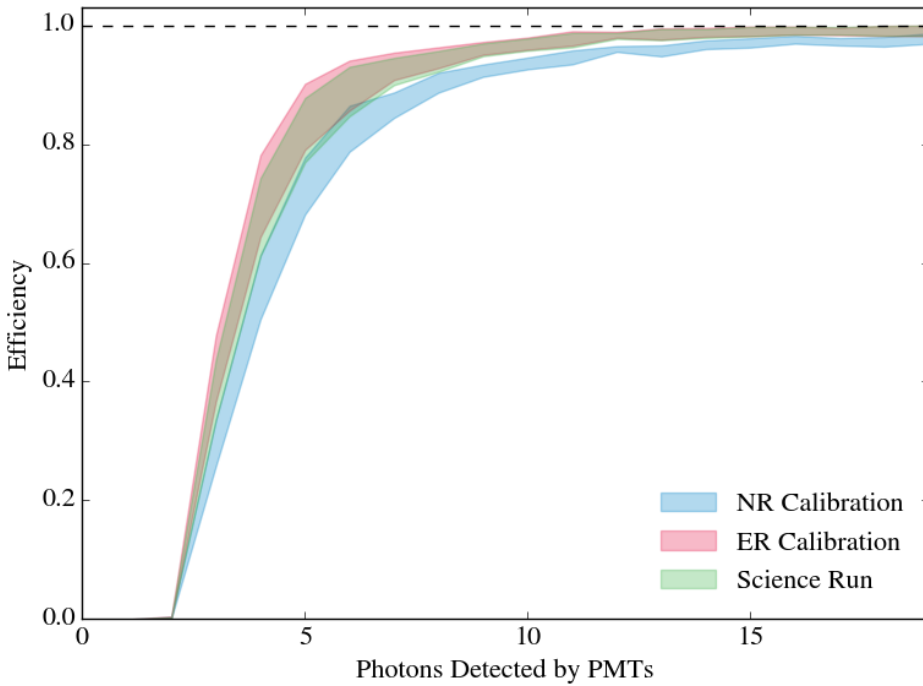


Figure 3.30: The estimated processor efficiency for identifying S1 signals in XENON1T. These efficiencies were found via simulation and the shaded region represents the equally probable values for the efficiency at a given photon level.

thought of as a uniform distribution from which the efficiency can take any value for a given number of photons detected.

The bias and the smearing represent the changing of the signal area due to processor and PMT effects. Like the processor efficiency, these effects are only expected to be relevant for very small signals and they are very hard to directly measure. The results from simulation using XENON1T’s waveform simulation are shown in Fig. 3.31. Both bias and smearing are shown as  $\frac{\text{Processed}-\text{Truth}}{\text{Truth}}$ . The shaded regions again can be thought of as a uniform distribution from which the bias and smearing can take any value for a given number of photons detected. Note that the bias and smearing for the first science run and the electronic recoil calibration were similar enough that they are not treated separately.

With the processor efficiency accounted for given the number of photons that create at least one photoelectron, we may now account for the double photoelectron effect.

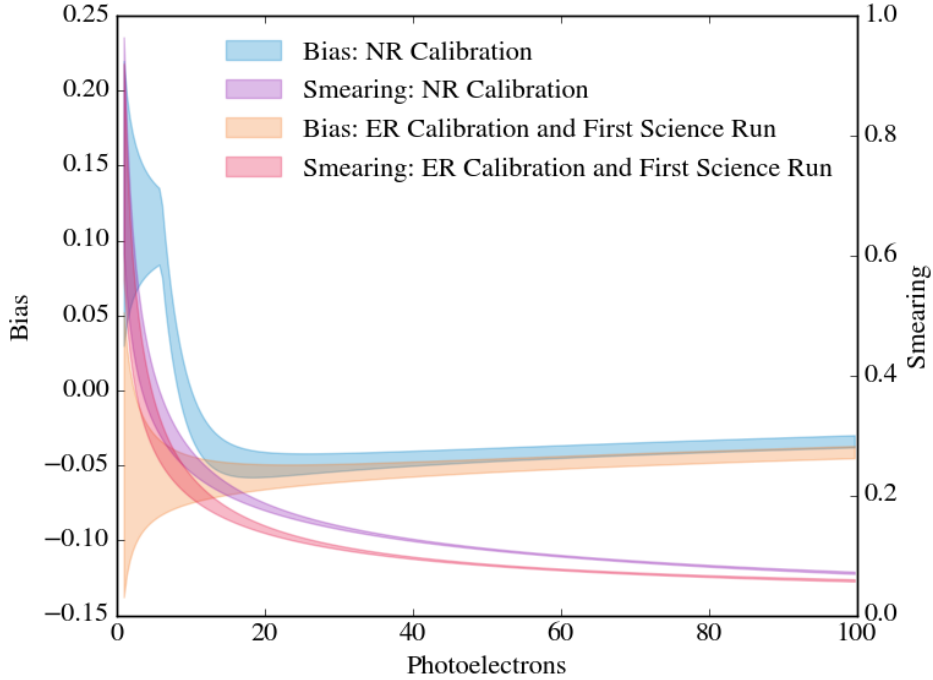


Figure 3.31: The estimated bias and smearing of S1 signals due to the processing of the waveform for scintillation signals.

$$N_{\text{PE}} \sim N_i + B(N = N_i, p = p_{\text{DPE}}) \quad (3.19)$$

While the processor efficiency is used to ultimately set a weight on a given Monte Carlo event for the histogram that will be compared to data, the effect of the bias and smearing were approximated using Eqn. 3.20 and Eqn. 3.21, respectively.

$$\text{S1}' = \frac{N_{\text{PE}}}{1 + b} \quad (3.20)$$

$$\text{S1} \sim N(\mu = \text{S1}', \sigma^2 = (\text{S1}' \cdot s)^2) \quad (3.21)$$

With the reconstructed and uncorrected S1 determined, we can find the probability that this good event would have been removed by a cut via the cut acceptance shown in Fig. 3.25. We will multiply this probability with the probability that the signal is found by the processor to ultimately set the weight of the event (after S2

losses are considered since we require both an S1 and S2 in an acceptable waveform).

With processor, PMT, and cut effects accounted for, we now have the uncorrected S1 for a given interaction along with the probability that it would actually be found in a waveform. Since the data that the Monte Carlo result will be compared to is corrected, we will also correct the simulated S1 signals. This correction is shown in Eqn. 3.22, where

$$cS1 = \frac{S1}{c_{LCE}(r, z)} \quad (3.22)$$

**Detection of Electrons** The first detector process that needs to be considered for the electrons extracted from the interaction site is their drifting to the liquid-gas interface. During this drifting, there is a measurable probability that an extracted electron will attach to an electronegative impurity. This probability, shown in Eqn. 3.1 (repeated below), is dependent on the depth, the drift velocity through the xenon at the given field, and the electron lifetime.

$$p_{EL}(z) = \frac{1}{\tau_{e^-}} e^{-\frac{z}{v_d \tau_e}} \quad (3.1)$$

The electron lifetime is a function of the outgassing rate of the various detector components and the rate at which the xenon is being cleaned and is thus constantly changing as a function of time. This change in time is clearly shown in Fig. 3.22.

We approximate the number of electrons that reach the liquid-gas interface by assuming that each of the extracted electrons is independent and thus the number of electrons reaching the interface is described by a binomial distribution as shown in Eqn. 3.23.

$$N_{L-G \text{ Interface}} \sim B(N = N_e, p = p_{EL}(z)) \quad (3.23)$$

In Eqn. 3.23,  $N_{L-G \text{ Interface}}$  is the number of electrons that reach to the liquid-gas interface,  $N_e$  is the number of electrons extracted from the interaction site, and  $p_{EL}(z)$  is the probability of an individual electron reaching the liquid-gas interface as given

### 3. THE FIRST DARK MATTER SEARCH WITH XENON1T

---

by Eqn. 3.1. Note that the variation in the number of electrons reaching the liquid-gas interface increases as the electron lifetime decreases.

As discussed in Sec. 3.3.5, not all electrons that reach the liquid-gas interface will be extracted into the gaseous xenon in a meaningful timeframe. Therefore, we approximate that the number of electrons extracted into the gas is described by another binomial process with the number of trials equal to  $N_{\text{L-G Interface}}$  and probability of extraction equal to the extraction efficiency, as shown in Eqn. 3.24.

$$N_{\text{extracted}} \sim B(N = N_{\text{L-G Interface}}, p = p_{\text{extracted}}) \quad (3.24)$$

With the number of electrons extracted from the gas, we can next account for excitation caused by these electrons in the gaseous xenon as well as the smearing due to the PMTs. We approximate the number of photoelectrons detected in this secondary amplification as a Gaussian process as shown in Eqn. 3.25 where  $G$  is the mean number of photoelectrons detected for a single extracted electron,  $\sigma_G$  is the width of the photoelectron distribution for a single extracted electron,  $c_G(x, y)$  is the position correction of the gas gain as shown in Fig. 3.20, and  $N_{\text{PE}}$  is the number of photoelectrons digitized after smearing from the PMTs.

$$N_{\text{PE}} \sim N(\mu = G \cdot c_G(x, y), \sigma^2 = (\sigma_G \cdot c_G(x, y))^2) \quad (3.25)$$

While no efficiency is applied to the total S2 signal from the processor or the trigger, we do remove uncorrected S2 signals under the defined threshold of 200 photoelectrons. This cut is made to ensure nearly 100% efficiency of the trigger.

Like the S1 signal, the S2 signal will also experience some bias and smearing during reconstruction of the event by the processor, albeit to a smaller degree. Again both bias and smearing are shown as  $\frac{\text{Processed}-\text{Truth}}{\text{Truth}}$  in Fig. 3.32 and the shaded regions again can be thought of as a uniform distribution from which the bias and smearing can take any value for a given number of photons detected.

We apply the effects of the processor bias and efficiency in the same way as the S1 signal in the Monte Carlo, as shown in Eqn. 3.26 and Eqn. 3.27.

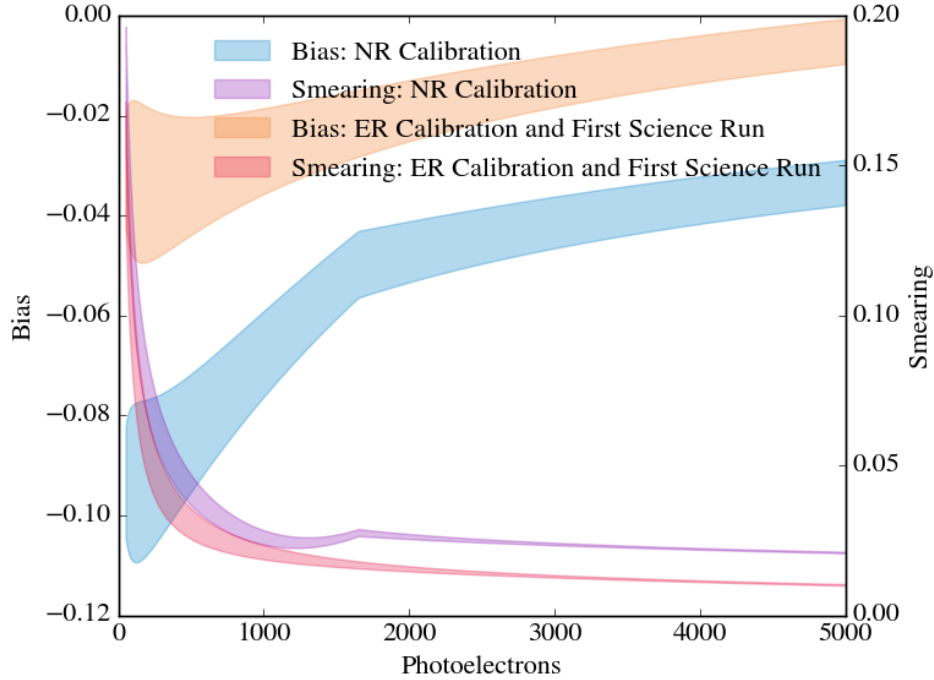


Figure 3.32: The estimated bias and smearing of S2 signals due to the processing of the waveform for scintillation signals.

$$S2' = \frac{N_{PE}}{1 + b} \quad (3.26)$$

$$S2 \sim N(\mu = S2', \sigma^2 = (S2' \cdot s)^2) \quad (3.27)$$

With the reconstructed and uncorrected S2 determined, we can find the probability that this good event would have been removed by a cut via the cut acceptance shown in Fig. 3.25. We will multiply this probability with the associated S1 signal's efficiencies to find the overall probability that the event would be seen in our dataset, as shown in Eqn. 3.28. This probability is used as the weight of the Monte Carlo event when filling the two-dimensional histogram for comparison to data.

$$p_{\text{event}} = p_{\text{Processor-S1}} \cdot p_{\text{Cuts-S1}} \cdot p_{\text{Cuts-S2}} \quad (3.28)$$

Finally, for comparison to data, we must finally correct our S2 signal according

to the electron lifetime and position correction of the gas gain, as shown in Fig. 3.29

$$cS2 = \frac{S2}{p_{EL}(z)c_G(x,y)} \quad (3.29)$$

#### 3.4.2.4 Comparing Data and Monte Carlo

With the full Monte Carlo simulation in place, examining the expected electronic or nuclear recoil distribution given input energy and position spectra is straightforward. At the end of the day, though, what we would like to do is find the probability distribution for the observables model given the data that was measured in XENON1T. This means that the ability to simulate the electronic or nuclear recoil spectra is not enough: we must be able to quantitatively compare the Monte Carlo results for a given set of parameters and the data.

Fortunately, this comparison is quite straightforward. In these analyses, the simple binned likelihood function was used to compare data and the fast Monte Carlo. We will cover the details, assumptions, and subtleties of this choice in App. A. The likelihood function is shown in Eqn. 3.30, where  $\mathcal{L}_i$  is the likelihood of a given bin,  $\hat{b}_i$  is the expected number of events in a given bin, and  $b_i$  is the measured number of events in a given bin.

$$\begin{aligned} \mathcal{L}_i &= \frac{\hat{b}_i^{b_i} e^{-\hat{b}_i}}{b_i!} \implies \mathcal{L} = \prod_i \mathcal{L}_i \\ ln(\mathcal{L}) &= \sum_i ln(\mathcal{L}_i) = \sum_i (b_i ln(\hat{b}_i) - \hat{b}_i - ln(b_i!)) \end{aligned} \quad (3.30)$$

As with any parameter estimation, the more parameters that you can independently constrain prior to the fit, the more you can say about parameters of interest. In both the electronic and nuclear recoil calibrations almost all of the detector parameters were constrained and in the nuclear recoil calibration the light and charge production model was also constrained. These constraints are also referred to as *prior distributions* in Bayesian analyses (and colloquially referred to as *penalty terms* in frequentist analyses). The prior distributions in these analyses all take the form of normal distributions (asymmetric if asymmetric uncertainties are given) and ranged

uniform distributions. Unknown parameters still require a prior — for example, many parameters, while unmeasured, we know cannot be negative. These unknown parameters are given uniform priors that are bounded by zero if necessary.

In Bayesian analyses, our ultimate goal is to estimate the posterior distribution of the parameters one is trying to measure given the data that was collected. The posterior probability is directly proportional to the likelihood multiplied by the prior distribution and given by Bayes' formula, shown in Eqn. 3.31 [117].

$$p(\vec{\theta}|\vec{x}) = \frac{p(\vec{x}|\vec{\theta})p(\vec{\theta})}{p(\vec{x})} = \frac{\mathcal{L}(\vec{\theta})p(\vec{\theta})}{p(\vec{x})} \quad (3.31)$$

In the above equation,  $p(\vec{x}|\vec{\theta})$  is the probability of the data given the parameters, otherwise known as the likelihood, and  $p(\vec{\theta})$  is the prior probabilities of the parameters. The denominator in Bayes' formula is not as simple.  $p(\vec{x})$  is the probability of the data given the model, which is given by Eqn. 3.32.

$$p(\vec{x}) = \int_{\Theta} p(\vec{x}|\vec{\theta})d\vec{\theta} \quad (3.32)$$

While it may not appear daunting,  $p(\vec{x})$  is simply incalculable for almost all models and the models used in these analyses are no exception. We will discuss in Sec. 3.4.2.5 a clever way around this problem using a Markov Chain Monte Carlo (MCMC).

### 3.4.2.5 Estimating the Posterior Probability Distribution Using a Markov Chain Monte Carlo

Markov Chain Monte Carlos (MCMCs) have arguably become one of the most popular statistical tools in the last decade. In essence, they operate by randomly sampling from the posterior distribution. Given enough samples from your MCMC, you can approximate the complete shape of the posterior. With computer processors drastically increasing in speed, the ultimate cost of more function calls versus a traditional parameter estimation tool is dominated by the gain in getting a full understanding of the posterior probability distribution and not just the mean and covariance matrix.

### 3. THE FIRST DARK MATTER SEARCH WITH XENON1T

---

While a proof that an MCMC can randomly sample from the posterior distribution is far beyond the scope of this work, it is worthwhile to briefly discuss an intuitive description of how an MCMC works. In the previous section, we mentioned Bayes' formula and how we might directly calculate the posterior probability distribution. However, we ran into an issue with the denominator, which for all practical purposes is incalculable. An MCMC uses a simple alternative to get around this issue:

1. Start at a given position in parameter space and calculate the likelihood function multiplied by the prior probability of that position,  $f_0 = \mathcal{L}(\vec{\theta}_0)p(\vec{\theta}_0)$ .
2. Examine a new, randomly chosen position in parameter space and calculate  $f_1 = \mathcal{L}(\vec{\theta}_1)p(\vec{\theta}_1)$ .
3. Calculate the ratio  $\mathcal{A} = \frac{f_1}{f_0}$ . If  $\mathcal{A} \geq 1$ , we accept the proposed step and “move” to this position in parameter space. If  $\mathcal{A} < 1$ , we accept the proposed step with a probability  $\mathcal{A}$  and otherwise stay in place in parameter space.
4. Record the current position in parameter space,  $\theta_0$  or  $\theta_1$ , and repeat the above procedure.

This procedure, if allowed to continue indefinitely, will produce random samples from the posterior distribution. The reason for this can be seen in our calculation of  $\mathcal{A}$ . If we can manipulate our definition of to put it in a more familiar form.

$$\mathcal{A} = \frac{f_1}{f_0} = \frac{\mathcal{L}(\vec{\theta}_1)p(\vec{\theta}_1)}{\mathcal{L}(\vec{\theta}_0)p(\vec{\theta}_0)} \cdot \frac{p(\vec{x})}{p(\vec{x}')} = \frac{\frac{\mathcal{L}(\vec{\theta}_1)p(\vec{\theta}_1)}{p(\vec{x})}}{\frac{\mathcal{L}(\vec{\theta}_0)p(\vec{\theta}_0)}{p(\vec{x}')}} = \frac{p(\vec{x}'|\vec{\theta}_1)}{p(\vec{x}'|\vec{\theta}_0)} \quad (3.33)$$

It turns out that our acceptance ratio is simply the ratio of the posterior probability distribution at our two points in parameter space. We don't simply climb to higher positions in the posterior because we allow for non-zero probability jumps to lower positions in the posterior.

In these analyses, and all others discussed in this work that use a MCMC, the affine-invariant implementation of the MCMC algorithm was used. This implementation is discussed in detail in Ref. [118] but in summary it uses multiple MCMC chains to probe the parameter space more efficiently. These chains use each other to decide

their next step in a more intelligent way versus the very basic Metropolis-Hastings single chain algorithm [119]. Ultimately, all of the MCMC chains will randomly sample the posterior and can be combined such that the efficiency gains from “intelligent” step choices are not lost to high levels of redundancy.

In theory, an MCMC is not guaranteed to converge until infinite steps are taken. In practice, however, MCMCs typically converge in reasonable amounts of steps. Several tests can be performed to test the convergence of the chain into the posterior, a few of which are discussed in detail in Ref. [120]. In this work, we will use the Gelman-Rubin statistic to check the convergence of our MCMC [121]. The Gelman-Rubin statistic in essence examines the average variance of individual chains to the variance between chains. For chains that begin separated from each other in parameter space, this mixing is a good proxy for convergence of the chains.

### 3.4.3 ER and NR Calibration Results

With the procedure, models, and Monte Carlo details outlined, we can move to the results of the two calibrations. Ideally, these calibrations would be performed simultaneously due to the overlap between the two from the detector model. However, for the first science run they were performed separately as a proof of principle.

#### 3.4.3.1 Results of the Electronic Recoil Calibration

The electronic recoil calibration was performed with the microphysics model described in Sec. 3.4.2.1 and the detector physics model described in Sec. 3.4.2.3. The list of model parameters included in the fit for the light and charge production model for electronic recoils is shown in Tab. 3.2 while the parameters of the detector model are shown in Tab. 3.3. Note that the detector physics parameters will be shared with the nuclear recoil calibration.

In total, eight free parameters were included in the observables production model for electronic recoils: five from the fourth-order polynomial used to describe the light yield relative to a reference curve, one from the energy threshold for recombination

### 3. THE FIRST DARK MATTER SEARCH WITH XENON1T

---

(below which recombination no longer is considered), and two for the parameterization of the recombination fluctuation ( $\Delta r = A \cdot (1 - e^{E/\tau_r})$ ). The reference curve used for the light yield is given by Ref. [122] with a mean field of 120 V/cm. With the light yield, mean energy per quanta, and exciton-to-ion ratio, the mean value for recombination can be reconstructed.

One parameter that has not been mentioned prior to now is the accidental coincidence background rate. In XENON1T, it has been found that there is a relatively high rate of lone-S1 signals and lone-S2 signals. While the causes of each vary from interactions in the liquid xenon below the cathode to interactions in the gaseous xenon, if an S1 and S2 are coincident within a given time window they can together be mistaken for a real event. This background is source dependent and will therefore be different for dark matter data and the electronic recoil calibrations (the accidental coincidence background was found to be negligible for the nuclear recoil calibration). The probability distribution for the accidental coincidence background is shown in Fig. 3.33.

With the models and parameter estimation framework in place, the electronic recoil calibration can be performed. The best-fit PDF, which can be predicted with the posterior distribution of the parameters, is shown in Fig. 3.34. Additionally, a comparison of the band shape, specifically the band median and width, is shown in Fig. 3.36. One can see from both of these comparisons that the  $^{220}\text{Rn}$  data agrees extremely well with the model used.

Parameter	Value	Prior Distribution	Note
$w$	$13.7 \pm 0.2$ eV	Normal	-
$F$	0.059	Fixed	-
$N_{\text{ex}}/N_{\text{ion}}$	0.06–0.20	Uniform	Taken from Ref. [123].
Accidental Coincidence Background	$1.09 \cdot 10^{-5} \pm 5.45 \cdot 10^{-7}$ Hz	Normal	-
Photon Yield (5)	-	Free	-
Recombination Fluctuation (2)	-	Free	-
Energy Threshold (1)	-	Free	-

Table 3.2: The parameters of the light and charge model for electronic recoils in liquid xenon. Note that the parameters described as free in the fit are unrestricted (barring physical limitations).

One can also see the comparison of the model to data in S1 and S2 signal space only in Fig. 3.36. Again, there are no significant deviations or flaws in the model that are evident.

While  $^{220}\text{Rn}$  has proven to be a very useful calibration source, in future runs the hope is that tritiated methane ( $\text{CH}_3\text{T}$ ) can be used. Tritium has a beta decay spectrum with a maximum energy of 18.6 keV implying that all decays will be useful. This is very different from the beta decay spectrum of  $^{212}\text{Pb}$  (the actual beta decay used in the  $^{220}\text{Rn}$  chain) which has a maximum energy of 570 keV, implying that only a small fraction of decays are used for the calibration.

### 3.4.3.2 Results of the Nuclear Recoil Calibration

The nuclear recoil calibration was performed with the microphysics model described in Sec. 3.4.2.2 and the detector physics model described in Sec. 3.4.2.3. Since the detector model parameters are the same as for the electronic recoil calibration, the list shown in Tab. 3.3 also applies for the nuclear recoil calibration. The observables

Parameter	Value	Prior Distribution	Note
$g_1$	$0.1442 \pm 0.0068$	Normal	-
$p_{\text{DPE}}$	0.18–0.24	Uniform	Taken from Ref. [116].
$p_{\text{extracted}}$	$0.961 \pm 0.046$	Normal	-
$G_{\text{bottom}}$	$11.69 \pm 0.26$	Normal	-
$\sigma_{G_{\text{bottom}}}$	2.80	Fixed	-
Processor Efficiency	-	Uniform	Uniform inside bounds of Fig. 3.30.
Processor S1 Bias	-	Uniform	Uniform inside bounds of Fig. 3.31.
Processor S1 Smearing	-	Uniform	Uniform inside bounds of Fig. 3.31.
Processor S2 Bias	-	Uniform	Uniform inside bounds of Fig. 3.32.
Processor S2 Smearing	-	Uniform	Uniform inside bounds of Fig. 3.32.
S1 Correction Map	-	Fixed	Shown in Fig. 3.19.
S2 Correction Map	-	Fixed	Shown in Fig. 3.20.
Electron Lifetime	-	Fixed	Randomly drawn from measured electron lifetimes.
S2 Fraction - Bottom	0.38	Fixed	-
Total S2 Threshold	200	Fixed	-
S1 Cut Acceptance	-	Normal	Mean and width shown in Fig. 3.25.
S2 Cut Acceptance	-	Normal	Mean and width shown in Fig. 3.25.

Table 3.3: The detector model parameters and their associated priors. Note that all of these parameters are constrained by independent calibrations.

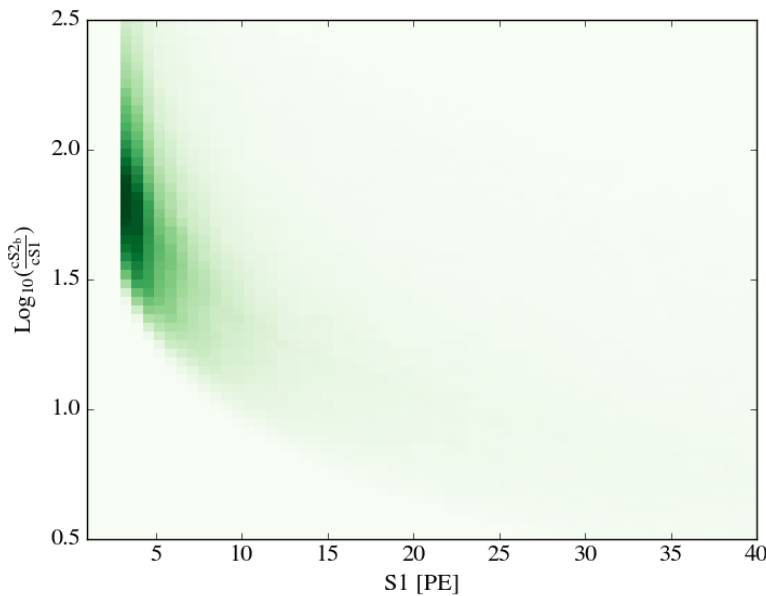


Figure 3.33: The PDF of accidental coincidence background events in  $\log\left(\frac{cS2_b}{cS1}\right)$  versus  $cS1$  space for the first dark matter run.

production parameters will be different for the nuclear recoil calibration and the parameters are listed in Tab. 3.4.

Note that the probability of an electronic recoil event is left free. This parameter is a proxy for the electronic recoil background rate during the AmBe calibration. The reason this must be included is simply because the  $^{222}\text{Rn}$  background rate is not negligible during the nuclear recoil calibration and could potentially skew the fit to predict higher light and charge yields. Therefore, we include this background by assuming that each event has a finite probability of being from the  $^{222}\text{Rn}$ . If the event is from our electronic recoil background, we use the best-fit model from the electronic recoil background and a uniform distribution in energy and position to simulate the event.

Unlike the electronic recoil calibration with  $^{220}\text{Rn}$ , the energy spectrum and distribution of positions in the detector cannot be assumed to be uniform in our region of interest for the nuclear recoil calibration. Instead, the energies for the fast Monte Carlo must be drawn from the distribution shown in Fig. 3.28 and the positions from the distribution shown Fig. 3.29.

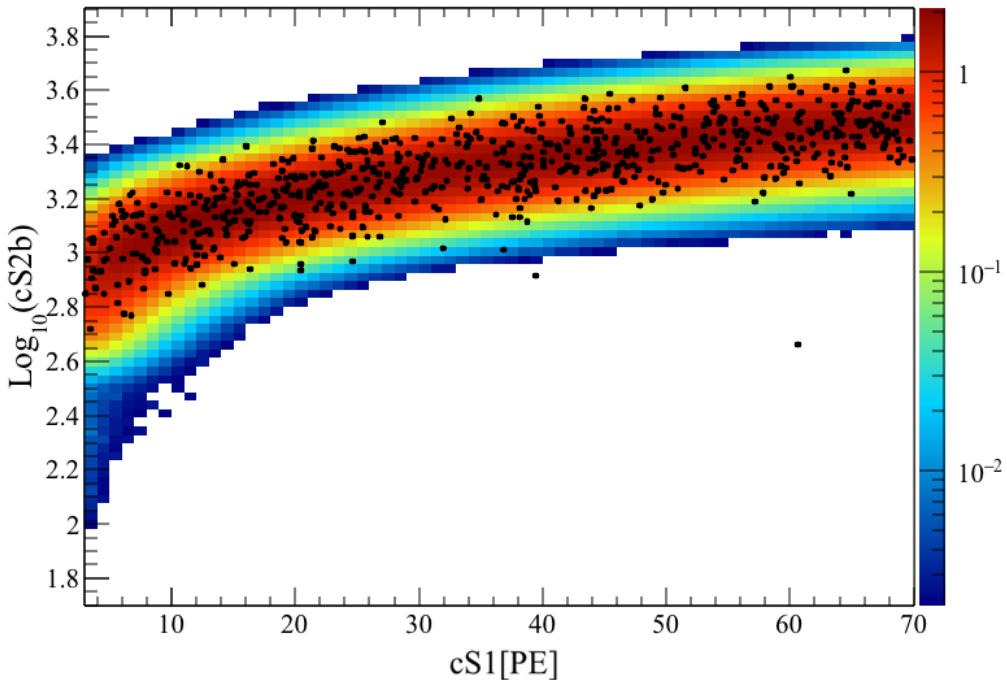


Figure 3.34: The best-fit PDF for electronic recoils during the  $^{220}\text{Rn}$  electronic recoil calibration. Outside of the two outliers, the agreement between the model and data is extremely good.

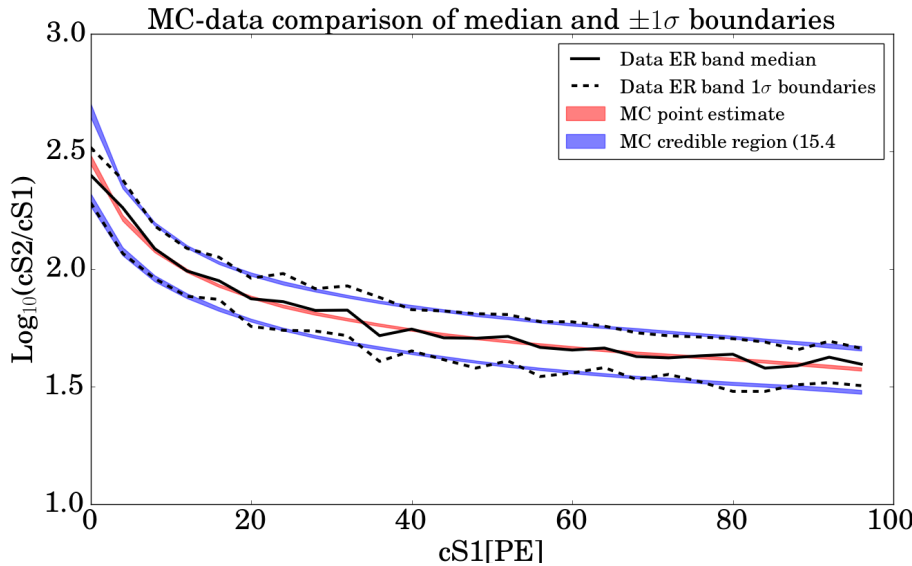


Figure 3.35: Comparison of the band median and width during the electronic recoil calibration. One can see that the fit provides excellent agreement in the region of interest.

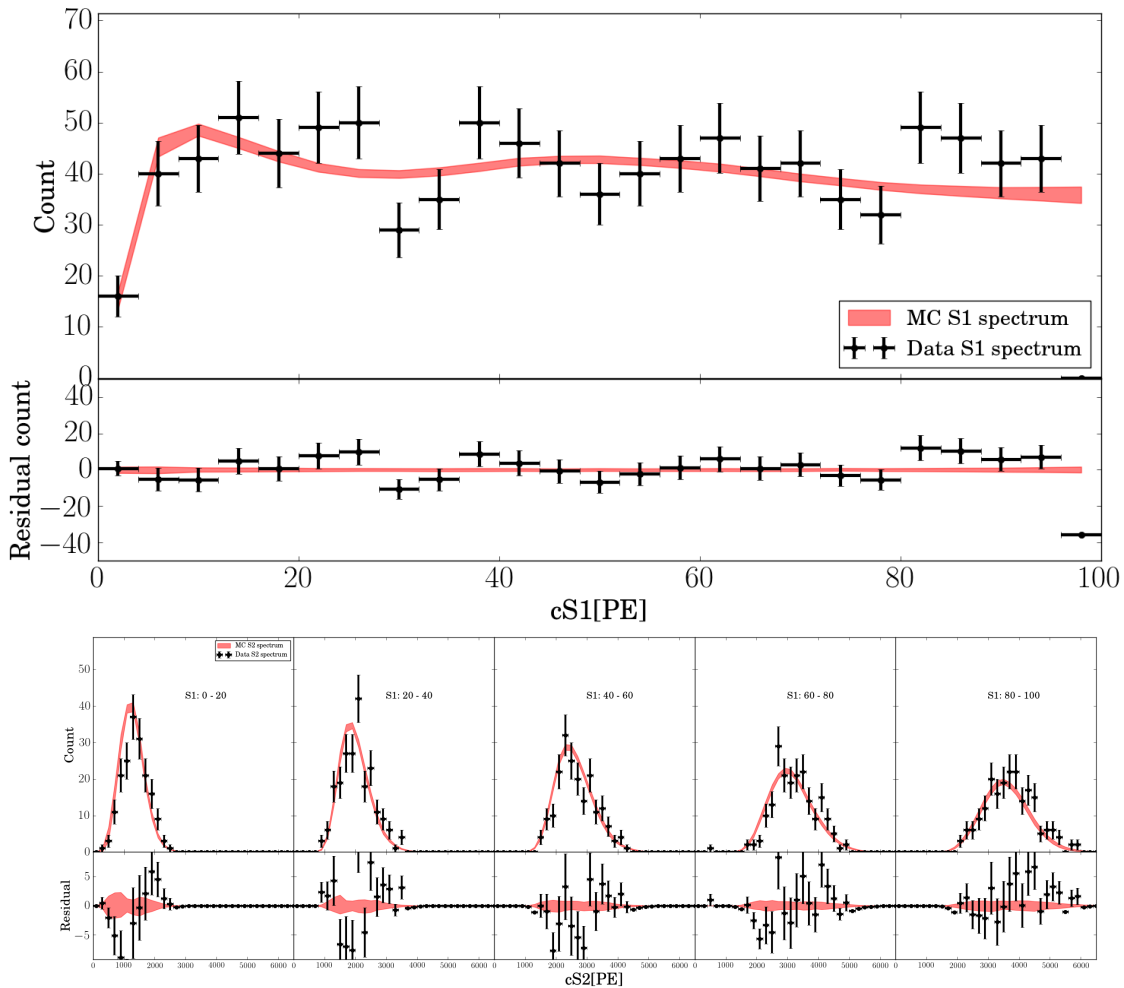


Figure 3.36: Comparison of the electronic recoil band in S1 signal space and S2 signal space in different S1 regions. Again, the band parameterization used describes the shape of the data very well.

With all of the inputs in place, the nuclear recoil calibration could be performed. The PDF overlaid with all of the data points taken with the AmBe source are shown in Fig. 3.37. Comparison of the nuclear recoil data and the best-fit Monte Carlo are shown in two dimensions and S1 signal space and S2 signal space in Fig. 3.38 and Fig. 3.39. While the nuclear recoil dataset includes more outliers than the electronic recoil calibration, likely due to the fact that AmBe is an external source, the shape of the band predicted by the model agrees well with data.

*In situ* nuclear recoil calibrations for large liquid xenon TPCs are inherently dif-

ficult due to the expected shape of the energy spectrum. Attempts to measure the energy of elastic neutron scatters have been made in large detectors, most notably by LUX in Ref. [124]. However, most studies performed to understand the light and charge yield of nuclear recoils and their field dependence in liquid xenon were done with smaller detectors optimized for the task. One of these measurements was performed by the author and will be the focus of chapter four.

### 3.4.4 Propagating Results to the WIMP Search

Now, having a handle on both the electronic recoil and nuclear recoil models, it is possible to move onto the WIMP search. Of course, as described in Sec. 1.4.3, at the end of the day a direct dark matter search in its most basic form is counting experiment. We could have proceeded with the rate estimates of our backgrounds from Sec. 3.2 but of course we would only be able to make a very weak statement on the limit since we are not using the discrimination power of liquid xenon or the different background shapes in energy. However, since we know the energy spectra, the position distributions, and the type of interaction (electronic or nuclear recoil)

Parameter	Value	Prior Distribution	Note
$w$	$13.7 \pm 0.2$ eV	Normal	-
$\alpha$	$1.240^{+0.079}_{-0.073}$	Normal	Taken from Ref. [86]
$\zeta$	$0.0472^{+0.0088}_{-0.0073}$	Normal	Taken from Ref. [86]
$\beta$	$239^{+28}_{-8.8}$	Normal	Taken from Ref. [86]
$\gamma$	$0.01385^{+0.00058}_{-0.00073}$	Normal	Taken from Ref. [86]
$\delta$	$0.0620^{+0.0056}_{-0.0064}$	Normal	Taken from Ref. [86]
$k$	$0.1394^{+0.0032}_{-0.0026}$	Normal	Taken from Ref. [86]
$\eta$	$3.3^{+5.3}_{-0.7}$	Normal	Taken from Ref. [86]
$\lambda$	$1.14^{+0.45}_{-0.09}$	Normal	Taken from Ref. [86]
Probability of ER Event	-	<b>Free</b>	-

Table 3.4: The parameters of the light and charge model for nuclear recoils in liquid xenon. Note that the parameters described as free in the fit are unrestricted (barring physical limitations).

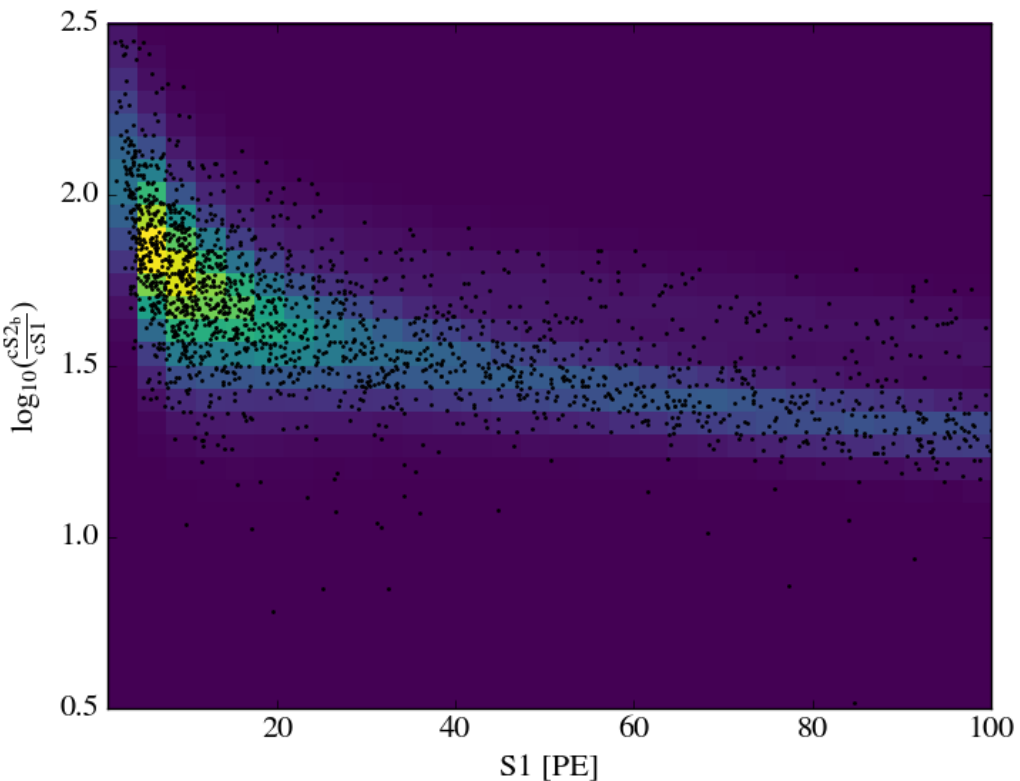


Figure 3.37: The best-fit PDF for nuclear recoils during the AmBe nuclear recoil calibration. Both the electronic and nuclear recoil band can clearly be seen.

as well as the rates, we can simulate the expected rate of these backgrounds in S1 and S2 signal space. Additionally, if we assume a model for WIMP scattering, such as the basic elastic scattering with nuclei (in the same way as neutrons), we can simulate the expected rate of WIMPs in S1 and S2 signal space by assuming a mass and cross-section for the scattering.

A subtle point is that changes in the model parameters from the fits will change how the different WIMP and background spectra will look in S1 and S2 signal space. Ideally, one would produce the spectra using parameters that are randomly sampled from the posterior distributions from the electronic and nuclear recoil calibrations (or the single posterior from the combined calibration). While accurate, the high dimensionality of the posteriors makes this approach technically impractical without using GPU-based servers (like the ones used for the electronic and nuclear recoil

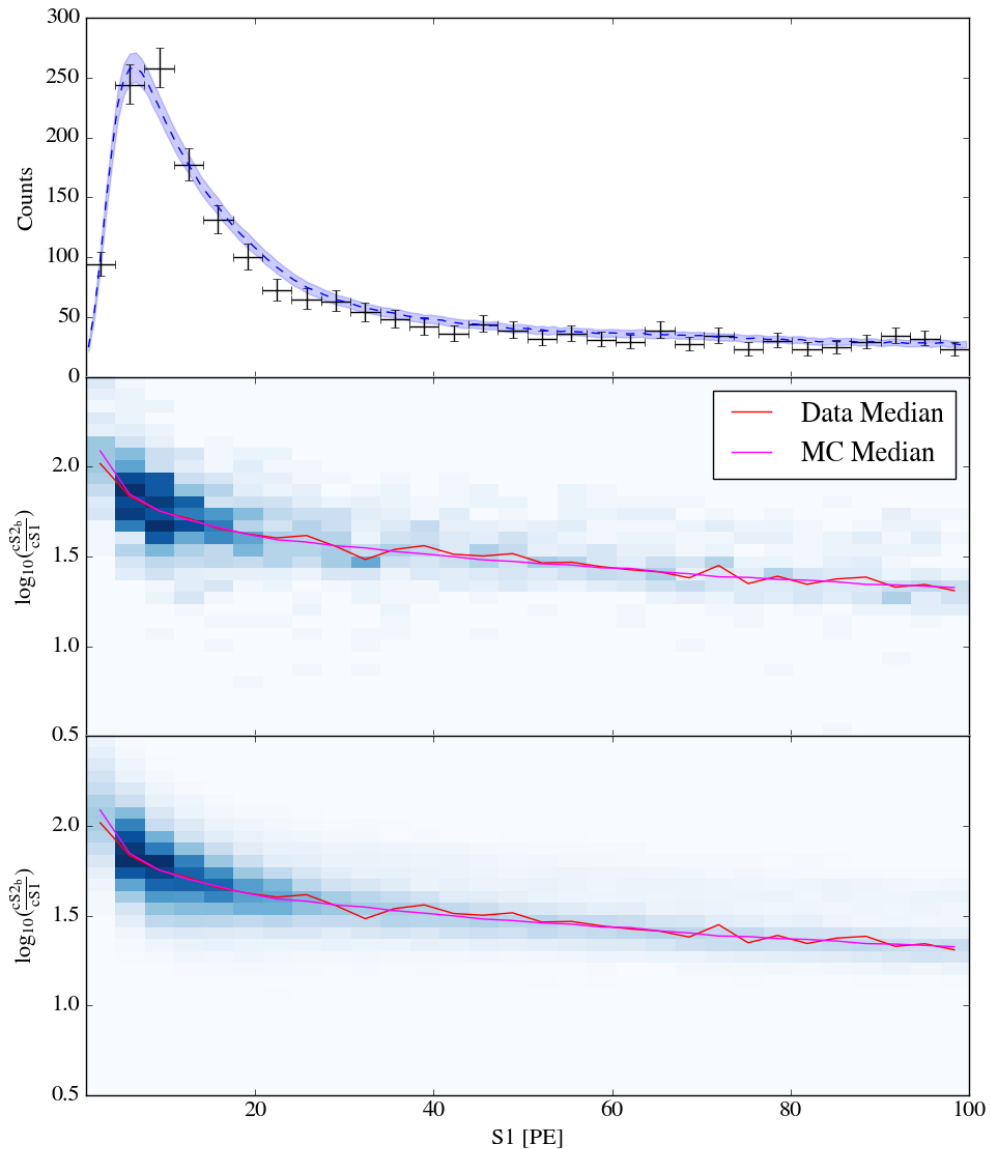


Figure 3.38: Shown on top is the nuclear recoil data in S1 space overlaid with the 68% credible region. In the middle panel is the nuclear recoil data in S1 and S2 signal space and in the bottom panel is the best-fit nuclear recoil Monte Carlo output in S1 and S2 signal space. Overlaid in both of these are the medians of each distribution.

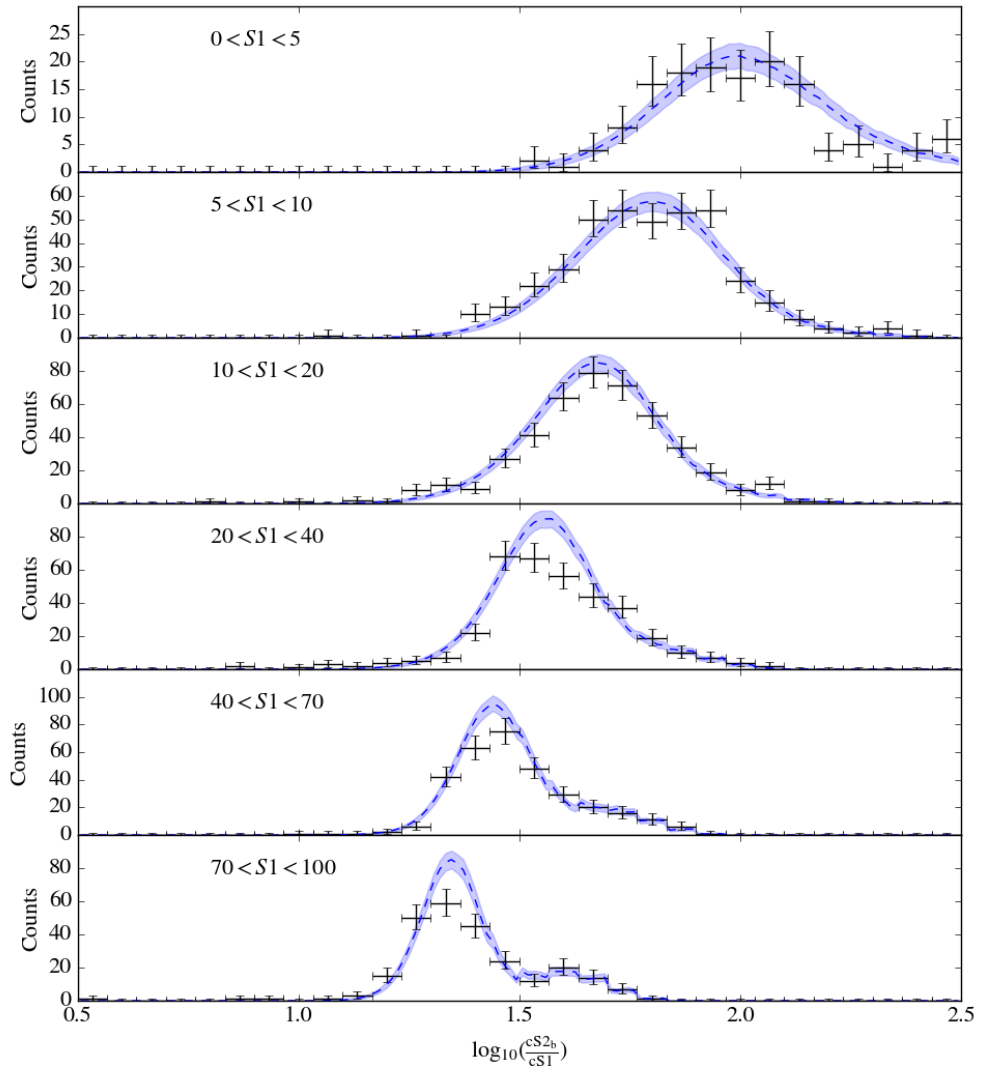


Figure 3.39: The nuclear recoil data in S2 signal space for various cuts in S1 signal space overlaid with the 68% credible region.

calibrations) since the Monte Carlo must be rerun for every new set of parameters. Instead, for the first science run it was decided that fixed spectra would be produced for a subset of the parameters that change the scale and shape of the spectra the most. For nuclear recoils, these parameters were  $\gamma$ ,  $\eta$ ,  $\alpha$ , and the processor efficiency. For electronic recoils, the photon yield and the recombination had the greatest effects. Spectra were produced for each expected type of event varying the parameters at a few fixed point (the mean,  $\pm 1\sigma$ , and  $\pm 2\sigma$  from the marginalized posterior) and bin-by-bin linear interpolations were used to estimate spectra not produced. By following this procedure, the analysis still accounted for the largest sources of uncertainty while avoiding the computationally expensive Monte Carlo<sup>3</sup>.

## 3.5 Results of the First WIMP Search with XENON1T

With all of the calibrations performed and armed with an understanding of the signal production model and its uncertainty in our detector, we can finally examine the data taken during the first science run. The first science run lasted 34.2 days, beginning on November 22, 2016 and unexpectedly ending on January 18, 2017 due to interrupted detector function as a result of a local earthquake. The drift field inside the TPC was maintained at  $116.7 \pm 7.5$  V/cm and the average electron lifetime over the course of the science run was  $452 \mu\text{s}$ . A cylindrical fiducial volume with a total mass of  $1,042 \pm 12$  kg was used for the first science run.

### 3.5.1 First Science Run Data

Data from the 34.2 day dark matter search of the first science run is shown in Fig. 3.40, along with the data from the  $^{220}\text{Rn}$  and AmBe used to define the electronic and nuclear recoil models and corresponding bands. The large majority of events appear to

---

<sup>3</sup>The hope is that in future runs that the Monte Carlo approach can be used to further improve on the accuracy of a limit or discovery.

be electronic recoils, as one would expect given that the background is dominated by electronic recoils. Additionally, there are a few events that appear to be potential nuclear recoils and there is a single event that has an S1 and S2 seemingly incompatible with both electronic and nuclear recoils.

### 3.5.2 Background Expectations

There are six sources of background that are considered for in the first science run of XENON1T: the electronic recoil background (due to  $^{222}\text{Rn}$  and  $^{85}\text{Kr}$  mostly), radiogenic neutrons from detector materials, neutrinos, accidental coincidences, wall leakage, and anomalous background. Neutrons produced by cosmogenic muons are not considered for this science run as the expected rate is several orders of magnitude below all other background sources. The expected number of events during the dark matter portion of the first science run are shown in Tab. 3.5 for the full cS1 and cS2<sub>b</sub> ([3, 70] PE in cS1 and [50, 8000] PE in cS2<sub>b</sub>) space and for all cS1 space and between the nuclear recoil band median and  $-2\sigma$  quantile in cS2<sub>b</sub> (referred to as the reference region).

We have discussed the first three sources of background in detail in Sec. 3.2. However now that we have working signal production models for our detector we can examine the expected spectra of these background sources in S1 and S2 space — these spectra are shown in Fig. 3.41. While the rates for the radiogenic neutron background and the neutrino background were constrained during the WIMP search, the electronic recoil background was left free even though precise measurements of the  $^{85}\text{Kr}$  and  $^{222}\text{Rn}$  contamination had been made<sup>4</sup>. The WIMP search ultimately found an electronic recoil background rate of  $(1.93 \pm 0.25) \cdot 10^{-4}$  events/(kg · day · keV) in agreement with the expectation of  $(2.3 \pm 0.2) \cdot 10^{-4}$  events/(kg · day · keV) [48].

The accidental coincidence background was discussed briefly with regards to the electronic recoil calibration. It is the result of uncorrelated S1 and S2 signals occurring within a time window that would put the depth of the event inside of the

---

<sup>4</sup>While searching for dark matter candidates that interact via electronic recoils, the electronic recoil background rate would need to be constrained.

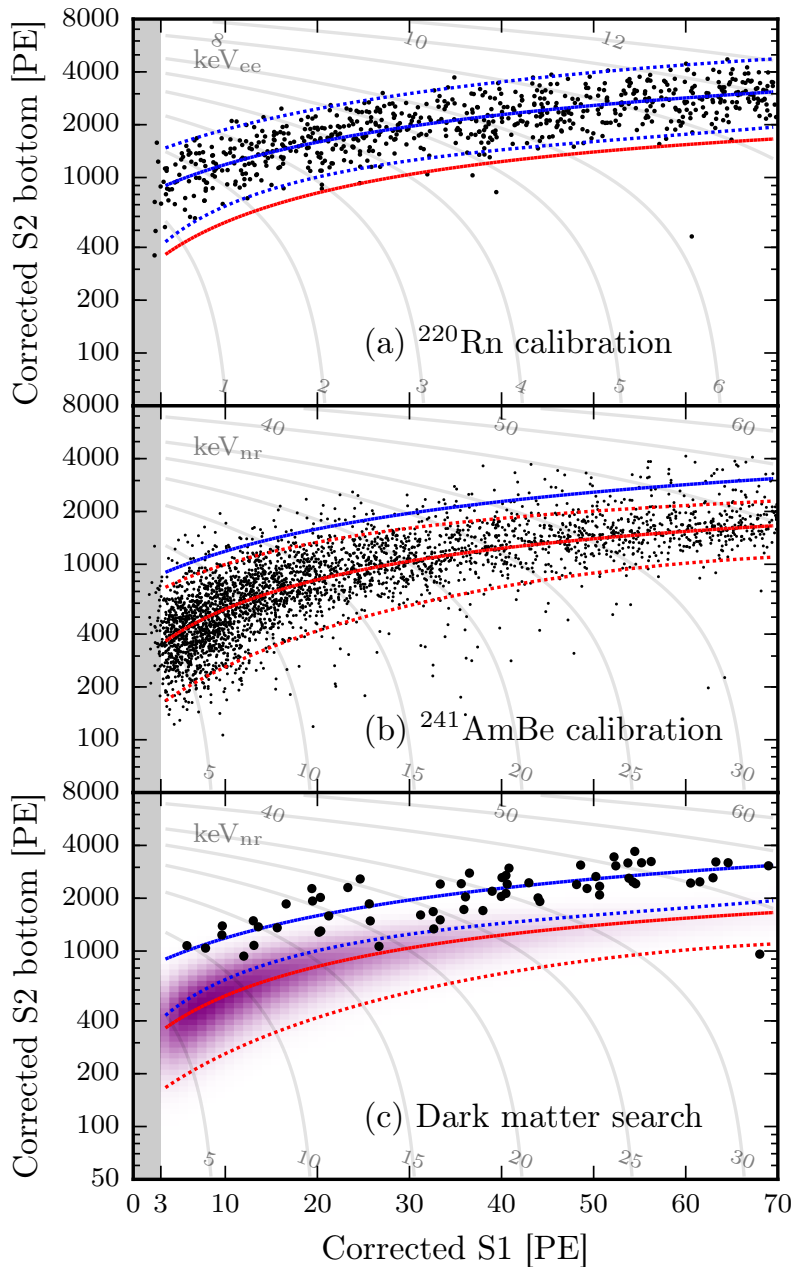


Figure 3.40: Observed data in cS2<sub>b</sub> vs. cS1 for (a)  $^{220}\text{Rn}$  electronic recoil calibration, (b) AmBe nuclear recoil calibration, and (c) the 34.2 day dark matter search. The lines shown represent the median (solid) and the  $\pm 2\sigma$  (dashed) quantiles of the electronic and nuclear recoils band as measured in the relevant calibration. In panel (c), the purple distribution shows the estimated probability distribution function of a 50 GeV/c<sup>2</sup> WIMP. Only data above 3 PE is used in all analyses (unused data shown in gray box). Image Credit: Ref. [48].

fiducial volume. Using the rates from lone S1 signals and lone S2 signals, it is estimated that during the span of the first science run  $0.22 \pm 0.01$  events of accidental coincidence background are expected. The spectra, made using a Kernel Density Estimator (KDE) based on lone S1 and S2 signal sizes, is shown in Fig. 3.41.

The fifth source of background is also determined empirically and is the result of events occurring near the wall (outside of the fiducial volume) being reconstructed inside of the fiducial volume. These events are referred to as wall leakage events. This type of background is expected to have an abnormally small S2 signal due to charge loss on the teflon. The rate of wall leakage events is extrapolated from analyzing the number of these events in areas outside of the fiducial volume below the nuclear recoil band and a KDE is used to approximate the probability distribution function of these types of events in S1 and S2 space. The expected distribution and rate of wall leakage events is shown in Fig. 3.41.

The six and final source of background considered in the WIMP search of the first science run is a flat background in  $(cS1, \log_{10}(cS2_b))$  space referred to as the anomalous leakage background. While this background source is not well understood, it has been observed both in XENON100 [125] and during the  $^{220}\text{Rn}$  calibration and dark matter data taking of first science run of XENON1T. Since the rate of this anomalous leakage does not scale with exposure, it is assumed that the rate of this background is linked to the electronic recoil rate. The rate of this flat background is shown in Fig. 3.41.

### 3.5.3 Searching for WIMPs

The dark matter search data was blinded below the 99<sup>th</sup> percentile of the electronic recoil band. In this way, cuts and backgrounds could be defined in an unbiased manner. In total, 63 events were seen during the 34.2 day run that passed all data selection criteria and were inside the predefined full analysis region. Two events in the WIMP search data are of particular note. The first was the event at  $cS1 = 26.7$  PE which is much more likely to be from a nuclear recoil rather than an electronic recoil, as can be seen in Fig. 3.40(c). The second is the event at  $cS1 = 68.0$  PE. This

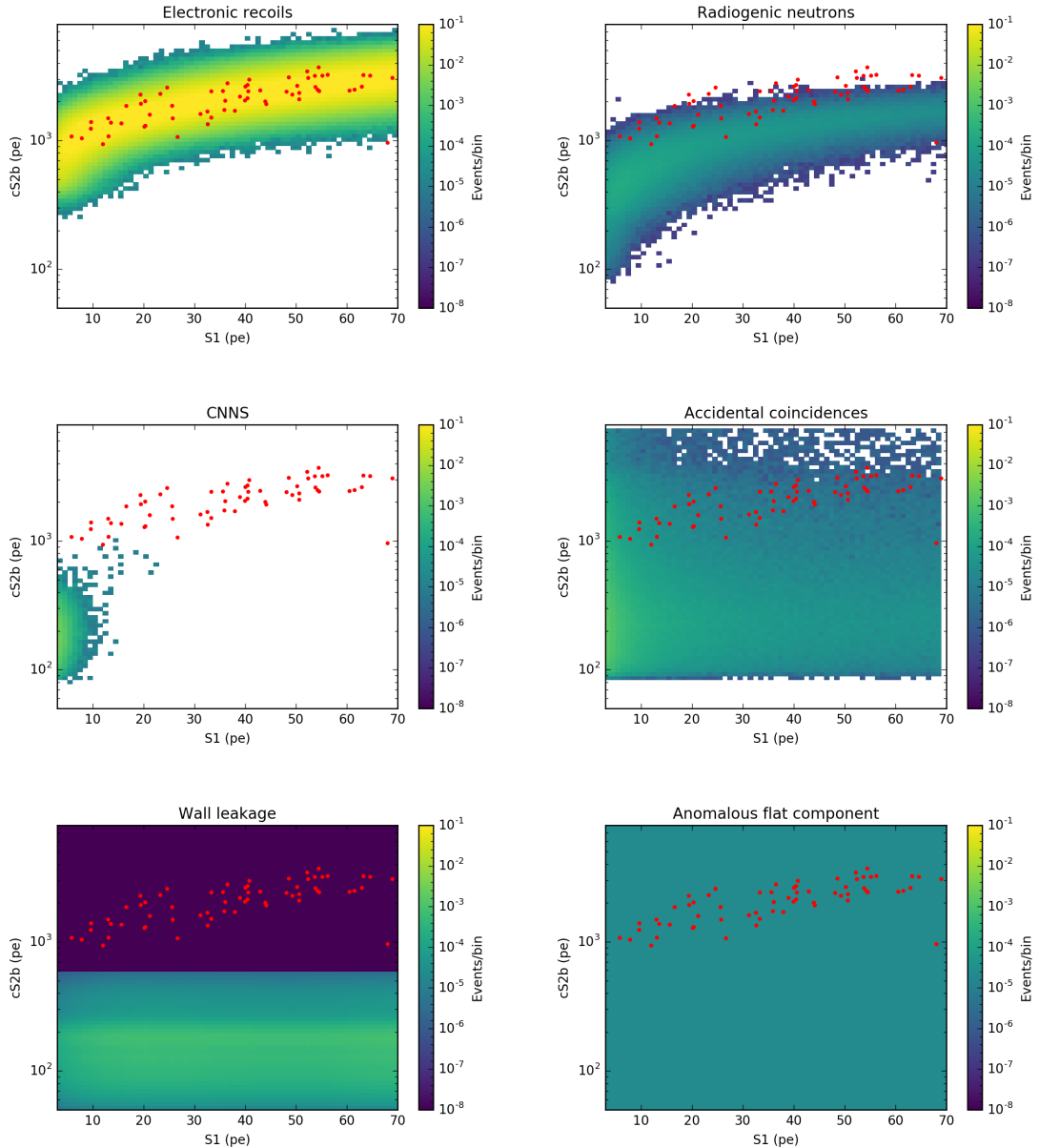


Figure 3.41: The expected backgrounds and their rates during the first science run of XENON1T. The electronic recoil and nuclear recoil backgrounds were found by inputting their respective energy spectra into the signal models found via the calibrations discussed earlier. The remaining background spectra were determined empirically.

### 3. THE FIRST DARK MATTER SEARCH WITH XENON1T

---

event is very unlikely to be from a nuclear recoil or electronic recoil and appears to either be the result of the wall leakage or some unknown source of background. The remaining events are most likely from the electronic recoil background in the detector.

An extended unbinned profile likelihood test statistic in cS1 and cS2<sub>b</sub> was used for the statistical interpretation of the data. Uncertainties from the nuclear recoil and electronic recoil signal model were included in addition to the rates on the various background sources. Standard assumptions were made for production of the WIMP energy spectra: the standard halo model was used ( $v_0 = 220$  km/s,  $\rho_{\text{DM}} = 0.3$  GeV/c<sup>2</sup>, and  $v_{\text{esc}} = 544$  km/s) and the Helm form factor was used for the nuclear recoil cross section [33, 37].

Ultimately, it was found that the data is consistent with the background-only hypothesis. The limit placed on each WIMP mass is shown in Fig. 3.42. Even though the first science run of XENON1T was cut short unexpectedly by an earthquake, it still placed the most stringent limits on WIMP dark matter for masses in the range of approximately 10 – 100 GeV/c<sup>2</sup> as of this writing. The second science run of XENON1T has already collected over 150 livedays of dark matter search data and will be sensitive to a large unexplored fraction of the WIMP parameter space.

Background Source	Full Space	Reference Region
Electronic recoils	$62 \pm 8$	$0.26^{+0.11}_{-0.07}$
Radiogenic neutrons	$0.05 \pm 0.01$	0.02
CNNs	0.02	0.01
Accidental coincidences	$0.22 \pm 0.01$	0.06
Wall leakage	$0.5 \pm 0.3$	0.01
Anomalous leakage	$0.10^{+0.10}_{-0.07}$	0.02
Total Background	$63 \pm 8$	$0.36^{+0.11}_{-0.07}$
$50 \text{ GeV}/c^2, \sigma^2 = 10^{-46} \text{ cm}^2$ WIMP	$1.66 \pm 0.01$	$0.82 \pm 0.06$

Table 3.5: The expected (measured in the case of electronic recoils) number of events for the six different background sources and a 50 GeV/c<sup>2</sup>,  $\sigma^2 = 10^{-46}$  cm<sup>2</sup> WIMP for the full analysis space ([3, 70] PE in cS1 and [50, 8000] PE in cS2<sub>b</sub>) and for the reference region (all cS1 space and between the nuclear recoil band median and  $-2\sigma$  quantile in cS2<sub>b</sub>).

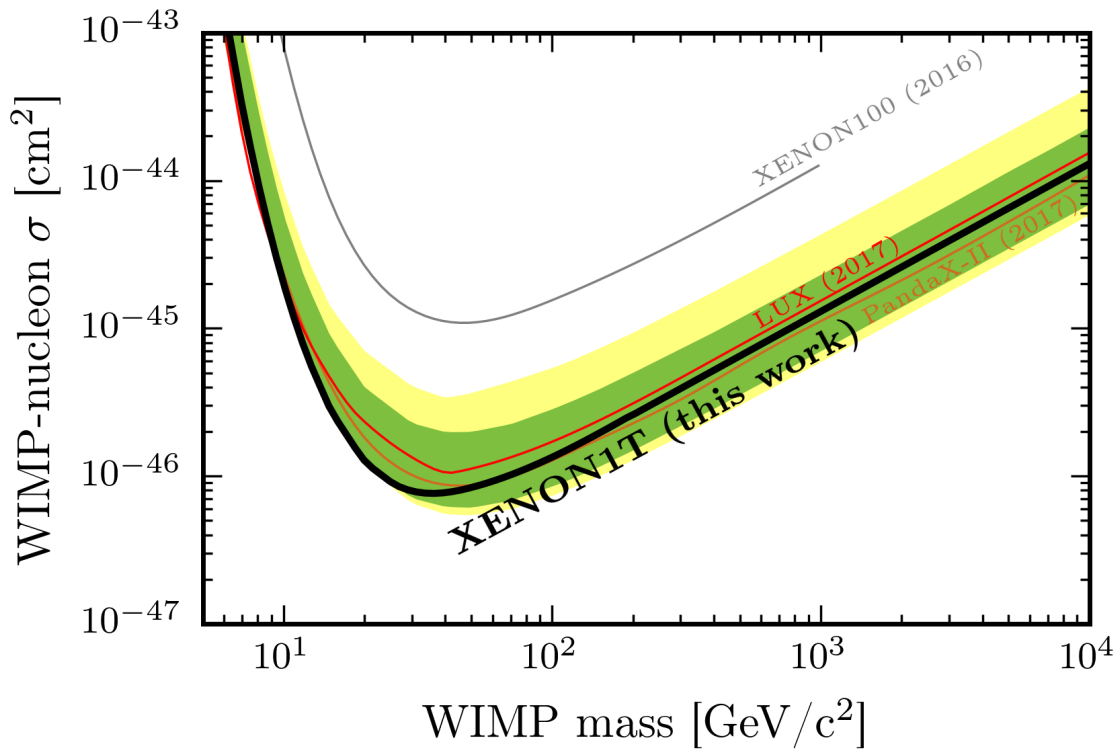


Figure 3.42: The spin-independent WIMP-nucleon cross section limits as a function of WIMP mass at 90% confidence level (black) for this run of XENON1T. In green and yellow are the 1 $\sigma$  and 2 $\sigma$  sensitivity bands. Shown for reference are the final XENON100 results [125] and the most recent results from LUX [53] and Panda-X II [49]. Image Credit: Ref. [48].



# Chapter 4

## Measuring the Low Energy Light and Charge Yield of Nuclear Recoils in Liquid Xenon

As was discussed in the previous chapters, dual-phase liquid xenon TPCs lead the search for WIMPs. These detectors continue to grow in size and reduce their background making them increasingly more sensitive to dark matter. As mentioned in the previous chapter, XENON1T is the largest and most sensitive of these detectors with a total mass of 3,200 kg of liquid xenon [48]. Since WIMPs are expected to interact primarily with atomic nuclei and the differential scattering rate of WIMPs and Standard Model particles are generally expected to increase with decreasing interaction energy, it is crucial to understand the properties of nuclear recoils in LXe down to the few keV energy scale.

While larger detector sizes (in the form of larger fiducial volumes) make WIMP searches more and more sensitive, they do come with a drawback: calibrations, especially calibrations with external sources, becoming significantly more difficult. However, understanding the signal output by a LXe TPC can essentially be broken down into two steps: the actual light and charge production and the detector physics. While the detector physics is unique for each detector used and therefore must be measured for each one, the light and charge production mechanisms are only unique to the

## 4. MEASURING THE LOW ENERGY LIGHT AND CHARGE YIELD OF NUCLEAR RECOILS IN LIQUID XENON

---

medium. Therefore, if we can effectively decouple the two steps, we can measure the light and charge production mechanism in a detector optimized for calibrations and use it in other detectors.

As LXe detectors have scaled in size, several of these optimized detectors have been built for exactly this purpose: to measure the light and charge production of liquid xenon to electronic and nuclear recoils. While each of these detectors was slightly different and designed for a specific purpose, they shared the same relatively simple operating procedure: measure the light and charge produced from an interaction of a known type (electronic or nuclear recoil) and energy. The neriX (Nuclear and Electronic Recoils in xenon) detector at Columbia University is one of these optimized detectors and has already successfully provided the most precise measurements of the light and charge yield (the number of photons and electrons produced per unit energy) of electronic recoils in liquid xenon at multiple electric fields.

While several measurements of the response of liquid xenon to nuclear recoils have been made, most measure only the light yield or charge yield. Two particular calibrations [62, 126] measure both the light and charge yield but do not capture the potential correlation of the yields. Without examining both light and charge simultaneously, it is impossible to fully understand the fundamental processes that occur in LXe to produce these signals. Additionally, only the two simultaneous studies [62, 126] have systematically measured the effect of an electric field on the light and charge yield. Unlike in the case of electronic recoils, these measurements found that the light and charge yield of nuclear recoils in liquid xenon change very little, if at all, with an applied electric field. However, additional measurements are necessary since it is expected that the recombination of electrons and ions produced in the interaction is energy dependent as well as field dependent [83] and both measurements cannot make conclusive statements below  $\sim 45$  keV. In this chapter the results of a new measurement of both the light and charge yield of nuclear recoils from 74 keV down to 3 keV at three electric fields using the fixed-angle scattering method are presented. Also, for the first time, a simulation of the light and charge production process in liquid xenon is used for the parameter estimation, which takes into account

the correlation between the light and charge signals.

## 4.1 Experimental Setup

In chapter three, we discussed the nuclear recoil calibration of XENON1T. In this calibration, an americium-beryllium (AmBe) source was used to irradiate the liquid xenon inside of the detector with MeV energy neutrons. Simulation is performed to determine the energy spectrum of single scatters in the detectors but, for the most part, the spectrum is defined by the relative cross-section of elastic scatters at different energies ultimately resulting in an exponentially falling energy spectrum as seen in Fig. 3.28. In this calibration setup, the energy of each individual event is unknown and we are using the entire energy spectrum to match our data. While this can be an effective way to measure the response of liquid xenon to nuclear recoils, it proves to be very difficult in practice with such a featureless energy spectrum. This type of measurement where one compares an energy spectrum to data is typically referred to as an *indirect* measurement and has been used successfully to measure the light and charge production process of electronic and nuclear recoils [70, 71, 115].

Measurements in neriX and other smaller, calibration optimized detectors follow a different approach. A monoenergetic source is used to irradiate the detector where the incoming particle will scatter a single time before scattering into a secondary detector. For electronic recoils, the secondary detector can be a high-purity germanium detector or sodium-iodide detector with an excellent energy resolution. When this is the case, assuming the incoming radiation did not scatter with other materials around the detector, the energy of the interaction is known very precisely. Unfortunately when measuring the response of liquid xenon to nuclear recoils in these detectors, no equivalent secondary detectors exist that will precisely measure the energy of the incoming neutron. Instead we can use the position of the secondary detector as a proxy for the energy since the energy transferred to a xenon nucleus by a neutron is completely determined by the scattering angle. This relationship between the energy of the recoiling nucleus and the angle is shown for non-relativistic neutron energies in

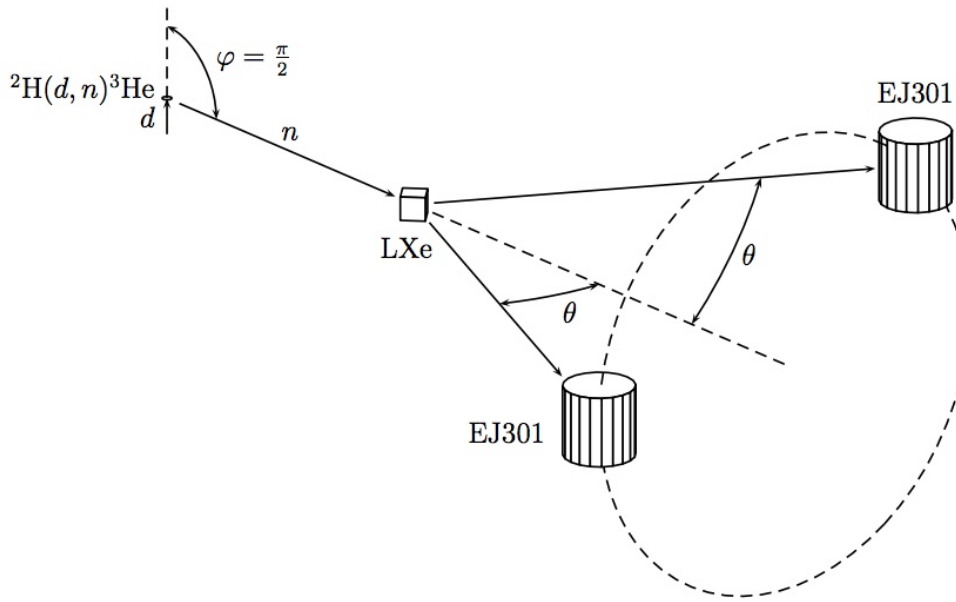


Figure 4.1: A schematic for the experimental setup used in this measurement of the light and charge yields for nuclear recoils. 2.45 MeV neutrons are produced at an angle of  $\frac{\pi}{2}$  in the neutron generator. Some of these neutrons scatter a single time in the liquid xenon and then deposit some of their energy in the M510 detectors, filled with EJ301 liquid scintillator, for discrimination versus background. Image Credit: Ref. [128].

Eqn. 4.1 where  $m_n$  is the mass of the neutron,  $m_{\text{Xe}}$  is the mass of the xenon nucleus,  $E_r$  is the energy of the recoiling nucleus,  $E_n$  is the energy of the incoming neutron, and  $\theta$  is the scattering angle [72].

$$E_r \approx E_n \frac{2m_n m_{\text{Xe}}}{(m_n + m_{\text{Xe}})^2} (1 - \cos \theta) \quad (4.1)$$

A schematic of the experimental setup for neriX using this *fixed-angle scattering* technique is shown in Fig. 4.1. The neutron source in this measurement was a  ${}^2\text{H}(d, n){}^3\text{He}$  generator provided by the Schlumberger Princeton Technology Center which produces 2.45 MeV neutrons at an angle of  $\frac{\pi}{2}$ . The secondary detectors used were Eljen Technologies M510 detectors filled with the EJ301 liquid scintillator, chosen for their excellent pulse shape discrimination [127].



Figure 4.2: A photo of the fixed-angle scattering setup with the neriX detector. On the left is our neutron generator inside of its stainless steel case. In the center is the outer portion of the cryostat and on the right are four of the M510 liquid scintillator detectors.

#### 4.1.1 neriX Detector

In this section we will discuss the neriX detector. neriX was specifically designed to minimize the amount of inactive xenon and materials surrounding the TPC to minimize undetectable energy depositions and with electronics such that it can systematically scan electric fields ranging from approximately 0.15 V/cm to 2.5 kV/cm in the LXe. These features make neriX an ideal detector for measuring the low-energy response of electronic and nuclear recoils at electric fields relevant to the dark matter search.

For more details on the design and construction of neriX, please refer to chapters four and five of Ref. [129].

## 4. MEASURING THE LOW ENERGY LIGHT AND CHARGE YIELD OF NUCLEAR RECOILS IN LIQUID XENON

---

### 4.1.1.1 TPC

The neriX TPC (shown in Fig. 4.4), like XENON1T, was also constructed with PTFE (teflon). The teflon pieces in neriX are stackable and compressed by stainless steel springs. The TPC at liquid xenon temperature has an inner diameter of 43 mm. neriX also included four stainless steel hexagonal meshes and a single field shaping ring to control the electric fields inside of the TPC. The cathode (used to produce the high voltage for the drift field inside the liquid xenon), the gate (kept at ground near the liquid surface), and the anode (used to extract electrons from the liquid surface and into the gas) were each made of  $125\ \mu\text{m}$  thick wires and 3 mm pitch (distance between parallel wire segments). A photo of the gate mesh from above is shown in Fig. 4.5. The final mesh was a screening mesh (labeled the “bottom grid” in Fig. 4.4) used to shield the bottom PMT and was also made with a 3 mm pitch but with  $25\ \mu\text{m}$  thick wires (to reduce its surface area). The field shaping ring is simply a copper coaxial wire embedded in the teflon wall of the TPC 7 mm above the cathode. The location of the shaping ring was to maximize uniformity of the drift field at an electric field of 1 kV/cm. The distance between the cathode and the gate mesh, the maximum drift distance of electrons in the TPC, was 23.4 mm.

Six PMTs are installed in neriX: a single 2” Hamamatsu R6041 PMT is installed below the screening mesh, four 1” multianode Hamamatsu R8520-M4 PMTs (each with 4 anodes) are installed above the anode mesh, and a single 1” Hamamatsu R8520-406 is installed in a light-tight stainless steel enclosure located above the TPC. This final PMT is coupled to the TPC via a 1 mm fiber optic cable placed in between the four 1” PMTs and is intended for measuring the decay times of singlet and triplet states in liquid xenon (although this measurement was not performed during the nuclear recoil calibration). Since almost all light from the scintillation signal in the LXe is reflected at the liquid-gas interface, the bottom PMT is the only PMT used for measuring S1 signals. For simplicity, we also only use the bottom PMT to measure the S2 signals as well (the bottom PMT sees  $\sim 50\%$  of the S2 light). The top PMTs are only used for the position reconstruction of an interaction.

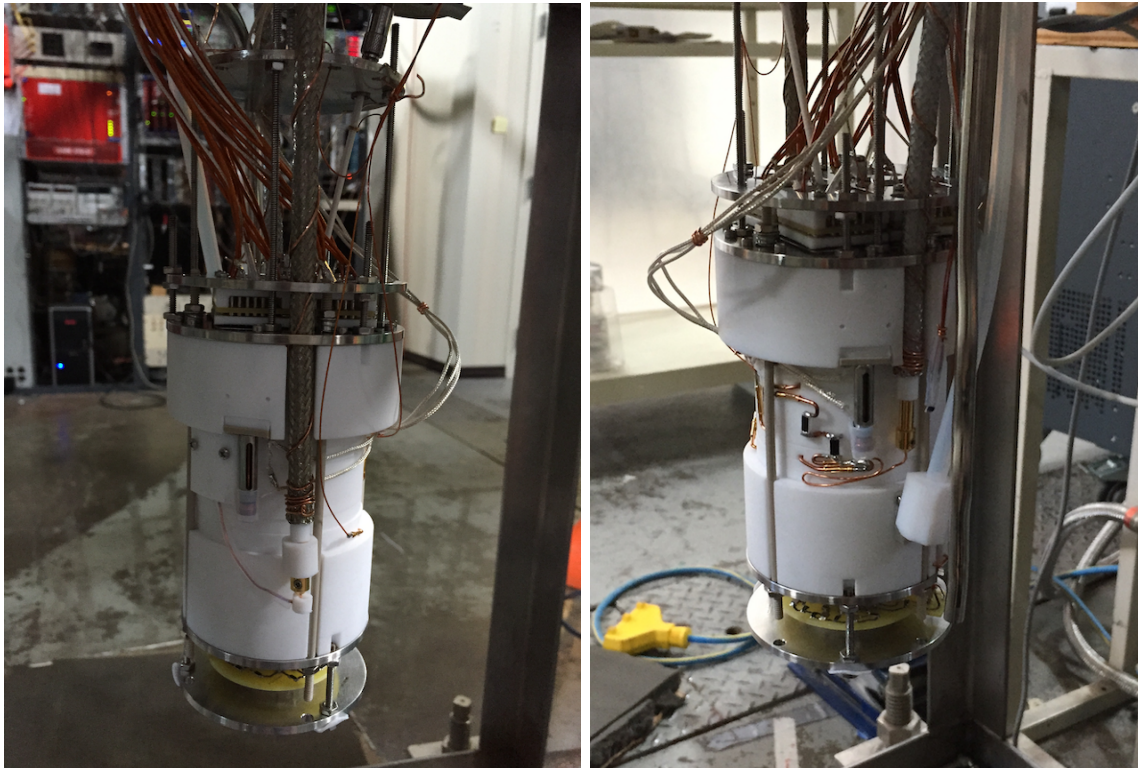


Figure 4.3: Two photos of the neriX TPC following routine detector maintenance. In both photos, one can see the plates holding the single 2" PMTs (bottom) and the array of four 1" PMTs (top). In the left image, one can see the high voltage feedthrough for the anode. In the right image, one can see the high voltage feedthrough for the cathode and the voltage divider for the field shaping ring. One can also see the stainless steel pipe used to extract xenon from the inner cryostat's buffer and the plastic tube used to feed re-condensed xenon into the system.

The TPC was connected to the cryostat via a stainless steel motion feedthrough that could be used to raise and lower the detector with a precision of  $\sim 25\ \mu\text{m}$ . This motion feedthrough could be used to raise and lower the liquid level relative to the TPC since the liquid level was kept constant via the buffer volume discussed in Sec. 4.1.1.2.

#### 4.1.1.2 Cryostat

The TPC is surrounded by a double-walled vacuum insulated cryostat. The inner cryostat was custom made for neriX such that the amount of inactive xenon is minimized. This inner cryostat, shown in Fig. 4.6, left only approximately 1 cm of space

#### 4. MEASURING THE LOW ENERGY LIGHT AND CHARGE YIELD OF NUCLEAR RECOILS IN LIQUID XENON

---

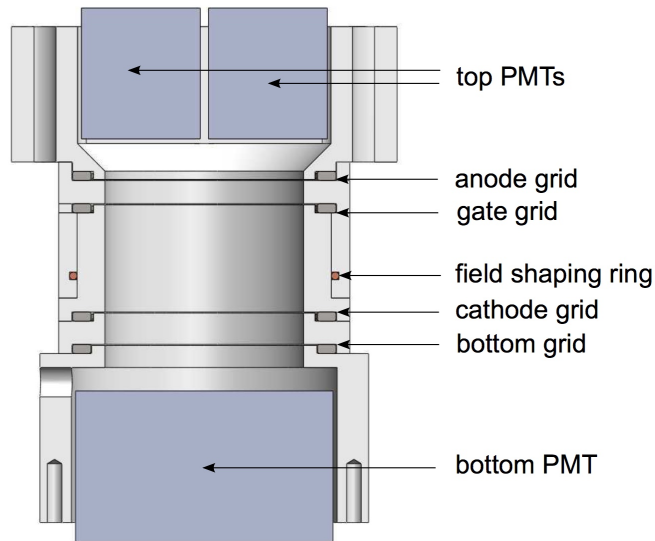


Figure 4.4: The neriX TPC with meshes and PMTs labelled.

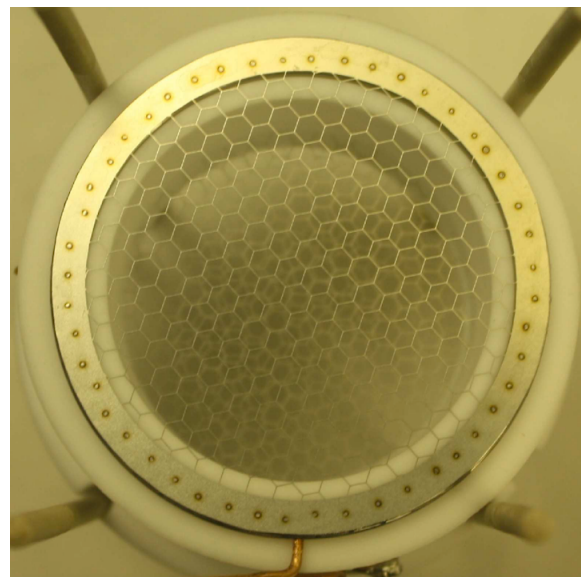


Figure 4.5: A photo of one of the meshes used in neriX.

between itself and the TPC with the exception of a  $\sim 165 \text{ cm}^3$  buffer volume used to maintain the liquid level and the space left for the high voltage feedthroughs. The inner and outer cryostats are only 1.5 mm thick. To reduce radiative heat transfer, the inner cryostat is blanketed with mylar in the same way as XENON1T.

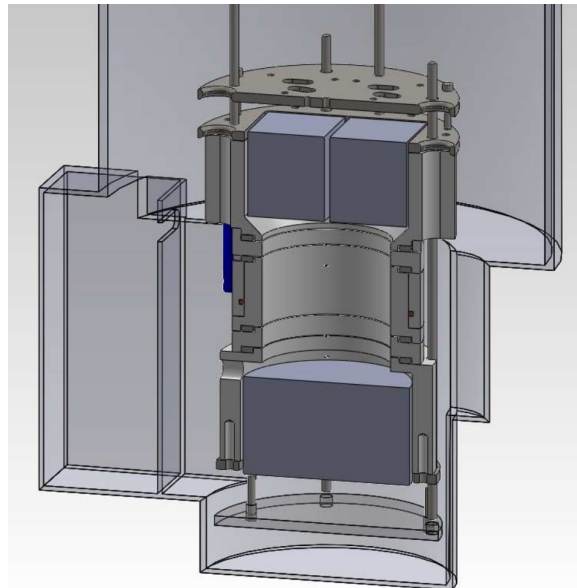


Figure 4.6: The neriX TPC inside of the cryostat. Note that excluding the buffer volume (left side of the image) and the space left for the high voltage feedthroughs (right side of the image), very little space is left between the cryostat and the TPC, effectively reducing the amount of inactive xenon for undetectable energy losses.

#### 4.1.1.3 Purification and Cryogenics System

A diagram of the cryogenics and purification system is shown in Fig. 4.7. The cryogenics and purification system used for this measurement is the same as the one used in the measurements of both Ref. [128] and Ref. [91].

As discussed in earlier chapters, electronegative impurities outgassed from the detector materials will absorb electrons extracted from the interaction site. Therefore, these impurities must constantly be removed from the xenon to ensure optimal detector operation. To remove impurities in neriX, the SAES PS4-MT3-R-1 hot getter is used. Gaseous xenon is flowed through the purification system at approximately 2 SLPM (standard liters per minute) using a KNF N 143 double-diaphragm pump. A heat exchanger, as described in Ref. [130], is used to simultaneously heat up the gaseous xenon coming from the detector and cool down the xenon going towards the detector (from the getter). This heat exchanger substantially lowers the cooling power required to operate the detector.

To maintain the temperature of the detector, Iwatani PDC08 cold head and SA101

## 4. MEASURING THE LOW ENERGY LIGHT AND CHARGE YIELD OF NUCLEAR RECOILS IN LIQUID XENON

---

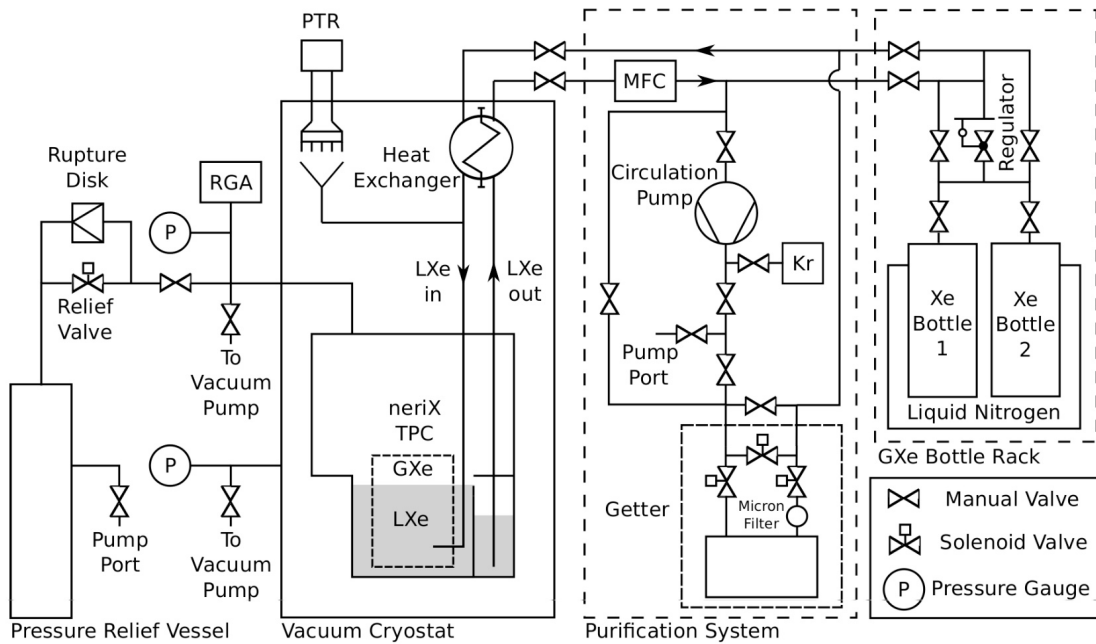


Figure 4.7: A schematic of the cryogenics and purification system for neriX. Also shown are the pressure relief system and the xenon storage system.

Helium compressor coupled to a copper cold finger are used. The xenon pressure inside of the cryostat is maintained via resistive heaters thermally connected to the copper cold fingers. These resistive heaters are controlled by a proportional-integral-derivative (PID) controller that adjusts the power of the heaters to maintain a desired cold-finger temperature.

### 4.1.1.4 Pressure Relief System

Unlike XENON1T, there is no redundant liquid nitrogen cooling in the event of a power loss for neriX. This means that if there is a power failure at the laboratory that cooling will be lost and the pressure of the detector will climb. To prevent damage to the system, especially the PMTs, a pressure relief system was built for neriX. This pressure relief system consists of a 190 liter stainless steel pressure vessel that is connected to the inner cryostat via a solenoid valve that will open in a controlled manner above a certain pressure in parallel with a rupture disk. The tank size was chosen such that all of the approximately 2.2 kg of xenon could be stored at room

temperature at a pressure below 2.5 bar. The pressure relief vessel was evacuated on a weekly basis to maintain the chemical purity of the xenon in the case of an emergency.

#### 4.1.1.5 Xenon Storage

The xenon for neriX was stored in two cylinders kept inside of a stainless steel dewar. When filling the detector, a regulator and a needle valve are used in conjunction with a mass flow meter to keep the detector pressure at reasonable levels. During recuperation, the dewars are filled with liquid nitrogen such that the xenon inside the bottle freezes and the vapor pressure is low enough to create a cryogenic pump from the cryostat to the storage bottles. While recuperation can be performed more quickly in an emergency situation, both operations could safely be performed in a single day<sup>1</sup>.

#### 4.1.1.6 Electric Field Strength and Uniformity

Since the goal of neriX is to measure the light and charge yield of nuclear recoils at different electric fields, it is obviously very important to know what electric field you are measuring the yields for and how uniform it is in the detector. Unlike in XENON1T, the fiducial volume of neriX is not meant to eliminate background but to exclude regions where the field differs drastically from the mean and where charge can be lost to the wall. To set the fiducial volume and determine the field strength in neriX, the COMSOL Multiphysics® Suite was used.

Simulation details can be found in Ref. [129] but we will present the results of the simulation here. Tab. 4.1 shows the cathode voltages used along with the corresponding fields given an anode voltage of 4.5 kV, a liquid level 2.5 mm above the gate mesh<sup>2</sup>, and the bottom mesh and gate mesh kept at ground. Simulations found

---

<sup>1</sup>Emptying the detector too quickly could lead to the formation of xenon ice which could damage the bottom PMT so care was always taken to maintain a consistent pressure throughout recuperation in non-emergency situations.

<sup>2</sup>The simulations find that the liquid level has a negligible effect though.

## 4. MEASURING THE LOW ENERGY LIGHT AND CHARGE YIELD OF NUCLEAR RECOILS IN LIQUID XENON

---

$V_C$ [kV]	-0.345	-1.054	-2.356
$E_D$ [kV/cm]	0.19	0.48	1.02
$\pm 1\sigma$ [kV/cm]	0.03	0.05	0.12

Table 4.1: The different cathode voltages used during the nuclear recoil measurement of neriX and the corresponding electric field strength and field variance. The simulation assumes an anode voltage of 4.5 kV, a liquid level 2.5 mm above the gate mesh, and the bottom mesh and gate mesh kept at ground.

that the variation of the drift field could be kept to within 20% with a radial cut at approximately 20 cm and cuts in depth at 1 mm below the gate mesh and 0.5 mm above the cathode. For the nuclear recoil calibration, a more conservative radial cut at 18.25 cm was made.

### 4.1.1.7 Data Acquisition System and Processing

Raw PMT signals are amplified and then digitized by three CAEN V1724, 14 bit, 100 MS/s flash ADCs (fADC). Each fADC has a voltage range of 2.25 V, and an input bandwidth of 40 MHz. Three flash ADCs were required to digitize the 18 PMT signals as well as the multiplexed liquid scintillator signals (multiplexing is discussed in Sec. 4.1.4). The trigger for the data acquisition system used in this measurement will be discussed in Sec. 4.1.4.

The data processing system, xerawdp, was originally developed for XENON100 [131] and modified for neriX. The processing software was used to reduce the raw waveforms into information about the S1, S2, and liquid scintillator signal sizes and timing.

### 4.1.2 Neutron Generator

As mentioned in Sec. 4.1, a small  $^2\text{H}(d, n)^3\text{He}$  generator, shown with a ruler for scale in Fig. 4.8, is used to produce neutrons. This generator is provided by the Schlumberger Princeton Technology Center and will be referred to in this work as the minitron. The tube of the generator is vacuum sealed and deuterium is produced inside by heating up a replenisher filament. These deuterium atoms are then ionized via electrons produced

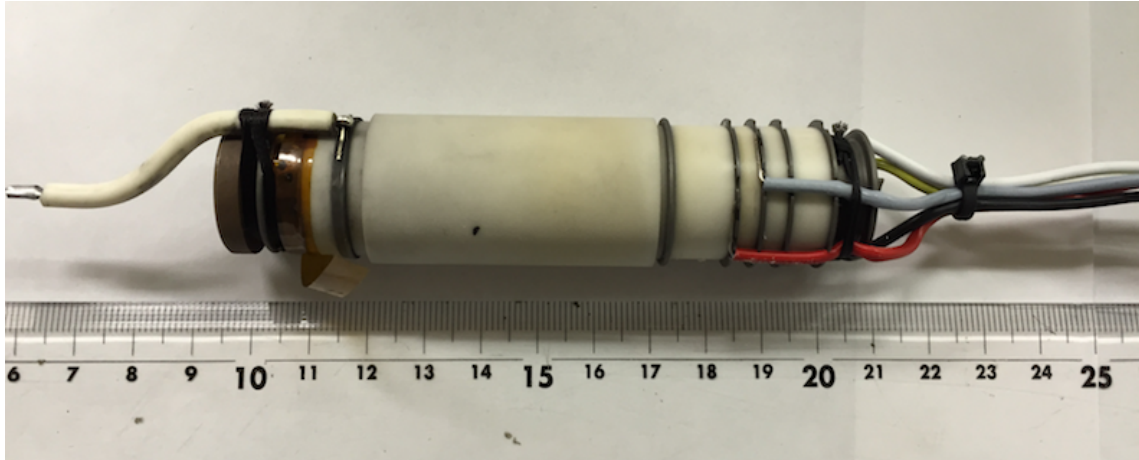


Figure 4.8: The deuterium-deuterium neutron generator used to produce 2.45 MeV neutrons.

from a cathode wire that are accelerated by a grid kept at  $\sim 200$  volts. Deuterium ions are then accelerated towards a titanium-deuteride ( $TiD_2$ ) target where they will either collide with a deuterium atom or be completely stopped. Deuterium ions that are completely stopped actually replenish the target and thus the target is considered self-regenerating<sup>3</sup>. A Heinzinger PNC 100000-3 power supply is used to supply up -100 kV of voltage to accelerate the deuterium ions and to read out the deuterium ion beam current. A schematic of the minitron electronics is shown in Fig. 4.9.

Because the minitron neutron generator utilizes very high voltage, a protective casing was used to prevent discharges from the high voltage connection. The casing was a stainless steel tube with a diameter of approximately 3 inches with teflon, due to its very large dielectric constant, supporting the minitron and filling in almost all excess space in the stainless steel tube. The small amount of remaining space was filled with mineral oil, which has a higher dielectric constant than air.

The neutron generator used in this work is the same as used in Ref. [128]. For more details on the minitron, please refer to Ref. [131].

---

<sup>3</sup>The thickness of the target is such that all deuterium ions are stopped.

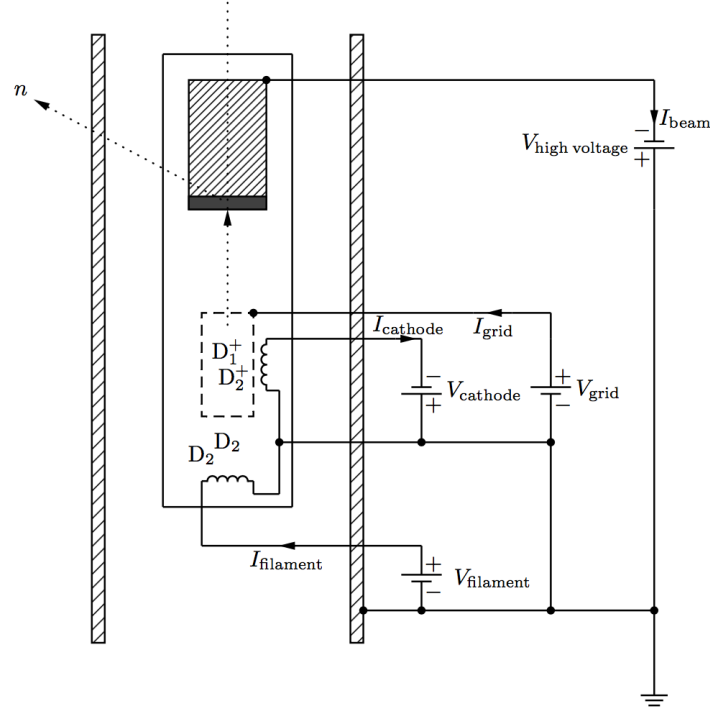


Figure 4.9: The electronics of the minitron neutron generator. Image Credit: Ref. [131].

#### 4.1.2.1 Neutron Energy Spectrum

For non-relativistic deuterons, the energy of the neutron produced from a deuterium-deuterium interaction is only dependent on the scattering angle and the energy of the deuteron. The exact energy, in this case, is given by Eqn. 4.2 [132].

$$E_n^{1/2} = \frac{(m_d m_n E_d)^{1/2}}{m_{\text{He}} + m_n} \cos \varphi + \frac{[m_d m_n E_d \cos^2 \varphi + (m_{\text{He}} + m_n)[m_{\text{He}} Q + (m_{\text{He}} - m_d) E_d]]^{1/2}}{m_{\text{He}} + m_n} \quad (4.2)$$

In Eqn. 4.2,  $m_{\text{He}}$ ,  $m_n$ , and  $m_d$  are the masses of helium, neutrons, and deuterium, respectively,  $Q$  is the  $Q$ -value of the reaction (3.269 MeV), and  $\varphi$  is the emission angle of the neutron in the laboratory frame. To approximate the energy spectrum as a function of the scattering angle and deuteron energy, we say that the yield as a function of these variables is proportional to the differential cross-section multiplied



Figure 4.10: On the left, the minitron in its partially constructed case. Notice that the teflon leaves very little room between the steel and minitron to maximize the potential voltage that can be used without causing an electrical breakdown. On the right, the minitron in its final set position. While not visible, the minitron case has been filled with mineral oil at this point to reduce risk of electrical breakdowns.

by the distribution of incident deuteron energies,  $f(E_d)$ <sup>4</sup>. We could assume that this distribution of deuteron energies is a delta function for the fixed target collision but this would ignore all of the other interactions that can occur in the  $\text{TiD}_2$ .

$$\frac{d^2N}{dE_dd\varphi} \sim \frac{d\sigma}{d\varphi} f(E_d) \quad (4.3)$$

Since the energy of the deuteron is directly related to the energy of the neutron produced by Eqn. 4.2, we can rewrite the above equation in terms of the neutron energy and the emission angle.

---

<sup>4</sup>This derivation of the angular dependence of the neutron energy spectrum is from Qing Lin (current institution: Columbia University)

$$\frac{d^2N}{dE_n d\varphi} \sim \frac{d\sigma}{d\varphi} f(E_d) \left( \frac{\partial E_n}{\partial E_d} \right)^{-1} \quad (4.4)$$

We now define two variables:  $\sigma_n$ , the total cross-section of deuterium-deuterium fusion into a neutron, and  $\sigma_{\text{tot}}$ , the total cross-section of all possible interactions. It turns out that  $\sigma_{\text{tot}} \gg \sigma_n$  due to Rutherford scattering. Therefore, we say that probability of a neutron being produced per interaction is given by  $p = \frac{\sigma_n}{\sigma_{\text{tot}}}$ . We say that the number of interactions is approximately given by the energy lost,  $E_l$ , divided by the average interaction energy,  $W$ . We define  $W$  in terms of the stopping power such that  $W = \frac{dE/dx(E_d) \cdot M}{\sigma_{\text{tot}} N_a}$ , where  $N_a$  is Avogadro's number and  $M$  is the molar mass of TiD<sub>2</sub>.

Therefore, we approximate the probability that the incoming deuteron fuses with a deuteron in the target after  $i = \frac{E_l}{W}$  interactions is given by Eqn. 4.5.

$$f(E_l) \sim \left( 1 - \frac{\sigma_n}{\sigma_{\text{tot}}} \right)^i = \left( 1 - \frac{\sigma_n}{\sigma_{\text{tot}}} \right)^{E_l \cdot \frac{\sigma_{\text{tot}} N_a}{dE/dx(E_d) \cdot M}} \quad (4.5)$$

This expression for the distribution of the energy lost by the incoming deuteron can be rearranged into a more convenient form.

$$f(E_l) \sim \left[ \left( 1 - \frac{1}{\frac{\sigma_{\text{tot}}}{\sigma_n}} \right)^{\frac{\sigma_{\text{tot}}}{\sigma_n}} \right]^{E_l \cdot \frac{\sigma_n N_a}{dE/dx(E_d) \cdot M}} \approx e^{-E_l \cdot \frac{\sigma_n N_a}{dE/dx(E_d) \cdot M}} \quad (4.6)$$

With an approximate distribution for the energy loss, and therefore the deuteron energy during the fusion interaction, we can simulate our expected angular distribution [74, 131]. The angular distribution assuming an incoming deuteron energy of 80 keV is shown in Fig. 4.11.

#### 4.1.2.2 Neutron Yield

While ultimately we did not include the neutron rate in our analysis of the yields, we did characterize the neutron generator to ensure that it was operating as expected. Ref. [131], following the analysis from Ref. [132], shows that the flux of neutrons generated should increase approximately exponentially with the high voltage used to

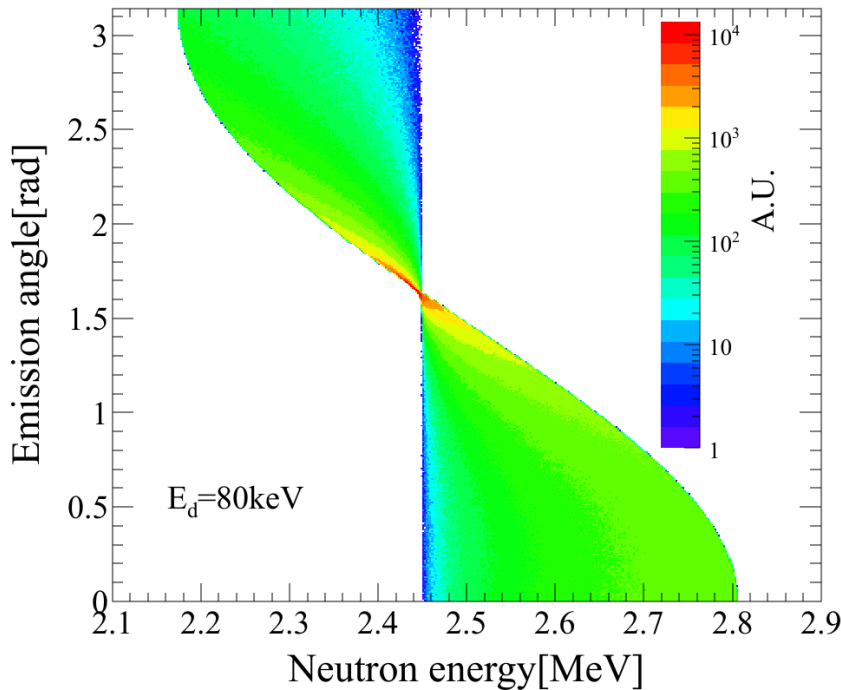


Figure 4.11: The expected angular distribution of neutrons as a function of emission angle for a maximum deuteron energy of 80 keV.

accelerate the ionized deuterium atoms and molecules and linearly with the deuterium ion beam current. We assume that these two effects are uncorrelated and therefore the neutron production rate can be written as  $\frac{dN}{dt} = f(I)g(V)$  where  $f(I)$  describes the rate's dependence on the beam current and  $g(V)$  describes the rate's dependence on the high voltage.

The neutron flux of the minitron neutron generator was measured using a Nuclear Research Corporation NP-2 portable neutron monitor [133]. The NP-2 neutron monitor uses a  $\text{BF}_3$  target housed inside of a polyethylene moderator that attenuates the fast neutrons such that they can be counted. The detector measures in units of dose rate which can be converted to flux by means of the fluence per unit dose equivalent of 2.45 MeV neutrons. As mentioned, we approximated that the current and high voltage could be treated separately and measured the change in one while holding the other fixed to characterize the neutron flux. For the measurement, the NP-2 detector was placed 180 cm away from the neutron generator (inside of its case) and at an

## 4. MEASURING THE LOW ENERGY LIGHT AND CHARGE YIELD OF NUCLEAR RECOILS IN LIQUID XENON

---

angle of  $\frac{\pi}{2}$  relative to the minitron. The rate measurements were then used to fit rate as a function of beam current and voltage (shown in Fig. 4.12). Using these functions, we can then predict the neutron flux of the minitron, as shown in Fig. 4.13.

### 4.1.3 Liquid Scintillators

In theory, any detector of ionizing radiation could act as the secondary detector in a nuclear recoil calibration. In practice, however, the gamma ray background rate is large enough in a laboratory setting that detectors with high levels of discrimination are needed to differentiate neutrons from background in the secondary detector.

For this measurement, the M510 detectors from Eljen Technologies were used. The M510 detector is filled with the liquid scintillator EJ301, chosen for its excellent pulse shape discrimination properties. The EJ301 compound has three characteristic decay times: 3.16, 32.3, and 270 ns [127, 134]. The first two states are related to the excitation of electrons to the singlet and triplet state, respectively, while the slowest decay time is from the delayed fluorescence of the triplet state [135]. Nuclear recoils in the liquid scintillator will exhibit much longer decay times than electronic recoils caused by gamma rays.

An initial characterization of the liquid scintillators was performed to determine the optimal voltage and integration window for nuclear and electronic recoil discrimination and calibrations were performed several times over the course of the run to ensure performance was still adequate. An example of the pulse discrimination from one the M510 detectors from coincidence data is shown in Fig. 4.14. Similar to Ref. [131], we set a threshold in the detectors' pulse size where discrimination is poor - however this was done via the hardware trigger and not a software cut to reduce data intake.

A fifth and smaller version of the M510 detector was placed 180 cm away from the neutron generator to monitor the minitron rate at all times.

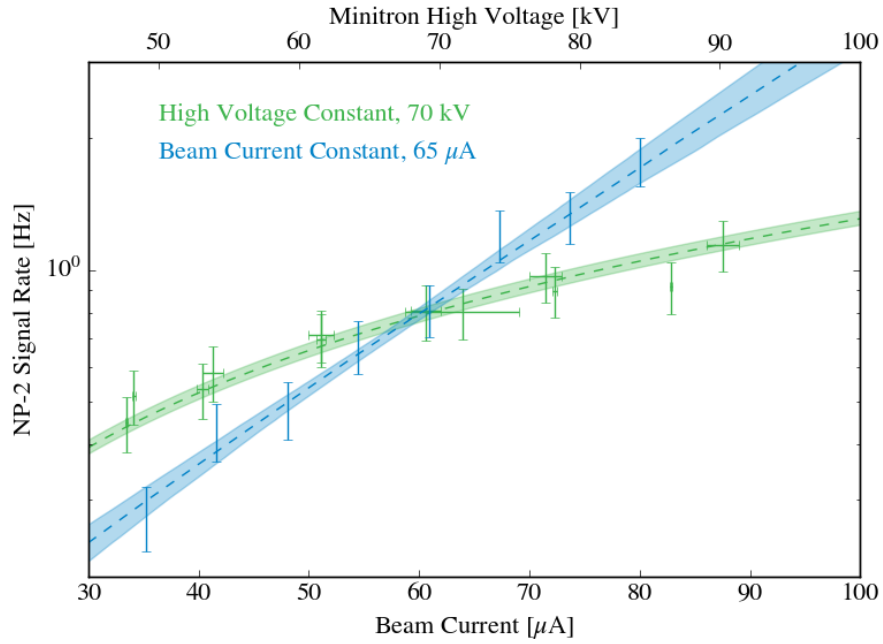


Figure 4.12: The NP-2 neutron detector signal rate as a function of beam current, holding the high voltage fixed, and high voltage, holding the beam current fixed. Shaded regions represents 68% credible region while dotted lines show the best fits.

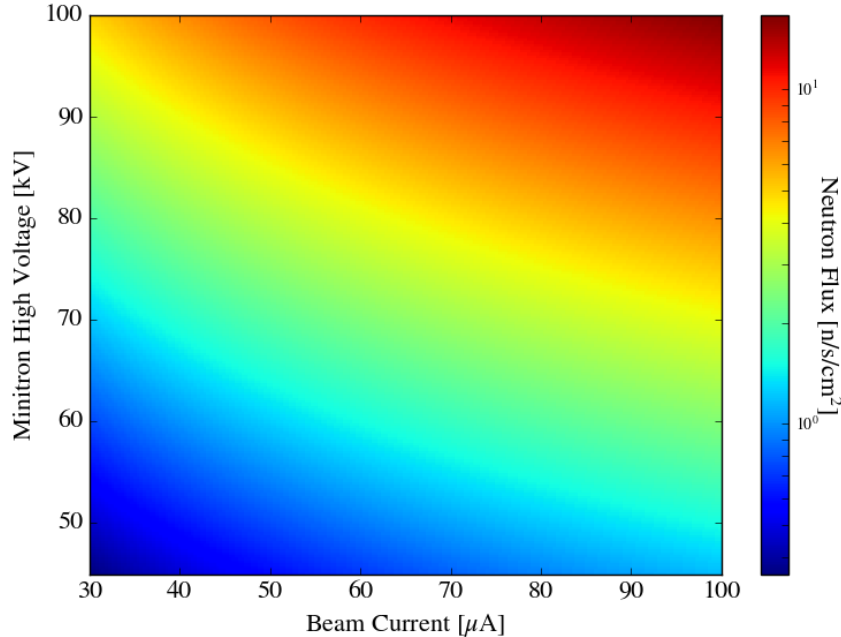


Figure 4.13: The expected neutron flux from the minitron neutron generator at a distance of 180 cm at an angle of  $\frac{\pi}{2}$ .

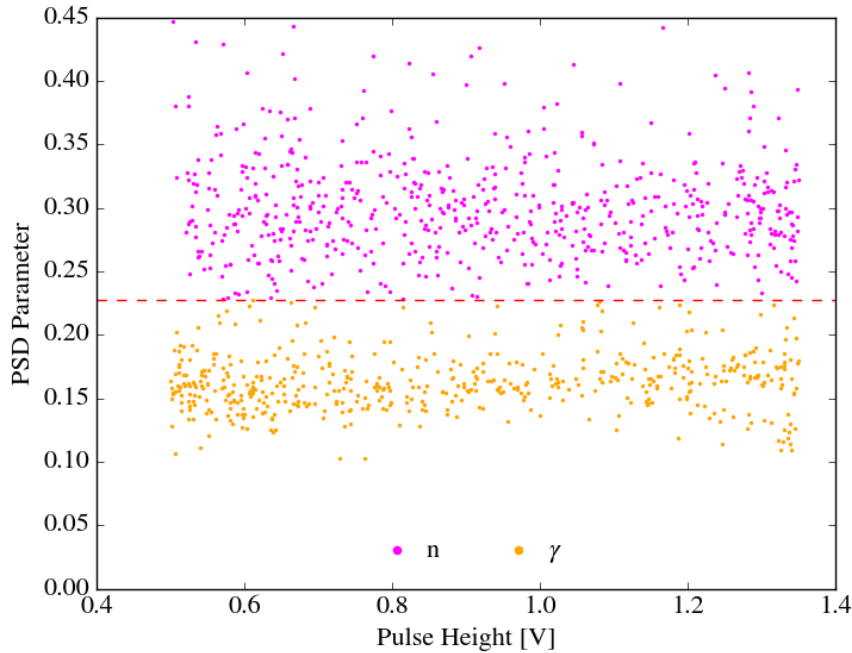


Figure 4.14: Discrimination space for one of the four M510 detectors from coincidence data. Notice that a hardware cut is made via a threshold discriminator at approximately 500 mV in order to remove events with poor pulse shape discrimination.

#### 4.1.4 Data Acquisition System

A schematic of each of these triggers is shown in Fig. 4.15 and the details of each are given below.

The data acquisition system for this measurement is identical to the one described in Ref. [91]. The system consisted of three 14-bit flash ADCs (model v1724 from CAEN) at 100 MS/s with 40 MHz bandwidth. When a trigger pulse was received by the VME crate controller, this memory would be written to the disk of our data acquisition server. The data acquisition server used was synchronized to a storage and processing server where data could be further analyzed.

All of the top signals are fed directly into 10x amplifiers which are then immediately fed into digitizer channels. The bottom PMT signal is the only channel used to form the trigger since it sees the majority of the light in the detector. The bottom PMT's signal is fed into a CAEN voltage divider. One of these two signals is sent directly to the digitizer unamplified (to avoid digitizer saturation in large S2 signals)

while the other copy of the signal is sent to a 10x amplifier where two copies are made. One of these two copies is sent directly to the digitizer while the other is sent to an updating threshold discriminator. This updating threshold discriminator produces a NIM pulse for as long as the signal is above the set threshold (5.16 mV for this measurement) making the width in time of the NIM pulse approximately the same as the width of the true signal. The output from the updating threshold discriminator is considered to be our S1 trigger.

The S1 trigger is used as the main building block for the S2 trigger. The S1 trigger is sent into a logic fan. One copy from the logic fan is sent to a variable width gate generator (set at 400 ns for this measurement) while the other is sent into a 24 ns delay. The gate generator produces a  $\overline{\text{NIM}}$  pulse that is combined in a logical AND with the delayed S1 trigger. In this way, only S1 triggers wider than the gate will cause a new trigger<sup>5</sup>. If the logical AND results in a pulse this is considered an S2 trigger (S2 pulses in general are much wider than S1 pulses). The width of the S2 trigger pulse is set to be 29.5  $\mu\text{s}$  for reasons that will be explained shortly.

This S2 trigger is passed into a logical fan where three copies are made. One is sent into a gate generator that produces a 100  $\mu\text{s}$   $\overline{\text{NIM}}$  pulse. The  $\overline{\text{NIM}}$  pulse is combined with another copy of the S2 trigger in a logical AND. Since there is no delay on the S2 pulse, the original S2 trigger will result in an output pulse however S2s occurring after the current S2 and before the end of the  $\overline{\text{NIM}}$  pulse will not produce an output pulse based on the logical AND. This therefore limits the maximum rate of triggers to one over the gate width (although typical data acquisition rates are < 100 Hz). The output signal from this logical AND is called the S2 hold-off trigger.

Four M510 detectors were used simultaneously such that two energy spectra could be measured at a time. Since the rate of signals in the liquid scintillators was low relative to the TPC, it was decided to use a single digitizer channel to capture all of the EJ pulses via multiplexing. The signals from the PMTs in the M510 detectors were first sent to a 10x amplifier where two amplified copies were produced. The first copy of the M510 signals was sent into a linear fan. The second copy of each of

---

<sup>5</sup>The delay is needed because the gate takes approximately 10 ns to create.

## 4. MEASURING THE LOW ENERGY LIGHT AND CHARGE YIELD OF NUCLEAR RECOILS IN LIQUID XENON

---

amplified M510 signals went to a threshold discriminator. The threshold was decided on a detector-by-detector basis such that signal sizes were eliminated where we had little discrimination power between nuclear and electronic recoils. Two copies of the output from the threshold discriminator were created. The first copy of each signal was sent into a delay generator that delays the logic pulse by a time unique to each detector (for example, one of the M510s' triggers was delayed by  $6\ \mu\text{s}$  while another was delayed by  $7\ \mu\text{s}$ ). The delayed triggers are then sent into the same linear fan as the original pulses. In this way, the processor can determine which M510 detector the signal came from based on where the M510 trigger is found in the waveform.

As was mentioned, the threshold discriminator for the M510 detectors creates two copies of each trigger. The second copy of these triggers is sent into a logical OR to produce a single logic signal. This logic signal is then delayed  $28\ \mu\text{s}$  and combined in a logical AND with the  $29\ \mu\text{s}$  S2 gate. The output of the logical AND forms our coincidence trigger. The long delay and gate may seem unnecessary at first but are actually needed since the M510 signal is very close in time to the S1 and not the S2. This means that the S2 signal can occur tens of  $\mu\text{s}$  after the M510 trigger is created. Therefore, by creating a gate on the S2 and delaying the M510 trigger we ensure that we will not lose any good events due to the electron drift time in the TPC.

## 4.2 Characterization and Calibration of neriX

As mentioned in chapters two and three, the process from energy deposition to the S1 and S2 signal read out of a waveform for analysis can essentially be broken down into two subsections: the signal production and the detector physics. If we want to measure the physics of the signal production mechanism, we must be able to decouple the detector physics. To do this, we must make independent measurements to characterize the detector as best as we can.

While many of the properties of the detector we are trying to characterize are the same as XENON1T, there are some differences in how we carry out the measurements simply due to the scale of XENON1T relative to neriX.

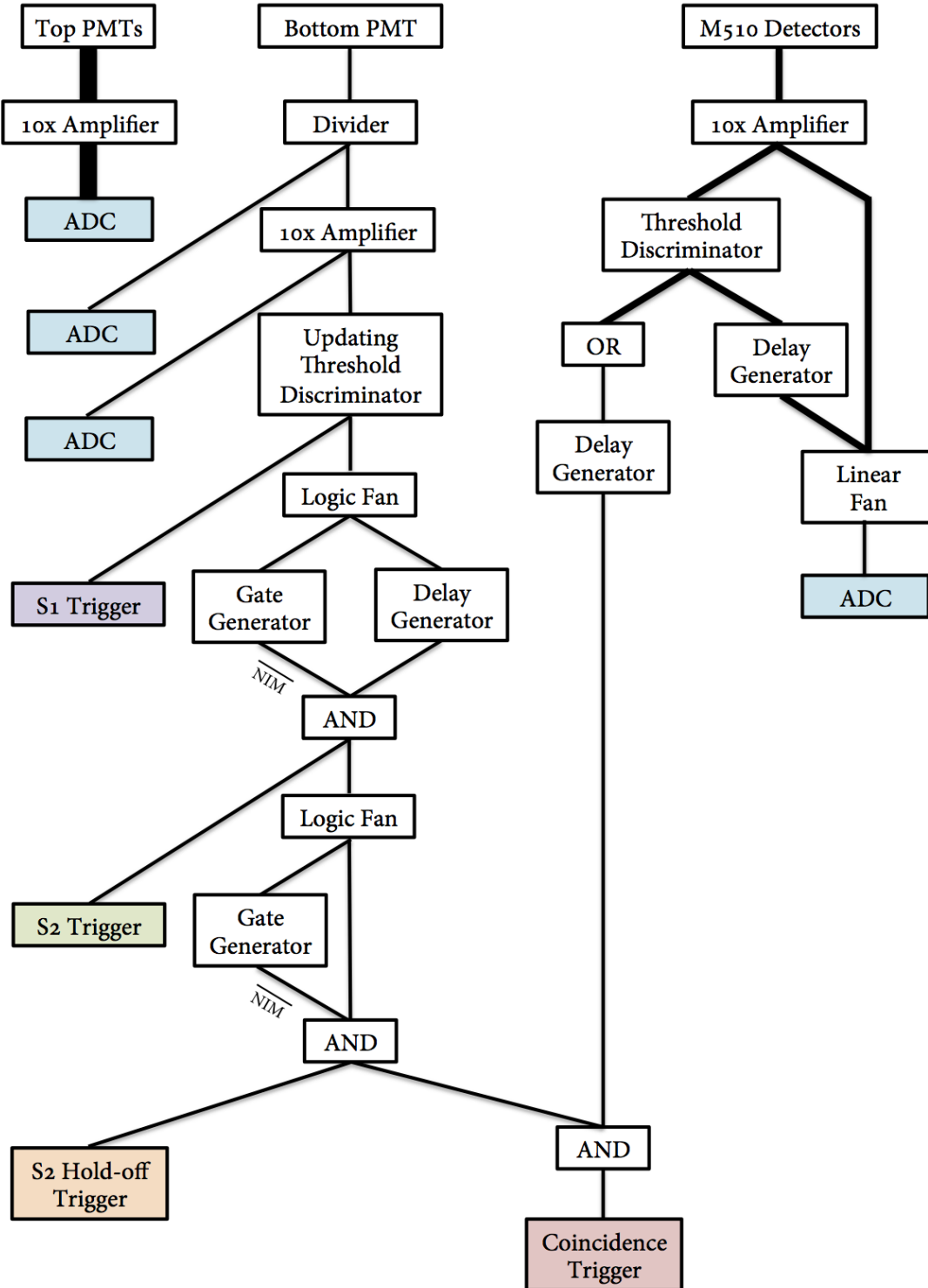


Figure 4.15: The trigger schematic for the neriX nuclear recoil measurement. For details on the triggers please refer to the text in Sec. 4.1.4.

### 4.2.1 PMT Characterization

As in XENON1T, the most basic task in characterizing the TPC is the PMT calibration. The goal of the PMT calibration is to understand the response of a PMT to incident photons. This task is typically performed by examining the response of the PMT to a single photoelectron (single electron ejected at the photocathode as the result of an incident photon) since larger signals can be estimated via the convolution of multiple single photoelectron response functions. Ideally, we would like to completely understand the shape of the response function of the PMT but at the same time, most experiments settle for the mean and variance of the response (since by the central limit theorem these will describe the response for large numbers of photons).

As in XENON1T, the low light calibration of PMTs is performed using a blue LED pulse generated by a digital pulse generator (BNC PB-5) and fed into the detector via a fiber optic cable. The standard way of calibrating a PMT in this type of experiment is to use a low light level (such that the given PMT only sees a signal 5–10% of the time) and either fit the data using a Gaussian model of the response or extract the mean and variance according to the statistical treatment in Ref. [113]. However, neither of these was satisfactory: the former was not satisfactory as it resulted in an unphysical signal for the PMT response approximately 15% of the time (since the Gaussian distribution is not bounded below by zero) and therefore has a large potential for bias and the latter was not satisfactory given that we could not guarantee identical operating conditions between the background-only data and pulser data, a required condition for the statistical approach. Therefore, a new model was developed by the author, called the *cascade model*, which tries to simulate the actual physics of a PMT including the underamplification of electrons and its dynode structure [136]. This model is discussed in further detail in App. B and uses a GPU-based analysis framework, like the measurement of the light and charge yield in neriX (the focus of this chapter) and the electronic and nuclear recoil calibration of XENON1T (discussed in Sec. 3.4), that will be discussed in App. A. Unlike the other two calibration methods, it is actually more effective to use a higher light level such

that 1–2 photoelectrons are seen on average<sup>6</sup>. A sample low-light spectrum is shown in Fig. 4.16 along with the best fits and 68% credible regions of both the Gaussian and cascade models. From this spectrum alone, it does not appear that the cascade model is a significant improvement but if one looks at Fig. 4.17, which shows the full-amplification SPE spectrum for both models, one can see the reason why the Gaussian model is not acceptable: it results in a negative signal a non-negligible fraction of the time.

Unlike Ref. [91], no gain instability was seen during this measurement in neriX.

To avoid issues of saturation with the PMTs, nuclear recoil data was taken with PMT gains ranging from  $5 - 10 \cdot 10^5 e^-$  while electronic recoil data where our concern was the full absorption peak (like the anticorrelation analysis in Sec. 4.2.4) was taken with gains two orders of magnitude smaller. Even using our GPU-based cascade model it is extremely difficult to fit such a small PMT response. Therefore, we used what is referred to in Ref. [129] as the MPE method. To use the MPE method you must first calibrate the response of the PMT at its normal operating voltage. Following a standard calibration, you illuminate the same PMT at the same voltage with a high light level and use the gain found from before to estimate the mean number of photoelectrons. You then reduce the PMT voltage and remeasure the response of the PMT to the high light level. Since the mean number of photoelectrons observed should be independent of voltage, you can use the response at the lower voltage and high light level to extract the gain of the PMT at a much lower voltage.

When measuring this effect, we varied the bottom PMT voltage from 800 V, our standard operating voltage, down to 500 V. At approximately 600 V, saturation effects in the 662 keV peak were no longer present. Ideally, one would expect the gain to decrease exponentially with voltage, however we noticed a significant deviation from this behavior. We believe that this deviation is due in part to the decreasing collection efficiency of photoelectrons of the PMT at lower voltages, an effect described in Ref. [137]. While the voltage dependence of the effect is PMT dependent,

---

<sup>6</sup>This does not affect the assumption that the number of photoelectrons seen follows a Poisson distribution that is standard in these types of measurements.

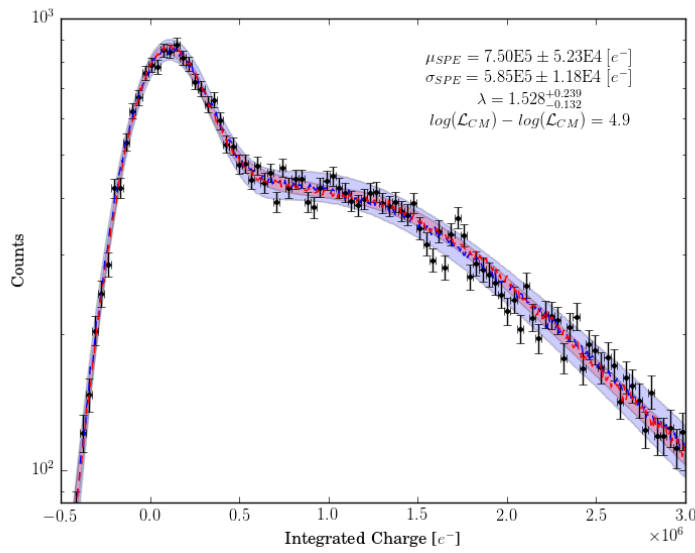


Figure 4.16: The fit of the cascade (blue) and Gaussian (red) single photoelectron response model for the bottom PMT at 800 V. The statistics shown are for the cascade model which results in a marginally better fit as can be seen from the log likelihood difference. The dotted lines shown are the best fits and the shaded region is the 68% credible region.

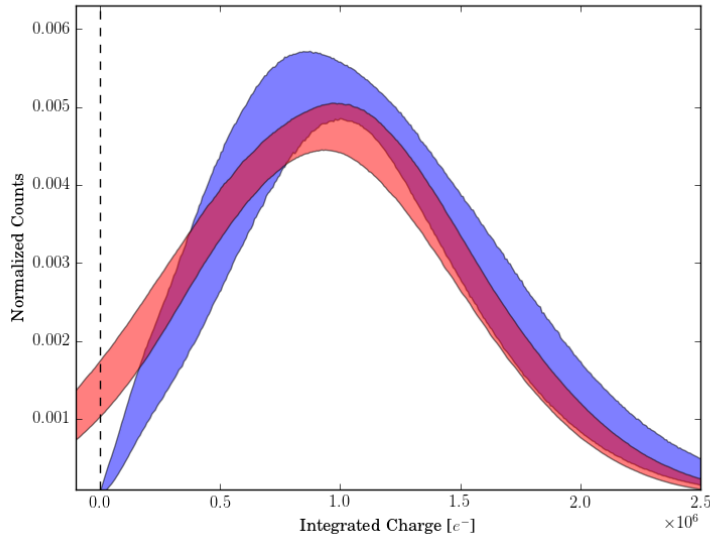


Figure 4.17: The 68% credible region for the single photoelectron response for fully-amplified electrons for the bottom PMT at 800 V. Notice that the Gaussian model (red) results in a non-physical response a non-negligible fraction of the time while the cascade model (blue) does not exhibit this behavior.

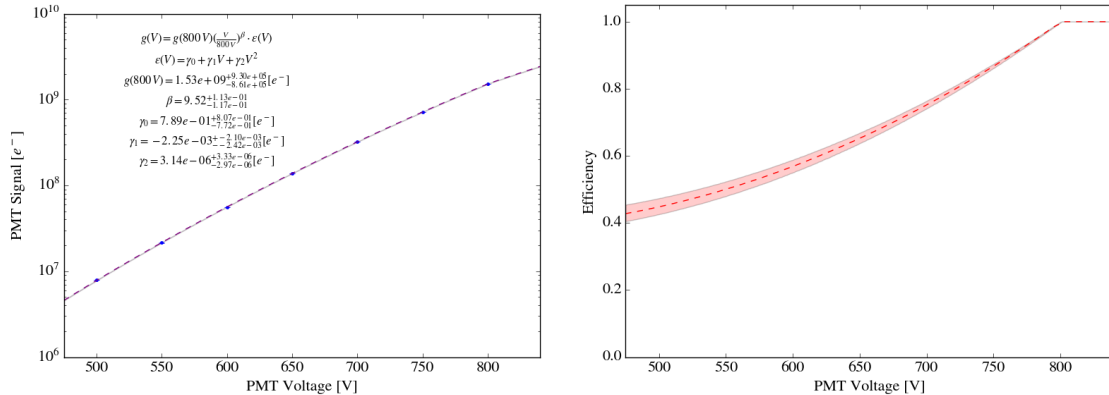


Figure 4.18: On the left is the neriX MPE spectrum for the bottom PMT including the collection efficiency function shown on the right.

we multiplied our power law by a generic second-order polynomial efficiency function in an attempt to describe it. The best fit of both the gain and collection efficiency are shown in Fig. 4.18.

### 4.2.2 Position Reconstruction and Position Dependence

Position reconstruction also plays an important role in neriX. While position reconstruction is not used to remove background events, a fiducial volume is still set to avoid edge effects from field non-uniformity and electrons capturing on the teflon. Additionally, we do expect a small amount of position dependence for both the S1 and S2.

To determine the transverse position of the event, we again use the S2 signal seen by the top PMTs. The four PMTs in the top array actually have four individual anodes that are essentially treated as separate channels — this means that our four multianode PMTs act as sixteen single anode PMT channels. While obviously our position reconstruction in the transverse position will be significantly more limited than XENON1T due to the prevalence of edge effects in the small detector and the limited number of pixels, however we can use a neural network trained on an optical simulation of photons produced in between the anode and the gate to estimate the position. The transverse positions of high-energy ( $> 40$  PE) nuclear recoils, which

#### 4. MEASURING THE LOW ENERGY LIGHT AND CHARGE YIELD OF NUCLEAR RECOILS IN LIQUID XENON

---

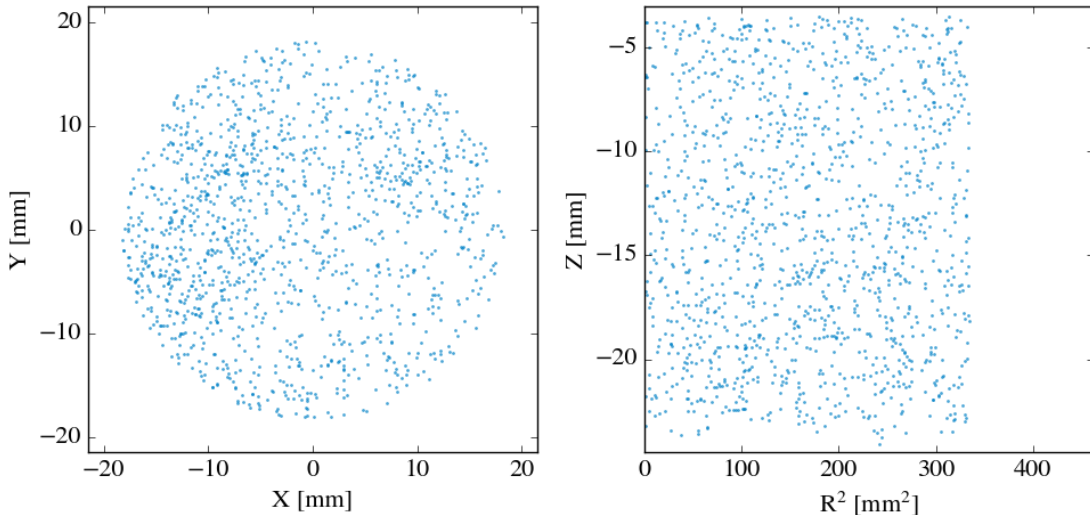


Figure 4.19: The spatial distributions of high-energy nuclear recoil events taken at 490 V/cm after fiducial volume and other quality cuts.

should be approximately uniformly distributed in the TPC, at a field of 490 V/cm is shown in the left panel of Fig. 4.19. The small defects in the position reconstruction are likely due to discrepancies in the unmeasured collection efficiencies of the individual PMT channels.

To determine the depth of the interaction, we look at the time between the S1 and S2, also referred to as the *drift time*. Since the electrons will drift through the liquid xenon at a fixed velocity, this time difference can be used to measure the depth. The drift velocity in liquid xenon will change as a function of the electric field applied so the drift velocity must be measured for each field used.

To measure the drift velocity, one uses the fact that the scintillation light produced from interactions in the liquid xenon can actually interact with the meshes, releasing electrons in the process. These photoionization electrons can be seen following large S1s and S2s in waveforms. Therefore, if one looks at the timing of small S2 signals following a large S1 or S2, one will actually see peaks in the spectrum due to these photoionization electrons, as shown in Fig. 4.20. By examining the time distance between the two peaks, we can determine the drift velocity since the distance between the meshes at liquid xenon temperatures is known (23.4 mm).

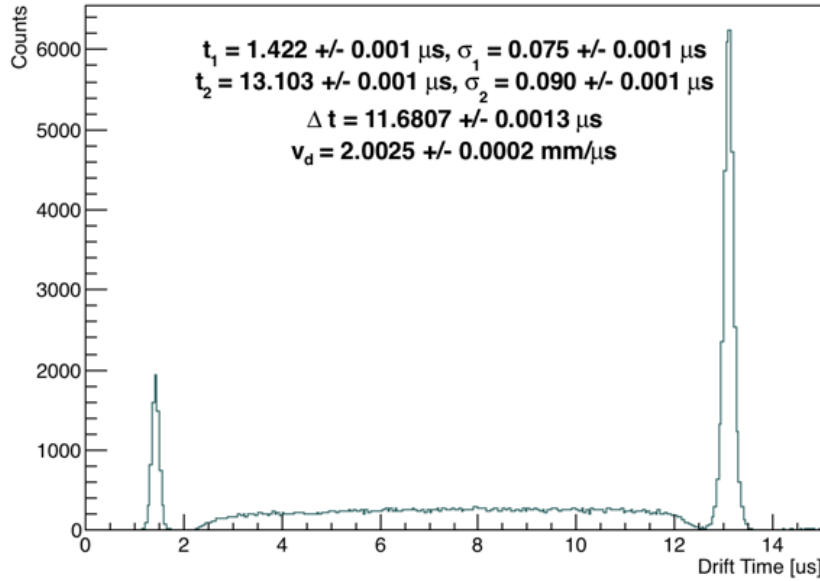


Figure 4.20: The distribution of small S2s in time after a large S2 at a field of 1020 kV/cm. Notice the two sharply spike peaks around 1.5 and 13  $\mu\text{s}$  — these peaks are due to electrons from the photoionization of the gate and cathode mesh, repectively. Since we know the distance between these two meshes we can measure the drift velocity at this field.

The drift velocities during this measurement and during the low-energy measurement of the yields of electronic recoils [91] are shown in Tab. 4.2. One can see that the drift velocities of all three runs in the detector agree very well with each other (within a few percent).

While due to the small size of the detector we do not observe a radial dependence of the S1 and S2 signals, we do observe effects due to the depth of the interaction

Drift Field	190 V/cm	490 V/cm	1020 V/cm
	$v_d$ [mm/ $\mu\text{s}$ ]		
ER Run 1	1.51	1.72	1.96
ER Run 2	1.54	1.75	1.97
This Work	1.56	1.77	2.00

Table 4.2: The measured drift velocities at 190, 490, and 1020 V/cm in neriX for the measurement of the yields of electronic recoils [91] and this work.

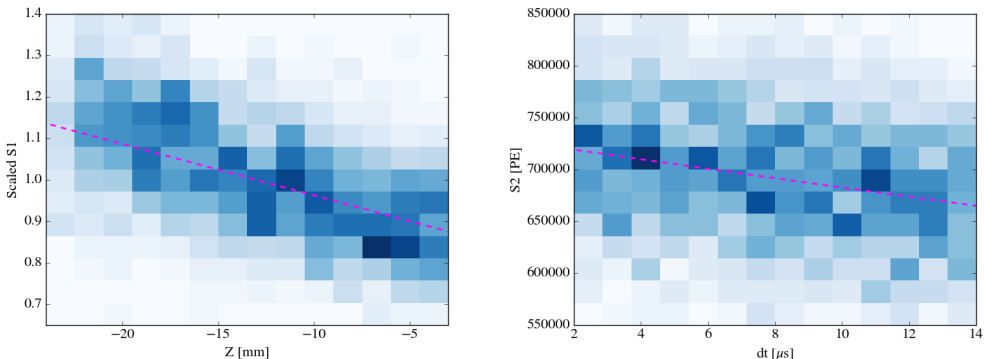


Figure 4.21: The depth correction of the S1 (left) and S2 (right) signals as a function of depth in the detector.

in the detector. The former effect is caused by the proximity of the interaction to the bottom PMT while the latter effect is caused by electrons drifting to the surface attaching to electronegative impurities. For more details on each of these effects, please refer to Sec. 3.3.3.1 and Sec. 3.3.3.3, respectively. While not as drastic as the effects in XENON1T, these effects are still on the order of 10–20% for S1s and 5% for S2s. To perform the correction, we use events from the 662 keV peak from  $^{137}\text{Cs}$  and fit the S1 and S2 size as a function of depth. As expected, we observe the same pattern as XENON1T: events closer to the bottom PMT have larger S1s than those events closer to the liquid-gas interface and events from lower in the detector are more likely to lose charge to impurities in the liquid xenon. Both of these effects can be seen in Fig. 4.21. Due to a getter failure, the purification system utilized a getter much further in distance compared to the one used in Ref. [91], leading to a non-negligible electron lifetime. Both of these effects were monitored over the course of the run and since no discernable time dependence was seen, a run average was taken.

### 4.2.3 Single Electron Response

One very important quantity for TPCs that was discussed in chapters two and three is the single electron response (also known as the gas gain). The single electron response measures how many photoelectrons we expect in our PMTs if a single electron is

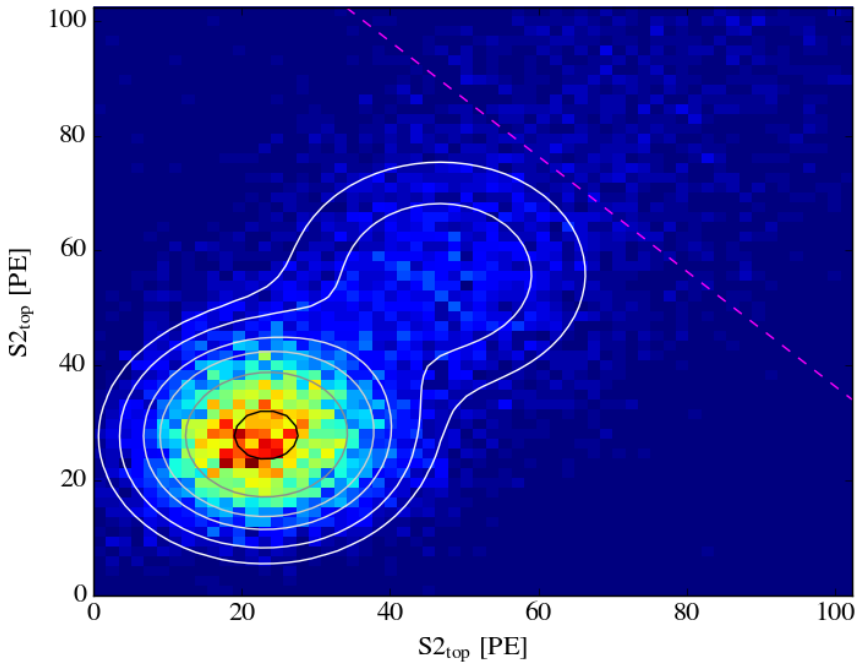


Figure 4.22: The single electron response as measured by the top and bottom PMTs in neriX. Note that the response, even for a single electron, appears to follow a Gaussian distribution. The contours show the outline of the fit and the pink line represents the edge of the fit range.

extracted from the liquid into the gas. Typically the response is approximated as a Gaussian distribution with a mean,  $\mu_G$ , and width,  $\sigma_G$ . While technically this quantity could be field-dependent due to leakage from the cathode, simulations show that this effect is only on the order of  $\sim 2\%$  [129].

We used a source of single electrons already discussed for this calibration: single electrons from the photoionization of the gate. By using these, we could make a strict time cut rather than search an entire waveform for single electrons which reduces the potential noise. Even though only the bottom PMT was used for all analyses, the single electron response was fit in two dimensions for extra discrimination power between single and double electron peaks. A sample fit is shown in Fig. 4.22. The response of the TPC to single electrons was assumed to be normal for both the top and the bottom PMTs with no correlation. As in Ref. [98] and Ref. [91], a roll-off was applied at low S2s to represent the loss due to the S2 peak finding efficiency.

## 4. MEASURING THE LOW ENERGY LIGHT AND CHARGE YIELD OF NUCLEAR RECOILS IN LIQUID XENON

---

As with the position correction, no clear time dependence was observed for the single electron response so both the mean and width of the distribution were averaged over the course of the run for all fields.

### 4.2.4 Anticorrelation

As discussed in Sec. 2.3.2 and Sec. 3.3.5, due to the lack of quenching factors in electronic recoils the energy of an interaction and the number of photons and free electrons produced are inextricably linked. This relationship is shown in Eqn. 4.7 where  $N_q$  is the number of quanta,  $E_{\text{ER}}$  is the energy of the electronic recoil,  $W$  is the average energy required to produce an exciton or electron-ion pair ( $13.7 \pm 0.2$  eV [79]),  $N_\gamma$  is the number of photons produced in the electronic recoil, and  $N_e$  is the number of free electrons extracted from the interaction site.

$$N_q = \frac{E_{\text{ER}}}{W} = N_\gamma + N_e \quad (4.7)$$

In the same way as Sec. 3.3.5, we can put this equation in terms of detector variables including our observables, S1 and S2, the average light collection efficiency,  $g_1$ , the extraction efficiency,  $\eta$ , and the mean single electron gain,  $G$ , as shown in Eqn. 4.8.

$$\frac{E_{\text{ER}}}{W} = \frac{S1}{g_1} + \frac{S2}{G\eta} \quad (4.8)$$

This implies that if we have a sample of S1 and S2 signals from a known monoenergetic peak that we can extract the otherwise very difficult to measure quantities  $g_1$  and  $\eta$ . This type of anticorrelation measurement is typically performed using a single full absorption peak at multiple electric fields (typically done in smaller detectors where the field can be changed easily) or using multiple full absorption peaks from different sources at a single electric field (typically done in larger detectors where electric fields are more difficult to manage and change large amounts). The latter is done in LUX [138] and XENON1T [48]. For neriX, we decided to vary both to make the measurement as robust as possible: two sources,  $^{137}\text{Cs}$  and  $^{22}\text{Na}$ , were used to ex-

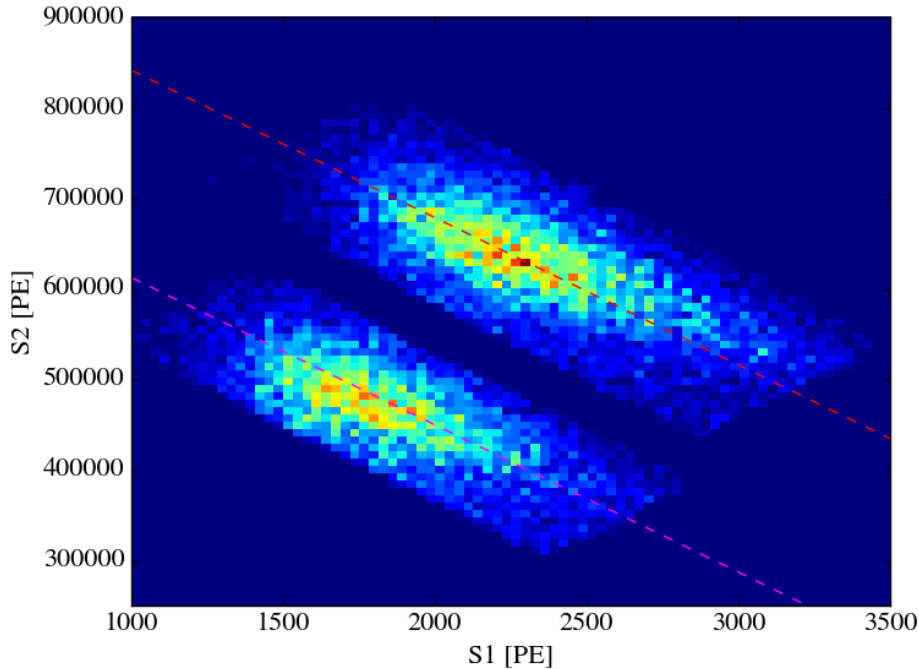


Figure 4.23: Anticorrelation analysis performed on the full absorption peaks  $^{137}\text{Cs}$  and  $^{22}\text{Na}$  at five different electric fields. One can also see the best fit of the model shown overlayed.

tract monoenergetic events at five different fields. These events are fit simultaneously to Eqn. 4.9 where  $E_{\text{ER}}$  is equal to 662 keV for  $^{137}\text{Cs}$  and 511 keV for  $^{22}\text{Na}$ .

$$\frac{\text{S2}}{E_{\text{ER}}} = \frac{G\eta}{g_1} \frac{\text{S1}}{E_{\text{ER}}} - \frac{G\eta}{W} \quad (4.9)$$

A sample fit is shown in Fig. 4.23. No discernable time dependence in the parameters was found and thus a run average was used to describe  $g_1$  and  $\eta$ .

### 4.2.5 Trigger Efficiency

As discussed in previous chapters the charge yield of nuclear recoils is significantly lower than an equivalent electronic recoil. Therefore, it is crucial to estimate the efficiency of the trigger as a function of S2 size. As discussed in Sec. 4.1.4, the S2 trigger is actually based on the width of the event however we will use the total S2 size (area) as a proxy to estimate the efficiency.

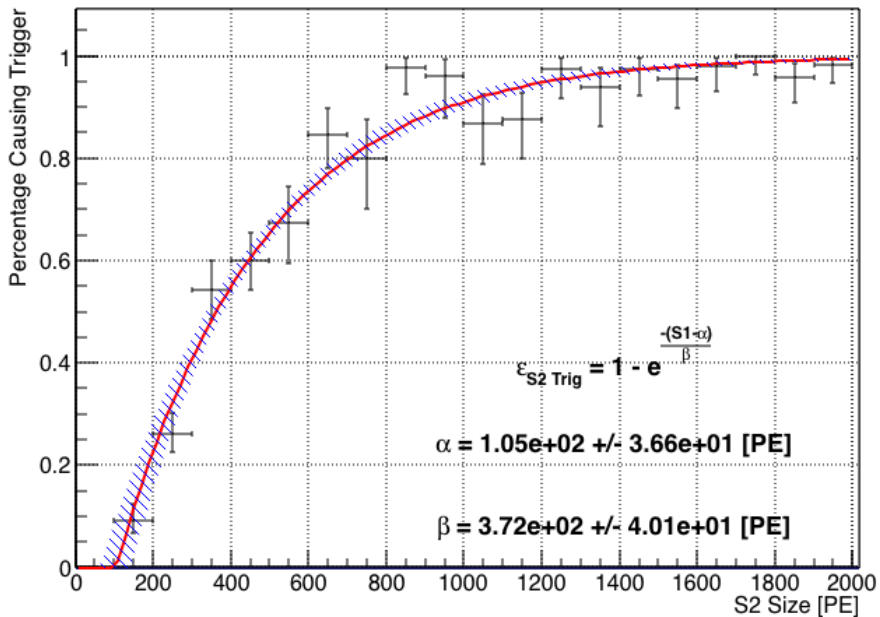


Figure 4.24: The neriX trigger efficiency as measured using a random trigger. Shown overlaid are the best fit alongside the 68% credible region.

The measurement of the trigger efficiency is quite simple. Rather than using the S2 trigger to record events, as is standard for almost all other TPC calibrations, we use a random trigger and digitize the S2 trigger while irradiating the detector with a  $^{22}\text{Na}$  source. In this way, we can check each waveform for an S2 and whether or not an S2 trigger was present. The random trigger ensures that we in no way bias our measurement of the trigger efficiency by requiring that an S2 be present in the waveform. While this does eliminate the bias, the measurement is very inefficient in terms of storage since many saved waveforms do not contain relevant data. While ideally one would measure the S2 trigger efficiency regularly, collecting sufficient statistics took approximately three weeks and therefore regular calibrations were impractical.

Once sufficient statistics were collected, one could use large S2 events to find the standard time difference between the S2 peak and the S2 trigger. With our trigger system, the time difference between the two was 600–800 ns. With this time cut in place, we could then look at smaller S2 events and determine whether or not a trigger was present. The results of the measurement are shown in Fig. 4.24.

### 4.2.6 Peak Finding Efficiency

The second efficiency loss in this measurement is actually on the software side of the analysis. Once raw data is saved, it is analyzed in a processor where important information is extracted such as the S1 and S2 sizes and locations in the waveform. While the peak-finding algorithm used to identify S1s and S2s in the waveform is excellent at finding even single electrons (as shown in the single electron response calibration), there is some loss for very small S1 signals.

Unlike the trigger efficiency, the peak finder's efficiency was not measured directly. Instead a realistic waveform simulator was developed to study this efficiency loss. This waveform simulator included effects such as the characteristic pulse shape of the PMT, the noise level in the TPC, and the shape of the S1 signal due to the excimer decay times [63]. The waveform simulator was then used to produce events with S1s of known sizes which were then fed into the data processor. Post-processing, we could then check how many of the S1s in a given range were discovered by the peak finder. The results of the waveform simulation are shown in Fig. 4.25.

## 4.3 Nuclear Recoil Data Collection

The data taking run of neriX lasted for approximately four and a half months. We began collecting coincidence data on March 30, 2016 and completed taking coincidence data on July 4, 2016. Calibrations and trigger efficiency measurements continued until August 9, 2016 when a power failure occurred overnight resulting in a pressure spike in which xenon was safely released into the pressure relief vessel via the solenoid valve discussed in Sec. 4.1.1.4.

With a total of four M510 liquid scintillator detectors, we were able to measure two scattering angles, and hence energy spectra, simultaneously. In total, six scattering angles were measured at three different electric fields. Ultimately, data at the lowest and highest energy were not used: the former due to lack of statistics due the efficiency losses discussed in Sec. 4.2.5 and Sec. 4.2.6 and the latter due the poor data quality (likely due to the M510 detectors' proximity to the TPC). On average, it took

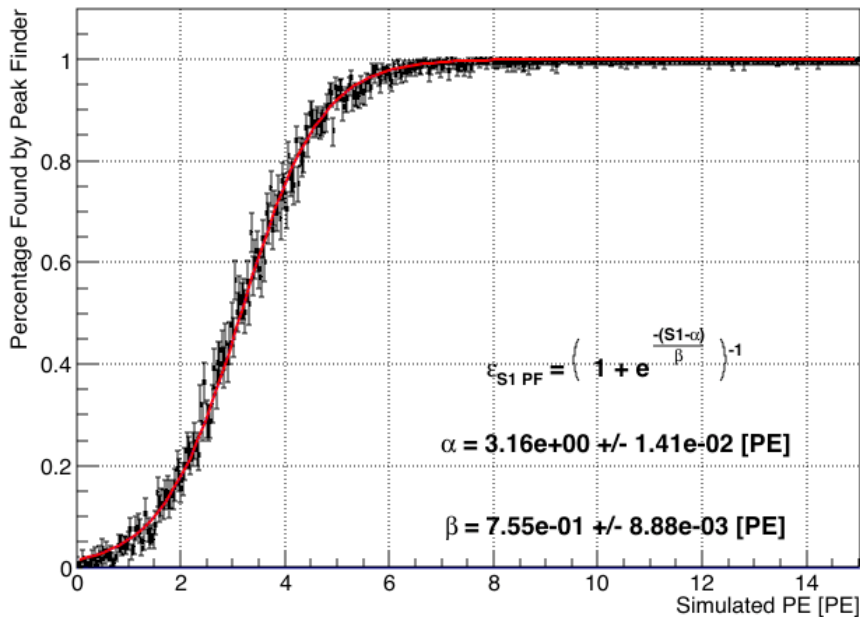


Figure 4.25: The neriX peak finding efficiency from empirically based waveform simulations.

approximately two weeks to measure two energy setups at a given cathode voltage.

As discussed in Sec. 4.1, we use the positions of the M510 liquid scintillator detectors to restrict the energy spectrum such that it is peaked around a specific energy and does not follow the standard exponentially falling energy spectrum for nuclear recoils in liquid xenon. The positions of the detectors (and the minitron) were set using an auto-levelling laser mounted on a tripod. Positions were measured relative to the center of the TPC and marked on the laboratory floor using tape. The positions of the M510 detectors were chosen such that an energy resolution of 15–25% was achieved. Tab. 4.3 shows the positions of the M510 detectors relative to the TPC center<sup>7</sup>. The estimated uncertainty in each dimension is 3 mm.

In addition to coincidence data, nuclear recoil data is taken without the coincidence requirement which we refer to as *band data*. This merely involves replacing the coincidence trigger described in Sec. 4.1.4 with the S2 hold-off trigger.

A few basic cuts were made to clean the data taken. The fiducial volume cut

---

<sup>7</sup>The minitron was placed at (0, -43.0, 0) cm in the coordinate frame as defined in Tab. 4.3.

$\theta$	Energy [keV]	M510 1 Position [cm]			M510 2 Position [cm]		
		x	y	z	x	y	z
30°	4.95 ± 0.83	38.1	66.4	-4.6	-38.3	66.4	0
35°	6.60 ± 1.52	24.3	34.2	0	-23.9	34.2	-4.6
45°	10.62 ± 1.54	-41.4	41.7	-4.6	41.7	41.7	0
53°	13.95 ± 2.46	29.5	22.3	0	-29.5	22.3	0

Table 4.3: The positions of the M510 liquid scintillator detectors during coincidence data taking. The energies and corresponding widths shown are found via a detailed Monte Carlo produced in Geant4 which will be discussed further in Sec. 4.4.1.

was made to ensure the electric field variations were limited to within 20% and an asymmetry cut, which removes events based on what fraction of the S1 and S2 signals are seen by the top versus bottom PMTs, is made to ensure the removal of noisy events. For coincidence data, two additional cuts are made based off of the liquid scintillators. The first selects neutrons in the M510 detectors using the pulse-shape discrimination of the EJ301 liquid scintillator. The second is a coarse time of flight cut, made using the time difference from the waveform, to ensure that the S1 signal discovered by the peak finder is within 100 ns of the liquid scintillator pulse to remove as many accidental coincidences as possible. A finer time of flight cut could not be made with a time to amplitude converter (TAC) since our average light collection efficiency is lower than the single phase liquid xenon detectors used to measure the light yield of nuclear recoils in the past [126, 128, 139]<sup>8</sup> and therefore we could not, with high efficiency, use the S1 signal to start the TAC.

For all data collected, no discernable differences were seen between the individual M510 detectors. Therefore, all distributions used in the analysis used data from both of the liquid scintillators. The resulting spectra are shown as a function of both S1 and S2 in Fig. 4.26, Fig. 4.27, Fig. 4.28, and Fig. 4.29.

<sup>8</sup>Technically, Manzur *et al.* used a dual phase detector operated in a “single phase” mode which drastically increased their average light collection efficiency.

#### 4. MEASURING THE LOW ENERGY LIGHT AND CHARGE YIELD OF NUCLEAR RECOILS IN LIQUID XENON

---

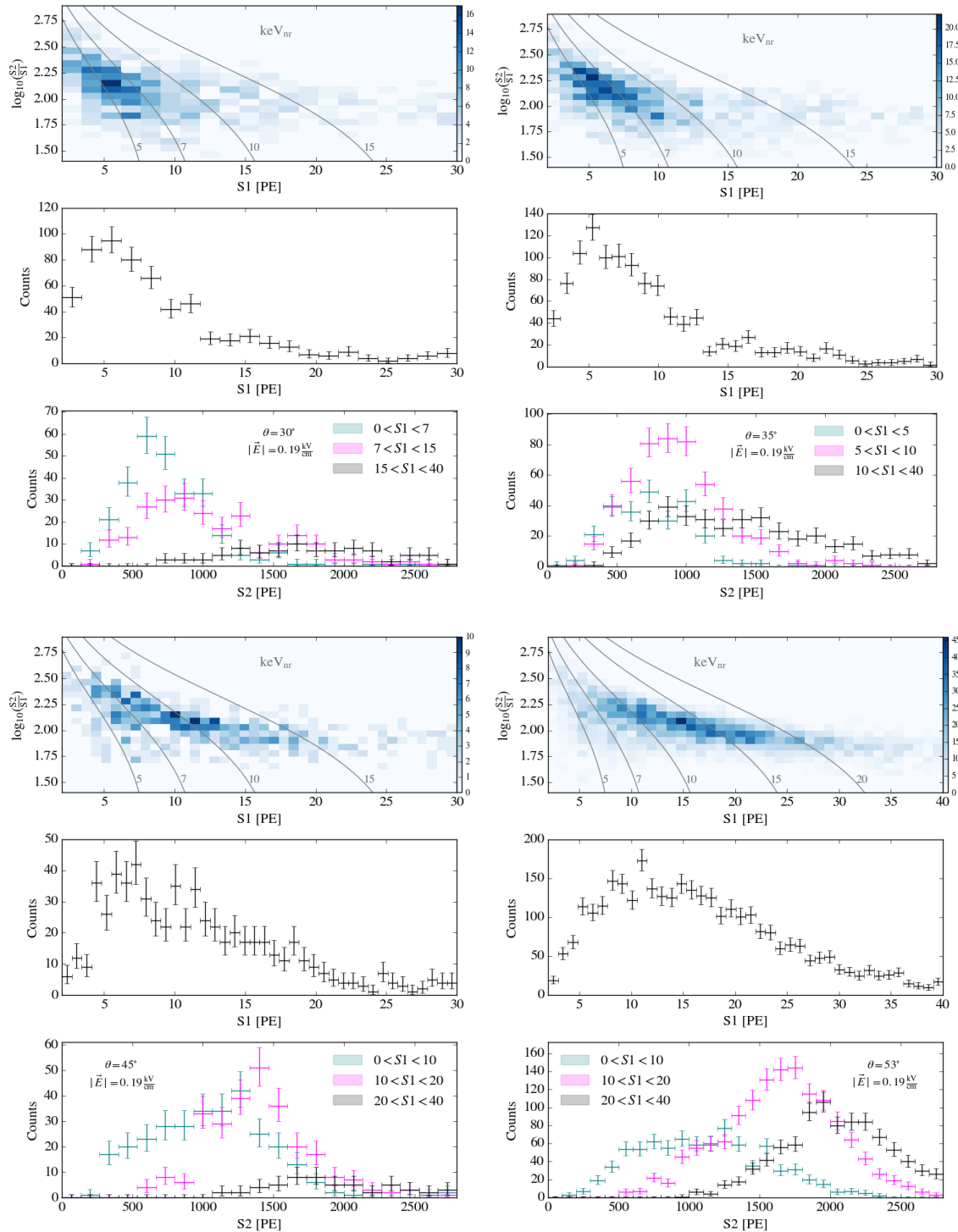


Figure 4.26: Coincidence data taken with a drift field of 190 V/cm.

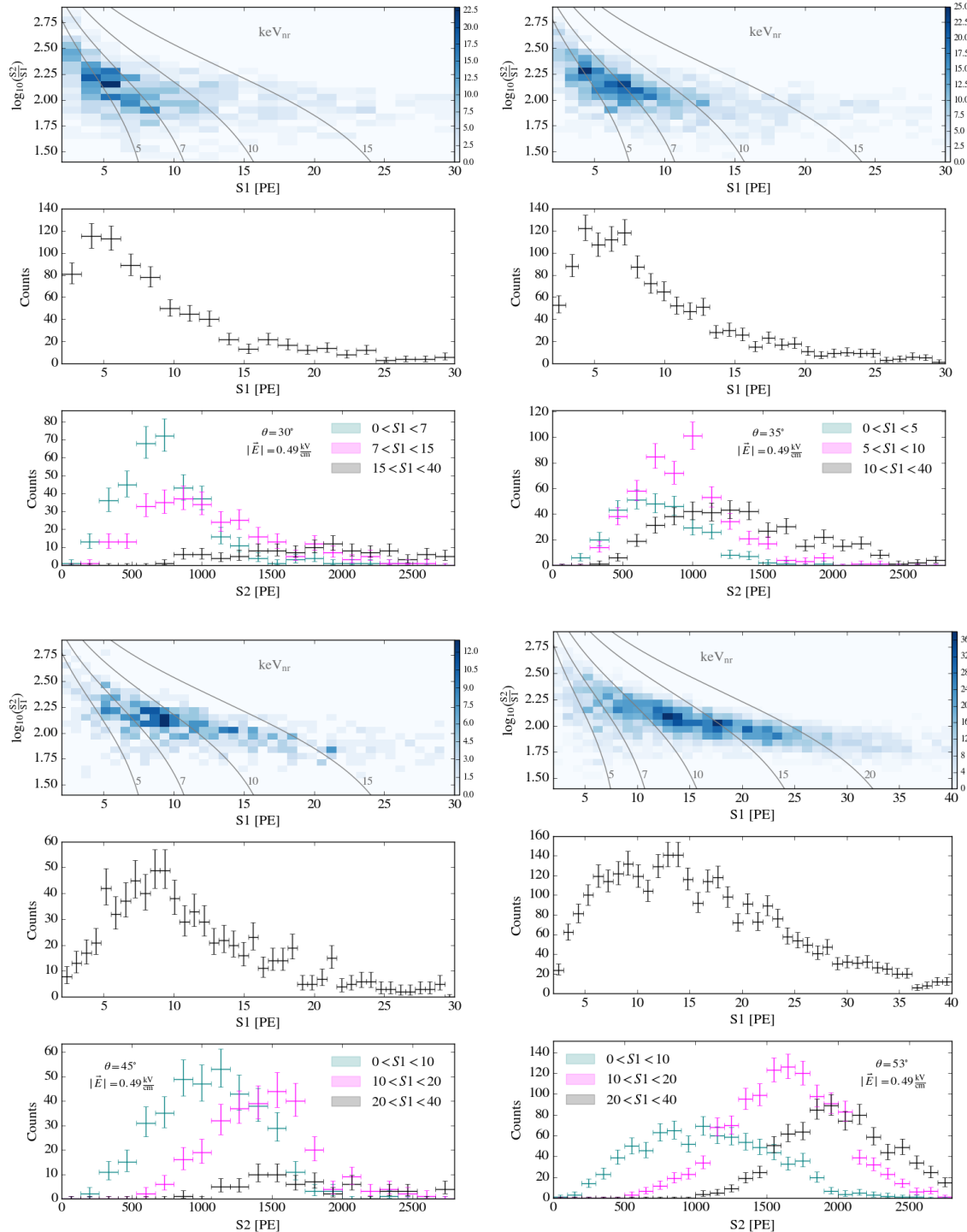


Figure 4.27: Coincidence data taken with a drift field of 490 V/cm.

#### 4. MEASURING THE LOW ENERGY LIGHT AND CHARGE YIELD OF NUCLEAR RECOILS IN LIQUID XENON

---

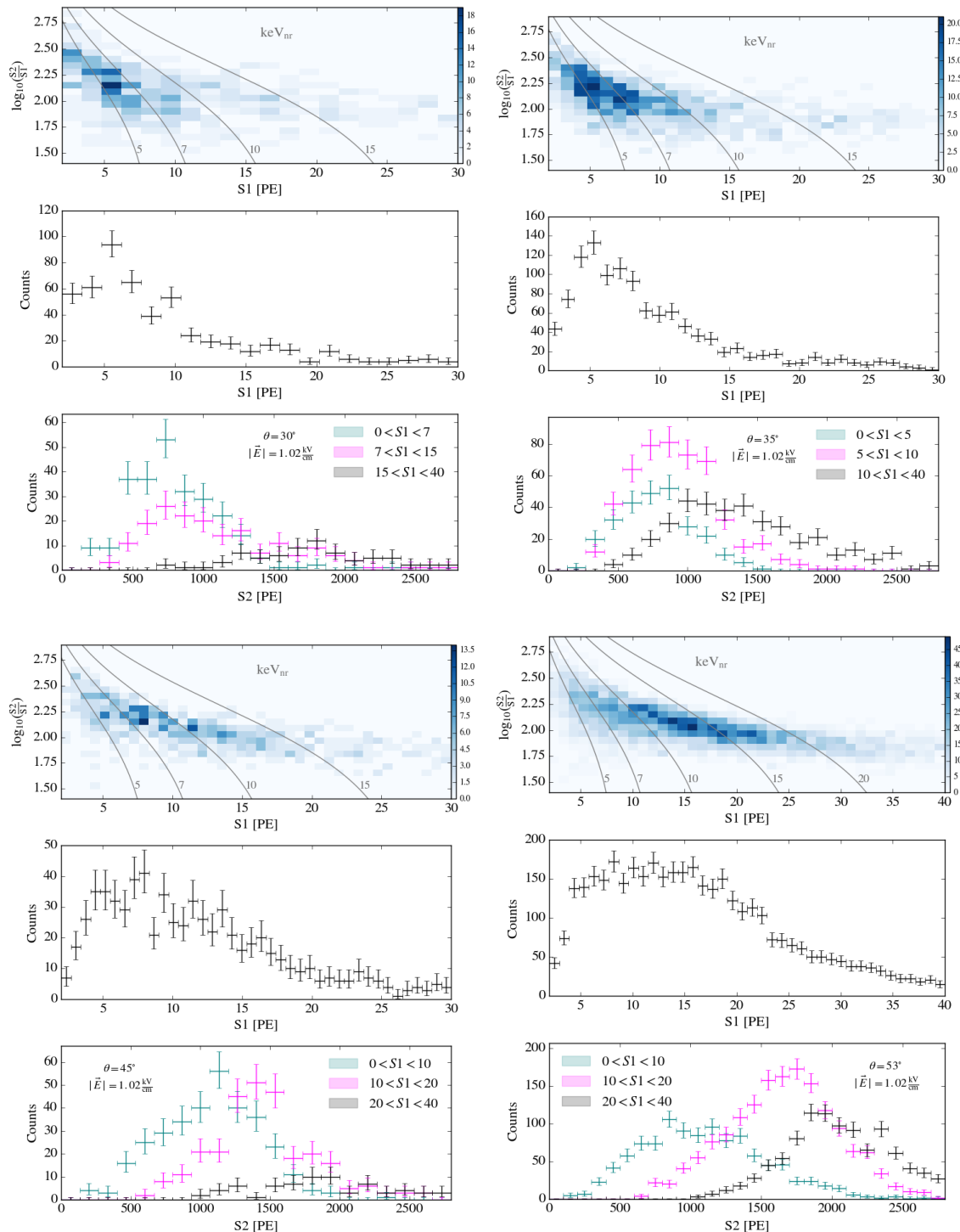


Figure 4.28: Coincidence data taken with a drift field of 1020 V/cm.

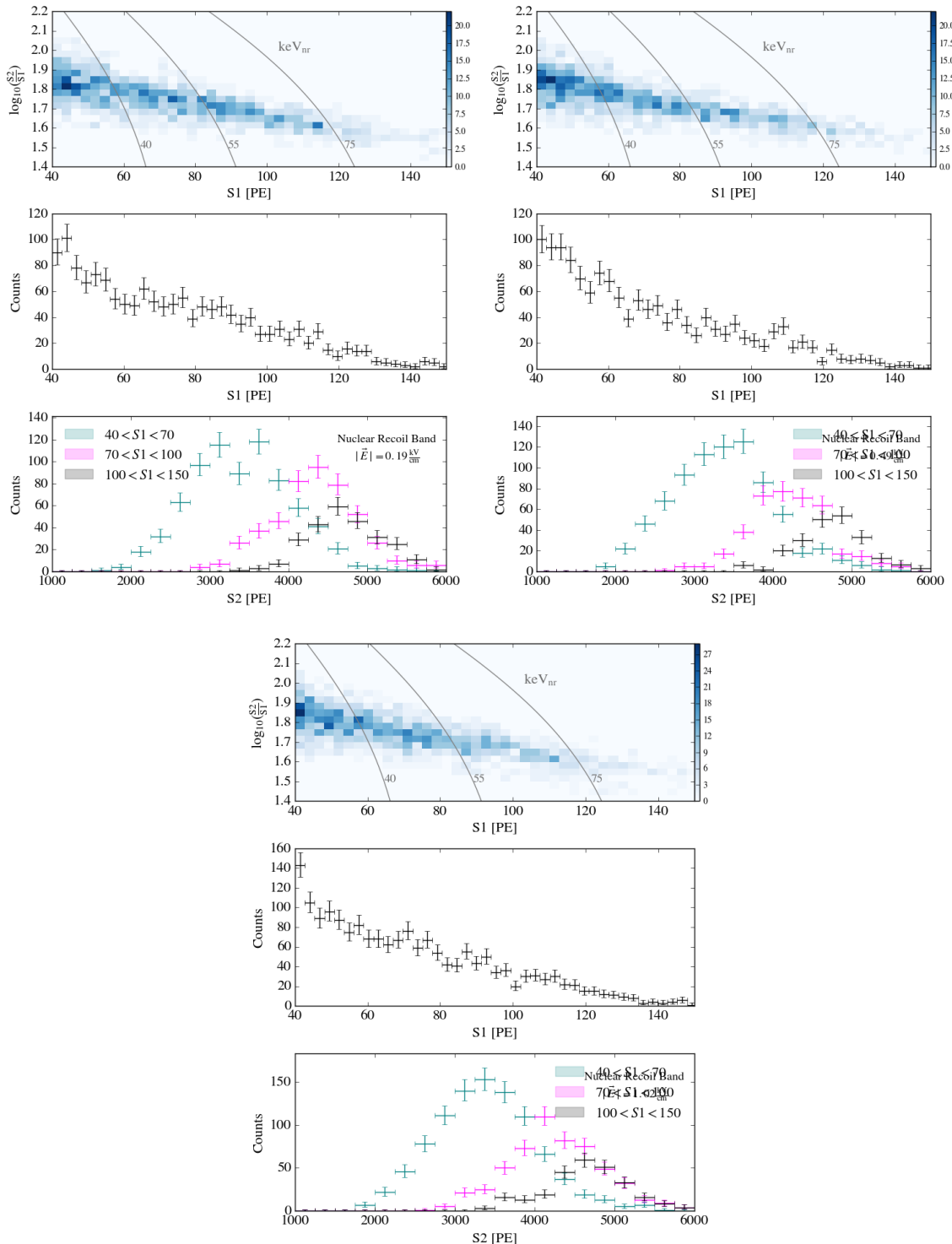


Figure 4.29: High energy nuclear recoil band data without a coincidence trigger at the three fields measured.

## 4.4 Analysis of Nuclear Recoils in Liquid Xenon

As it was stated at the beginning of this chapter, multiple measurements of the response of liquid xenon to nuclear recoils have been made. However, these previous measurements assumed a simple LXe physics models because they were limited to a single observable<sup>9</sup>: for each coincidence dataset a single parameter,  $\mathcal{L}_{eff}(E_{NR}) = L_y(E_{NR})/L_y(E_{ER} = 122 \text{ keV})$  or  $Q_y(E_{NR})$ , was used to map the energy to a one-dimensional observable space (S1 or S2) and a generic resolution was applied to account for the widening of the spectrum due to statistical fluctuations in the LXe microphysical process described in Sec. 2.4.2.

While this analysis approach has proved effective, it does have a few underlying issues. First, this procedure fails to account for correlations between the light and charge that is expected since it only looks at a single observable at a time and therefore we cannot build an effective model for the microphysics of liquid xenon. Second, the procedure itself is slightly inconsistent — the same energies in different coincidence spectra have different  $\mathcal{L}_{eff}$  applied to them. Finally, since we are measuring low energies, applying a large smearing term can potentially bias the measurements of the yields at energies close to the efficiency roll-offs. While the second and third issues can be reduced and carefully controlled, the inability to produce an effective two dimensional observables production model has impacts on the WIMP search, as we saw in Sec. 3.5.

In this work, a completely new procedure for analyzing nuclear recoil data in xenon was developed. This procedure was the basis for both the electronic and nuclear recoil calibration of XENON1T (Sec. 3.4) and the basic framework can be used for all different types of analyses, including the characterization of PMTs which is discussed in App. B. This framework, which used GPUs to run a fast Monte Carlo of the model given the parameters under test for likelihood calculations during parameter estimation, allowed us to test and measure light and charge production models for the response of liquid xenon to nuclear recoils for the first time.

---

<sup>9</sup>In some cases, data for both observables was taken but the analysis used only a single observable at a time.

As the procedure followed in Sec. 3.4 was based off of this work, many aspects will be similar. Therefore, special attention will be specifically devoted to the differences between the two.

#### 4.4.1 Monte Carlo Simulation of Energy Spectra

As mentioned during the discussion of the XENON1T nuclear recoil calibration, the first step is to predict the energy spectra you expect to measure. Even though the energy of the recoil is completely determined by the angle of the scatter, effects from the finite sizes of the detector, nuclear recoils in materials other than the fiducial volume, and accidental coincidences will make the spectra far from monoenergetic. Therefore, it is necessary to build a detailed Monte Carlo to predict the rate of nuclear recoils at different energies given the experimental setup.

The detailed Monte Carlo for this measurement was done in Geant4 [101]. The Monte Carlo is built with a realistic description of the neutron generator and its casing and stand, the TPC and the cryostat, the detector support frame, the laboratory floor (for neutron reflections), as well as the measured positions of the M510 liquid scintillator detectors listed in Tab. 4.3. Also included in the simulation is the neutron yield as a function of emission angle (shown in Fig. 4.11).

The Geant4 simulation records the track of each particle which includes information about each of the interactions it makes, where they occur, and at what time. For coincidence data, we are particularly interested in neutrons that elastically scatter in the liquid xenon and the M510 liquid scintillator detectors within a time window defined by our time of flight cut in the data. For nuclear recoil band data, we only place the condition that a neutron elastically scatters a single time in the fiducial volume with no other requirements. We cannot require that the neutron does not interact in other materials since this type of cut can, of course, not be made in measured data. The expected energy spectra for coincidence data and nuclear recoil data without a coincidence requirement are shown in Fig. 4.30.

There are two striking features of each of the coincidence spectra. The first is the Gaussian-looking peak around a mean energy — this peak is due to the exact

## 4. MEASURING THE LOW ENERGY LIGHT AND CHARGE YIELD OF NUCLEAR RECOILS IN LIQUID XENON

---

events we are trying to measure: a single elastic scatter in the liquid xenon and a scatter in the M510 detector. The width of the peak is almost completely due to the finite sizes of the detector. The second feature is the near exponential roll-off in energy. This is due to neutrons that scatter in other materials as well as in the fiducial volume of the TPC. The energy spectrum expected from nuclear recoils without any coincidence trigger is similar to the expected distribution of events for XENON1T with one critical exception. In XENON1T, we used an americium-beryllium (AmBe source) that radiates neutrons with energies up to 11 MeV. The minitron neutron generator, on the other hand, produces near monoenergetic neutrons at an angle of 90° to the target meaning that our TPC is irradiated with neutrons with an energy very close to 2.45 MeV (for the neutron yield as a function of angle for the minitron please refer to Fig. 4.11). This implies that there is a maximum energy that can be transferred to a xenon nucleus from neutrons back-scattering. This maximum energy transfer for 2.45 MeV neutrons on xenon nuclei ranges from 72 to 76 keV depending on which isotope of xenon the neutron interacts with. This roll-off can clearly be seen in the band energy spectra in Fig. 4.30 but is not present in the spectra from AmBe shown in Fig. 3.28.

### 4.4.2 Light and Charge Production for Nuclear Recoils

As discussed in Sec. 2.4.2, recoiling nuclei lose energy via atomic motion that cannot be detected in neriX or other dual-phase TPCs. We model this loss using Lindhard theory, which gives the energy lost to atomic motion as a function of energy. This is shown in Eqn. 4.10 in terms of the dimensionless energy  $\epsilon$ .

$$\begin{aligned}\epsilon &= 11.5 \left( \frac{E}{\text{keV}} \right) Z^{-7/3}, \\ L(\epsilon) &= \frac{kg(\epsilon)}{1 + kg(\epsilon)}, \quad g(\epsilon) = 3\epsilon^{0.15} + 0.7\epsilon^{0.6} + \epsilon\end{aligned}\tag{4.10}$$

The Lindhard factor,  $L$ , is then used to approximate the number of quanta as shown in Eqn. 4.11.

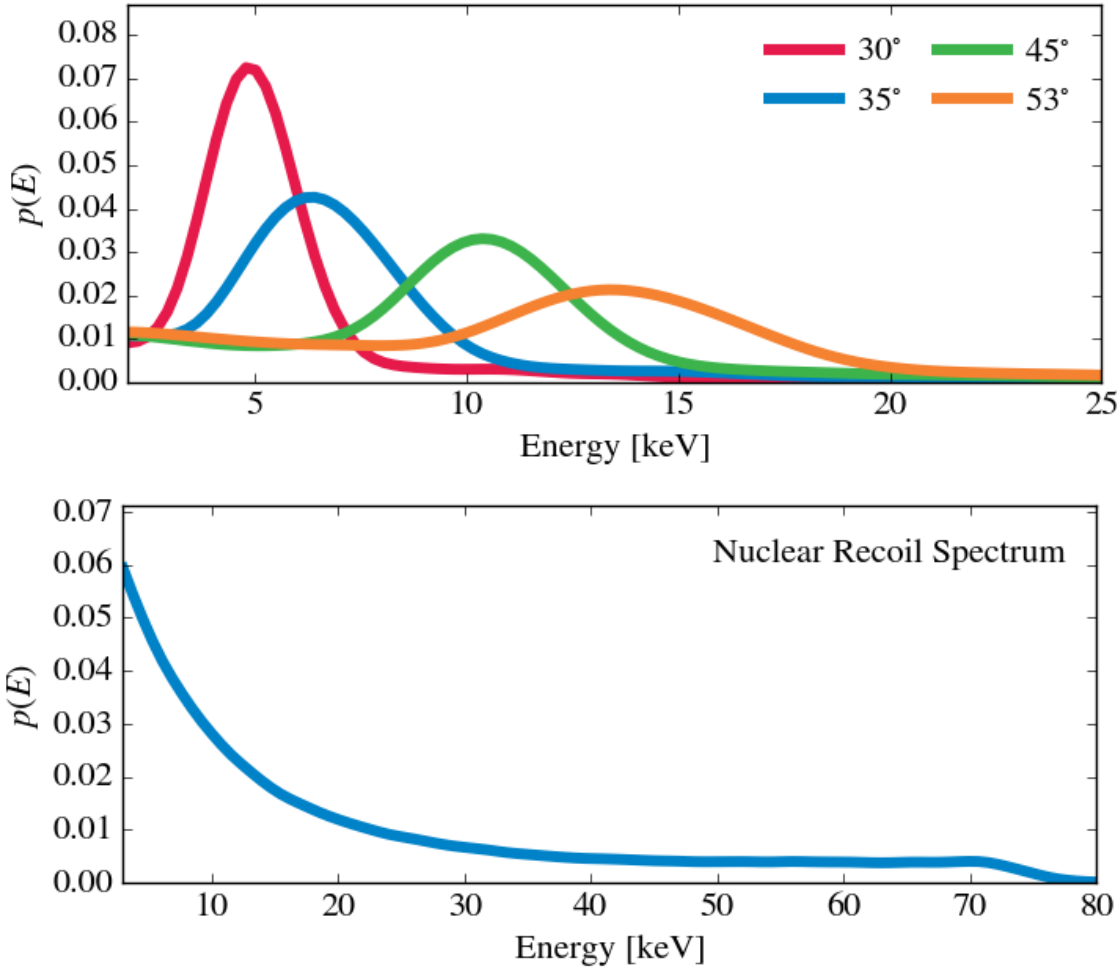


Figure 4.30: The expected energy spectra for coincidence data (top) and nuclear recoil band data (bottom). Both of these are used as inputs for the fast Monte Carlo used to estimate the PDF given assumptions on parameters in the signal response model.

$$N_q \sim P \left( \mu = \frac{E \cdot L}{W} \right) \quad (4.11)$$

The choice of the Poisson distribution is the same approximation as used in the XENON1T analysis and is not derived from first principles. The actual distribution is likely more complicated due to the complex track structure of nuclear recoils in liquid xenon.

With the total number of excitons and ions produced,  $N_q$ , we can use the exciton-to-ion ratio to simulate the individual numbers of excitons and electron-ion pairs, as

## 4. MEASURING THE LOW ENERGY LIGHT AND CHARGE YIELD OF NUCLEAR RECOILS IN LIQUID XENON

---

shown in Eqn. 4.12.

$$N_{\text{ion}} \sim B \left( N = N_q, p = \frac{1}{1 + \frac{N_{\text{ex}}}{N_{\text{ion}}}} \right), \quad N_{\text{ex}} = N_q - N_{\text{ion}} \quad (4.12)$$

We use the same parameterization as Ref. [86] for the exciton-to-ion ratio except that we do not include field dependence, as shown in Eqn. 4.13. Therefore, three constants for the exciton-to-ion ratio are included in the fit to describe each of the three fields. The energy dependence of the exciton-to-ion ratio, however, is assumed to be the same for all fields.

$$\frac{N_{\text{ex}}}{N_{\text{ion}} F} = \alpha_F (1 - e^{-\beta \epsilon}) \quad (4.13)$$

With the individual numbers of excitons and ions, we now must consider the possibility of electron-ion pairs recombining to form excitons, resulting in a single photon rather than an electron extracted from the site. Unlike the analysis performed for XENON1T which was dependent on Ref. [86] for the model and priors, we can actually test different parts of the light and charge production model in this analysis. One aspect of the model tested was the use of the Thomas-Imel model [83] versus a generic model of recombination. The generic models tested were polynomials of orders one through five (bounded to a range between zero and one) and a Gompertz function [140] with and without a constant offset added. The relative log-likelihoods of the best fits were used to compare the models and it was found that the Thomas-Imel model described the data the best. Therefore, we define the recombination probability as we did previously.

$$r = 1 - \frac{\ln(1 + N_{\text{ion}} \sigma_F)}{N_{\text{ion}} \sigma_F} \quad (4.14)$$

Unlike Ref. [86], though, we do not parameterize the field dependence of  $\sigma$  and instead keep three  $\sigma$  parameters included in the fit: one used at each field. In this way, no assumptions about the field dependence of recombination were made.

The recombination probability was used in the same way as before to simulate

the number of electron-ion pairs that recombine.

$$N_{\text{rec}} \sim B(N = N_{\text{ion}}, p = r), \quad (4.15)$$

$$N_{\text{ion}} \leftarrow N_{\text{ion}} - N_{\text{rec}}, \quad N_{\text{ex}} \leftarrow N_{\text{ex}} + N_{\text{rec}}$$

Finally, we consider biexcitonic quenching, which results from the collision of two excitons. We estimate this quenching using Birk's saturation law, as shown in Eqn. 4.16, since one would expect that the density of excitons in the track is proportional to the electronic stopping power [88–90].

$$f_B = \frac{1}{1 + a \frac{dE}{dx}} = \frac{1}{1 + \eta \epsilon^{-1/2}} \quad (4.16)$$

We choose to follow the treatment of Ref. [124] and fix the energy dependence of the stopping power, as seen in Eqn. 4.16. This is different than the treatment in the XENON1T analysis which was based off of the model in Ref. [86] and was chosen because track simulations see this sort of energy dependence up to a few hundred keV and to prevent the possibility of overfitting at the high-energy end of the nuclear recoil spectrum.

In summary, there are nine free parameters in the liquid xenon model:  $k$ , a constant relating the electronic stopping power to the velocity,  $\alpha_F$ , the exciton-to-ion ratio at each of the three fields,  $\beta$ , the energy dependence of the exciton-to-ion ratio,  $\sigma_F$ , the recombination constant at each of the three fields, and  $\eta$ , Birk's constant for liquid xenon. No priors outside of physical restrictions (all parameters greater than zero) are used.

#### 4.4.3 Detector Model for Signal Production

While the major steps of the detector model are the same as for XENON1T, since the TPCs operate in identical ways, several simplifications to the detector response model could be made such as the exclusion of position corrections.

## 4. MEASURING THE LOW ENERGY LIGHT AND CHARGE YIELD OF NUCLEAR RECOILS IN LIQUID XENON

---

### 4.4.3.1 Detection of Scintillation Photons

To begin the detector physics model, we consider the average light collection efficiency that was measured via the anticorrelation calibration discussed in Sec. 4.2.4. As in the XENON1T model, we also consider double photoelectron emissions [116] since the scintillation light has a wavelength of 178 nm. However, we do not consider effects due to the position of the interaction in the detector. The number of photons producing at least a single photoelectron,  $N_i$ , is simulated by Eqn. 4.17 in the fast Monte Carlo.

$$N_i \sim B\left(N = N_\gamma, p = \frac{g_1}{1 + p_{DPE}}\right), \quad (4.17)$$

With the number of photons causing at least a single photoelectron, we can account for how many photoelectrons were produced in total again using the probability for double photoelectron emission.

$$N_{PE} \sim N_i + B(N = N_i, p = p_{DPE}) \quad (4.18)$$

We now apply a smearing on the size of the S1 PMT signal according to the measured resolution of the bottom PMT of the TPC. Note that we do not use the cascade model to simulate the charge distribution from the PMT due to simulation time constraints and instead approximate the response with a normal distribution.

$$S1' \sim N(\mu = N_{PE}, \sigma^2 = R^2 \cdot N_{PE}) \quad (4.19)$$

With an approximation of the charge signal output by the PMT, we can consider processor effects. First, a probability of the processor finding the S1,  $p_{PF}$ , is determined using the size of the signal and the efficiency curve determined via the simulation discussed in Sec. 4.2.6.

We then apply a smearing to mainly capture the non-zero resolution of the processor reconstruction but also effects due to noise, position dependence of the light collection efficiency, and time variation of detector parameters. We assume that ef-

fects due to processor reconstruction should diminish as a function of the S1 signal size (this assumption was corroborated via the waveform simulator) and the other effects should be independent of signal size. The functional form of the generic smearing is shown in Eqn. 4.20.

$$\begin{aligned}\sigma_{S1} &= a_{S1} + b_{S1} \cdot e^{-S1/c_{S1}} \\ S1 &\sim N(\mu = S1', \sigma^2 = \sigma_{S1}^2)\end{aligned}\tag{4.20}$$

Since no position dependent effects are considered, the S1 from Eqn. 4.20 can be matched to the corrected S1 data.

#### 4.4.3.2 Detection of Electrons

We do not consider effects from the electron lifetime of the detector in the fast Monte Carlo of neriX since it is much larger than the maximum drift time of electrons in the TPC and since we compare to corrected data. We assume that all electrons reach the liquid surface where they have a probability of extraction into the gas,  $p_{\text{extracted}}$ .

$$N_{\text{extracted}} \sim B(N = N_{\text{L-G Interface}}, p = p_{\text{extracted}})\tag{4.21}$$

With the number of electrons extracted from the gas, we can next account for excitation caused by these electrons in the gaseous xenon as well as the smearing due to the PMTs. We approximate the number of photoelectrons detected in this secondary amplification as a Gaussian process as shown in Eqn. 4.22 where  $G$  is the mean number of photoelectrons detected for a single extracted electron,  $\sigma_G$  is the width of the photoelectron distribution for a single extracted electron, both of which are measured in the calibration described in Sec. 4.2.3, and  $N_{\text{PE}}$  is the number of photoelectrons digitized after smearing from the PMTs.

$$N_{\text{PE}} \sim N(\mu = G, \sigma^2 = \sigma_G^2)\tag{4.22}$$

With an approximation of the charge signal output by the PMT for the S2, we can consider the probability of a signal of a given size causing a trigger such that

## 4. MEASURING THE LOW ENERGY LIGHT AND CHARGE YIELD OF NUCLEAR RECOILS IN LIQUID XENON

---

the event is digitized and saved. To determine this probability,  $p_{\text{Trigger}}$ , we simply input the S2 signal size into the curve measured in the trigger efficiency calibration discussed in Sec. 4.2.5.

The final step in the fast Monte Carlo for the S2 of an event is to apply a smearing term in the same way as the S1 to cover effects such as processor reconstruction, electron lifetime, and the variation of detector parameters in time (such as the gas gain). The functional form of this generic smearing, shown in Eqn. 4.23, is the same as the form used for the S1.

$$\begin{aligned}\sigma_{\text{S2}} &= a_{\text{S2}} + b_{\text{S2}} \cdot e^{-\text{S2}/c_{\text{S2}}} \\ \text{S2} &\sim N(\mu = N_{\text{PE}}, \sigma^2 = \sigma_{\text{S2}}^2)\end{aligned}\tag{4.23}$$

The peak-finding and processor efficiency are combined such that the weight of the event in the histogram that is used to compare the model with the given parameters to data is  $w = p_{\text{PF}} \cdot p_{\text{Trigger}}$ .

### 4.4.4 Energy Inputs for Fast Monte Carlo

Of course the first ingredient for the fast Monte Carlo is the energy spectra. For nuclear recoil band data (no coincidence requirement), we simply input the expected nuclear recoil spectrum, shown in Fig. 4.30, given our experimental setup. For coincidence data, we of course use the expected energy spectra, also shown in Fig. 4.30, but we must also consider the potential for accidental coincidences between nuclear recoils in the TPC and nuclear recoils in the liquid scintillator since we do not have a fine time-of-flight cut. In this analysis, we use the nuclear recoil band energy spectrum as the accidental coincidence energy spectrum. To estimate this background in the data, we introduce an additional parameter into the fit,  $p_{\text{acc}}$ , that defines the probability that the event simulated is from the accidental coincidence spectrum rather than the true coincidence spectrum. This parameter is unique to each coincidence dataset since the accidental coincidence rate is dependent on the location of the M510 liquid scintillator detectors and on the minitron neutron generator rate, which was

not fixed even for data collected with the M510 detectors in the same position (e.g., 35° data taken at two different electric fields).

#### 4.4.5 Posterior Estimation

The posterior estimation procedure is almost identical to the one outlined for XENON1T in Sec. 3.4.2.4 and Sec. 3.4.2.5 with only a minor modification since we have fifteen spectra for fitting.

As in the XENON1T analysis, we use a binned likelihood to compare the data spectra and Monte Carlo spectra. However, unlike all previous fixed-angle measurements, we analyze all of the datasets simultaneously to maximize the amount of information used since many parameters are shared between some or all datasets (e.g.,  $k$  is shared between all datasets while the recombination constant  $\sigma_F$  is only shared between datasets taken with the same electric field. While this is a more ambitious approach, it does have costs in terms of the time required to estimate the posterior since this will increase the dimension of the posterior space and the required time for parameter estimation goes as  $\mathcal{O}(d^2)$ . Therefore, our likelihood is given by Eqn. 4.24 where  $i$  is the index of the bins and  $j$  is the index of the dataset.

$$\mathcal{L}_{i,j} = \frac{\hat{b}_{i,j}^{b_{i,j}} e^{-\hat{b}_{i,j}}}{b_{i,j}!} \implies \mathcal{L} = \prod_j \prod_i \mathcal{L}_{i,j} \quad (4.24)$$

$$\ln(\mathcal{L}) = \sum_j \sum_i \ln(\mathcal{L}_{i,j}) = \sum_j \sum_i (b_{i,j} \ln(\hat{b}_{i,j}) - \hat{b}_{i,j} - \ln(b_{i,j}!))$$

In this analysis, as in the analysis performed for XENON1T, the affine-invariant implementation of a Markov Chain Monte Carlo (MCMC) was used to sample from the posterior. For a brief summary on MCMCs, please refer to Sec. 3.4.2.5. The priors used were based on the independent calibrations discussed in Sec. 4.2 and physical constraints.

Due to the random nature of the fast Monte Carlo simulation used to estimate the PDF in observables space given the parameter, we expect fluctuations in the log-likelihood. These fluctuations do not effect the outcome of the parameter estimation

however they do slow down convergence. To speed up convergence, one can artificially suppress the log-likelihood but this has the effect of widening the posterior compared to an unsuppressed version of the log-likelihood[136]. In this work, we decided to suppress the log-likelihood by a factor of 10 such that fits could be done on a reasonable time-scale and so systematic studies could be performed. This implies that the results shown could have been improved by increasing the number of fast Monte Carlo events used to estimate the PDF or by allowing the parameter estimation to run for a longer amount of time without suppression.

#### 4.4.6 Results

All fifteen datasets were fit simultaneously using a server optimized for this type of analysis, designed by the author. The most important feature of the server relevant for this analysis are the six GPU cards that can be used in parallel to provide further increases in speed beyond the CPU versus GPU gap discussed in App. A. The full estimation of the posterior takes approximately 1.5 weeks of 24 hour run time on five of the GPUs.

The results of parameter estimation are shown with the data in Fig. 4.31, Fig. 4.32, Fig. 4.33, and Fig. 4.34. For the one-dimensional plots, the data is overlaid by the best-fit result and the 68% credible region of the fit.

One can see visually that our data agrees quite well with the model within the statistical uncertainty. The Peacock-Fasano-Franchesini test, whose results are shown in Tab. 4.4, does seem to indicate a potential issue with the 10 keV ( $45^\circ$ ) data however one should note that this test does not account for the uncertainty in our parameter estimation and only uses the best-fit parameters. One can also notice a slight mismatch at low S2 values — we believe that this is due to anomalous background events where the neutron scatters once in the fiducial volume and another time below the cathode or very close to the wall, where the charge of the interaction cannot be collected. These types of interactions would be indistinguishable from single scatters (since we cannot resolve the time difference between the S1 signals) and would cause disagreements below the nuclear recoil band (since the S2 would be

smaller relative to the expected S1). We believe that the width of the S2 distribution was artificially expanded via the generic S2 smearing function to try to account for these events that are not included in the simulation.

The marginalized results of parameter estimation are shown in Tab. 4.5 for the parameters of microphysics model and in Tab. 4.7 for the parameters of the detector model. The background probabilities measured are shown in Tab. 4.6. A flattened form of the posterior is shown in Fig. 4.35 for the parameters of the light and charge production model.

To compare this work with previous measurements, we plot the light and charge yield predicted by our model with the 68% credible region alongside recent studies that measured either the light or charge yield in Fig. 4.36. Also included in Fig. 4.36 are our measurements of  $L_y$  and  $Q_y$  using the traditional method described at the beginning of Sec. 4.4. One striking feature of the yields is that this work found no statistically significant difference in the yields at the fields used at all energies. This supports the results of Ref. [62] and Ref. [126] which only measured the effect above  $\sim 45$  keV. Also of note is the slight disagreement in results when using a physical model (band) versus the traditional model where a single light and charge yield, along with generic smearing terms, are used (points). In this analysis, the disagreement is likely due to the close proximity of the liquid scintillator detectors to neriX, which broadens the expected energy spectrum, relative to Ref. [128]. However, for this reason, future fixed-angle scattering measurements should consider this effect in their analysis and attempt to avoid this potential bias completely by utilizing a more physically motivated model.

#### 4.4.6.1 Remarks on the Light and Charge Production Model

**Field Dependence of Exciton-to-Ion Ratio and Recombination** As mentioned in the previous section, both the light and charge yields at all three fields match with each other well within uncertainty. This is in agreement with the results of Ref. [62] and Ref. [126] although we extend their observations down from  $\sim 45$  keV to 3 keV. However, Ref. [86], which performed a global analysis of all previous

#### 4. MEASURING THE LOW ENERGY LIGHT AND CHARGE YIELD OF NUCLEAR RECOILS IN LIQUID XENON

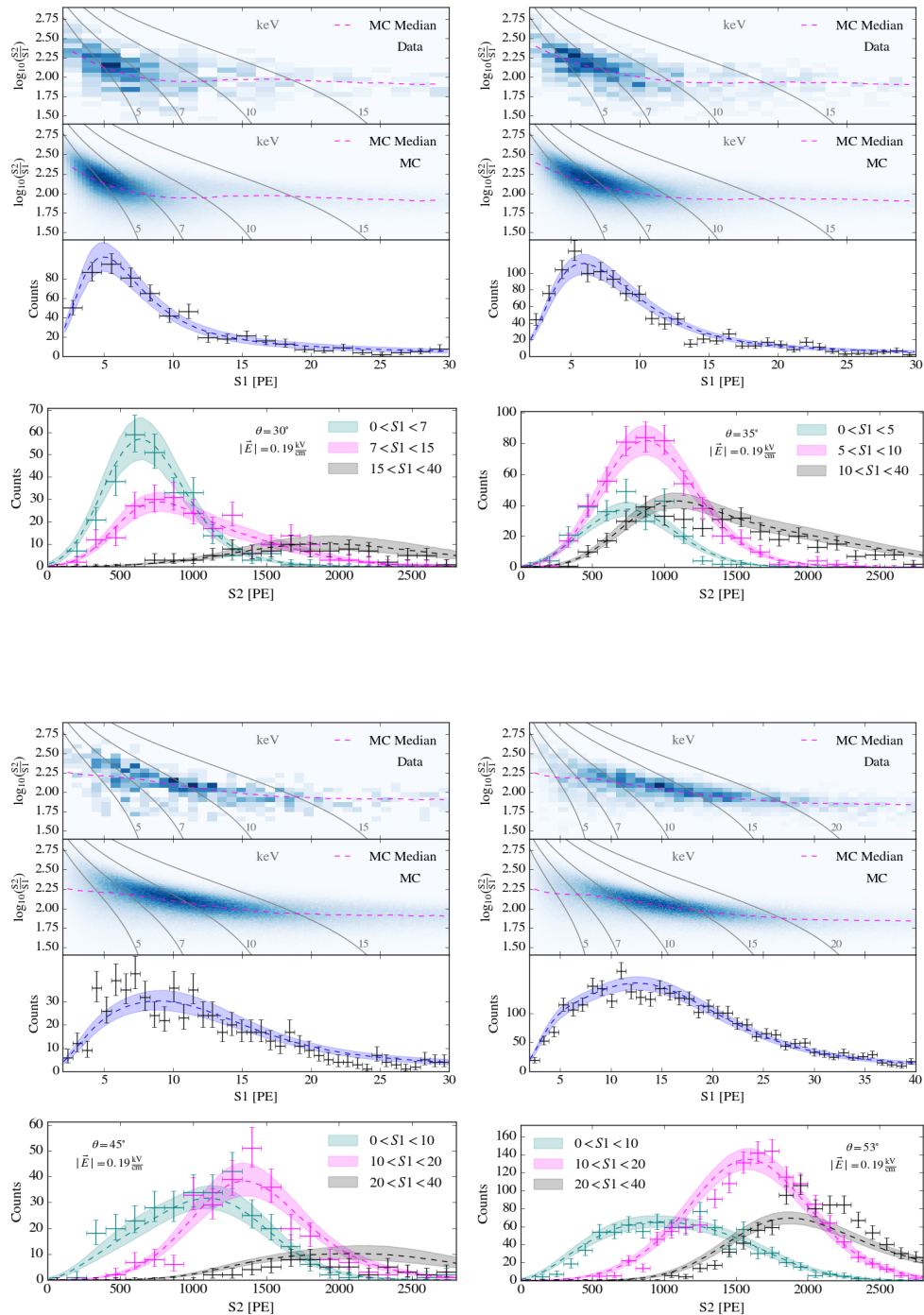


Figure 4.31: Coincidence data taken with a drift field of 190 V/cm compared to Monte Carlo generated spectra. From top to bottom: data in two-dimensions, the best-fit results in two dimensions, data projected into S1 space overlaid with the best-fit model and 68% credible region, and data projected into S2 space in different S1 regions overlaid with the best-fit model and 68% credible region.

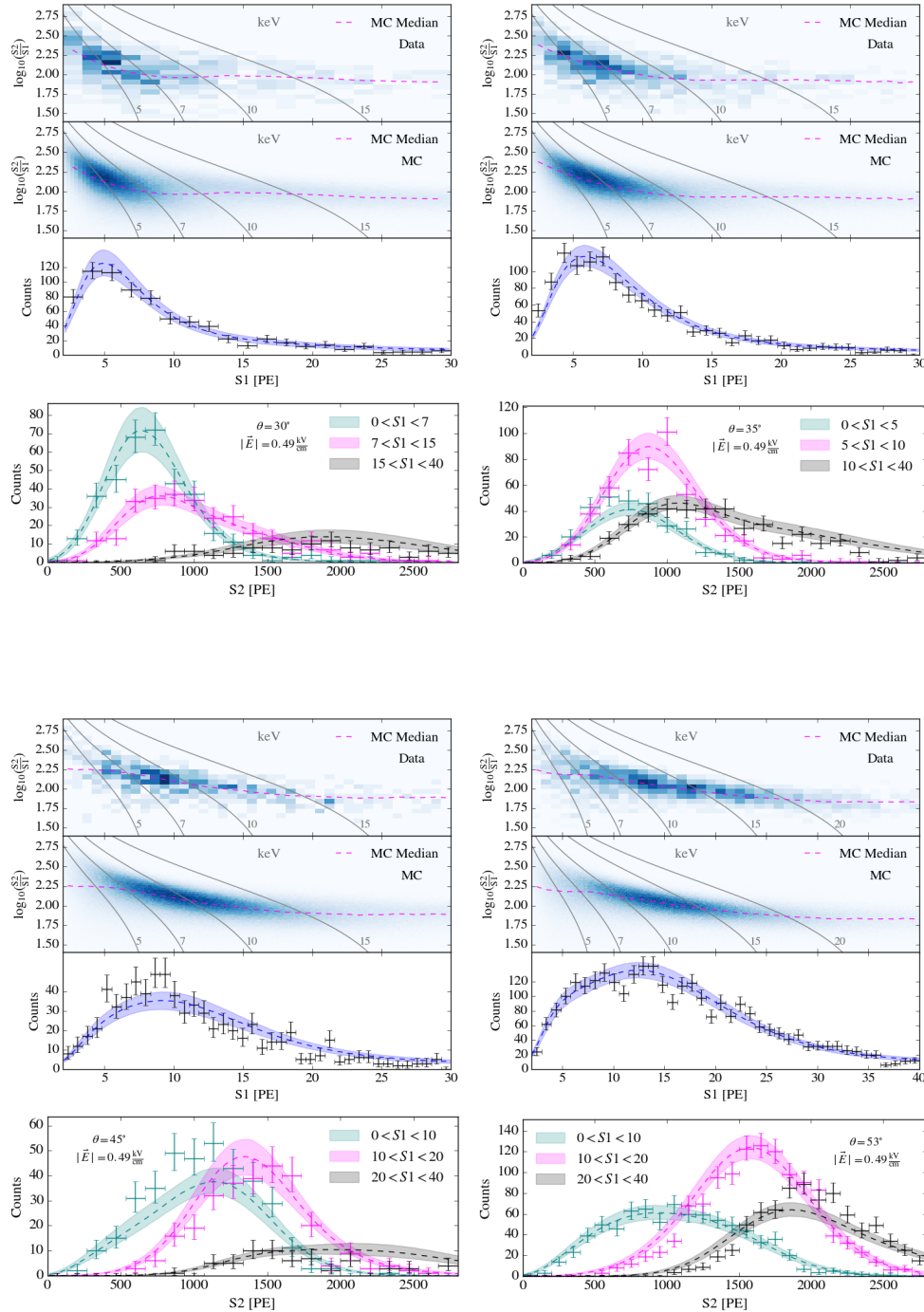


Figure 4.32: Coincidence data taken with a drift field of 490 V/cm compared to Monte Carlo generated spectra. From top to bottom: data in two-dimensions, the best-fit results in two dimensions, data projected into S1 space overlaid with the best-fit model and 68% credible region, and data projected into S2 space in different S1 regions overlaid with the best-fit model and 68% credible region.

#### 4. MEASURING THE LOW ENERGY LIGHT AND CHARGE YIELD OF NUCLEAR RECOILS IN LIQUID XENON

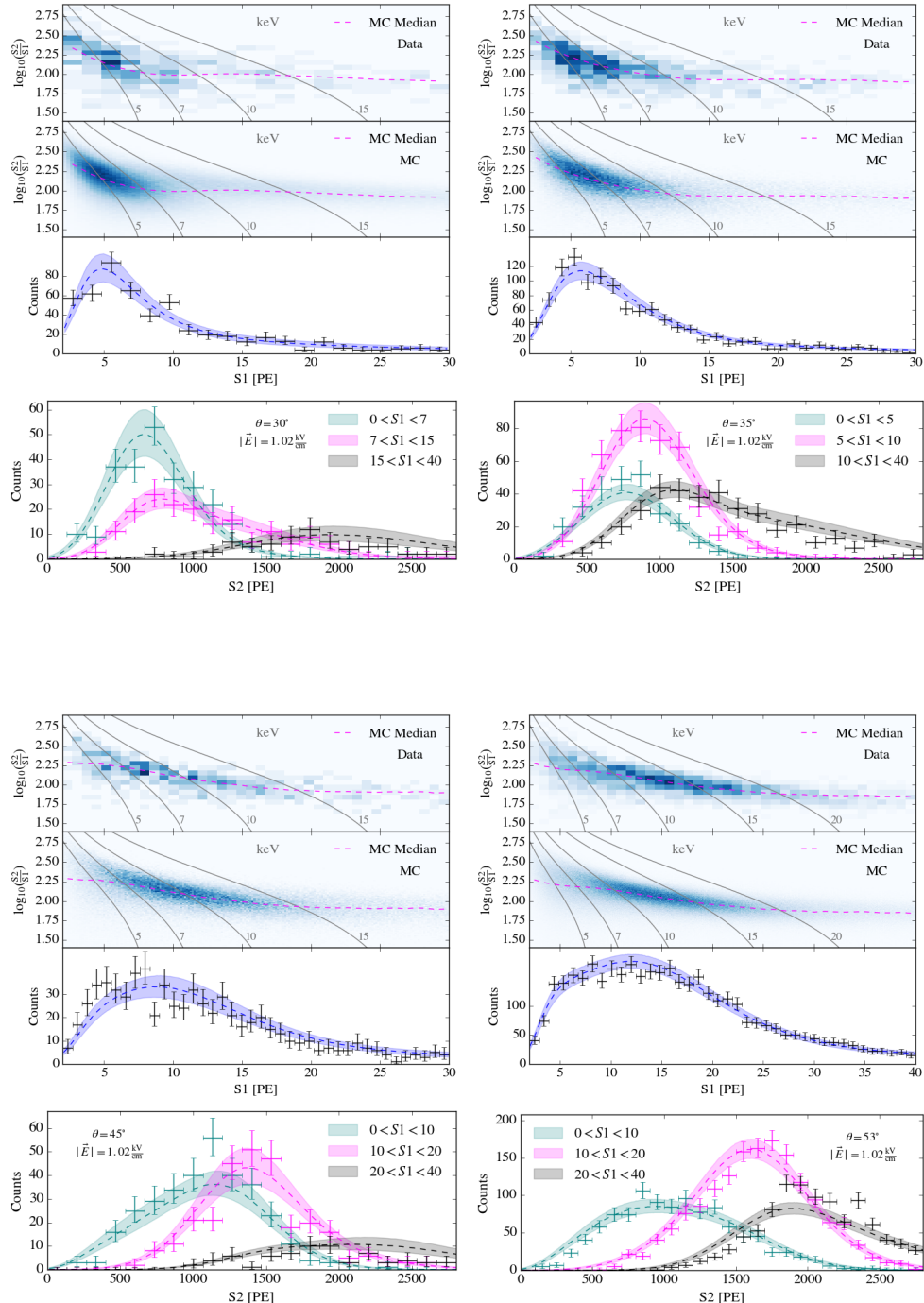


Figure 4.33: Coincidence data taken with a drift field of 1020 V/cm compared to Monte Carlo generated spectra. From top to bottom: data in two-dimensions, the best-fit results in two dimensions, data projected into S1 space overlaid with the best-fit model and 68% credible region, and data projected into S2 space in different S1 regions overlaid with the best-fit model and 68% credible region.

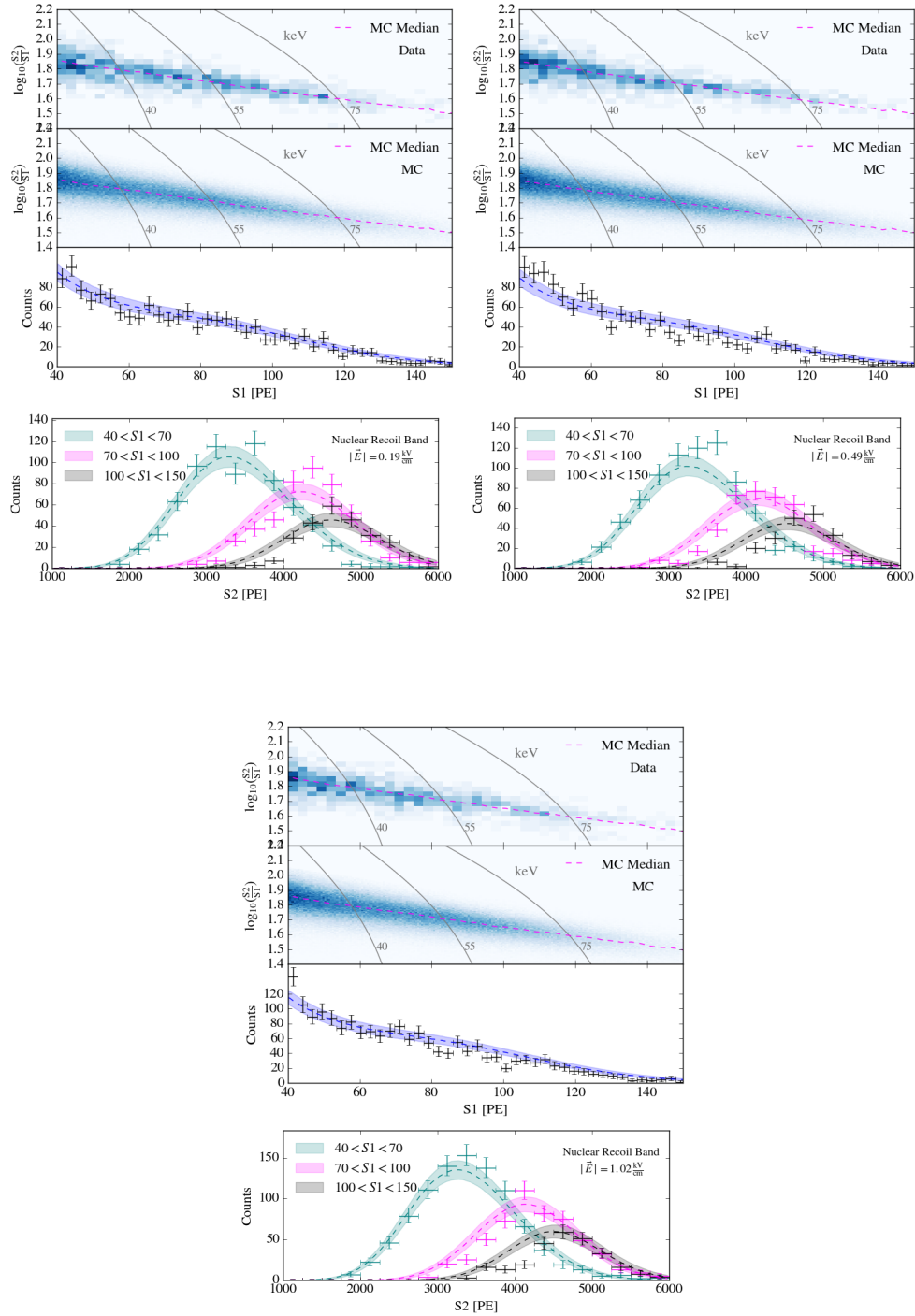


Figure 4.34: The high-energy nuclear recoil band data at all three fields compared to Monte Carlo generated spectra. From top to bottom: data in two-dimensions, the best-fit results in two dimensions, data projected into  $S_1$  space overlaid with the best-fit model and 68% credible region, and data projected into  $S_2$  space in different  $S_1$  regions overlaid with the best-fit model and 68% credible region.

#### 4. MEASURING THE LOW ENERGY LIGHT AND CHARGE YIELD OF NUCLEAR RECOILS IN LIQUID XENON

---

	NR Band	5 keV	7 keV	10 keV	15 keV
190 V/cm	0.227	0.241	0.188	0.017	0.392
490 V/cm	0.036	0.120	0.157	0.011	0.376
1020 V/cm	0.080	0.249	0.186	0.054	0.412

Table 4.4: The estimated p-values of the best-fit model calculated using the Peacock-Fasano-Franceschini test statistic.

Parameter	Result	Prior
$w$ [eV]	$13.7 \pm 0.2$	$13.7 \pm 0.2$
$k$	$0.188^{+0.008}_{-0.007}$	-
$\beta$	$2650^{+1690}_{-1590}$	-
$\sigma_{190}$ V/cm	$0.00837 \pm 0.00014$	-
$\sigma_{490}$ V/cm	$0.00864^{+0.00047}_{-0.00041}$	-
$\sigma_{1020}$ V/cm	$0.00904^{+0.00046}_{-0.00040}$	-
$\alpha_{190}$ V/cm	$1.10 \pm 0.06$	-
$\alpha_{490}$ V/cm	$1.07^{+0.07}_{-0.05}$	-
$\alpha_{1020}$ V/cm	$0.99 \pm 0.05$	-
$\eta$	$1.85^{+0.27}_{-0.26}$	-

Table 4.5: The median of the marginalized posterior for each parameter in the light and charge production model along with 16<sup>th</sup> and 84<sup>th</sup> percentiles.

Field [V/cm]	Angle	Probability of Accidental Coincidence
190	30°	$0.309^{+0.135}_{-0.123}$
190	35°	$0.117^{+0.131}_{-0.083}$
190	45°	$0.401^{+0.227}_{-0.238}$
190	53°	$0.169^{+0.123}_{-0.108}$
490	30°	$0.359^{+0.133}_{-0.124}$
490	35°	$0.125^{+0.116}_{-0.086}$
490	45°	$0.283^{+0.195}_{-0.178}$
490	53°	$0.189^{+0.138}_{-0.121}$
1020	30°	$0.384^{+0.150}_{-0.154}$
1020	35°	$0.108^{+0.115}_{-0.071}$
1020	45°	$0.364^{+0.247}_{-0.203}$
1020	53°	$0.264^{+0.109}_{-0.113}$

Table 4.6: The median of the marginalized posterior for the accidental coincidence background probabilities along with 16<sup>th</sup> and 84<sup>th</sup> percentiles.

Parameter	Result	Prior
$g_1$ [PE/ $\gamma$ ]	$0.125 \pm 0.001$	$0.125 \pm 0.003$
$R_{\text{SPE}}$	$0.645 \pm 0.006$	$0.644 \pm 0.006$
$p_{\text{extracted}}$	$0.905^{+0.024}_{-0.027}$	$0.903 \pm 0.028$
$G$ [PE]	$22.9 \pm 0.6$	$22.9 \pm 0.6$
$\sigma_G$ [PE]	$8.59^{+0.33}_{-0.31}$	$8.62 \pm 0.31$
$p_{\text{DPE}}$	$0.205^{+0.023}_{-0.024}$	$0.17 - 0.24$
$\alpha_{S1}$ [PE]	$3.16 \pm 0.01$	$3.16 \pm 0.01$
$\beta_{S1}$ [PE]	$0.754^{+0.010}_{-0.009}$	$0.755 \pm 0.009$
$\alpha_{S2}$ [PE]	$117 \pm 28$	$114 \pm 28$
$\beta_{S2}$ [PE]	$374^{+33}_{-36}$	$382 \pm 34$
$a_{S1}$	$0.185^{+0.014}_{-0.015}$	-
$b_{S1}$	$2.76^{+5.62}_{-2.12}$	-
$c_{S1}$	$0.514^{+0.624}_{-0.357}$	-
$a_{S2}$	$0.0955^{+0.0141}_{-0.0152}$	-
$b_{S2}$	$0.509^{+0.156}_{-0.123}$	-
$c_{S2}$	$658^{+208}_{-121}$	-

Table 4.7: The median of the marginalized posterior for each parameter in detector model along with 16<sup>th</sup> and 84<sup>th</sup> percentiles.  $\alpha_{S1}$  and  $\beta_{S1}$  are the parameters for peak finding efficiency, whose functional form is shown in Fig. 4.25, while  $\alpha_{S2}$  and  $\beta_{S2}$  are the parameters of the trigger efficiency, whose functional form is shown in Fig. 4.24. The parameters  $a$ ,  $b$ , and  $c$  are for the generic S1 and S2 smearing functions described by Eqn. 4.20 and Eqn. 4.23.

direct measurements of the light and charge yield observe a power law dependence of the field on the exciton-to-ion ratio,  $\alpha$ , and the recombination constant,  $\sigma$ . Therefore, we perform a likelihood ratio test to determine whether we can rule out a field dependence given our measured values of  $\alpha_F$  and  $\sigma_F$ .

For both  $\alpha$  and  $\sigma$  our null hypothesis is a constant function (representing no field dependence) while we try both a linear function and a power law (like Ref. [86]). The p-values found from the likelihood ratio are shown in Tab. 4.8. As one can see, there is no evidence against the null hypothesis (no field dependence) and therefore we can rule out field dependence in the energy ranges examined between 190–1020 V/cm.

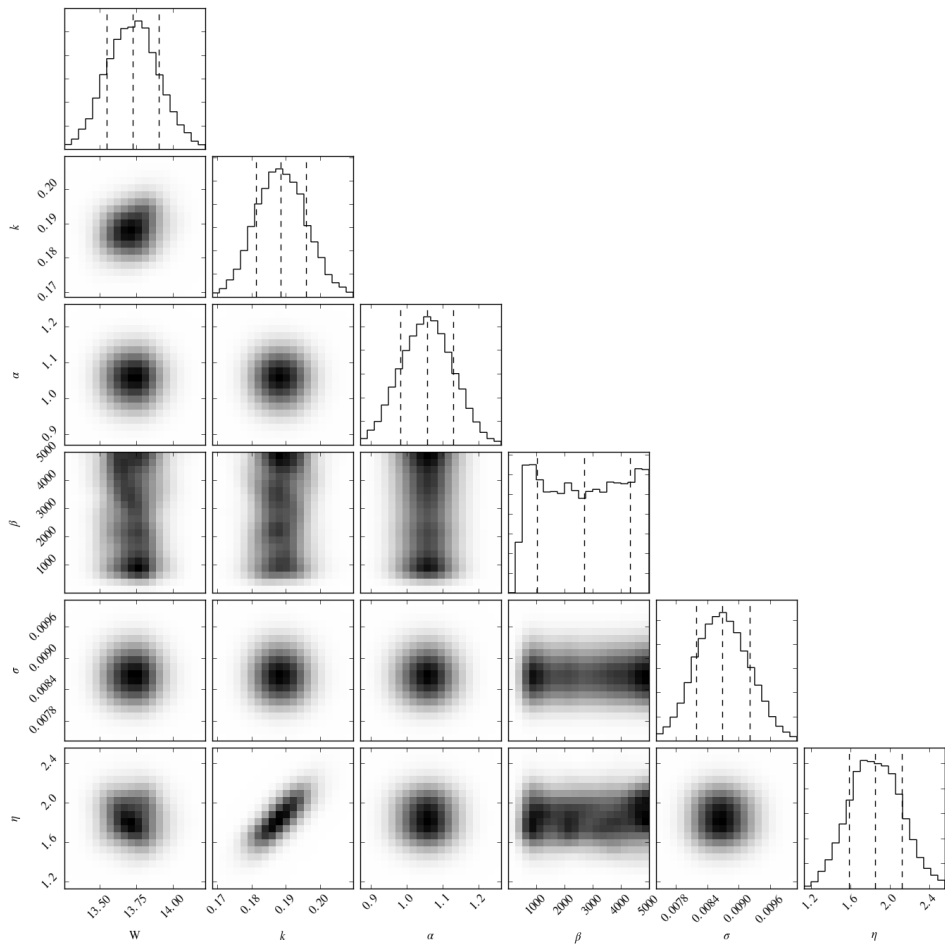


Figure 4.35: Our estimate of the posterior for the light and charge production model from the MCMC.

**Energy Dependence of the Exciton-to-Ion Ratio** In their global fit to direct measurements, Ref. [86] assigns an energy dependence to the exciton-to-ion ratio such that the light yield approaches zero with decreasing energy. The energy dependence that was assigned was of the form shown in Eqn. 4.13 such that for a larger values of  $\beta$  the energy dependence onset becomes lower. For our energy threshold of 3 keV, we would only expect a 5% effect for  $\beta \approx 1000$  whereas at  $\beta \approx 2000$  the effect is essentially zero. As one can see clearly in Fig. 4.35, a  $\beta \lesssim 500$  is almost completely ruled and that the parameter is essentially uniform above this level. This implies that down to 3 keV, our data is compatible with a model without energy dependence in the exciton-to-ion ratio.

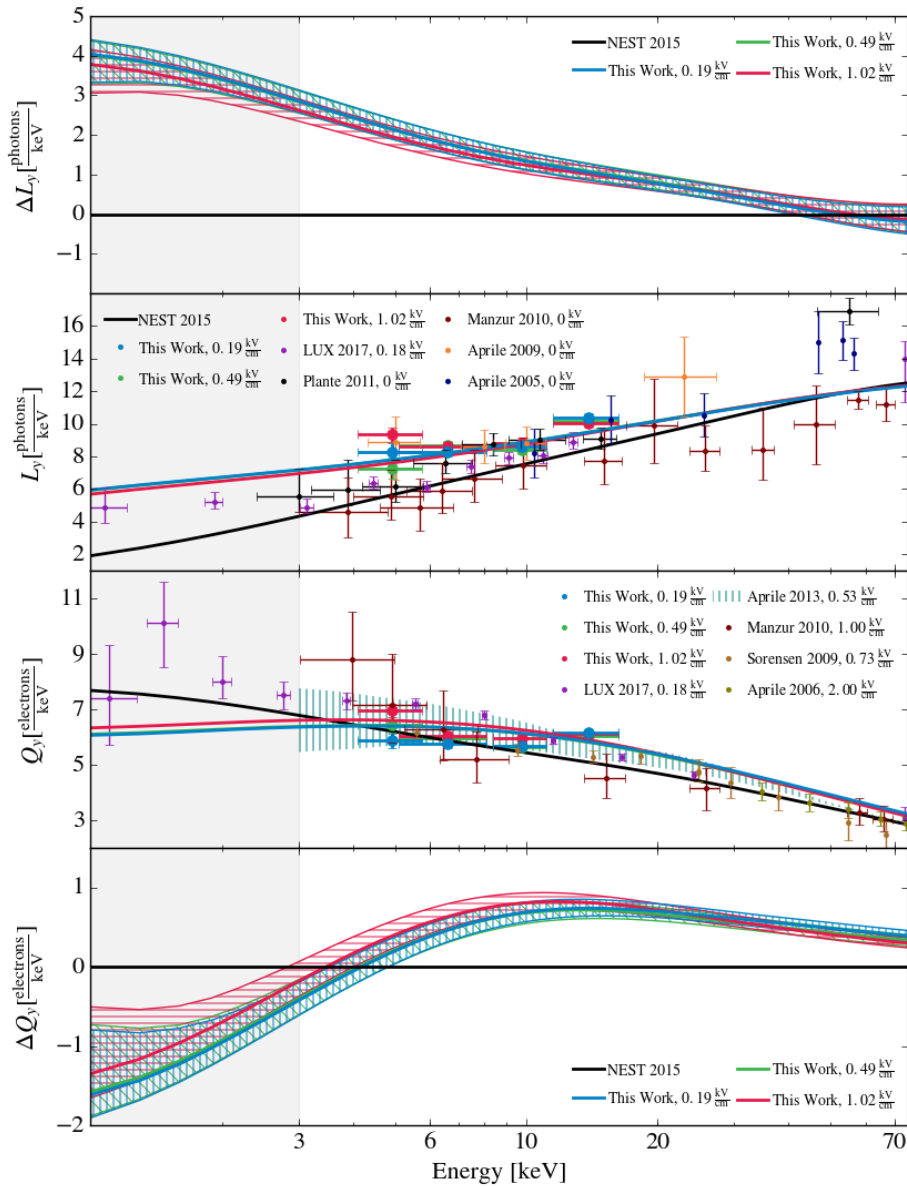


Figure 4.36: Measured light and charge yields in this work (red, green, and blue band) compared with previous measurements [62, 115, 124, 126, 128, 139, 141–143]. The red, green, and blue bands are the results from using the physical observables model while the points come from the matching technique used in previous fixed-angle scattering measurements. The reference line is the best-fit global result from Ref. [86] at 490 V/cm. An energy cutoff of 3 keV is chosen as this represents an approximately 10% detection efficiency assuming a light yield of 5.5 photons/keV and charge yield of 7.5 electrons/keV (shown in gray). Note that all measurements of light yield with the exception of this work and of Ref. [124] are extrapolations from  $\mathcal{L}_{eff}$  using a light yield of 63 photons/keV for 122 keV electronic recoils..

#### 4. MEASURING THE LOW ENERGY LIGHT AND CHARGE YIELD OF NUCLEAR RECOILS IN LIQUID XENON

---

	Linear Field Dependence	Power Law Field Dependence
$\alpha$	0.154	0.182
$\sigma$	0.227	0.277

Table 4.8: The estimated p-values from the likelihood ratio test determining whether or not field dependence in the exciton-to-ion ratio and recombination constant are observed. The likelihood ratio test finds no evidence against our null hypothesis and thus we conclude that no field dependence is observed in our data.

	$w$	$k$	$\alpha$	$\sigma$	$\eta$
Means	13.7	0.189	1.06	$8.70 \times 10^{-3}$	1.85
Std. Deviation	0.2	0.007	0.07	$5.1 \times 10^{-4}$	0.26
$w$	$3.09 \times 10^{-2}$	$2.69 \times 10^{-4}$	$-2.16 \times 10^{-4}$	$-9.74 \times 10^{-8}$	$-3.41 \times 10^{-3}$
$k$	-	$5.58 \times 10^{-5}$	$-1.03 \times 10^{-6}$	$3.66 \times 10^{-9}$	$1.56 \times 10^{-3}$
$\alpha$	-	-	$5.29 \times 10^{-3}$	$-2.12 \times 10^{-8}$	$-3.43 \times 10^{-6}$
$\sigma$	-	-	-	$2.57 \times 10^{-7}$	$9.56 \times 10^{-8}$
$\eta$	-	-	-	-	$7.01 \times 10^{-2}$

Table 4.9: The multivariate normal approximation of the posterior of our analysis for the light charge production model only. The means of the multivariate normal distribution are shown in the first row, the standard deviation of that parameter is shown in the next row, and the covariance matrix comprises the remaining rows. Note that the units of  $w$  are excluded.

**Physical Model Summary** A summary of the posterior of the light and charge production model is shown in Tab. 4.9. In this table, we do not include  $\beta$  since our data is consistent with a constant exciton-to-ion ratio and we combine the posteriors of  $\sigma$  and  $\alpha$  at all fields. For simplicity, we assume that the posterior is described by a multivariate normal distribution (with the means and standard deviations in the first two rows and the covariance matrix encompassing the remainder of the table) which, with the exclusion of  $\beta$ , is clearly an appropriate approximation from Fig. 4.35. It is the author’s recommendation that future experiments using the same physical model and not attempting to independently measure the parameters use this posterior as a prior in their work.

As discussed above, our data ruled out any field dependence in the model and is consistent with a constant exciton-to-ion ratio in the energy range examined. Our

constant exciton-to-ion ratio is in agreement with global analyses of past direct measurements which estimate the exciton-to-ion ratio to be  $\approx 1$  [85]. Our constant recombination constant is also in agreement with global analyses of past direct measurements which estimate it to be in the range  $0.007 - 0.01$  [85].

The constant,  $k$ , that relates the electronic stopping power to the velocity of the xenon nucleus agrees with the original range proposed by Lindhard of  $0.1 - 0.2$ . However we find that our value disagrees with the theoretically calculated value from Hitachi of  $0.110$  [66, 85]. Our result also disagrees with the global analysis performed in Ref. [86] where they find  $k = 0.1394^{+0.0032}_{-0.0026}$ . The most recent measurement from Ref. [124] that uses neutron double scatters in the LUX TPC shows only a very small disagreement with  $k = 0.1735 \pm 0.0060$ .

Finally, Birk's constant,  $\eta$ , used during parameter estimation to describe biexcitonic quenching at high energies is in good agreement with Ref. [124] where  $\eta = 2.19 \pm 0.38$  was found. Both of these measurements are slightly lower than the global analysis from Ref. [86] which found  $\eta = 3.3^{+5.3}_{-0.7}$ .

#### 4.4.6.2 Remarks on the Detector Physics Model

As is shown in Tab. 4.7, all parameters that were constrained with a prior agree quite well with the independent measurement. Our parameters for the generic S1 smearing show that we likely could have simplified the model used as the exponential term,  $c_{S1}$ , is very small and we only look at data above 2 PE. This implies that our S1 smearing is essentially just a constant 18.5%. The S2 smearing parameters are actually larger than originally expected for our detector. However, in looking at the model relative to data (especially the 15 keV and NR band data), it appears that anomalous low S2 events are the cause of this larger broadening (the S2 cuts appear wider than data to “reach” these anomalous events). These low S2 events, as discussed in Sec. 4.4.6 are likely from second neutron scatters in charge-insensitive regions such as below the cathode and near the TPC walls.

#### 4.4.7 Systematic Uncertainties

Two main sources of systematic uncertainty were considered in this measurement: the position of the liquid scintillators relative to the TPC and the neutron generator and the binning used during parameter estimation.

We approximated our uncertainty in the placement of the liquid scintillators and the minitron to be 3 mm. While seemingly small, due to the distance of the liquid scintillators from the TPC even a small discrepancy can cause a noticeable change to the shape of the expected energy spectrum. To estimate the effect of a displacement, within our uncertainty, on our final light and charge yields, we performed the parameter estimation again using energy spectra produced assuming that the liquid scintillators and neutron generator had a displacement of 3 mm in each coordinate that shifted the mean of the energy spectrum the most. Even with this conservative estimation procedure, we found that with shifts of 3 mm the yields only changed  $\lesssim 1\%$  which is much less than the 5 – 10% statistical uncertainty observed.

We also considered the uncertainty due to our choice of binning since the number of events is relatively low, especially considering that the analysis is performed in two dimensions. To test this effect, we fit all spectra assuming a linear and logarithmic binning in S1 and compared the results. This also appeared to have very little effect on the yields, changing them by less than 1% which is much smaller than our statistical uncertainty.

### 4.5 Conclusions

In this chapter, we discussed the liquid xenon TPC, the experimental setup, and the new analysis technique used to measure the response of liquid xenon to low energy nuclear recoils at three electric fields relevant to the dark matter search. For the first time, both light and charge were examined simultaneously allowing for the use of a full effective light and charge production model. The resulting posterior from this model applied to our data is included and can either be used for future global analyses or as a prior to calibrations in larger detectors. From this posterior, we

concluded that no field dependence in the nuclear recoil response at the fields and energies measured is observed in our data.

The data analysis framework, developed by the author, allowed for the change in paradigm of measuring or analyzing observables one at a time, which does not take full advantage of the information taken in a dual-phase TPC. This framework has already become the basis for complicated and previously unfeasible calibrations in XENON1T and hopefully more uses will be found in the near future.



# Bibliography

- [1] S. M. Carroll, “Lecture notes on general relativity,” *arXiv preprint gr-qc/9712019*, 1997.
- [2] F. Zwicky, “The redshift of extragalactic nebulae,” *Helv. Phys. Acta*, vol. 6, p. 110, 1933.
- [3] K. Begeman, A. Broeils, and R. Sanders, “Extended rotation curves of spiral galaxies: dark haloes and modified dynamics,” *Monthly Notices of the Royal Astronomical Society*, vol. 249, no. 3, pp. 523–537, 1991.
- [4] V. C. Rubin and W. K. Ford Jr, “Rotation of the andromeda nebula from a spectroscopic survey of emission regions,” *The Astrophysical Journal*, vol. 159, p. 379, 1970.
- [5] D. Clowe, M. Bradač, A. H. Gonzalez, M. Markevitch, S. W. Randall, C. Jones, and D. Zaritsky, “A direct empirical proof of the existence of dark matter,” *The Astrophysical Journal Letters*, vol. 648, no. 2, p. L109, 2006.
- [6] A. A. Penzias and R. W. Wilson, “A measurement of excess antenna temperature at 4080 mc/s.,” *The Astrophysical Journal*, vol. 142, pp. 419–421, 1965.
- [7] D. Fixsen, E. Cheng, J. Gales, J. C. Mather, R. Shafer, and E. Wright, “The cosmic microwave background spectrum from the full cobe\* firas data set,” *The Astrophysical Journal*, vol. 473, no. 2, p. 576, 1996.
- [8] P. A. Ade, V Salvatelli, V Stolyarov, F. Desert, J Knoche, M Giard, X Dupac, M Liguori, S Matarrese, Z Huang, *et al.*, “Planck 2015 results. xiii. cosmological parameters,” *Astron. Astrophys.*, vol. 594, no. arXiv: 1502.01589, A13, 2015.
- [9] C. L. Bennett, A. J. Banday, K. M. Górski, G Hinshaw, P Jackson, P Keegstra, A Kogut, G. F. Smoot, D. T. Wilkinson, and E. L. Wright, “Four-year cobe\* dmr cosmic microwave background observations: maps and basic results,” *The Astrophysical Journal Letters*, vol. 464, no. 1, p. L1, 1996.

- [10] E. Komatsu, K. Smith, J. Dunkley, C. Bennett, B. Gold, G. Hinshaw, N. Jarosik, D. Larson, M. Nolta, L. Page, *et al.*, “Seven-year wilkinson microwave anisotropy probe (wmap\*) observations: cosmological interpretation,” *The Astrophysical Journal Supplement Series*, vol. 192, no. 2, p. 18, 2011.
- [11] J. F. Navarro, “The structure of cold dark matter halos,” in *Symposium-international astronomical union*, Cambridge University Press, vol. 171, 1996, pp. 255–258.
- [12] V. Springel, C. S. Frenk, and S. D. White, “The large-scale structure of the universe,” *arXiv preprint astro-ph/0604561*, 2006.
- [13] M. Vogelsberger, S. Genel, V. Springel, P. Torrey, D. Sijacki, D. Xu, G. Snyder, D. Nelson, and L. Hernquist, “Introducing the *illustris* project: simulating the coevolution of dark and visible matter in the universe,” *Monthly Notices of the Royal Astronomical Society*, pp. 1518–1547, 2014.
- [14] R. D. Peccei and H. R. Quinn, “Cp conservation in the presence of pseudoparticles,” *Physical Review Letters*, vol. 38, no. 25, p. 1440, 1977.
- [15] A. Alavi-Harati, I. Albuquerque, T. Alexopoulos, M. Arenton, K. Arisaka, S. Averitte, A. Barker, L. Bellantoni, A. Bellavance, J. Belz, *et al.*, “Observation of direct CP violation in  $K_{S,L} \rightarrow \pi\pi$  decays,” *Physical Review Letters*, vol. 83, no. 1, p. 22, 1999.
- [16] V. Fanti, A. Lai, D. Marras, L. Musa, A. Bevan, T. Gershon, B. Hay, R. Moore, K. Moore, D. Munday, *et al.*, “A new measurement of direct CP violation in two pion decays of the neutral kaon,” *Physics Letters B*, vol. 465, no. 1, pp. 335–348, 1999.
- [17] B. Aubert, D. Boutigny, I. De Bonis, J.-M. Gaillard, A. Jeremie, Y. Karyotakis, J. Lees, P. Robbe, V. Tisserand, A. Palano, *et al.*, “Measurement of CP-violating asymmetries in  $B^0$  decays to CP eigenstates,” *Physical Review Letters*, vol. 86, no. 12, p. 2515, 2001.
- [18] K. Abe, R. Abe, I. Adachi, B. S. Ahn, H. Aihara, M. Akatsu, G. Alimonti, K. Asai, M. Asai, Y. Asano, *et al.*, “Observation of large CP violation in the neutral B meson system,” *Physical Review Letters*, vol. 87, no. 9, p. 091802, 2001.
- [19] R. Aaij, C. A. Beteta, B. Adeva, M. Adinolfi, C. Adrover, A. Affolder, Z. Ajaltouni, J. Albrecht, F. Alessio, M. Alexander, *et al.*, “First observation of CP violation in the decays of  $B_s^0$  mesons,” *Physical review letters*, vol. 110, no. 22, p. 221601, 2013.

- 
- [20] P. W. Graham, I. G. Irastorza, S. K. Lamoreaux, A. Lindner, and K. A. van Bibber, “Experimental searches for the axion and axion-like particles,” *Annual Review of Nuclear and Particle Science*, vol. 65, pp. 485–514, 2015.
  - [21] I. Stern, “Admx status,” *arXiv preprint arXiv:1612.08296*, 2016.
  - [22] A. Garcon, D. Aybas, J. W. Blanchard, G. Centers, N. L. Figueroa, P. Graham, D. F. J. Kimball, S. Rajendran, M. G. Sendra, A. O. Sushkov, *et al.*, “Searching for dark matter with nuclear magnetic resonance: the cosmic axion spin precession experiment,” *arXiv preprint arXiv:1707.05312*, 2017.
  - [23] G. Jungman, M. Kamionkowski, and K. Griest, “Supersymmetric dark matter,” *Physics Reports*, vol. 267, no. 5-6, pp. 195–373, 1996.
  - [24] G. Bertone, *Particle dark matter: Observations, models and searches*. Cambridge University Press, 2010.
  - [25] X.-J. Bi, P.-F. Yin, and Q. Yuan, “Status of dark matter detection,” *Frontiers of Physics*, vol. 8, no. 6, pp. 794–827, 2013.
  - [26] J. Stadel, D. Potter, B. Moore, J. Diemand, P. Madau, M. Zemp, M. Kuhlen, and V. Quilis, “Quantifying the heart of darkness with ghalo—a multibillion particle simulation of a galactic halo,” *Monthly Notices of the Royal Astronomical Society: Letters*, vol. 398, no. 1, pp. L21–L25, 2009.
  - [27] A. V. Macciò, A. A. Dutton, F. C. Van Den Bosch, B. Moore, D. Potter, and J. Stadel, “Concentration, spin and shape of dark matter haloes: scatter and the dependence on mass and environment,” *Monthly Notices of the Royal Astronomical Society*, vol. 378, no. 1, pp. 55–71, 2007.
  - [28] J. Read, “The local dark matter density,” *Journal of Physics G: Nuclear and Particle Physics*, vol. 41, no. 6, p. 063 101, 2014.
  - [29] B. Zitzer *et al.*, “Search for dark matter from dwarf galaxies using veritas,” *arXiv preprint arXiv:1509.01105*, 2015.
  - [30] J. Conrad, “Indirect detection of wimp dark matter: a compact review,” *arXiv preprint arXiv:1411.1925*, 2014.
  - [31] F. S. Queiroz, “Dark matter overview: collider, direct and indirect detection searches,” *arXiv preprint arXiv:1605.08788*, 2016.
  - [32] J. Kopp, V. Niro, T. Schwetz, and J. Zupan, “Dama/libra data and leptonically interacting dark matter,” *Physical Review D*, vol. 80, no. 8, p. 083 502, 2009.

- [33] J. Lewin and P. Smith, “Review of mathematics, numerical factors, and corrections for dark matter experiments based on elastic nuclear recoil,” *Astroparticle Physics*, vol. 6, no. 1, pp. 87–112, 1996.
- [34] T. M. Undagoitia and L. Rauch, “Dark matter direct-detection experiments,” *Journal of Physics G: Nuclear and Particle Physics*, vol. 43, no. 1, p. 013 001, 2015.
- [35] T. Piffl, C. Scannapieco, J. Binney, M. Steinmetz, R.-D. Scholz, M. E. Williams, R. S. De Jong, G. Kordopatis, G. Matijević, O. Bienayme, *et al.*, “The rave survey: the galactic escape speed and the mass of the milky way,” *Astronomy & Astrophysics*, vol. 562, A91, 2014.
- [36] M. Kuhlen, N. Weiner, J. Diemand, P. Madau, B. Moore, D. Potter, J. Stadel, and M. Zemp, “Dark matter direct detection with non-maxwellian velocity structure,” *Journal of Cosmology and Astroparticle Physics*, vol. 2010, no. 02, p. 030, 2010.
- [37] J Engel, “Nuclear form factors for the scattering of weakly interacting massive particles,” *Physics Letters B*, vol. 264, no. 1-2, pp. 114–119, 1991.
- [38] R Strauss, G Angloher, A Bento, C Bucci, L Canonica, X Defay, A Erb, F. v. Feilitzsch, N. F. Iachellini, P Gorla, *et al.*, “Exploring low-mass dark matter with cresst,” *Journal of Low Temperature Physics*, vol. 184, no. 3-4, pp. 866–872, 2016.
- [39] C Amole, M Ardid, I. J. Arnquist, D. M. Asner, D Baxter, E Behnke, P Bhattacharjee, H Borsodi, M Bou-Cabo, P Campion, *et al.*, “Dark matter search results from the pico- 60 c 3 f 8 bubble chamber,” *Physical review letters*, vol. 118, no. 25, p. 251 301, 2017.
- [40] R Bernabei, P Belli, F Cappella, R Cerulli, C. Dai, A d’Angelo, H. He, A Incicchitti, X. Ma, F Montecchia, *et al.*, “Particle dark matter and dama/libra,” in *AIP Conference Proceedings*, AIP, vol. 1223, 2010, pp. 50–59.
- [41] C. Aalseth, P. Barbeau, J. D. Leon, J. Fast, T. Hossbach, A Knecht, M. Kos, M. Marino, H. Miley, M. Miller, *et al.*, “Maximum likelihood signal extraction method applied to 3.4 years of cogent data,” *arXiv preprint arXiv:1401.6234*, 2014.
- [42] X. collaboration *et al.*, “Direct dark matter search by annual modulation in xmass-i,” *Physics Letters B*, vol. 759, pp. 272–276, 2016.
- [43] E Aprile, J Aalbers, F Agostini, M Alfonsi, F. Amaro, M Anthony, F Arneodo, P Barrow, L Baudis, B. Bauermeister, *et al.*, “Search for electronic recoil event

- rate modulation with 4 years of xenon100 data,” *Physical Review Letters*, vol. 118, no. 10, p. 101 101, 2017.
- [44] T Heindl, T Dandl, A Fedenev, M Hofmann, R Krücken, L Oberauer, W Potzel, J Wieser, and A Ulrich, “Table-top setup for investigating the scintillation properties of liquid argon,” *Journal of Instrumentation*, vol. 6, no. 02, P02011, 2011.
- [45] P.-A. Amaudruz, M Baldwin, M Batygov, B Beltran, C. Bina, D Bishop, J Bonatt, G Boorman, M. Boulay, B Broerman, *et al.*, “First results from the deap-3600 dark matter search with argon at snolab,” *arXiv preprint arXiv:1707.08042*, 2017.
- [46] C. Aalseth, P. Barbeau, J Colaresi, J. Collar, J. D. Leon, J. Fast, N. Fields, T. Hossbach, A Knecht, M. Kos, *et al.*, “Search for an annual modulation in three years of cogent dark matter detector data,” *arXiv preprint arXiv:1401.3295*, 2014.
- [47] E Armengaud, Q Arnaud, C Augier, A Benoit, L Bergé, T Bergmann, J Billard, J Blümer, T De Boissière, G Bres, *et al.*, “Constraints on low-mass wimps from the edelweiss-iii dark matter search,” *Journal of Cosmology and Astroparticle Physics*, vol. 2016, no. 05, p. 019, 2016.
- [48] E Aprile, J Aalbers, F Agostini, M Alfonsi, F. Amaro, M Anthony, F Arneodo, P Barrow, L Baudis, B Bauermeister, *et al.*, “First dark matter search results from the xenon1t experiment,” *arXiv preprint arXiv:1705.06655*, 2017.
- [49] P.-I. Collaboration, X. Cui, A. Abdukerim, W. Chen, X. Chen, Y. Chen, B. Dong, D. Fang, C. Fu, K. Giboni, *et al.*, “Dark matter results from 54-ton-day exposure of pandax-ii experiment,” *arXiv preprint arXiv:1708.06917*, 2017.
- [50] R Agnese, A. Anderson, M Asai, D Balakishiyeva, D Barker, R. B. Thakur, D. Bauer, J Billard, A Borgland, M. Bowles, *et al.*, “Improved wimp-search reach of the cdms ii germanium data,” *Physical Review D*, vol. 92, no. 7, p. 072 003, 2015.
- [51] C. Savage, G. Gelmini, P. Gondolo, and K. Freese, “Compatibility of dama/libra dark matter detection with other searches,” *Journal of Cosmology and Astroparticle Physics*, vol. 2009, no. 04, p. 010, 2009.
- [52] A. Tan, M. Xiao, X. Cui, X. Chen, Y. Chen, D. Fang, C. Fu, K. Giboni, F. Giuliani, H. Gong, *et al.*, “Dark matter results from first 98.7 days of data from the pandax-ii experiment,” *Physical review letters*, vol. 117, no. 12, p. 121 303, 2016.

- [53] D. Akerib, S Alsum, H. Araújo, X Bai, A. Bailey, J Balajthy, P Beltrame, E. Bernard, A Bernstein, T. Biesiadzinski, *et al.*, “Results from a search for dark matter in the complete lux exposure,” *Physical Review Letters*, vol. 118, no. 2, p. 021 303, 2017.
- [54] G Angloher, A Bento, C Bucci, L Canonica, X Defay, A Erb, F von Feilitzsch, N. F. Iachellini, P Gorla, A Gütlein, *et al.*, “Results on light dark matter particles with a low-threshold cresst-ii detector,” *The European Physical Journal C*, vol. 76, no. 1, p. 25, 2016.
- [55] F Ruppin, J Billard, E Figueroa-Feliciano, and L Strigari, “Complementarity of dark matter detectors in light of the neutrino background,” *Physical Review D*, vol. 90, no. 8, p. 083 510, 2014.
- [56] J. Albert, M Auger, D. Auty, P. Barbeau, E Beauchamp, D Beck, V Belov, C Benitez-Medina, J Bonatt, M Breidenbach, *et al.*, “Improved measurement of the  $2\nu\beta\beta$  half-life of  $^{136}\text{xe}$  with the exo-200 detector,” *Physical Review C*, vol. 89, no. 1, p. 015 502, 2014.
- [57] K Ni, R Hasty, T. Wongjirad, L Kastens, A Manzur, and D. McKinsey, “Preparation of neutron-activated xenon for liquid xenon detector calibration,” *Nuclear Instruments and Methods in Physics Research Section A: Accelerators, Spectrometers, Detectors and Associated Equipment*, vol. 582, no. 2, pp. 569–574, 2007.
- [58] K Abe, J Hosaka, T Iida, M Ikeda, K Kobayashi, Y Koshio, A Minamino, M Miura, S Moriyama, M Nakahata, *et al.*, “Distillation of liquid xenon to remove krypton,” *Astroparticle Physics*, vol. 31, no. 4, pp. 290–296, 2009.
- [59] E Aprile, J Aalbers, F Agostini, M Alfonsi, F. Amaro, M Anthony, F Arneodo, P Barrow, L Baudis, B. Bauermeister, *et al.*, “Removing krypton from xenon by cryogenic distillation to the ppq level,” *The European Physical Journal C*, vol. 77, no. 5, p. 275, 2017.
- [60] N Barros, J Thurn, and K Zuber, “Double beta decay searches of  $^{134}\text{xe}$ ,  $^{126}\text{xe}$  and  $^{124}\text{xe}$  with large scale xe detectors,” *Journal of Physics G: Nuclear and Particle Physics*, vol. 41, no. 11, p. 115 105, 2014.
- [61] D. W. Rankin, *Crc handbook of chemistry and physics, edited by david r. lide*, 2009.
- [62] E. Aprile, C. Dahl, L de Viveiros, R. Gaitskell, K.-L. Giboni, J Kwong, P Majewski, K Ni, T Shutt, and M Yamashita, “Simultaneous measurement of ionization and scintillation from nuclear recoils in liquid xenon for a dark matter experiment,” *Physical review letters*, vol. 97, no. 8, p. 081 302, 2006.

- [63] A. Hitachi, T. Takahashi, N. Funayama, K. Masuda, J. Kikuchi, and T. Doke, “Effect of ionization density on the time dependence of luminescence from liquid argon and xenon,” *Physical Review B*, vol. 27, no. 9, p. 5279, 1983.
- [64] T. Doke, A. Hitachi, J. Kikuchi, K. Masuda, H. Okada, and E. Shibamura, “Absolute scintillation yields in liquid argon and xenon for various particles,” *Japanese journal of applied physics*, vol. 41, no. 3R, p. 1538, 2002.
- [65] J. Lindhard, V Nielsen, M Scharff, and P. Thomsen, “Integral equations governing radiation effects,” *Mat. Fys. Medd. Dan. Vid. Selsk*, vol. 33, no. 10, pp. 1–42, 1963.
- [66] A. Hitachi, “Properties of liquid xenon scintillation for dark matter searches,” *Astroparticle Physics*, vol. 24, no. 3, pp. 247–256, 2005.
- [67] W. Cottingham and D. Greenwood, *An Introduction to Nuclear Physics*. Cambridge University Press, 1987.
- [68] J Mantel, “The beta ray spectrum and the average beta energy of several isotopes of interest in medicine and biology,” *The International journal of applied radiation and isotopes*, vol. 23, no. 9, pp. 407–413, 1972.
- [69] E Aprile, J Aalbers, F Agostini, M Alfonsi, F. Amaro, M Anthony, F Arneodo, P Barrow, L Baudis, B. Bauermeister, *et al.*, “Results from a calibration of xenon100 using a source of dissolved radon-220,” *Physical Review D*, vol. 95, no. 7, p. 072008, 2017.
- [70] D. Akerib, H. Araújo, X Bai, A. Bailey, J Balajthy, P Beltrame, E. Bernard, A Bernstein, T. Biesiadzinski, E. Boulton, *et al.*, “Tritium calibration of the lux dark matter experiment,” *Physical Review D*, vol. 93, no. 7, p. 072009, 2016.
- [71] E Aprile, J Aalbers, F Agostini, M Alfonsi, F. Amaro, M Anthony, F Arneodo, P Barrow, L Baudis, B Bauermeister, *et al.*, “Signal yields of kev electronic recoils and their discrimination from nuclear recoils in liquid xenon,” *arXiv preprint arXiv:1709.10149*, 2017.
- [72] G. F. Knoll, *Radiation detection and measurement*. John Wiley & Sons, 2010.
- [73] M. Berger, “Xcom: photon cross sections database,” *NIST Standard Reference Database 8 (XGAM)*, 2013.
- [74] M. Chadwick, M Herman, P Obložinský, M. E. Dunn, Y Danon, A. Kahler, D. L. Smith, B Pritychenko, G. Arbanas, R Arcilla, *et al.*, “Endf/b-vii. 1 nuclear data for science and technology: cross sections, covariances, fission product

- yields and decay data," *Nuclear Data Sheets*, vol. 112, no. 12, pp. 2887–2996, 2011.
- [75] J. Timar, Z. Elekes, and B. Singh, "Nuclear data sheets for  $a=129$ ," *Nuclear Data Sheets*, vol. 121, pp. 143–394, 2014.
- [76] Y. Khazov, I Mitropolsky, and A Rodionov, "Nuclear data sheets for  $a=131$ ," *Nuclear Data Sheets*, vol. 107, no. 11, pp. 2715–2930, 2006.
- [77] E Aprile, J Aalbers, F Agostini, M Alfonsi, F. Amaro, M Anthony, L Arazi, F Arneodo, C Balan, P Barrow, *et al.*, "Physics reach of the xenon1t dark matter experiment.," *Journal of Cosmology and Astroparticle Physics*, vol. 2016, no. 04, p. 027, 2016.
- [78] T. Franarin and M. Fairbairn, "Reducing the solar neutrino background in dark matter searches using polarized helium-3," *Physical Review D*, vol. 94, no. 5, p. 053 004, 2016.
- [79] E. Dahl, "The physics of background discrimination in liquid xenon, and first results from xenon10 in the hunt for wimp dark matter.," PhD thesis, Princeton University, 2009.
- [80] T. Takahashi, S Konno, T Hamada, M. Miyajima, S. Kubota, A Nakamoto, A. Hitachi, E. Shibamura, and T. Doke, "Average energy expended per ion pair in liquid xenon," *Physical Review A*, vol. 12, no. 5, p. 1771, 1975.
- [81] E Aprile, K. Giboni, P Majewski, K Ni, and M Yamashita, "Observation of anticorrelation between scintillation and ionization for mev gamma rays in liquid xenon," *Physical Review B*, vol. 76, no. 1, p. 014 115, 2007.
- [82] J. B. Birks, *The Theory and Practice of Scintillation Counting: International Series of Monographs in Electronics and Instrumentation*. Elsevier, 2013, vol. 27.
- [83] J Thomas and D. Imel, "Recombination of electron-ion pairs in liquid argon and liquid xenon," *Physical Review A*, vol. 36, no. 2, p. 614, 1987.
- [84] J Angle, E Aprile, F Arneodo, L Baudis, A Bernstein, A. Bolozdynya, L. Coelho, C. Dahl, L DeViveiros, A. Ferella, *et al.*, "Search for light dark matter in xenon10 data," *Physical Review Letters*, vol. 107, no. 5, p. 051 301, 2011.
- [85] P. Sorensen and C. E. Dahl, "Nuclear recoil energy scale in liquid xenon with application to the direct detection of dark matter," *Physical Review D*, vol. 83, no. 6, p. 063 501, 2011.

- 
- [86] B. Lenardo, K. Kazkaz, A. Manalaysay, J. Mock, M. Szydagis, and M. Tripathi, “A global analysis of light and charge yields in liquid xenon,” *IEEE Transactions on Nuclear Science*, vol. 62, no. 6, pp. 3387–3396, 2015.
  - [87] G Jaffé, “On the theory of ionization in columns,” *Ann. Phys.(Leipzig)*, vol. 42, pp. 303–344, 1913.
  - [88] D.-M. Mei, Z.-B. Yin, L. Stonehill, and A. Hime, “A model of nuclear recoil scintillation efficiency in noble liquids,” *Astroparticle Physics*, vol. 30, no. 1, pp. 12–17, 2008.
  - [89] V. Tretyak, “Semi-empirical calculation of quenching factors for ions in scintillators,” *Astroparticle physics*, vol. 33, no. 1, pp. 40–53, 2010.
  - [90] F. Bezrukov, F. Kahlhoefer, and M. Lindner, “Interplay between scintillation and ionization in liquid xenon dark matter searches,” *Astroparticle Physics*, vol. 35, no. 3, pp. 119–127, 2011.
  - [91] L. Goetzke, E Aprile, M Anthony, G Plante, and M Weber, “Measurement of light and charge yield of low-energy electronic recoils in liquid xenon,” *arXiv preprint arXiv:1611.10322*, 2016.
  - [92] C Silva, J Pinto da Cunha, V Chepel, V Solovov, F Neves, A Pereira, and M. Lopes, “Reflectance of polytetrafluoroethylene (ptfe) for xenon scintillation light,” *J. Appl. Phys.*, vol. 107, no. arXiv: 0910.1056, p. 064 902, 2009.
  - [93] J. Haefner, A. Neff, M. Arthurs, E. Batista, D. Morton, M. Okunawo, K. Pushkin, A. Sander, S. Stephenson, Y. Wang, *et al.*, “Reflectance dependence of polytetrafluoroethylene on thickness for xenon scintillation light,” *Nuclear Instruments and Methods in Physics Research Section A: Accelerators, Spectrometers, Detectors and Associated Equipment*, vol. 856, pp. 86–91, 2017.
  - [94] F Neves, A Lindote, A Morozov, V Solovov, C Silva, P Bras, J. Rodrigues, and M. Lopes, “Measurement of the absolute reflectance of polytetrafluoroethylene (ptfe) immersed in liquid xenon,” *Journal of Instrumentation*, vol. 12, no. 01, P01017, 2017.
  - [95] E Aprile, F Agostini, M Alfonsi, L Arazi, K Arisaka, F Arneodo, M Auger, C Balan, P Barrow, L Baudis, *et al.*, “Lowering the radioactivity of the photomultiplier tubes for the xenon1t dark matter experiment,” *The European Physical Journal C*, vol. 75, no. 11, p. 546, 2015.
  - [96] V. Atrazhev, A. Berezhnov, D. Dunikov, I. Chernysheva, V. Dmitrenko, and G Kapralova, “Electron transport coefficients in liquid xenon,” in *Dielectric*

- Liquids, 2005. ICDL 2005. 2005 IEEE International Conference on*, IEEE, 2005, pp. 329–332.
- [97] E. Aprile, J Aalbers, F Agostini, M Alfonsi, F. Amaro, M Anthony, B Antunes, F Arneodo, M Balata, P Barrow, *et al.*, “The xenon1t dark matter experiment,” *arXiv preprint arXiv:1708.07051*, 2017.
  - [98] E Aprile, M Alfonsi, K Arisaka, F Arneodo, C Balan, L Baudis, B Bauermeister, A Behrens, P. Beltrame, K Bokeloh, *et al.*, “Observation and applications of single-electron charge signals in the xenon100 experiment,” *Journal of Physics G: Nuclear and Particle Physics*, vol. 41, no. 3, p. 035 201, 2014.
  - [99] D.-M. Mei and A Hime, “Muon-induced background study for underground laboratories,” *Physical Review D*, vol. 73, no. 5, p. 053 004, 2006.
  - [100] E Aprile, F Agostini, M Alfonsi, K Arisaka, F Arneodo, M Auger, C Balan, P Barrow, L Baudis, B Bauermeister, *et al.*, “Conceptual design and simulation of a water cherenkov muon veto for the xenon1t experiment,” *Journal of instrumentation*, vol. 9, no. 11, P11006, 2014.
  - [101] S. Agostinelli, J. Allison, K. a. Amako, J Apostolakis, H Araujo, P Arce, M Asai, D Axen, S Banerjee, G Barrand, *et al.*, “Geant4—a simulation toolkit,” *Nuclear instruments and methods in physics research section A: Accelerators, Spectrometers, Detectors and Associated Equipment*, vol. 506, no. 3, pp. 250–303, 2003.
  - [102] E Aprile, J Aalbers, F Agostini, M Alfonsi, F. Amaro, M Anthony, F Arneodo, P Barrow, L Baudis, B Bauermeister, *et al.*, “Material radioassay and selection for the xenon1t dark matter experiment,” *arXiv preprint arXiv:1705.01828*, 2017.
  - [103] A. Fieguth, “Distillation column for the xenon1t experiment,” in *J. Phys. Conf. Ser.*, vol. 718, 2016, p. 042 020.
  - [104] E. Aprile, T. Yoon, A. Loose, L. W. Goetzke, and T. Zelevinsky, “An atom trap trace analysis system for measuring krypton contamination in xenon dark matter detectors,” *Review of Scientific Instruments*, vol. 84, no. 9, p. 093 105, 2013.
  - [105] E Aprile, J Aalbers, F Agostini, M Alfonsi, F. Amaro, M Anthony, F Arneodo, P Barrow, L Baudis, B. Bauermeister, *et al.*, “Online rn222 removal by cryogenic distillation in the xenon100 experiment,” *The European Physical Journal C*, vol. 77, no. 6, p. 358, 2017.

- [106] D. Akerib, S Alsum, H. Araújo, X Bai, A. Bailey, J Balajthy, P Beltrame, E. Bernard, A Bernstein, T. Biesiadzinski, *et al.*, “Kr83m calibration of the 2013 lux dark matter search,” *arXiv preprint arXiv:1708.02566*, 2017.
- [107] P Barrow, L Baudis, D. Cichon, M. Danisch, D. Franco, F. Kaether, A Kish, M. Lindner, T. M. Undagoitia, D Mayani, *et al.*, “Qualification tests of the r11410-21 photomultiplier tubes for the xenon1t detector,” *Journal of Instrumentation*, vol. 12, no. 01, P01024, 2017.
- [108] R. K. Kirby, “Thermal expansion of polytetrafluoroethylene (teflon) from -190° to + 300° c,” *Journal of Research of the National Bureau of Standards*, vol. 57, no. 2, pp. 91–94, 1956.
- [109] *User manual um3248: v1724/vx1724*, Rev. 32, CAEN, Via Vetraia, 11 55049 Viareggio (LU), Italy, Apr. 2017.
- [110] E Aprile, J Aalbers, F Agostini, M Alfonsi, F. Amaro, M Anthony, F Arneodo, P Barrow, L Baudis, B. Bauermeister, *et al.*, “Results from a calibration of xenon100 using a source of dissolved radon-220,” *Physical Review D*, vol. 95, no. 7, p. 072 008, 2017.
- [111] X Du, K Bailey, Z.-T. Lu, P Mueller, T. O’Connor, and L Young, “An atom trap system for practical 81 kr dating,” *Review of Scientific Instruments*, vol. 75, no. 10, pp. 3224–3232, 2004.
- [112] O. Ponkratenko, V. Tretyak, and Y. G. Zdesenko, “Event generator decay4 for simulating double-beta processes and decays of radioactive nuclei,” *Physics of Atomic Nuclei*, vol. 63, no. 7, pp. 1282–1287, 2000.
- [113] R Saldanha, L Grandi, Y Guardincerri, and T Wester, “Model independent approach to the single photoelectron calibration of photomultiplier tubes,” *Nuclear Instruments and Methods in Physics Research Section A: Accelerators, Spectrometers, Detectors and Associated Equipment*, 2017.
- [114] T. Doke, A. Hitachi, S. Kubota, A Nakamoto, and T. Takahashi, “Estimation of fano factors in liquid argon, krypton, xenon and xenon-doped liquid argon,” *Nuclear Instruments and Methods*, vol. 134, no. 2, pp. 353–357, 1976.
- [115] E Aprile, M Alfonsi, K Arisaka, F Arneodo, C Balan, L Baudis, B Bauermeister, A Behrens, P. Beltrame, K Bokeloh, *et al.*, “Response of the xenon100 dark matter detector to nuclear recoils,” *Physical Review D*, vol. 88, no. 1, p. 012 006, 2013.
- [116] C. Faham, V. Gehman, A Currie, A Dobi, P Sorensen, and R. Gaitskell, “Measurements of wavelength-dependent double photoelectron emission from single

- photons in vuv-sensitive photomultiplier tubes,” *Journal of Instrumentation*, vol. 10, no. 09, P09010, 2015.
- [117] T. Bayes, “An essay towards solving a problem in the doctrine of chances,” 1763.
- [118] D. Foreman-Mackey, D. W. Hogg, D. Lang, and J. Goodman, “Emcee: the mcmc hammer,” *Publications of the Astronomical Society of the Pacific*, vol. 125, no. 925, p. 306, 2013.
- [119] S. Chib and E. Greenberg, “Understanding the metropolis-hastings algorithm,” *The american statistician*, vol. 49, no. 4, pp. 327–335, 1995.
- [120] S. P. Brooks and A. Gelman, “General methods for monitoring convergence of iterative simulations,” *Journal of computational and graphical statistics*, vol. 7, no. 4, pp. 434–455, 1998.
- [121] A. Gelman and D. B. Rubin, “Inference from iterative simulation using multiple sequences,” *Statistical science*, pp. 457–472, 1992.
- [122] M. Szydagis, A. Fyhrie, D. Thorngren, and M. Tripathi, “Enhancement of nest capabilities for simulating low-energy recoils in liquid xenon,” *Journal of Instrumentation*, vol. 8, no. 10, p. C10003, 2013.
- [123] M Szydagis, N Barry, K Kazkaz, J Mock, D Stolp, M Sweany, M Tripathi, S Uvarov, N Walsh, and M Woods, “Nest: a comprehensive model for scintillation yield in liquid xenon,” *Journal of Instrumentation*, vol. 6, no. 10, P10002, 2011.
- [124] D. Akerib, S Alsum, H. Araújo, X Bai, A. Bailey, J Balajthy, P Beltrame, E. Bernard, A Bernstein, T. Biesiadzinski, *et al.*, “Low-energy (0.7-74 kev) nuclear recoil calibration of the lux dark matter experiment using dd neutron scattering kinematics,” *arXiv preprint arXiv:1608.05381*, 2016.
- [125] E Aprile, J Aalbers, F Agostini, M Alfonsi, F. Amaro, M Anthony, F Arneodo, P Barrow, L Baudis, B. Bauermeister, *et al.*, “Xenon100 dark matter results from a combination of 477 live days,” *Physical Review D*, vol. 94, no. 12, p. 122001, 2016.
- [126] A Manzur, A Curioni, L Kastens, D. McKinsey, K Ni, and T Wongjirad, “Scintillation efficiency and ionization yield of liquid xenon for monoenergetic nuclear recoils down to 4 kev,” *Physical Review C*, vol. 81, no. 2, p. 025808, 2010.

- [127] *Neutron/gamma psd liquid scintillator ej-301, ej-309*, Eljen Technology, 1300 W. Broadway, Sweetwater, TX 79556, 2016.
- [128] G. Plante, E Aprile, R Budnik, B Choi, K.-L. Giboni, L. Goetzke, R. Lang, K. Lim, and A. M. Fernandez, “New measurement of the scintillation efficiency of low-energy nuclear recoils in liquid xenon,” *Physical Review C*, vol. 84, no. 4, p. 045805, 2011.
- [129] L. W. Goetzke, *Low-Energy Electronic Recoils in Liquid Xenon: Search for Annual Modulation with XENON100, Measurement of Charge and Light Yield with neriX, and Measurement of Krypton in Xenon with ATTA*. Columbia University, 2015.
- [130] K. Giboni, E Aprile, B Choi, T Haruyama, R. Lang, K. Lim, A. Melgarejo, and G Plante, “Xenon recirculation-purification with a heat exchanger,” *Journal of Instrumentation*, vol. 6, no. 03, P03002, 2011.
- [131] G. Plante, *The XENON100 Dark Matter Experiment: Design, Construction, Calibration and 2010 Search Results with Improved Measurement of the Scintillation Response of Liquid Xenon to Low-Energy Nuclear Recoils*. Columbia University, 2012.
- [132] G. Csikai, *CRC handbook of fast neutron generators*. CRC Press Inc., Boca Raton, FL, 1987.
- [133] *Technical manual for an/pdr-70 (snoopy np-2) neutron survey meter*, Canberra Industries, 800 Research Parkway Meriden, CT 06450, 2003.
- [134] F. T. Kuchnir and F. J. Lynch, “Time dependence of scintillations and the effect on pulse-shape discrimination,” *IEEE Transactions on Nuclear Science*, vol. 15, no. 3, pp. 107–113, 1968.
- [135] R. Lang, D Masson, J Pienaar, and S Röttger, “Improved pulse shape discrimination in ej-301 liquid scintillators,” *Nuclear Instruments and Methods in Physics Research Section A: Accelerators, Spectrometers, Detectors and Associated Equipment*, vol. 856, pp. 26–31, 2017.
- [136] M Anthony, E Aprile, L Grandi, Q Lin, and R Saldanha, “Characterization of photomultiplier tubes with a realistic model through gpu-boosted simulation,” *arXiv preprint arXiv:1710.00219*, 2017.
- [137] D. Carter, “Photomultiplier handbook: theory, design, application,” *Lancaster, (PA): Burle Industries, Inc*, 1980.

## BIBLIOGRAPHY

---

- [138] D. Akerib, H. Araújo, X Bai, A. Bailey, J Balajthy, P Beltrame, E. Bernard, A Bernstein, T. Biesiadzinski, E. Boulton, *et al.*, “Improved limits on scattering of weakly interacting massive particles from reanalysis of 2013 lux data,” *Physical review letters*, vol. 116, no. 16, p. 161 301, 2016.
- [139] E Aprile, L Baudis, B Choi, K. Giboni, K Lim, A Manalaysay, M. Monzani, G Plante, R Santorelli, and M Yamashita, “New measurement of the relative scintillation efficiency of xenon nuclear recoils below 10 kev,” *Physical Review C*, vol. 79, no. 4, p. 045 807, 2009.
- [140] B. Gompertz, “On the nature of the function expressive of the law of human mortality, and on a new mode of determining the value of life contingencies,” *Philosophical transactions of the Royal Society of London*, vol. 115, pp. 513–583, 1825.
- [141] E Aprile, K. Giboni, P Majewski, K Ni, M Yamashita, R Hasty, A Manzur, and D. McKinsey, “Scintillation response of liquid xenon to low energy nuclear recoils,” *Physical Review D*, vol. 72, no. 7, p. 072 006, 2005.
- [142] P Sorensen, A Manzur, C. Dahl, J Angle, E Aprile, F Arneodo, L Baudis, A Bernstein, A Bolozdynya, L. Coelho, *et al.*, “The scintillation and ionization yield of liquid xenon for nuclear recoils,” *Nuclear Instruments and Methods in Physics Research Section A: Accelerators, Spectrometers, Detectors and Associated Equipment*, vol. 601, no. 3, pp. 339–346, 2009.
- [143] M Horn, V. Belov, D. Y. Akimov, H. Araújo, E. Barnes, A. Burenkov, V Chepel, A Currie, B Edwards, C Ghag, *et al.*, “Nuclear recoil scintillation and ionisation yields in liquid xenon from zeplin-iii data,” *Physics Letters B*, vol. 705, no. 5, pp. 471–476, 2011.
- [144] G. R. Terrell and D. W. Scott, “Variable kernel density estimation,” *The Annals of Statistics*, pp. 1236–1265, 1992.
- [145] *Nvidia geforce gtx 1080*, 2016.
- [146] E. Bellamy, G Bellettini, J Budagov, F Cervelli, I Chirikov-Zorin, M Incagli, D Lucchesi, C Pagliarone, S Tokar, and F Zetti, “Absolute calibration and monitoring of a spectrometric channel using a photomultiplier,” *Nuclear Instruments and Methods in Physics Research Section A: Accelerators, Spectrometers, Detectors and Associated Equipment*, vol. 339, no. 3, pp. 468–476, 1994.
- [147] R. Dossi, A. Ianni, G. Ranucci, and O. J. Smirnov, “Methods for precise photoelectron counting with photomultipliers,” *Nuclear Instruments and Methods*

- in Physics Research Section A: Accelerators, Spectrometers, Detectors and Associated Equipment*, vol. 451, no. 3, pp. 623–637, 2000.
- [148] J. De Haas and P Dorenbos, “Methods for accurate measurement of the response of photomultiplier tubes and intensity of light pulses,” in *Nuclear Science Symposium Conference Record (NSS/MIC), 2010 IEEE*, IEEE, 2010, pp. 205–210.
  - [149] H. H. Tan, “A statistical model of the photomultiplier gain process with applications to optical pulse detection,” in *International Telemetering Conference Proceedings*, International Foundation for Telemetering, 1982.
  - [150] N. C. Dwarakanath and S. D. Galbraith, “Sampling from discrete gaussians for lattice-based cryptography on a constrained device,” *Applicable Algebra in Engineering, Communication and Computing*, vol. 25, no. 3, pp. 159–180, 2014.
  - [151] D. Mayani, “Photomultiplier tubes for the xenon1t dark matter experiment and studies on the xenon100 electromagnetic background,” PhD thesis, University of Zurich, 2017.



# Appendix A

## GPUs and Fast Monte Carlo Matching for Parameter Estimation

In this appendix we will go into more detail about the analysis framework that was briefly mentioned in the previous chapters that was used for the electronic and nuclear recoil calibration. This framework, proposed and developed by the author for the analysis discussed in chapter four, enables the use of non-analytical models for parameter estimation in a reasonable time frame.

### A.1 Motivation

Oftentimes in physics, very complicated processes can be very well approximated by very simple and analytical probability distributions. There are many examples of these useful approximations in this work alone, including the majority of the calibrations for XENON1T (Sec. 3.3) and neriX (Sec. 4.2).

However, the work in this appendix is an answer proposed by the author to the question of what do we do when no such approximation exists or is not appropriate? This situation arises several times in this work: for the electronic and nuclear recoil calibration in XENON1T (Sec. 3.4), the measurement of the nuclear recoil response of

liquid xenon in neriX (Sec. 4.4), and the characterization of the single photoelectron response of the neriX and XENON1T photomultiplier tubes (App. B).

## A.2 Parameter Estimation through Monte Carlo

### A.2.1 Overview

For parameter estimation, the ultimate requirement is that you have a likelihood function that can be used to compare different sets of parameters with each other. Many models are well approximated by an analytical distribution, such as a normal, Poisson, or exponential distribution to name a few of the most common. When this is the case, as it often is, there are several common approaches to assigning a likelihood function. One simple solution is to use the probability distribution function (PDF) of the distribution with the parameters under test evaluated at all points as the likelihood function, as shown in Eqn. A.1 where  $m$  is indexed over all of the data points. Another approach is to use a binned likelihood, as shown in Eqn. A.2 where  $i$  is indexed over each of the bins, where we use the distribution to estimate the expected number of events in a given bin.

$$\mathcal{L} = \prod_m f(\vec{x}_m; \vec{\theta}) \quad (\text{A.1})$$

$$\mathcal{L} = \prod_i \frac{\hat{b}_i^{b_i} e^{-\hat{b}_i}}{b_i!} \quad (\text{A.2})$$

In Eqn. A.1,  $f$  is the probability distribution function of the distribution,  $\vec{x}_m$  is the  $m^{\text{th}}$  data point, and  $\vec{\theta}$  are the parameters under test. In Eqn. A.2,  $b_i$  is the number of data points that fall into bin  $i$  and  $\hat{b}_i$  is the expected number of events in the bin given a PDF  $f$  and parameters under test  $\vec{\theta}$  (usually found via integration of  $f$  at the bin or evaluating  $f$  at the bin's midpoint). The former method is typically preferred since more information is utilized however the second is an oft-used approximation since the former method is more computationally intensive.

When our data is most likely described by a model that does not have an analytical form of the PDF this leaves us with significantly more limited options. These non-analytical models, in other words, are not well approximated by distributions whose PDF has a functional form for the parameters under test. One approach, is to use a Monte Carlo simulation of the model to produce an estimate of the PDF that is then compared to data. This estimate of the PDF can be a Kernel Density Estimator [144] in which case an unbinned likelihood function can be used to evaluate the likelihood for the parameters under test however we will focus on using a Monte Carlo simulation to produce an estimate of the PDF in the form of a histogram for which we can use the binned likelihood function to evaluate the likelihood for the parameters under test.

### A.2.2 Estimating the Likelihood Using Monte Carlo

As mentioned in the previous section, we can, in a fairly straightforward way, provide a likelihood function for parameter estimation using a Monte Carlo simulations whose output is subsequently binned in a histogram. Let us assume that our model has a true PDF  $f(x)$  for parameters  $\vec{\theta}$ . This implies that the probability that a single event lies in a given bin is given by the integral of the PDF. This is shown in Eqn. A.3 where  $F$  is the cumulative distribution function  $x_0$  is the bin's left edge and  $h$  is the width of the bin.

$$p_i = F(x_0 + h; \vec{\theta}) - F(x_0; \vec{\theta}) \quad (\text{A.3})$$

Bin sizes may almost always be chosen such that  $p_i$  is consistently small ( $p_i \lesssim 5\%$ ). In Monte Carlo we typically simulate very large numbers of events,  $N$ . Therefore, we say the probability distribution for the number of events in a given bin  $i$ ,  $X_i$ , is well approximated by a Poisson distribution as shown in Eqn. A.4.

$$X_i \sim P(\mu_i = p_i N) \quad (\text{A.4})$$

The first two moments of  $X_i$ , the mean and variance, will both be equal to  $p_i N$  in

this case. With our estimation of the distribution events in the given bin, we can now estimate the probability of a given event occurring in a particular bin,  $\hat{p}_i$ . To do this, we run a Monte Carlo simulation and set the number of events from the simulation in that given bin,  $x_i$ , equal to the expectation value for that bin, as shown in Eqn. A.5.

$$x_i = \hat{p}_i N \implies \hat{p}_i = \frac{x_i}{N} \quad (\text{A.5})$$

Since  $x_i$  is actually drawn from a Poisson distribution,  $\hat{p}_i$  is also a random variable with a variance given by Eqn. A.6.

$$\sigma_{\hat{p}_i}^2 = \frac{\sigma_{X_i}^2}{N^2} = \frac{p_i}{N} \quad (\text{A.6})$$

Eqn. A.6 shows, as expected, that the variance of our estimator decreases as the number of Monte Carlo trials increases. As seen in Eqn. A.2, we actually need the expectation for the number of events in a given bin. Assuming that we have  $M$  data points, from a rate which can be left as an additional free parameter during estimation, and this number is large we can again assume that the distribution for the number of events in a given bin is Poisson with a mean of  $\hat{p}_i M$ . Therefore, we say that the expected number of events in a given bin,  $\hat{b}_i$  is equal to the expectation value  $\hat{p}_i M$  and the variance is given by Eqn. A.7.

$$\sigma_{\hat{b}_i}^2 = \sigma_{p_i}^2 M = \frac{p_i M^2}{N} \quad (\text{A.7})$$

Therefore, by running a high-statistic Monte Carlo and binning the results, we can approximate the expectation for a given bin and use the binned likelihood function, allowing us to proceed with parameter estimation.

### A.2.3 Drawbacks of Monte Carlo Likelihood Estimation

While the above approach is a very useful solution to a common problem, it is rarely used. The reason is that there are drawbacks that must be addressed when utilizing this approach.

First,  $\hat{b}_i$  is a random variable which implies that the likelihood and log-likelihood are also random variables. In other words, for the same parameters under test one will get different values for the log-likelihood. It is important to be aware of this effect when using this method and to ensure that the fluctuations in log-likelihood are small. It is also important to note that these fluctuations will not affect the end result but could pose technical challenges for given choices of minimizers (particularly ones that are dependent on the gradient of the log-likelihood) and slow down convergence. It is recommended to use minimizers based on genetic algorithms or a Markov Chain Monte Carlo (MCMC) to perform the parameter estimation due to this technical challenge.

Two simple solutions to reduce the fluctuations in log-likelihood and improve the convergence speed are to increase the number of Monte Carlo iterations or to increase the size of each bin. A less desirable but alternate solution when performing a Bayesian analysis is to suppress the log-likelihood at each stage of the iteration, artificially decreasing the fluctuations. This likelihood suppression allows for faster convergence and is useful if it is unreasonable to increase Monte Carlo statistics but it means that you cannot be as precise as you otherwise could (note that the maximum in the log-likelihood will still be the maximum in the modified space).

Second, if  $p_i$  for a given bin is nearly zero it is possible that the Monte Carlo run will produce no events in that bin. This implies that  $\hat{p}_i$  and  $\hat{b}_i$  would be exactly equal to zero which is unacceptable for the Poisson distribution implicit in the binned log-likelihood. Again, there are many ways to handle this type of issue but the simplest is to alter the binning such that each  $p_i$  is approximately the same.

The third drawback is that the computational cost of running a large MC on each iteration of a fit is extremely high. This issue and the solution used are discussed in more detail in Sec. [A.3](#).

## A.3 Graphical Processing Units for Monte Carlo Matching for Parameter Estimation

### A.3.1 Graphical Processing Units

A graphical processing unit, also known as a GPU, is a programmable processor specialized for highly parallelizable tasks. While CPUs typically consist of a few very powerful cores for processing, GPUs have a very large collection of less powerful cores. Originally developed for graphics displays, as the name would imply, in recent years GPU card manufacturers have made it easier for the cards to be put to use in scientific settings by creating GPU computing platforms that abstract away many of the difficulties in GPU programming.

While a single task on a single core of a GPU will run significantly more slowly than that task on a core of a CPU, the power of GPUs comes from the number of cores that it has. A standard GPU will now have thousands of these cores fit onto a single board. While not every task can be accelerated by using a GPU, tasks that are highly parallelizable and relatively simple, such as graphics operations, can see orders of magnitude improvements in computing speed. Monte Carlo simulations are usually fairly simple, typically only requiring draws from well-known probability distributions, and require massive numbers of iterations making them a prime candidate for speed improvements on a GPU.

### A.3.2 GPU-Based MC Matching Framework

Despite the name, the bulk of the MC Matching framework is not built for use on the GPU — only the most computationally intensive and massively-parallelizable parts, the Monte Carlo and its sorting into a histogram, is done on the GPU. The rest of the framework, including the actual log-likelihood calculations and the Markov Chain Monte Carlo (or minimizer) are controlled by the CPU.

This implies that communication between the CPU and GPU is essential. While memory transfers are increasing in speed with each generation of GPU card, a large

memory ( $\gtrsim 1$  MB) transfer can still noticeably reduce the speed gain from migrating the Monte Carlo from the CPU to the GPU. Therefore, one must take care to avoid large repetitive memory transfers. For example, in the nuclear recoil response calibrations discussed in chapters three and four an input energy was needed to begin the Monte Carlo and the spectrum had no analytical form such that it could be generated quickly on the GPU. Transferring energies at each Monte Carlo simulation would be extremely slow given that the size of the array to be copied to the GPU was on the order of several hundred MB. Fortunately, NVIDIA includes a feature called *pinned memory*, where information can be stored and retrieved as long as the GPU is active. This feature allowed us to transfer the input energies a single time (since the energy spectrum was not dependent on the parameters in the fit) and spared us the repetitive memory transfers. This pinned memory is used for all single-use inputs, like the energy and the binning, in this framework.

As mentioned, the GPU in the framework is used for the most computationally intensive parts of the procedure: the Monte Carlo simulation and the sorting into a histogram. The actual code for both of these parts is written in CUDA C and using the libraries included in the CUDA computing platform — both of which are specifically designed by NVIDIA for easy use with their GPUs.

CUDA comes preloaded with many random number generators in the cuRAND library for use in the Monte Carlo, including the normal, uniform, and Poisson distributions. One can easily build short functions using these distributions to create generators for other required distributions such as the binomial and exponential distributions. CUDA also comes loaded with an extensive library of mathematical functions if those are also required in a simulation.

CUDA does not, however, come preloaded with the ability to produce histograms. However, basic functions to provide this capability can easily be written by the user.

Once the histogram is filled the GPU can pass the histogram back to the CPU where it is then used to calculate the likelihood.

Fig. A.1 shows the memory flow described above. The black arrows represent memory transfers that are performed a single time while orange arrows represent

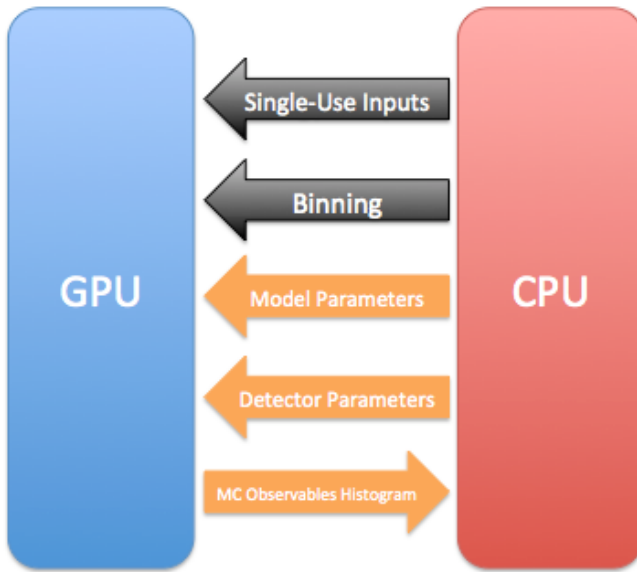


Figure A.1: The memory flow in the Monte Carlo Matching Framework. The black arrows represent memory transfers that are performed a single time while orange arrows represent memory transfers that are performed in each log-likelihood calculation.

memory transfers that are performed in each log-likelihood calculation.

### A.3.3 Speed Gains for GPUs versus CPU

While the speed increase for the Monte Carlo varies on the content and the type of CPU and GPU used, in each of our applications we saw speed increases of roughly 100–1000 times on the GPUs used versus the CPUs when performing the Monte Carlo simulation and filling histograms. This easily pulls otherwise unfeasible tasks into the realm of possibility.

### A.3.4 Parallelizing GPUs

Due to the high level of computing power needed to perform the parameter estimation for the *neriX* nuclear recoil response measurement, we found that the speed increase seen with a single GPU was not quite enough for our purposes. Therefore we built a custom GPU-based server that could hold and use eight GPU cards at a time. This



Figure A.2: The GPU-based server used for the analyses in this work. The actual GPU cards can be seen towards the back of the server (three on the left and right sides).

server was filled with six GTX 1080 cards from NVIDIA [145] for a maximum speed of roughly 54 TFLOPs<sup>1</sup>. A photo of the GPU server mounted and in use is shown in Fig. A.2.

The parallelization model that proved the most efficient also proved to be the simplest. Each GPU card was activated and managed by a single CPU thread. The MCMC used for each fit utilized the affine-invariant algorithm [118] that requires multiple “walkers” calculating the log-likelihood at different positions in the parameter space at each step<sup>2</sup>. Therefore, a first-in-first-out queue data structure was used to pass the parameters of the fit of each walker to each CPU thread which in turn used its individual GPU card to run the Monte Carlo simulation and sorting for the log-likelihood calculation. We found that this implementation had negligible efficiency losses so the speed of parameter estimation increased linearly with the number of GPU cards used.

---

<sup>1</sup>A typical CPU falls in the range of tens to hundreds of GFLOPs.

<sup>2</sup>In all analyses in this work, either 256 or 512 walkers were used to sample the posterior.

## A.4 Discussion

GPU-based Monte Carlo matching methods open the door to many exciting possibilities — all of the major analyses discussed in this work, including the electronic and nuclear recoil calibrations of XENON1T, the nuclear recoil response measurement of neriX, and the characterization of the single photoelectron response of PMTs, were only made possible through the methods discussed in this appendix. While other methods have been used to perform these measurements, they typically involved large simplifications. With GPUs, however, our models can be significantly more complicated than they could have been in the past. Even more exciting is that GPU technology is rapidly improving every year and each new card introduced is a significant improvement on the previous generation so the gains are only likely to improve.

Since the GPU code is very specific to the application, individual examples have not been included in this appendix. However, all of the author’s work and countless examples from other sources are publicly available for reference online.

# Appendix B

## Characterization of Photomultiplier Tubes with the Cascade Model

### B.1 Motivation

Photomultiplier tubes (PMTs) are widely used to detect low levels of light in many fields of physics, especially in the field of dark matter detection. However, despite their ubiquitousness, calibration and characterization of the single photoelectron (SPE) charge response of PMTs remains in a fairly basic state. PMTs are very complicated devices yet they are often treated with a simple approximation: that the SPE charge response is Gaussian [146, 147]. While this approximation is satisfactory for specific PMTs within certain voltage ranges, it is far from true in general. Since the Gaussian distribution is not bounded below by zero, the response function cannot be correct for a SPE and oftentimes, when PMT calibrations are performed with low PMT voltages, the response function will have a large probability of producing a non-physical signal.

Several alternatives have been proposed to improve upon existing methods for determining the single photoelectron response. An empirical approach is presented

## B. CHARACTERIZATION OF PHOTOMULTIPLIER TUBES WITH THE CASCADE MODEL

---

in Ref. [148] but is only relevant when the height of the PMT output is needed and not the integral of the pulse. Another widely used model independent approach is presented in Ref. [113]. The model independent approach provides a simple way to accurately determine the mean and variance of the single photoelectron response function. In many cases, the mean and variance of the SPE response are enough since at moderate numbers of photoelectrons the response function converges to a Gaussian described by these parameters. However, at small numbers of photoelectrons, it is important to account completely for the SPE response shape. Additionally, the results of the model independent method become more susceptible to bias when the background distribution width is large and the PMT gain is low and it requires a consistent and dedicated background measurement, which is not always possible as was the case for neriX. Background, in this work, is used to describe all signals that are not induced by the laser or diode, such as noise from the electronics, dark counts, or photoelectrons from light sources other than the laser or diode.

In this appendix, we discuss a more realistic model, henceforth referred to as the *cascade model*, which aims at capturing the actual behavior and mechanics of the PMT. As with the other major analyses presented in this work(see Sec. 3.4 and Sec. 4.4 for more details on these analyses), the model does not have an analytical form that can be used for parameter estimation but rather relies on running a Monte Carlo (MC) simulation with each set of parameters under test to find the posterior and the best-fit parameters given the data. These MC simulations also are performed using the GPU framework discussed in App. A.

## B.2 The Cascade Single Photoelectron Charge Response Model

With almost countless varieties of PMTs used in different settings, it is impossible to describe a single model that will accurately characterize all PMTs under all circumstances. However, in this work, we present a SPE response model that has been

found to be successful for two very different PMTs and which is physically motivated according to Ref. [137].

In the cascade model, there are three different physical processes that can produce an output signal. Each of these scenarios is depicted in Fig. B.1.

1. Full amplification: this is the most common process for producing a signal from the PMT. This occurs when a photon is absorbed by the photocathode which then releases an electron (referred to as a photoelectron). This electron is then accelerated to the first of the multiple dynodes found inside of the PMT. This electron will then strike the surface of the dynode and release more electrons in the process. These secondary electrons are then accelerated towards the second dynode. This process continues through all the dynode stages and results in a signal that is proportional to the number of photons initially absorbed by the photocathode.
2. Bad trajectory amplification of photoelectrons from the photocathode: this is very similar to full amplification with a single important change. The electron released from the photocathode may follow a non-ideal trajectory which will result in secondary electrons potentially not reaching the next stage of amplification. This will ultimately result in lower amplification and is caused by electric field imperfections in the PMT.
3. Amplification from direct excitation of the first dynode: this occurs when a photon passes through the photocathode and strikes the first dynode, in turn releasing an electron. This electron then follows the chain of amplification, albeit with one less dynode. The initial electron may also follow a non-ideal trajectory which results in smaller than normal amplification even accounting for the loss of a dynode stage.

To approximate these three physical processes in the SPE response, eight parameters were used:

- $p_{pc}$ : the probability that an incident photon produces a photoelectron from the photocathode that is amplified.

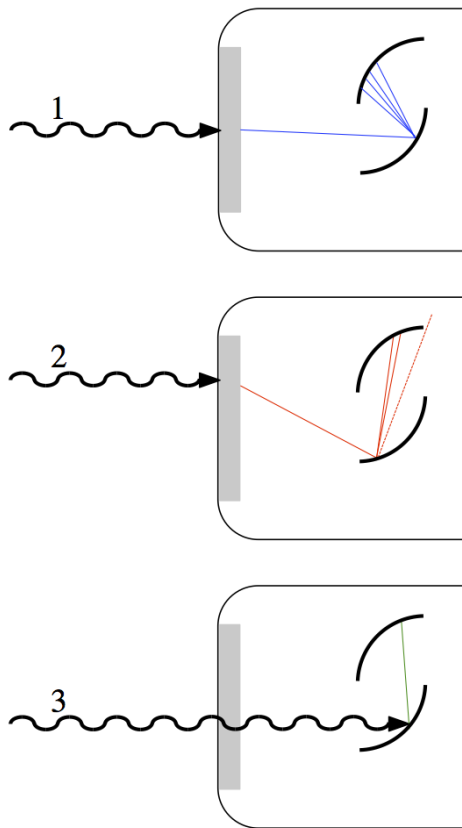


Figure B.1: The three possible scenarios for photoelectrons in the cascade model. Scenario 1 shows the standard full-amplification: a photon is absorbed in the photocathode and an electron is amplified through the dynode chain. Scenario 2 shows a non-ideal trajectory: a photon is absorbed in the photocathode but the electron follows a slightly different trajectory, due to field imperfections, and suffers a slightly lower amplification. Scenario 3 shows a photon passing through the photocathode and releasing an electron on the first dynode. Note that in this scenario the amplification at each dynode may depend on where the incident photon strikes the first dynode.

- $p_{fd}$ : the probability that an incident photon produces a photoelectron from the first dynode that is amplified. Note that an incident photon cannot create a photoelectron on both the photocathode and the first dynode.
- $p_{bt}$ : the probability that a photoelectron from the photocathode will follow a non-ideal trajectory through the dynodes and will require a correction to the resulting amplification.
- $\mu_{epd}, \sigma_{epd}^2$ : the mean and variance of the truncated discrete Gaussian, used to

find how many secondary electrons are produced by each incoming electron at each dynode stage, for the smallest electric field in the dynode chain. These parameters are increased linearly with the electric field at each dynode stage.

- $p_c$ : the probability that secondary electrons escape the surface of the dynode and reach the following dynode.
- $c_{fd}$ ,  $c_{bt}$ : the corrections applied to  $p_c$  accounting for differences in photoelectron amplification from the first dynode and for underamplification due to bad trajectories.

The photoelectron of the SPE response in the cascade model has two potential points of origin: (1) the photocathode or (2) the first dynode. This implies that the origination is described by a binomial process with a single trial.

$$n_{pc} \sim B\left(n = 1; p = \frac{p_{pc}}{p_{pc} + p_{fd}}\right), \quad n_{fd} = 1 - n_{pc}. \quad (\text{B.1})$$

In the above equation,  $n_{pc}$  accounts for all electrons coming from the photocathode and  $n_{fd}$  accounts for all electrons coming directly from the first dynode.

It is important to note that certain PMTs are found to produce two photoelectrons instead of a single photoelectron at the photocathode with a measured probability,  $p_{DPE}$ , at certain wavelengths of incident light. A measurement of this effect is described in Ref. [116]. One can simply account for this double photoelectron effect by adding a binomial process.

$$n_{pc} \leftarrow n_{pc} + B(n = n_{pc}, p = p_{DPE}). \quad (\text{B.2})$$

Further dividing electrons from the photocathode, the model assumes a fixed probability that the electron will follow a bad trajectory.

$$n_{bt} \sim B(n = n_{pc}, p = p_{bt}), \quad n_{fa} = n_{pc} - n_{bt}. \quad (\text{B.3})$$

In the above equation,  $n_{bt}$  is the number of electrons from the photocathode that follow a bad trajectory, resulting in underamplification, and  $n_{fa}$  is the number of

## B. CHARACTERIZATION OF PHOTOMULTIPLIER TUBES WITH THE CASCADE MODEL

---

electrons that are fully amplified from the photocathode through the entire dynode chain.

With all three potential signal sources accounted for, one can now consider the dynode chain. For the dynode chain, it is assumed that the electrons follow a Galton-Watson branching process as described in Ref. [149]. However, instead of the Poisson distribution as described in Ref. [149], the model assumes that the the number of secondary electrons at each dynode stage is described by a discrete Gaussian (as described in Ref. [150]) and a binomial process (with probability of success  $p_c$ ) to be as general as possible (since the shape and variance of a Poisson distribution are fixed by its mean). This iterative process is described in Eqn. B.4 and Eqn. B.5. In these equations,  $h_i$  is the number of secondary electrons leaving the  $i^{th}$  dynode while  $m_i$  is the number of electrons that reach the  $i^{th}$  dynode.

$$h_i \sim DG(n = m_i \mu_{epd}, \sigma^2 = m_i \sigma_{epd}^2). \quad (\text{B.4})$$

$$m_{i+1} \sim B(n = h_i, p = p_c). \quad (\text{B.5})$$

For the bad trajectory electrons from the photocathode and the electrons from the direct excitation of the first dynode, the Galton-Watson process is modified such that  $p_c \rightarrow p_c c_{fd}$  or  $p_c \rightarrow p_c c_{bt}$  to account for their non-ideal trajectory. This correction is applied identically to each dynode in the chain. Differences in the electric fields between dynodes are accounted for by proportionally increasing the mean and variance of the discrete Gaussian ( $\mu_{epd}$  and  $\sigma_{epd}^2$  represent the mean and variance of the Galton-Watson process for the smallest electric field in the chain).

While there is not an analytical function to describe the SPE response in the cascade model, we can use the procedure outlined in App. A to define a likelihood and ultimately sample the posterior.

## B.3 Data Collection

Low light level data was used from two independent experiments using two different methods of data collection and PMTs. The first set of data was provided by the experiment described in Ref. [113]. This data is from a Hamamatsu R11410, a 3 inch PMT, the low-background version of which was used in the XENON1T experiment [77]. The PMT was operated in a dark box with a 405 nm pulsed laser behind a filter with an attenuation factor  $\eta$ . By changing  $\eta$ , one can change the mean number of incident photons. Background measurements were also taken for this data in the exact same operating conditions except with the laser light blocked.

The second set of data is from the neriX detector discussed in chapter four. This data is from a Hamamatsu R6041-406 SEL 2" PMT in LXe illuminated by a blue pulsed LED located inside the detector. The PMT used to collect this data operates at a significantly lower gain than the PMT used in Ref. [113] and has worse noise conditions. Also, identical conditions during background measurements could not be guaranteed and therefore the model independent approach could not be used to characterize this PMT.

In both experiments, the digitized waveforms were integrated with consistent acquisition windows.

Also, the light used to illuminate the PMTs in both experiments had a wavelength larger than 400 nm so double photoelectron emission (DPE) effects were not included [116]. As mentioned in Sec. B.2, DPE effects can straight-forwardly be added to the cascade model if needed.

## B.4 Results

### B.4.1 Response Characterizations

Three methods were used to characterize the PMTs for which data was collected. The first was the cascade model, for which the SPE response was described in detail in Sec. B.2. With the model of the SPE response, we can approximate the response

## B. CHARACTERIZATION OF PHOTOMULTIPLIER TUBES WITH THE CASCADE MODEL

---

of larger signals by convolving the SPE response function ( $f_1$  in Eqn. B.7) with itself for the number of photoelectrons needed. Finally, one must consider detector specific effects by convolving the signal with the background spectrum ( $f_0$  as defined in Eqn. B.6). In this work, the background is approximated as Gaussian from independent measurements.

$$f_0(x) = N(\mu = \mu_{bkg}, \sigma^2 = \sigma_{bkg}^2). \quad (\text{B.6})$$

$$f_n(x) = f_0(x) \circledast \overbrace{f_1(x) \circledast f_1(x) \circledast \dots \circledast f_1(x)}^{\text{n times}}. \quad (\text{B.7})$$

To perform parameter estimation, one must consider how the PMT is illuminated. Since low light levels are used, one expects the number of photoelectrons produced per light pulse to follow a Poisson distribution with a mean  $\lambda$ . One then combines the individual contributions to define the PDF of the full spectrum at a certain light level that will be used (Eqn. B.8).

$$f(x) = P(k = 0, \mu = \lambda) \cdot f_0(x) + \sum_{i=1}^{\infty} (P(k = i, \mu = \lambda) \cdot f_i(x)). \quad (\text{B.8})$$

The second method used was the model independent characterization, which is described in detail in Ref. [113]. The model independent method uses the statistical properties of the laser calibration charge spectra and a background-only charge spectra to estimate the mean and variance of the single photoelectron response, as well as the mean number of photoelectrons produced per light pulse. This method has the advantage that it does not assume any specific functional form for the SPE response as the PMT response converges to a Gaussian for signals with more than roughly five to ten photoelectrons. However the method requires a dedicated background measurement in identical operating conditions, and additional parameters may be needed if one needs to simulate the full functional response of a PMT at very low light levels.

The third method used to characterize the PMTs was the Gaussian approximation with an underamplified peak. In this case, the SPE response is the sum of two Gaussians - one representing fully-amplified photoelectrons and the other representing

underamplified photoelectrons. One can estimate larger signals in the same way as the cascade model: by convolving the SPE response function ( $s_1$  as defined in Eqn. B.9) with itself for the number of photoelectrons needed and then with the background as shown in Eqn. B.10.

$$s_1(x) = N(\mu = \mu_1, \sigma^2 = \sigma_1^2) + w \cdot N(\mu = \mu_u, \sigma^2 = \sigma_u^2), \quad 0 \leq w \leq 1. \quad (\text{B.9})$$

$$g_n(x) = f_0(x) \circledast \overbrace{s_1(x) \circledast s_1(x) \circledast \dots \circledast s_1(x)}^{\text{n times}}. \quad (\text{B.10})$$

Finally, to produce the PDF for parameter estimation, one defines a mean number of photoelectrons per pulse and sums each peaks individual contributions weighted by a Poisson distribution (Eqn. B.11). This is done in the same way as the cascade model.

$$g(x) = P(k = 0, \mu = \lambda) \cdot f_0(x) + \sum_{i=1}^{\infty} (P(k = i, \mu = \lambda) \cdot g_i(x)). \quad (\text{B.11})$$

In these equations,  $\lambda$  is the mean number of PE and  $\mu_u$  and  $\sigma_u$  are the mean and standard deviation of the underamplified peak. The Gaussian model is motivated by the work in Ref. [151].

### B.4.2 Hamamatsu R11410 Analysis

The R11410 data includes a dedicated background measurement that can be used to constrain the model. For example, an exponential contribution to the background (as suggested in Ref. [146]) is ruled out and  $\mu_{bkg}$  and  $\sigma_{bkg}$  are constrained with a prior during the fits for both the cascade and Gaussian model (the background spectrum is shown figures 4, 6, and 7 in Ref. [113]).

While in a standard experiment one could take multiple datasets while varying light levels and fit all data simultaneously to calibrate the SPE response, in this work it was decided to fit each light level individually in order to compare these results

## B. CHARACTERIZATION OF PHOTOMULTIPLIER TUBES WITH THE CASCADE MODEL

Voltage [V]		1400	1500	1600	1700	1700
$\eta$		2E5	2E5	2E5	2E5	1E5
$\lambda$	MI	$1.257 \pm 0.005$	$1.289 \pm 0.005$	$1.324 \pm 0.005$	$1.351 \pm 0.005$	$2.395 \pm 0.008$
	CM	$1.226_{-0.043}^{+0.123}$	$1.256_{-0.010}^{+0.010}$	$1.300_{-0.008}^{+0.009}$	$1.315_{-0.009}^{+0.008}$	$2.372_{-0.022}^{+0.025}$
	GM	$1.188_{-0.018}^{+0.022}$	$1.201_{-0.008}^{+0.009}$	$1.234_{-0.009}^{+0.011}$	$1.275_{-0.013}^{+0.014}$	$2.284_{-0.032}^{+0.029}$
$\lambda_{FA}$	CM	$1.063_{-0.007}^{+0.007}$	$1.039_{-0.007}^{+0.007}$	$1.039_{-0.006}^{+0.006}$	$1.042_{-0.006}^{+0.006}$	$1.842_{-0.016}^{+0.015}$
$\mu$ [ $e^-$ ]	MI	$1.88E6 \pm 7E3$	$3.10E6 \pm 1E4$	$4.98E6 \pm 2E4$	$7.88E6 \pm 2E4$	$7.90E6 \pm 2E4$
	CM	$1.87E6 \pm 1.5E5$	$3.17E6 \pm 2E4$	$5.12E6 \pm 3E4$	$8.03E6 \pm 4E4$	$7.88E6 \pm 8E4$
	GM	$1.96E6 \pm 3E4$	$3.30E6 \pm 2E4$	$5.34E6 \pm 5E4$	$8.19E6 \pm 9E4$	$8.08E6 \pm 7E4$
$\sigma$ [ $e^-$ ]	MI	$8.64E5 \pm 1E4$	$1.56E6 \pm 2E4$	$2.84E6 \pm 2E4$	$4.49E6 \pm 5E4$	$4.51E6 \pm 5E4$
	CM	$9.05E5 \pm 9E4$	$1.56E6 \pm 1E4$	$2.66E6 \pm 2E4$	$4.26E6 \pm 3E4$	$4.34E6 \pm 5E4$
	GM	$7.73E5 \pm 3E4$	$1.38E6 \pm 2E4$	$2.35E6 \pm 2E4$	$3.80E6 \pm 3E4$	$3.81E6 \pm 3E4$
$\ln\left(\frac{\mathcal{L}_{CM}}{\mathcal{L}_{GM}}\right)$		-14.5	17.2	257.4	567.2	183.8

Table B.1: Comparison of model independent (MI), cascade model (CM), and Gaussian model (GM) using the R11410 PMT.

directly to the model independent method and the Gaussian model.

The results of the fit are shown in Tab. B.1. In the table,  $\eta$  is the attenuation factor of the filter in between the laser and PMT,  $\lambda$  is the mean number of photoelectrons per light pulse, and  $\mu$  and  $\sigma$  are the mean and standard deviation of the resulting SPE response function. All uncertainties shown are statistical. Note that the model independent (MI) results and the cascade model (CM) results agree typically within a few percent and never disagree by more than 10%.

Also of note in Tab. B.1 is the row  $\lambda_{FA}$  denoting the mean number of photoelectrons fully amplified. Unlike the other  $\lambda$  measurements,  $\lambda_{FA}$  should be approximately voltage independent since underamplification effects are removed. As can be seen, all  $\lambda_{FA}$  with the same attenuation  $\eta$  agree within  $\sim 1\%$ , providing a cross-check on the cascade model fit.

Another very important feature of the table is the last row, which compares the best-fit log-likelihood of the cascade model to the best-fit log-likelihood of the Gaussian model. The cascade model significantly outperformed the Gaussian model in four out of five of the datasets. Unsurprisingly, the dataset where the Gaussian model outperforms the cascade model is when the voltage is lowest and the valley in between the background and single photoelectron peak plays the smallest role in the fit. This

Voltage [V]	$\eta$	Reduced $\chi^2$	$p_{\chi^2}$	$p_{KS}$
1400	2E5	0.67	0.991	0.274
1500	2E5	0.95	0.604	0.259
1600	2E5	0.90	0.742	0.287
1700	2E5	1.28	0.037	0.327
1700	1E5	0.98	0.539	0.279

Table B.2: Goodness of Fit Tests For R11410 with Cascade Model.

improvement is likely due to the increased freedom in the Gaussian model since the underamplified peak is almost entirely independent of the fully-amplified peak.

Fig. B.2 shows the best-fits for both the cascade model (blue) and the Gaussian model (red) compared to laser calibration charge data along with the 95% credible regions of each fit. Notice that as the gain increases, the Gaussian model is unable to explain the behavior in the valley while the cascade model predicts this behavior well in all five spectra.

In Fig. B.3 one can see the predicted SPE charge response for the R11410 PMT at 1500 V without background convolution. The region shown is again the 95% confidence interval. One can see the three major features going from left to right: the underamplified peak from photons striking the first dynode, the underamplified peak from a non-ideal trajectory, and the fully-amplified peak. Note that the signal can naturally never be less than zero unlike most analytical models that are either truncated or allowed to extend into a non-physical region. The fully-amplified signal (right-most peak) is fairly symmetric - this is because this PMT operates at high gain and has good resolution. This, however, will not be the case when looking at the fully-amplified peak for the R6041-406 PMT in Sec. B.4.3.

Shown in Tab. B.2 are the results of the goodness of fit tests for the best-fit parameters. Since the parameter estimation is performed in a single dimension, one can look at the relatively simple  $\chi^2$  test and the more robust Kolmogorov-Smirnov (KS) test. While there is more fluctuation from the  $\chi^2$  test, all tests show little or no evidence against the cascade model.

## B. CHARACTERIZATION OF PHOTOMULTIPLIER TUBES WITH THE CASCADE MODEL

---

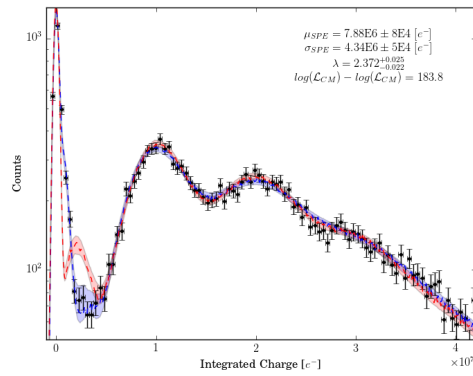
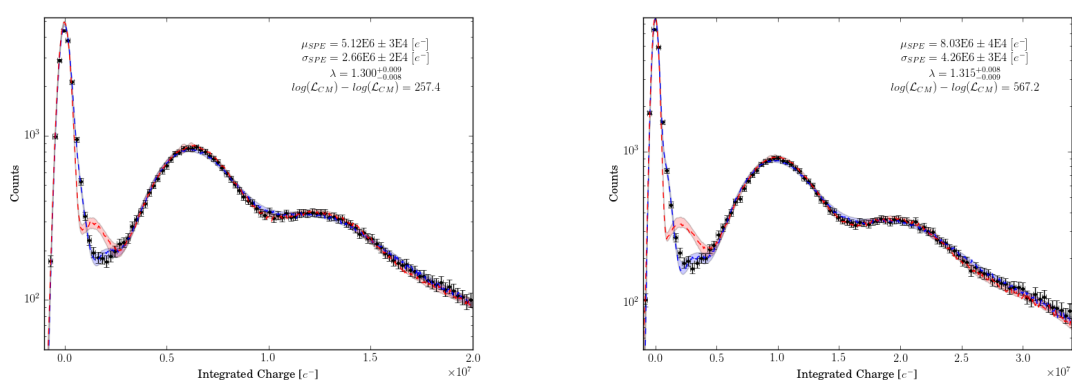
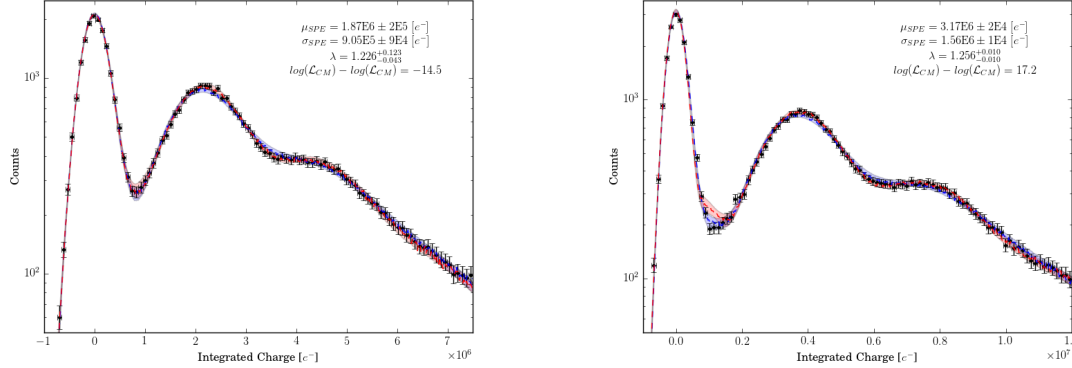


Figure B.2: The laser calibration charge spectra for the R11410 PMT at different voltages and attenuation levels with the best-fit models and 95% credible regions overlaid. The cascade model is shown in blue while the Gaussian model is shown in red. The statistics shown are for the cascade model.

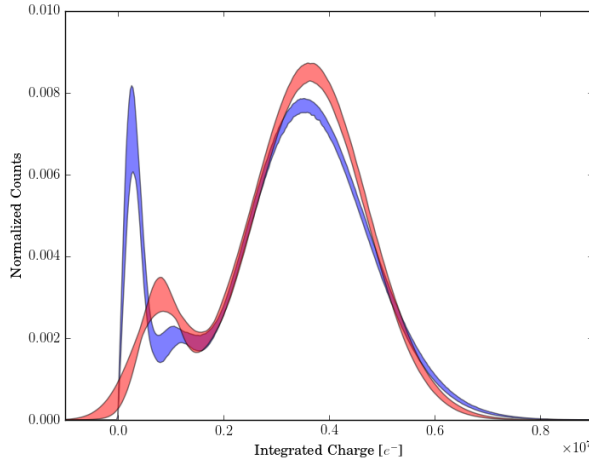


Figure B.3: The predicted SPE charge response for the R11410 PMT at 1500 V for the cascade model (blue) and the Gaussian model (red). In the cascade model SPE charge response spectrum one can see, from left to right, the three major features: the underamplified peak from photons striking the first dynode, the underamplified peak from a non-ideal trajectory for electrons from the photocathode, and the fully-amplified peak. At such a high gain the fully-amplified peak (right-most) of the cascade and Gaussian models agree. However, there is a large discrepancy in the region of underamplified electrons.

Voltage [V]		800	800
Light Level		I	II
$\lambda$	CM	$1.237^{+0.070}_{-0.042}$	$2.455^{+0.148}_{-0.140}$
	GM	$1.403^{+0.064}_{-0.046}$	$2.709^{+0.108}_{-0.098}$
$\mu$ [e <sup>-</sup> ]	CM	$8.43E5 \pm 4.8E4$	$8.53E5 \pm 6.8E4$
	GM	$7.57E5 \pm 3.2E4$	$7.50E5 \pm 2.3E4$
$\sigma$ [e <sup>-</sup> ]	CM	$5.61E5 \pm 1.7E4$	$5.89E5 \pm 1.7E4$
	GM	$5.79E5 \pm 1.1E4$	$6.00E5 \pm 1.2E4$
$\ln\left(\frac{L_{CM}}{L_{GM}}\right)$		4.9	11.9

Table B.3: Comparison of cascade and Gaussian models using the R6041-406 PMT.

### B.4.3 Hamamatsu R6041-406 Analysis

In addition to the analysis performed with a PMT capable of large gains, the cascade model was also used to calibrate a PMT that must operate at significantly lower gains and with worse noise conditions. While a background measurement was taken, since

## B. CHARACTERIZATION OF PHOTOMULTIPLIER TUBES WITH THE CASCADE MODEL

---

Voltage [V]	Light Level	Reduced $\chi^2$	$p_{\chi^2}$	$p_{KS}$
800	I	1.39	0.009	0.361
800	II	1.50	0.002	0.353

Table B.4: Goodness of Fit Tests For R6041-406 with Cascade Model.

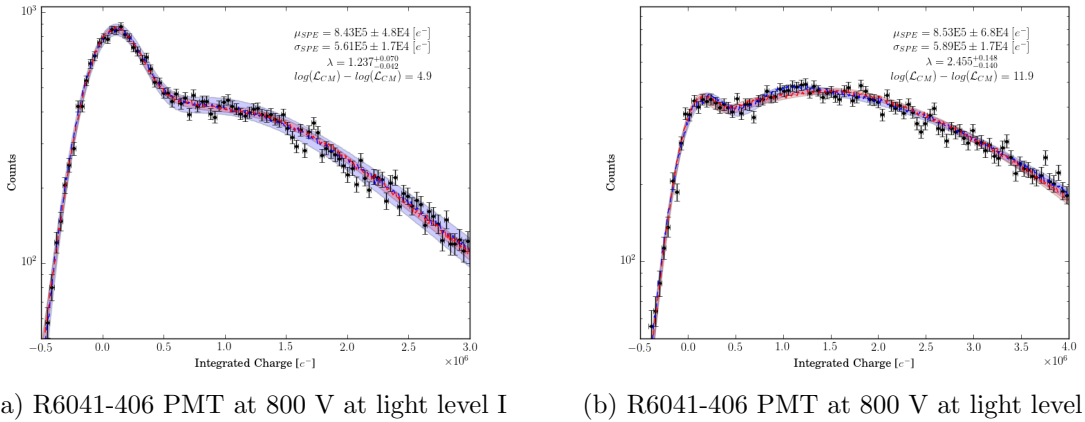
the calibration is done *in situ* with an LED and pulser it is impossible to confirm that noise conditions were the same between the dedicated background measurement (pulser off) and the measurements with the pulser on. For this reason and given that the width of the background peak is on the order of the SPE response, the model independent approach cannot be used.

Since the dedicated background measurements for this PMT could not be used, one would normally try multiple background models to study the potential systematic effects. However, in this work, only the Gaussian background model is examined for consistency.

In this specific calibration, two light levels were used which are denoted I and II corresponding to different pulser voltages used in conjunction with a blue LED. While for the detector discussed in Ref. [91] these two light levels were fit simultaneously, only the results from individual fits are shown for consistency.

The results of the parameter estimation and the goodness of fit tests are shown in Tab. B.3 and Tab. B.4. The best fit and the 95% credible region for each light level can be found in Fig. B.4. While the  $\chi^2$  test shows evidence against the cascade model, it seems that this is solely due to the behavior in a handful bins that fall outside of the 95% credible region as seen in both spectra in Fig. B.4. This hypothesis is further supported by the results of the Kolmogorov-Smirnov test, which shows no evidence against the cascade model. As a further cross-check, one can also compare the mean and standard deviation of the response function from both light levels which agree with each other well within uncertainty.

While the cascade model outperforms the Gaussian model in fit quality, as seen in the log-likelihood difference, the real power of the cascade model can be seen in Fig. B.5, which shows the fully-amplified peak only for both models without background convolution. Notice again that the cascade model naturally begins at zero



(a) R6041-406 PMT at 800 V at light level I      (b) R6041-406 PMT at 800 V at light level II

Figure B.4: The diode calibration charge spectra for the R6041-406 PMT at 800 V with the best-fit models and 95% credible regions overlaid. The cascade model is shown in blue while the Gaussian model is shown in red. The statistics shown are for the cascade model.

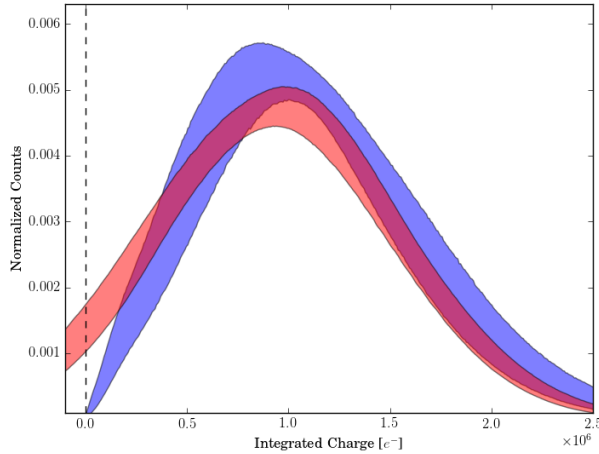


Figure B.5: The predicted fully-amplified photoelectron response for the R6041-406 PMT at 800 V. Notice the asymmetry in the cascade model response (shown in blue) and how far into the unphysical regime the Gaussian model response goes (shown in red).

signal and has the asymmetry that one would expect while the Gaussian model predicts negative signal roughly 15% of the time from the fully-amplified peak. Clearly this prediction is not physical and would cause issues in MC simulations of the PMT.

## B.5 Conclusions

While the form of the cascade model presented will change for each type of PMT used in a different setting, we have shown that for the PMTs used in these two experiments that the cascade model is a much more realistic approximation of the photomultiplication process, agrees well with data, and is a drastic improvement in almost all cases versus the Gaussian model that is typically used for characterization of photomultipliers. It is important that in future applications, the analyzer checks different sources of underamplified electrons and different background models if a dedicated background measurement was not performed. Parameters of the model may be further constrained by estimating them with multiple light levels fit simultaneously.

We recommend that the cascade model be used in conjunction with the model independent prescription described in detail in Ref. [113]. Since it is relatively unlikely for a PMT’s characteristics to change during a measurement, we recommend that an initial characterization be performed using the cascade model and cross-checked with the model independent estimation. Following the initial characterization, performance can be monitored solely by the model independent estimation with the cascade model reserved for spot checks and diagnosis if PMT performance changes.